ENGINEERING CRITICAL ASSESSMENT OF THE CYLINDRICAL STEEL SHELL STRUCTURES

Teză destinată obţinerii
titlului ştiinţific de doctor inginer
la
Universitatea Politehnica Timişoara
în domeniul "INGINERIE CIVILĂ"
de către

Eng. Dorin RADU

Conducător ştiinţific: Prof.univ.dr.ing. Radu BĂNCILĂ
                           Prof.univ.dr.ing. Aleksandar SEDMAK
Referenţi ştiinţifici: Prof.univ.dr. ………………………..
                           Prof.univ.dr.ing. ………………………….
                           Conf.univ.dr.ing. ………………………….

2017

Seriile Teze de doctorat ale UPT sunt:

1. Automatică
2. Chimie
3. Energetică
4. Ingineria Chimică
5. Inginerie Civilă
6. Inginerie Electrică
7. Inginerie Electronică şi Telecomunicaţii
8. Inginerie Industrială

9. Inginerie Mecanică
10. Ştiinţa Calculatoarelor
11. Ştiinţa şi Ingineria Materialelor
12. Ingineria sistemelor
13. Inginerie energetică
14. Calculatoare şi tehnologia informaţiei
15. Ingineria materialelor
16. Inginerie şi Management

Universitatea Politehnica Timişoara a iniţiat seriile de mai sus în scopul diseminării expertizei, cunoştinţelor şi rezultatelor cercetărilor întreprinse în cadrul Şcolii doctorale a universităţii. Seriile conţin, potrivit H.B.Ex.S Nr. 14 / 14.07.2006, tezele de doctorat susţinute în universitate începând cu 1 octombrie 2006.

Copyright © Editura Politehnica – Timişoara, 2017

Cuvânt înainte

Teza de doctorat a fost elaborată pe parcursul activităţii mele de cercetare în cadrul Univeristăţii din Belgrad – Facultatea de Inginerie Mecanică precum şi în cadrul Universităţii Politehnica din Timişoara, Facultatea de Construcţii, departamentul de Construcţii Metalice şi Mecanica Construcţiilor.

Aş dori să mulţumesc tuturor celor care m-au sprijinit şi inspirat pe parcursul stagiului doctoral.

Doresc sa le aduc mulţumirile mele şi profundă recunoştinţă conducătorilor ştiinţifici ai pezentei teze de doctorat, Prof. dr. Ing. Radu Băncilă şi Prof. dr. Ing. Aleksandar Sedmak, pentru îndrumarea cercetării, realizarea experimentelor, sprijinul şi încrederea acordate pe întreaga perioada a stagiului.

Sunt în mod special recunoscător d-lui Conf. Dr. Ing. Edward Petzek şi d-lui Dr. Ing. Horia Daşcău, care au fost o sursă constantă de sfaturi şi sprijin în toată această perioadă.

Nu în ultimul rând aş dori să le mulţumesc colegilor, în special ing. Ciprian BRATU pentru sprijinul acordat.

Nu în ultimul rând aş dori să mulţumesc familiei, în special soţiei şi fiicei mele pentru că m-au înţeles atunci când eu nu am putut sa-mi aloc timp ca să fiu alături de ele.

Timişoara, Ianuarie, 2017   Ing. Dorin RADU

Numele autorului tezei, Prenumele autorului tezei

Titlul tezei

Teze de doctorat ale UPT, Seria X, Nr. YY, Editura Politehnica, 2017, 309 pagini, 283 figuri, 442 tabele, 4 anexe.

Cuvinte cheie: structuri metalice de tip shell, mecanica ruperii, evaluarea duratei de viata a structurilor

Rezumat, Teza prezintă în mod detaliat o metodologie de evaluare și determinare a acceptabilității defectelor decelate în structurile metalice de tip shell. Pe baza principiilor mecanicii ruperii, sunt prezentate proceduri și reguli necesare în intreținerea, expertizarea și verificarea acestor tipuri de structuri. Această metoda de evaluare a defectelor/fisurilor reprezintă primul pas intr-o metodologie complexă bazată pe principiile mecanicii ruperii și urmată apoi de o analiza la oboseală a elementelor evaluate, analiză prin care se determină durata în exploatare până la cedare pentru structura/elementele structurii

Contents

Tables list

Figures list

1. INTRODUCTION

1.1. Scope and objectives of the research

Codes for design and execution of buildings, bridges, offshore structures, process plants etc. normally contain acceptance criteria that are based on workmanship standards that may be somewhat arbitrary. Most welding fabrication codes specify maximum tolerable flaw sizes and minimum tolerable Charpy energy, based on good workmanship, i.e. what can reasonably be expected within normal working practices.

During the construction phase or in service, there may be situations where materials properties or observed defects do not meet the strict code requirements. In such cases a **fitness-for-service assessment** can be applied. Such an approach is nowadays becoming accepted by many codes as it is recognised that the requirements or acceptance criteria inherent in the codes may be unnecessarily conservative. Using this alternative approach it can be shown that the structure or component can be acceptable if the conditions for failure are not reached within its service life. There are many possible damage or degradation mechanisms which must be considered. These include brittle and ductile fracture, fatigue, environmental assisted cracking and creep at higher temperatures.

The fitness for service assessment procedure is also known as **Engineering Critical Assessment (ECA)**. An ECA can therefore be used:

1. During design, to assist in the choice of welding procedure and/or inspection techniques.
2. During fabrication, to assess the significance of:
   a) known defects which are unacceptable to a given fabrication code, or
   b) a failure to meet the toughness requirements of a fabrication code.
3. During operation, to assess flaws found in service and to make decisions as to whether they can safely remain, or whether down-rating/repair are necessary.

There are several standards and provisions available that describe the fitness-for-service and ECA approaches. The analysis is carried out in accordance with the British Standard procedure BS 7910 (*'Guide to methods for assessing the acceptability of flaws in metallic structures'*) [1.5].

An ECA can also be used to assess the significance of growing flaws, e.g. fatigue, creep or stress corrosion cracks, in order to make decisions on life extension and safe inspection intervals.

Analysis of a welded structure with flaws or flaw indications can document the assessor if there are critical cracks within the remaining service life and whether the structure may be used without risk of failure.

The flaws may be found after completed welding or after a subsequent inspection. Fracture mechanics analyses may reduce the costs of flaws found in a structure as not all flaws are critical.

The present research is focussed around fracture mechanics analysis of critical flaws in welds, considering both crack growth and sudden fractures for steel shell structures.

If the repair is costly or comprehensive, fracture mechanics is a very serviceable tool with which to assess flaws found in welds. Not all flaws are critical to the service life, and by analysis can be assessed whether the flaw will reach a critical size within the structure's service life.

In order to make a fracture mechanics analysis, knowledge of the mechanical properties of the material including fracture mechanics values such as K_{IC}, *CTOD* or J_{IC} are required. There must be known also the stress to which the weld is exposed.

Flaws in welds are often found by visual inspection or various NDT methods such as ultrasound or x-ray. When there is detected a flaw, the repair may be very costly if the structure is hard-to-get-to, or if the repair requires out of service of the structure. When flaws or flaw indications have been detected in a weld, many companies choose the immediate solution - repair.

Considering a fracture mechanics approach for a specific structure with a large number of welded joints, with analysis of all flaw indications, the with flaw elements can be divided in with various indications into three categories:

- o Safe in which the flaw/flaws will not grow to a critical size during the service life
- o safe if regularly inspected, the flaw/flaws is on the borderline of reaching a critical flaw size during the service life, and regular inspection is therefore necessary
- o repair is mandatory – the flaw/flaws are already so critical that there is every possibility of failure and they thus exceed the permissible risk in terms of safety

The research is considering the steel shell structures and structure shell elements and is addressed to the following types of structures:

- o buildings steel structures.
- o wind turbines
- o offshore industry
- o bridges

The main research objectives are:

- Describing the assessment parameters for ECA
- Assessment procedures and standards applied
- Fracture mechanics approach in steel shell structures flaws assessment
- Types of flaws – assess structural implications
- Risk analysis for different flaws
- Life time service assessment for steel shell structures
- Determining the inspections intervals
- Study case - FEM approach to a steel shell structure – detailed analysis
- Experimental research – determining the material characteristics and fracture mechanics parameters

1.2. Shell Structures

Shell structures have a long history and have existed since before structural engineering and architecture were even recognised sciences; one of the oldest known example of a concrete shell being the Pantheon dome in Rome which was completed sometime around 125AD.

From an early age the aesthetics of shells and their natural strength and stability has been well known, despite the lack of mathematical reasoning behind them. Dome structures continued to be the most significant shell structure for quite some time and are visible throughout history as part of many cathedrals, mosques and mausoleums up until the early 20th century where shell structures underwent a revival.

During the 20th century a greater understanding of the mechanical properties of shell structures was developed, not only were their aesthetics appreciated but also the economy of such structures due to their efficient load distribution. This knowledge however was mainly only applicable to geometrically regular curved surfaces which can be easily described by analytical mathematical functions. With the advent of computational technology and in particular FEM (Finite Element Modelling) engineers and architects could model more complex shapes and venture into the analysis of more free form structures. The increased capability and desire for free form shell structures is evident in many designs from well known architects such as Zaha Hadid architects, Future Systems, ONL Oosterhuis, Norman Foster and Partners, Asymptote Architects and UN Studios.

With this drive toward more complex geometry there is a demand for increased research and design procedures for these structures and in the instance of shells, where form and force are so intricately linked, it seems that the engineering aspects are lagging behind the architectural demand.

Steel shell structures experienced a vast development in the last decade and nowadays there is a large demand on shell type elements due to various possibilities of structures – from silos and wind turbines, to marine platforms.

Cylindrical shell structures are often subjected to compressive stresses in the direction of the cylinder axis, which can be either uniform or varying throughout the cylinder.

Structural members subjected to compression are susceptible to Euler buckling, and the Euler buckling stress of a given quantity of material is at its greatest when all the material is placed as far as possible from the axis. This makes the thin cylindrical tube or shell the most efficient form for compression members. However, as the tube wall becomes thinner, other local forms of buckling intervene, and these shell buckling modes control the strength of steel shell cylinders. Compression members of this form include aircraft, spacecraft and terrestrial vehicles, as well as components of bridges, offshore platforms and other civil engineered structures.

Shell structures are also very efficient for containment of fluids and solids, with thin walled vessels being commonly used for both tanks and silos. The low resistance to shell buckling of shells means that buckling is a primary design concern.

1.3. Cracking as a welding flaw

When the weld procedure is wrong, or the welder lacks sufficient skill, a number of welding defects can occur, but the most damaging type of defect to the integrity of the weld are **cracks**. The term '*crack*' to a welding engineer usually means a sharp planar defect with a metallurgical cause, such as *hydrogen cracks* or *solidification cracks*. Many welding quality standards differentiate between metallurgical '*cracks*' and lack-of-fusion flaws, although the latter may also be planar (and can be just as damaging to the structural integrity). To a welding engineer a '*crack*' implies that the weld procedure is inherently flawed, whereas lack-of-fusion defects may simply occur sporadically because of the welder's (lack of) skill [1.1].

1.3.1. Types and leading cause of welding cracks occurrence

Hydrogen cracking
For carbon steels, the principal type of weld cracking to avoid is hydrogen cracking (also called cold cracking or sometimes hydrogen-induced cold cracking or HICC [1.1]) (Figure 1.1.). Atomic hydrogen is very mobile (i.e. diffuses very quickly) within steel at temperatures above about 250 °C, since hydrogen's small atoms can move easily through the gaps in the crystal structure ('*lattice*') of iron and carbon atoms which make up the steel.
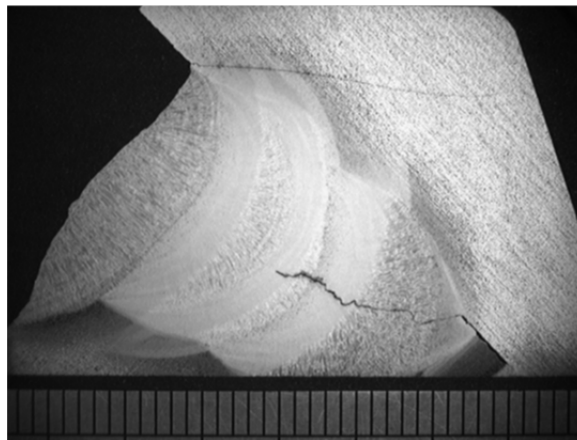
Fig. 1.1 *Hydrogen crack initiated from the root of a multipass weld (scale bar is in millimetres) [1.1]*

Hydrogen can enter steel during welding from the breakdown of hydrocarbons such as oil or grease, or from moisture, either on the parent plate or welding consumables. When the weld then cools to ambient temperature the hydrogen atoms subsequently become trapped in the steel's crystal structure, reducing its ductility and causing it to become **embrittled**. Under the application of a stress (which can simply be the residual stress from welding) cracking can occur in susceptible microstructures, typically those with high hardness. The critical combination of all four factors (presence of hydrogen, stress, low temperature, and

a susceptible microstructure such as one with high hardness) is necessary for hydrogen cracking to occur, and its avoidance is based on removing or reducing one or more of these four factors. The joint inevitably cools to ambient temperature eventually, but by delaying the cooling it is possible to allow any remaining hydrogen to diffuse out of the steel while it is still mobile in the hot steel. Preheating the workpiece slows the rate of cooling, as does applying further heating before the weld has had a chance to cool. Once the steel has cooled down, it can take up to 48 h for hydrogen cracking to occur, so inspection might have to wait some time after welding in order not to 'miss' any hydrogen cracks in the weld.

High hardness is most likely in steels with higher amounts of carbon and manganese. The risk of hydrogen cracking is linked to the carbon equivalent of the steel – a parameter calculated from the steel's composition of all susceptible elements proportionate to their relative contribution to hardness. Steels with medium and high carbon equivalent levels are more '*hardenable*', which means they are more likely to form hard phases such as *martensite* in the HAZ upon rapid cooling. A weld in steel with a carbon equivalent of 0.4–0.5 or above is hard enough to give a significant risk of hydrogen cracking. Hydrogen cracks occur in the location of the weld where the hardness is highest, which can either be the HAZ or the weld metal depending on the type of steel and welding procedure. Welding procedures for medium and high carbon equivalent steels include requirements for preheat, a minimum interpass temperature to maintain between welding passes until the joint is completed, and usually a post-weld heat treatment (PWHT). The PWHT not only helps retard the cooling rate, avoiding martensite formation, and allowing any atomic hydrogen to escape from the steel while at a temperature where it is still mobile, but also reduces the level of residual stress [1.1].

For all welding it is important to de-grease plate surfaces, ensure adequate gas shielding of the weld pool and remove moisture. If hydrogen cracking is a likely risk when welding it is possible to select low-hydrogen welding consumables which must be stored in carefully dried conditions (or supplied in vacuum packs). Gas-shielded welded processes are less susceptible to hydrogen cracking than flux-shielded electrodes in MMA welding, which can absorb moisture in the porous flux.

Solidification cracking

The second major type of cracking to avoid when welding carbon steels is solidification cracking (also known as **hot cracking**), shown in Figure 1.2. This type of cracking occurs in steels with relatively high levels of impurities such as sulphur and phosphorus, as well as those welds with a susceptible deep and narrow weld cross section profile. Solidification cracking occurs as the weld pool is solidifying, when new metal grains nucleate and grow from the edges of the weld pool toward the centre of the weld. In a perfectly round, hemispherical weld pool, the solidifying grains grow at the same rate from all the outer surfaces of the weld pool and meet at the point in the middle. However, a weld pool is not static, but moves as the welding torch moves, so the hemisphere of molten steel moves along the joint line, and solidifies behind the direction of travel, with the final solidification effectively tracing a line along the middle of the surface of the weld. In sufficiently deep and narrow welds, the solidification fronts do not grow in from the outer edges of a circle, however, but effectively grow as a straight line from the sides of a cylinder. These solidification fronts meet along a plane down the centre of the weld. The last liquid to solidify is iron sulphide, formed from the sulphur in the steel which has a lower melting point than the steel. This iron sulphide then forms along the centreline plane and tries to accommodate all the shrinkage stresses of the weld. However,

iron sulphide has poor ductility, thus causing ruptures in the form of a solidification crack along the centreline of the weld.
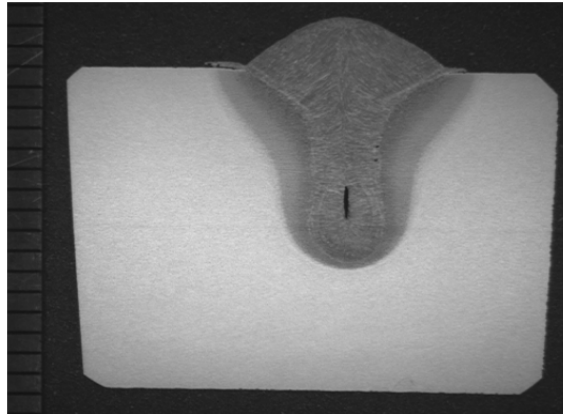
Fig. 1.2 *Solidification crack along the centreline near the root of a bead-on-plate laser-arc hybrid weld (scale bar is in millimetres) [1.1]*

Deep and narrow weld beads are susceptible to solidification cracking owing to the shape of the solidification front (Figure 1.2). This type of weld profile could be from high heat input arc welding processes such as GMAW and SAW. Alternatively, 'keyhole' welding processes such as laser welding and electron beam welding usually result in very deep and narrow welds. Susceptible arc weld profiles can be improved by changing the welding procedure to include a larger number of smaller, shallower weld passes.

The avoidance of solidification cracking is also achieved through the reduction of the amounts of sulphur and phosphorus in the parent steel, as well as modification of the weld joint design. Cleaner, more modern, steels have very low sulphur levels and therefore solidification cracking is very rare. However, when steel is sourced from less established suppliers it is possible to find that solidification cracking problems return owing to the presence of sulphur and phosphorus in these steels. A multipass weld with a larger number of shallower weld passes instead of a single deep penetration weld bead is less susceptible to solidification cracking, but imposes a penalty in terms of productivity and weld completion time.

Other types of weld defect

In general, weld shape imperfections are often the result of either a lack of welder skill or poor weld fi t-up, whereas cracking during welding is often caused by either using an inappropriate welding procedure, choosing the wrong consumable, handling consumables poorly, or contamination in the weld. Once the weld enters service however, it then becomes susceptible to a further set of cracking mechanisms, including fatigue, corrosion, creep, or various kinds of stress corrosion cracking. The susceptibility of a joint to different failure mechanisms resulting from its in-service conditions can be assessed by mechanical testing. For example, a weld which is to be exposed to potentially corrosive conditions in service can be subjected to a corrosion test in which a piece of weld is exposed to that chemical environment, to see whether cracking occurs or not.

There are other types of fabrication and service cracking associated with welds in specific alloys, such as reheat cracking in the course-grained HAZ in Cr–

Mo–V steels for high-temperature service; sigma-phase embrittlement in the ferrite phase of stainless steels exposed to elevated temperatures; lamellar tearing in rolled carbon steel plates containing stringer inclusions and through-thickness weld stresses, etc.

The welding engineer needs to have a thorough appreciation of all the weldability issues associated with the particular alloy being welded and of its intended service conditions. However, the intention of this book is not to be a compendium of weld cracks, but to give an indication of the most common kinds of weld defects and their significance in terms of fracture and fatigue.

All cracks and planar defects are significant when considering the resistance of a welded structure to fracture and fatigue. These defects are the most likely initiation site for a brittle fracture, or for the propagation of a fatigue crack and, therefore, an understanding of the causes of possible weld flaws is the first stage in avoidance of failure.

Welding residual stresses

Even in nominally '*defect-free'* welds, there is still a hidden source of concern for the structural integrity engineer. The heating and cooling of the weld pool and surrounding material is associated with thermal expansion and then contraction, but the small weld pool is constrained within the solid parent material and thus the localised thermal expansion and contraction cannot happen freely. This is illustrated schematically in Figure 1.3 a, where the weld metal which has just solidified, is hot and takes up the same volume as the weld groove. If this weld metal could cool down in an unrestrained way it would contract owing to thermal shrinkage (Figure 1.3 b).

However, the weld metal is not able to cool in an unrestrained way, because the surrounding parent metal prevents this contraction. As the weld metal cools down, it is not allowed to shrink and therefore high tensile residual stresses are introduced in the weld metal (Figure 1.3 c). These residual stresses remain after the joint is completed and can be as high as the yield strength of the parent material. Any stress greater than this causes localised yielding of the material which then limits the residual stress to the yield strength. The actual residual stress distribution varies through the thickness of the weld, and is different along the length of the weld and across the weld. The tensile residual stresses near the surface of the weld are balanced by compressive residual stresses elsewhere in the joint. The residual stress distribution also depends on the weld size and the heat input used for welding. Therefore making any assumptions about the residual stresses locked inside a welded joint can be very tricky and it is often simply assumed that the residual stresses in the vicinity of an as-welded joint are tensile and of yield magnitude.
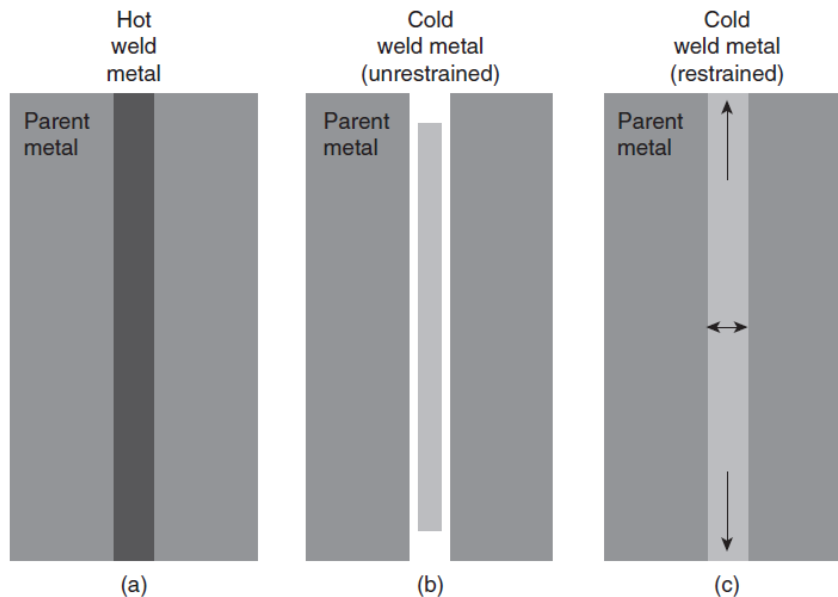
Fig. 1.3. *Schematic diagram of residual stresses resulting from differential thermal expansion and contraction between the weld metal and surrounding parent metal [1.1]*

Although there are a number of techniques that can measure residual stresses, many of them are destructive techniques that can be used on test welds, but not on welds in-service. Some of the simpler methods to apply, such as centre hole drilling, only measure the residual stress at the plate surface, giving no information about the residual stresses in the centre of the plate. The most accurate methods, such as **neutron diffraction**, are very expensive research techniques which are not applied commercially. Usually, it is necessary to make some conservative assumptions about the residual stresses in a weld joint when making calculations about the effect the residual stresses might have on the joint's resistance to fracture or fatigue.

Residual stresses alone can be enough to cause brittle fracture in steels with sufficiently low fracture toughness. This was the then unknown cause of many of the Liberty ship failures that cracked without the ships seeing any seaborne service.

Where brittle fracture is a risk, particularly for steel greater than 25 mm thick, then post-weld heat treatment (PWHT, also called stress relief) is routinely required in order to bring the residual stresses down to 20–40% of the yield strength from as high as yield magnitude. For carbon manganese steels, PWHT is usually performed at a temperature of 550–625 °C and held for around an 'hour per inch' (25 mm) of plate thickness, in addition to a controlled heating and cooling period. The residual stresses associated with welds can also make so-called 'repair' welds critical to the integrity of an overall structure, because it is often difficult to control PWHT of repair welds, if PWHT is performed at all. Repair welds can leave yield strength level residual stresses (and defects) in a location which had previously been stress relieved. This could be more damaging to the structural integrity of the structure than simply leaving the existing flaw alone [1.1].

Distortion

The thermal expansion and contraction stresses in the weld (which are initially greater than the yield strength of the steel) cause localised yielding to occur around the weld. In some situations, permanent and significant deformation may result from this localised yielding at the weld, known as weld distortion. In thinner section material and sheet metal, or in alloys with a low yield strength or large thermal expansion coefficient (such as aluminium and stainless steel), the residual stresses are sufficient to deform the whole sheet and significantly distort the welded structure.

Weld distortion can present itself in a number of ways. Simple shrinkage of the weld metal, both along the weld, and transverse to the weld alters the dimensions of the final welded component. Where this shrinkage is not uniform through the thickness of the plate, angular distortion may be introduced where the two sides of a butt weld bend upwards, or a fillet welded attachment moves away from vertical.

The buckling of welded structures can significantly affect their performance as well as their appearance. Buckling occurs when the distortion of a structure under loading causes the beam or member to distort in an unstable elastic and unrecoverable manner. A welded structure which has suffered from weld distortion no longer has the most rigid dimensional shape, and a distorted beam is susceptible to an unstable buckling condition under much lower loading than a beam without the weld distortion [1.3].

Most steels have high stiffness and do not deform significantly under load, so weld distortion tends to be a cosmetic concern rather than a safety issue. However, for aluminium structures which have inherently lower stiffness than steels, but are also susceptible to weld distortion, buckling resistance is a main design failure mode, and excessive distortion associated with welds can cause a component to be scrapped. Even in steel structures, remedying distortion can form a major cost of a welding project.

Distortion can be avoided or reduced by using jigs and fixtures for welding, but this may introduce higher residual stresses. Plates can be pre-set at an angle equal to the expected distortion so that the welding subsequently brings them flat. Correcting distortion is mainly based on localised pressing or hammering to restore the correct dimensions to the component. It is also possible to use thermal techniques such as local flame heating to introduce deformation to oppose the weld distortions. There is great skill in applying thermal techniques correctly so that the required shape is achieved without damaging the mechanical properties of the structure.

Studies of brittle fracture have shown that failure occurs by the initiation of a crack, usually at a notch or stress raiser. The crack then propagates extremely rapidly across the load-bearing area at a velocity approaching the speed of sound in the material. In some instances, the running brittle crack may stop or arrest, particularly if it grows into a region of lower stress or higher toughness material. The brittle fracture usually initiates at a single point (at the notch or stress raiser) and, therefore, the material toughness and microstructure at this particular location is of vital importance. In structures, brittle fracture can occur without warning as there is usually no prior plastic deformation at the initiation of fracture. The first evidence of a brittle fracture may be when a plate cracks or a pressure vessel explodes. Furthermore, because the brittle crack propagates very rapidly across the load-bearing member, catastrophic failure often results in loss of life and significant damage to equipment. Welded joints are particularly susceptible to brittle fracture

because they are inevitably associated with a stress concentration and the complex microstructures in the vicinity of the joint may contain a region of very poor toughness even if the parent material has good toughness.

Figure 1.4. gives a schematic overview of the cracks in welded joint according to size, propagation and cause.
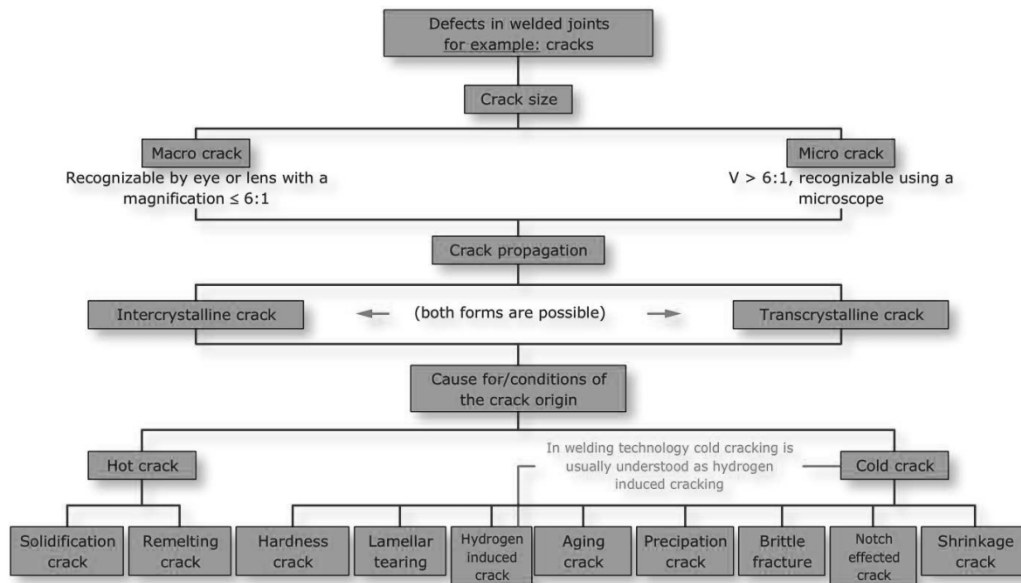
Fig. 1.4. *Scheme of cracks in welded joints according to size, propagation and cause*

Considering the fusion welded joints, can be made a classification of the welding imperfections (figure 1.5.):
- Direction of the crack
    o Longitudinal crack (a)
    o Transversal crack (b)
- Inclusions and pores
    o Pore (c)
    o Wormhole (d)
    o Localized porosity (e)
    o Linear porosity (f)
- Cavities, notches and discontinuities
    o Slag inclusion (h)
    o Shrinkage cavity (g)
    o Incomplete penetration (i)
    o Lack of inter-run fusion (j)
    o Lack of sidewall fusion (k)
    o Root notch (l)
    o Incompletely filled groove (o)
- Misalignment of steel parts
- Overlap (p)
- Edge misalignment (q)
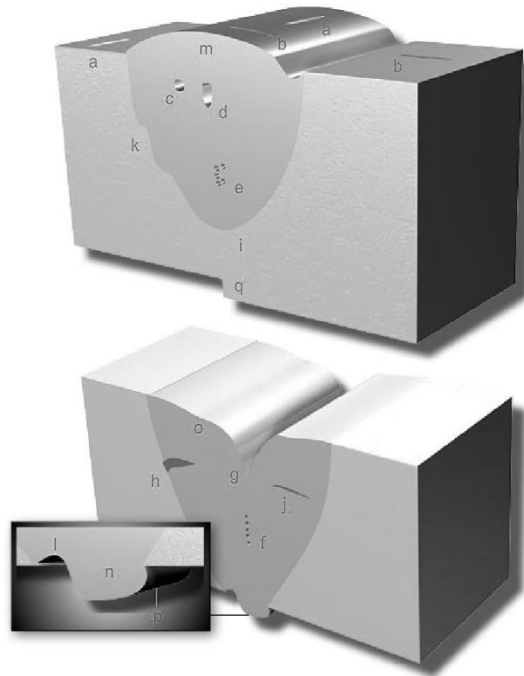
Fig. 1.5. *Fusion welding imperfections*

ISO 5817 standard – Arc welding joints in steel, guidance on quality levels for imperfections [1.2], is presenting 26 types of weld imperfections for ease of assessment during visual inspection or NDT testing of the welded joints. The main causes for these imperfections and their implications, are presented below (figure 1.6.):

- Spatter and arc strikes. These are surface flaws that are potential fatigue flaw initiation types
- Gas porosity. This type of flaw is due to the contamination of the damp electrodes
- Centerline cracking resulted from too high tensile stresses on cooling
- Heated affected zone (HAZ) cracking due to formation of martensite (brittle) on cooling of austenite
- Martensite formation in the HAZ – change of HAZ microstructure
- Overlapping is a flaw induced by the high speed welding process or as result of low power welding
- Lack of penetration is a flaw induced also by the non stable welding speed process – too low speed
- Undercutting and root concavity is a flaw produced by the too high power in the welding process
- Slag entrapment is a flaw produced by the unclean slag between different welding seams
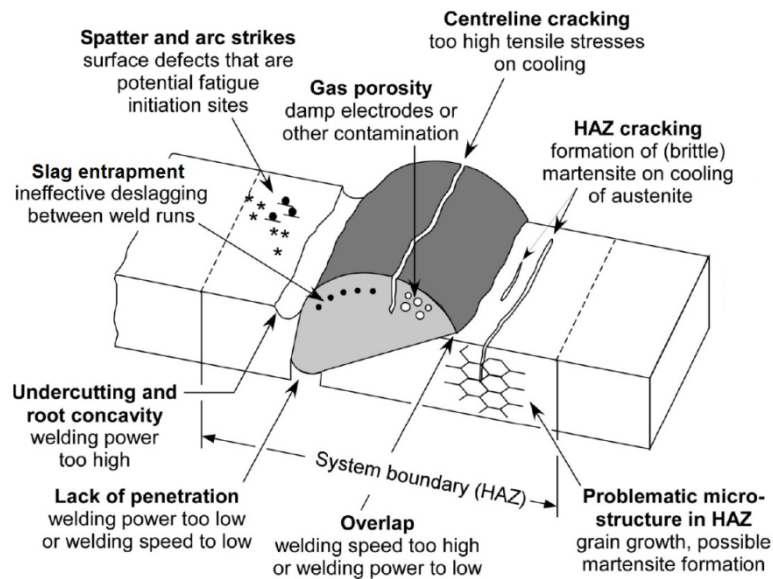
Fig. 1.6. *ISO 5817 main flaw types with causes in the welding joints [1.6]*

Effects and Assessment of Imperfections

a) Increase of general stress level

This is the effect of all types of misalignment due to secondary bending. The additional stress magnification factor can be calculated by appropriate formulae.

The fatigue resistance of the structural detail under consideration is to be lowered by division by this factor.

b) Local notch effect

Here, interaction with other notches present in the welded joint is decisive. Two cases are to be distinguished:

- *Additive notch effect* If the location of the notch due to the weld imperfection coincides with a structural discontinuity associated with the geometry of the weld shape (e.g. weld toe), then the fatigue resistance of the welded joint is decreased by the additive notch effect. This may be the case at weld shape imperfections.
- *Competitive notch effect.* If the location of the notch due to the weld imperfection does not coincide with a structural geometry associated with the shape geometry of the weld, the notches are in competition. Both notches are assessed separately. The notch giving the lowest fatigue resistance is governing.

c) Crack-like imperfections

Planar discontinuities, such as cracks or crack-like imperfections, which require only a short period for crack initiation, are assessed using fracture mechanics on the basis that their fatigue lives consist entirely of crack propagation.

After inspection and detection of a weld imperfection, the first step of the assessment procedure is to determine the type and the effect of the imperfection as given here.

If a weld imperfection cannot be clearly identified as a type or an effect of the types listed here, it is recommended that it is assumed to be crack-like.

Together or in part, these flaws can produce different crack type flaws in the area of the welded joints, mostly in the HAZ. Figure 1.7. shows a possibilities of the crack directions and positions in a fillet type welding.
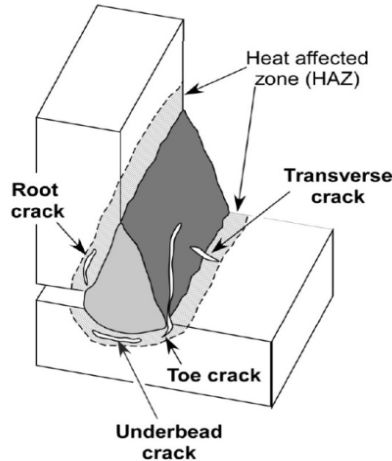
Fig. 1.7. *Crack directions and positions in a fillet welded joint [1.6]*

1.3.2. Factors for brittle fracture

Unlike ductile failure which is caused simply by excessive loading on a structure to beyond its ultimate tensile strength, brittle fracture requires a critical combination of three factors: a sufficiently low toughness material, a stress, and a flaw (or other stress concentration).

Weld flaws
Welds, in addition to presenting a stress concentration at weld toes, may also contain a flaw or crack. The types of flaws that most commonly initiate brittle fracture are the typical welding defects, such as lack-of-fusion flaws or hydrogen cracking, or a fatigue crack that has grown sufficiently large. A flaw or crack increases stress and is a very likely point at which brittle fracture may initiate.

Weld stress
Brittle fracture is perhaps of most concern in welded structures because a residual stress alone is sufficient to propagate a brittle fracture, without any external loading. In a thick plate containing a butt weld, if it is left alone, the butt weld will not exhibit a ductile failure because it cannot deform and yield without an external applied load. However, a welding defect in such a plate may initiate brittle fracture with no external load, because of the effect of the welding residual stress alone. In order to avoid brittle fracture (or to reduce the residual stress) a post-weld heat treatment (PWHT) of welded structures is necessary. Any applied external loading and stress concentrations in the structure's design also contribute to the risk of brittle fracture.

Low toughness
The low toughness factor becomes important in a number of different instances. The main set of materials at risk of brittle fracture are ferritic steels, because they have a crystal structure which shows a ductile-to-brittle transition at a

certain temperature. Austenitic type metals, such as austenitic stainless steel or aluminium alloys, do not show a transition between ductile and brittle behaviour with temperature in this way. However, the ductile-to-brittle transition is not the only cause of low fracture toughness. We have already seen that yield strength is strongly dependent on microstructure; toughness is also very dependent on microstructure.

The influence of microstructure can be seen in low heat input welds in steels with a moderately high carbon equivalent by the formation in the HAZ of martensite which has low toughness. In high heat input welds, the coarse grains formed in the HAZ also result in low fracture toughness. Reduction in fracture toughness also occurs as a result of embrittling mechanisms such as strain ageing in carbon steels or sigma phase formation in stainless steels. Adding even a small amount of nickel to a steel improves its fracture toughness. The only steel microstructure which is both strong and tough is a fi ne grain structure; this is how high-strength low-alloy steels achieve this optimum combination of mechanical properties. When welding fi ne-grained steels, the heat input and welding procedure play a crucial part in the potential reduction in fracture toughness within the HAZ and weld metal and, therefore, need to be closely controlled.

1.3.3. Misalignment in shell elements welded joints

Misalignment in axially loaded joints leads to an increase of stress in the welded joint due to the occurrence of secondary shell bending stresses (figure 1.8).
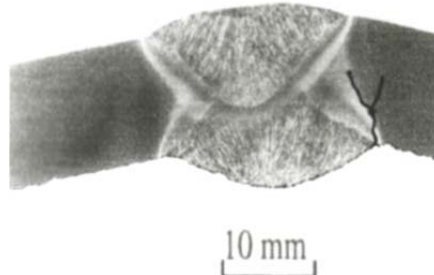
Fig.1.8. *Misalignment type crack*

Secondary shell bending stresses do not occur in continuous welds longitudinally loaded or in joints loaded in pure bending, and so misalignment will not reduce the fatigue resistance.

Types of misalignments:
- Axial misalignment between flat plates
- Angular misalignment between flat plates
- Angular misalignment in a fillet welded joint

A detailed matter of the misalignment flaws will be presented in Chapter 6.

1.4. Case study – Alexander Kielland Disaster

Alexander L Kielland was a Norwegian semi-submersible drilling rig (named after the Norwegian writer) that capsized while in service in March 1980 killing one hundred twenty three people. The capsize was the worst disaster in Norwegian waters since World War II.

The rig (figure 1.9) was built as a mobile drilling unit in France at the Dunkirk Shipping Yards, and delivered to Stavanger Drilling in July 1976. The floating drill rig was not used for drilling purposes but served as a semi-submersible 'flotel' providing living quarters for offshore workers. Initially, its capacity was for 80 beds and by 1978, additional accommodation blocks had been added to the platform, so that up to 386 persons could be accommodated. Altogether, eleven platforms of this type have been built, of which nine are currently in service in the North Sea.

Fig. 1.9. *Alexander L Kielland oil platform*

On the evening of 27th March, 1980, a couple of minutes before 6.30 p.m., the Alexander Kielland, started to capsize and within 20 minutes had overturned killing 123 of 212 people on board. The reason for the failure was later traced to a small 6 mm fillet weld which joined a non load-bearing flange plate to one of the main bracings (figure 1.10). The purpose of the flange plate was to hold a sonar device used in connection with drilling operations.

Fig. 1.10. *Part of the bracing that failed during the accident (on display in the Norwegian Petroleum Museum)*

This case study is concerned with the possible factors that contributed to the failure of the weld.

The characteristic form of a pentagon design is shown in figure 1.11. The main concern herein is the 'D' column and the bracing D-6. A detail of this part of the rig is given in figure 1.11 (a), which shows the location of the sonar flange plate. A detail of the flange plate as welded to the main bracing (D-6) is shown in figure 1.11 (b). The D-6 bracing is 24,00 m long, circular, hollow beam of diameter 2,60 m and thickness 26 mm. It is left open to the sea and allowed to contain sea water in order to increase the rig's stability. For this purpose, the bracing contains an elongated opening (300 x 800 mm) located on the bottom of the bracing next to the sonar flange plate. Since no sonar device was ever fitted to the rig, this hole was also left open to the sea. Although not shown in figure 1.11 (a), an air hole of 150 mm diameter was located on the upper side of the bracing (this can actually be seen in figure 1.15(a)). Both the air hole and the elongated opening were fitted with flanges in order to reduce the stress concentrations at these openings. This aspect is discussed later.
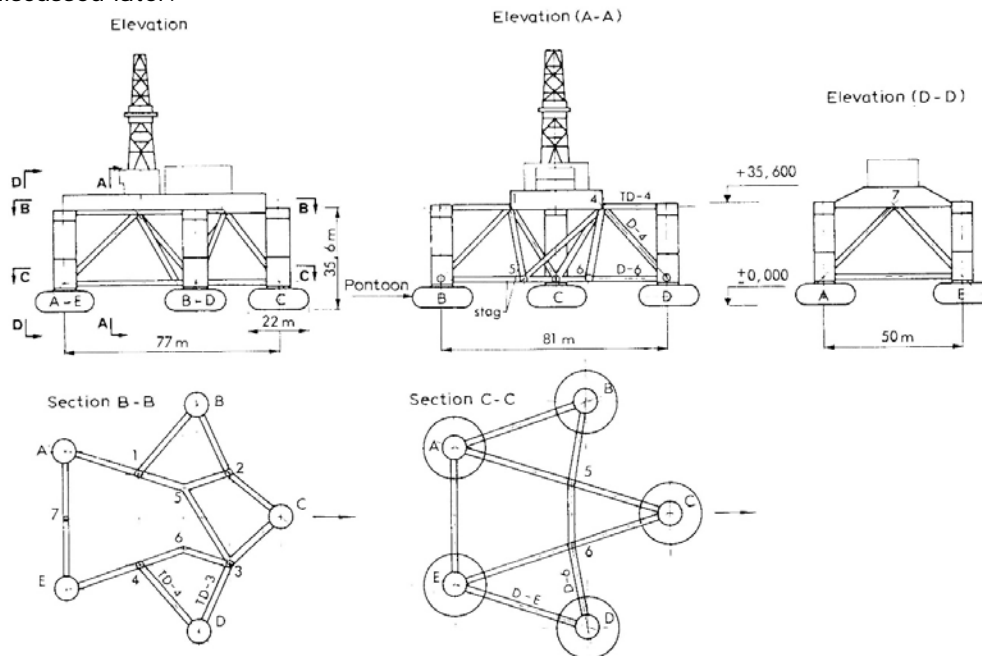
Fig. 1.11. *Geometry of the platform*

The production schedule was such that the assembly work was divided between two teams, one team being responsible for the main welding and fitting operations and the other taking care of the welding and fitting of auxiliary equipment. In this respect, for example, the welding of the flanges to the elongated opening and air hole was included among the duties of the main installation team, while the welding of the non load-bearing sonar flange plate was the responsibility of the other team. Furthermore, it was not considered necessary in the design work to carry out any stress analysis of the sonar flange plate fitting, although a stress analysis of the oval hole flange plate was carried out. This turned out to be a vital omission. The main braces were of a welded construction and made from a Nb – micro alloyed fine-grained steel.

The construction and fitting of the sonar flange plate

As shown in figure 1.12 the flange plate is essentially a short, circular, hollow cylinder, ca. 228 mm long and 325 mm diameter, with wall thickness 20 mm. Similar flange plates were fitted to three of the main braces, i.e. B-5, D-6 and A-5. The flange plate material was of a fine-grained pearlitic-ferritic steel, shaped by bending and butt welding. The profile of the butt weld was of an 'X' form, i.e. it was welded both from inside and outside employing 2 runs on the inside and up to four on the outside. The welding method was MMA, using flux-covered electrodes.
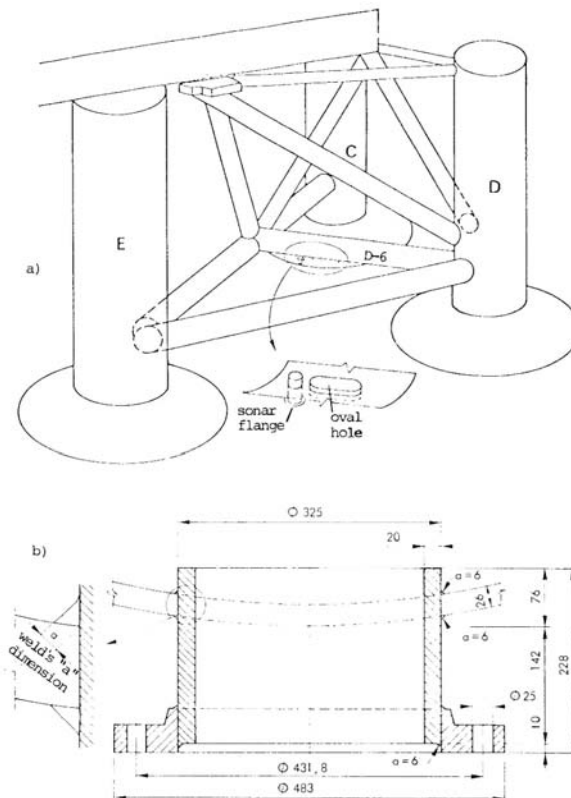
Fig. 1.12. – a) Detailed geometry of the D, E and C columns together with the bracings with the indication of the sonar flange; b) Position and welding joint detail for sonar flange plate

The sonar flange plate was located at a flame-cut hole in the bracing, of approximately 3-5 mm larger diameter than the flange itself. The flange plate was then welded in position using MMA welding of 2-3 runs per weld, employing fillet welds both inside and outside the main brace plate, figure 1.12(b). Flux-covered electrodes of 'basic' type, 5 mm diameter, were specified for this purpose. The "*a*" dimension of the weld was given as 6 mm, but the number of runs per weld was not specified. Preheat was neither specified nor employed.

Capsize of the Alexander Kielland

On the 27th March, 1980, the day of the disaster, the weather in the North Sea was stormy with mist and rain and visibility down to about a kilometre. It was

also cold, with an air temperature of 4-6 ^{0}C and a sea temperature of 6°C. As the day progressed the weather deteriorated, with the wind blowing at 20 m/s, churning up waves of 6-8 m in height. About half an hour later, at 6.28 p.m., the radio officer on board the Kielland heard a loud thump from below. Not too much notice was paid to begin with, since such noises are not unusual in heavy seas. Soon after the first thump, however, came another and this was followed by a definite listing of the platform. Minutes after the second thump was heard, the platform had already listed over to an angle of 30-35^0 from the horizontal. Indeed, it was apparent that only the anchor wire, 'as taut as a violin string', prevented the platform from turning over completely. At 6.53 p.m., 24 minutes after the 'Mayday' was sent out, it was recorded that the Alexander Kielland had completely overturned.

It was later established by the Norwegian Commission that investigated this incident, that the first thump heard by the radio officer was certainly caused by the *fracture of the main brace, D-6*. Then followed, in rapid succession, failures of the other bracings which connected column D to the platform, these resulting presumably from overloading. The positions of the various fractures of the bracings are shown in figure 1.13 The spacing of the latter fractures led the Commission to conclude that failure of bracings other than D-6 was due to bending.
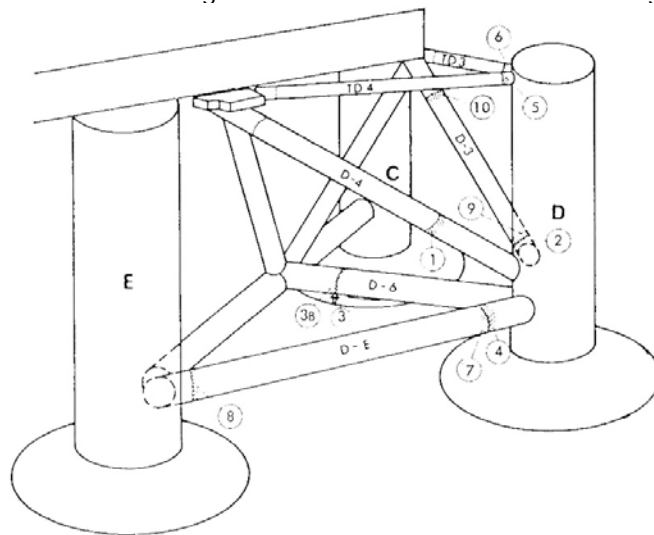
Fig. 1.13 – The various fractures found on the bracings are indicated. The cross-hatching and numbers refer to sections investigate metallographically

The failure in bracing D-6, which initiated the structural failure, was clearly due to fatigue. Indeed, it was later established that prior to the final fracture, **the crack had grown to a length of over 5 m, or ca. 2/3 the circumference of the bracing**! Figure 1.14 (a) shows the recovered D-6 bracing with the positions of the elongated hole and sonar flange plate indicated. Figure 1.14 (b) is a detail from the flange plate region which shows that the main fracture had occurred quite independently of the main butt weld of the main bracing (shown to the right); it is, however, clearly associated with the fillet weld of the flange plate. Studies of the characteristic river patterns of the main fracture confirm this, as illustrated in figure 1.15, in which the fracture pattern has been mapped out. As shown in the detail of figure 1.15; fatigue initiated at two parts of the fillet weld, first at *point I* and then at *point II*.
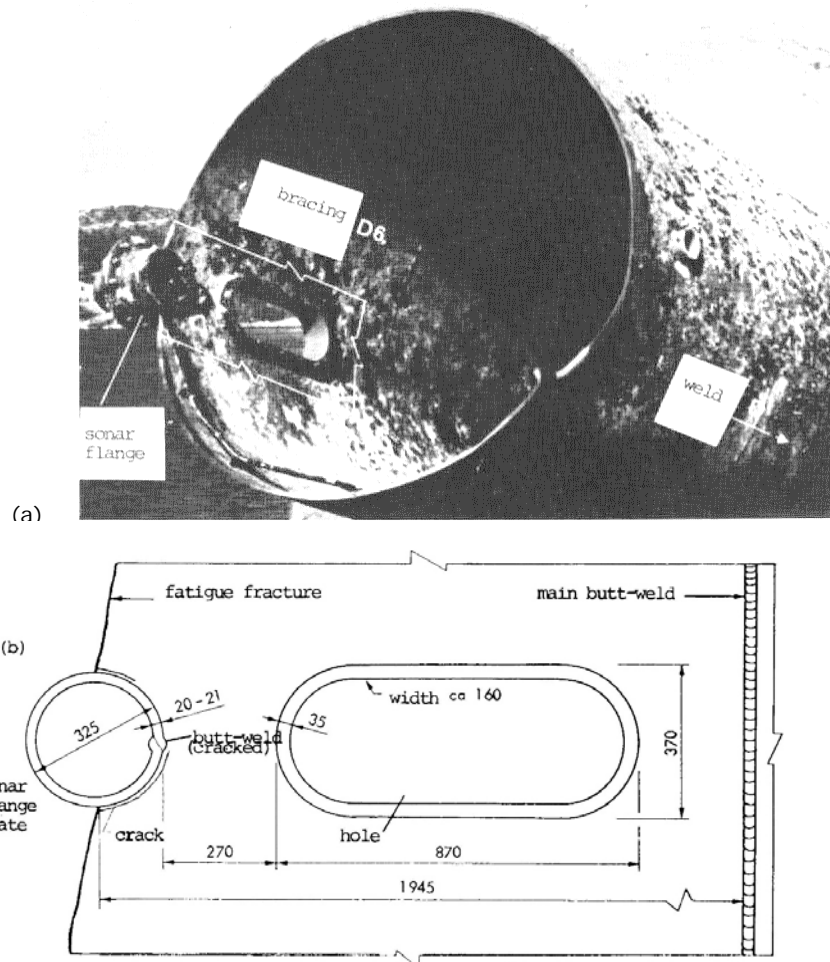
Fig. 1.14. (a) The recovered D-6 bracing with the positions of the elongated hole and sonar flange; (b) detail of the sonar flange plate region

Metallographic examination of the sonar flange plate welds

A metallographic examination of the fractured D-6 bracing revealed (amongst other things) the following factors [1.4]:

1. The butt weld of the sonar flange plate contained both toe and root cracks, the latter extending the whole length of the weld. Lamellar tearing in the flange plate material was also observed (figure 1.15).
2. Secondary cracking associated with the butt weld was observed at the cross-over between the butt weld and the fillet weld
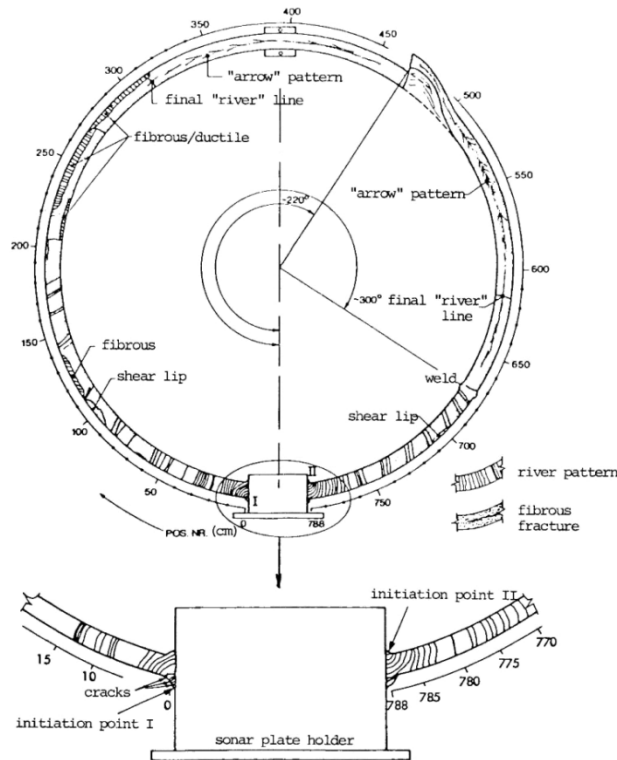
Fig. 1.15 *Mapping of the fracture surface (metallographical investigation) – detailing of the sonar plate to bracing welded joint [1.4]*

3. The quality of the butt weld was generally poor, exhibiting unsatisfactory penetration of the base material (figure 1.16).
4. The quality of the fillet welds, connecting the flange plate to the main bracing, was generally poor, showing insufficient penetration and uneven profiles, Figure 4.52. Indeed, the 'a'-dimension (specified as 6 mm) was found to vary in practice between 5 and 9 mm.
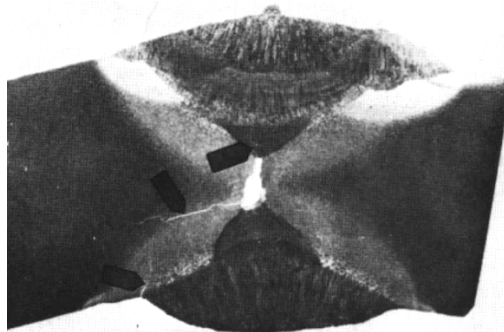
Fig. 1.16. *Butt weld of the sonar flange plate. Root and toe cracks, as well as lamellar tearing are indicated by the markers [1.4]*
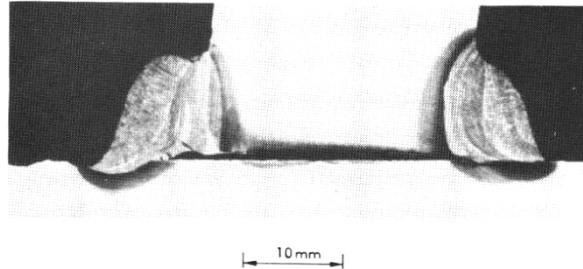
Fig. 1.17 *Section of the fillet weld between the flange plate (horizontal) and the main bracing (vertical) – poor penetration [1.4]*

5. Significant amounts of lamellar tearing of the flange plate material were observed in association with the fillet welds. However, there was no evidence of lamellar tearing in the bracing plate material.
6. Cracks running parallel to the edges of the fillet welds and joining up with the main fracture were observed (see, e.g., figure 1.14 (b)).
7. Several small cracks were found associated with the fatigue initiation point I, as illustrated in figure 1.18. The appearance of these cracks is not unlike that associated with cold cracking.
8. Small traces of paint, of the type originally used in the Dunkirk Yards, were discovered in the fracture surface of the fillet weld, implying that some cracking had occurred in this weld already during manufacture of the rig and prior to it going to sea.
9. Macro hardness measurements were carried out on the fillet-welded joint, and these results are illustrated in figure 1.17. Significantly, the maximum hardness is associated with the HAZ, reaching values of 350 HV, compared with ca. 160 HV in the base material. The hardness of the as-solidified weld metal lies between these values.
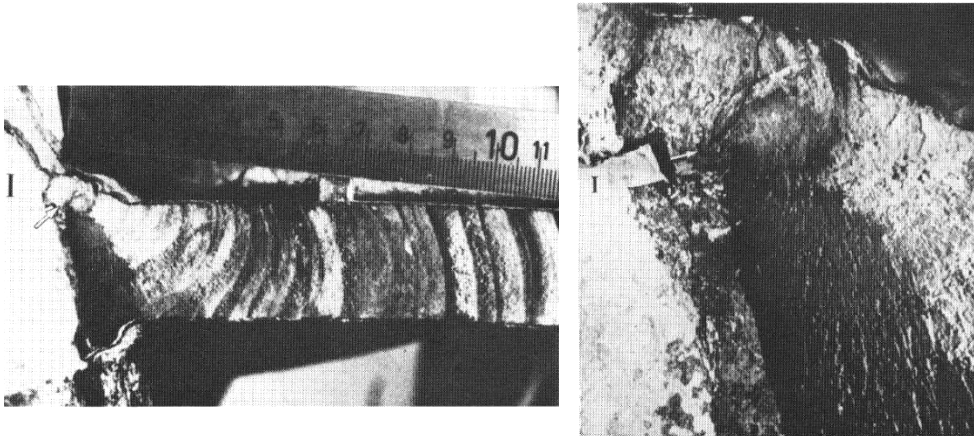
Fig.1.18 *Two details of the main initiation point of the crack in the fillet weld between the bracing (horizontal plate) and the sonar flange (vertical) [1.4]*

11. Stress analysis of the effect of the sonar flange hole on stress concentration in the bracing material, with and without the flange plate in position, was carried out. This showed that if the flange plate had not been present the stress

concentration would almost double, reaching a value of about three times that of the mean stress in the bracing. If the flange plate had been intact, the maximum stress concentration would be about 1.8.
12. Examination of bracing A-5 and B-5, also containing sonar flanges, revealed no obvious signs of failure.

Mechanism of failure: main conclusions

There appears to be a number of factors which could possibly have contributed to the failure of the D-6 bracing, with the resulting capsize of the Alexander Kielland. Of these the following are probably the most important:
1. The considerable amounts of lamellar tearing in the flange plate and the extensive root crack in the butt weld both contribute to the weakening of the sonar flange-plate in its capacity as structural strengthener. This, together with the resulting increased stress concentration at the hole, evidently induced cracking (or caused existing cracks to grow) around the periphery of the flange plate in the fillet weld.
2. The poor profile of the fillet weld contributed to a reduction in fatigue strength of the weld.
3. The rapid cooling rate of the fillet weld, the dissolution of NbC precipitates, and some grain growth in the HAZ of the bracing plate, all (together with the increased stress concentrations) helped produce just the conditions likely to give rise to cold cracking.
4. Given the presence of cold cracks in the fillet welds, the increase in stress concentration due to weakening of the flange plate, the poor weld profile, and the cyclic stresses experienced at sea then all the necessary conditions for fatigue crack growth appear to be present.

As with most case studies, there are some unanswered questions. For example, why did significant cracking occur in bracing D-6, but not in bracings A-5 and B-5, which also contained sonar flange plates? A possible variable might be the dryness of the electrodes used for the fillet weld, particularly in view of the fact that this weld was considered of secondary importance at the manufacturing stage. It is also not clear that the loading conditions are the same for all three bracings under normal service at sea, and this may be another important variable.

References

[1.1] Philippa Moore, Geoff Booth, "*The Welding Engineer's Guide to Fracture and Fatigue*", Wood Publishing, 2015

[1.2] ***, ISO 5817 standard – "*Arc welding joints in steel, guidance on quality levels for imperfections*"

[1.3] Easterling, K. – "*Introduction to the Physical Metallurgy of Welding*", Second Edition, Butterworth-Heinemann 1992

[1.4] ***, The Alexander L. Kielland accident, Report of a Norwegian public commission appointed by royal decree of March 28, 1980, presented to the Ministry of Justice and Police March, 1981 ISBN B0000ED27N

[1.5] ***, BS 7910, *'Guide to methods for assessing the acceptability of flaws in metallic structures'*

[1.6] U. Zerbst, et all, „*Review on fracture and crack propagation in weldments – A fracture mechanics perspective",* Engineering Fracture Mechanics, Volume 132, December 2014, Pages 200–276, Elsevier

[1.7] ISO 13822:2010 - Bases for design of structures -- Assessment of existing structures

[1.8] Hobbacher A (Ed), *Fatigue Design of Welded Joints and Components – Recommendations of IIW Joint Working Group XIII-XV*, IIW Doc XIII-1539-96/ XV-845-96, Cambridge, Abington Publishing, 1996; IIW Doc XIII-1965-03/XV-1127-03 (updated ed. 2005)

[1.9] S. Sedmak, A. Sedmak, "Fracture Mechanics and Non-Destructive Testing for Structural Integrity Assessment ", Key Engineering Materials, Vol. 399, pp. 27-36, 2009

2. FRACTURE MECHANICS AND FATIGUE DESIGN OF THE STEEL SHELL STRUCTURES

2.1. Introduction

Fracture mechanics is a quite new discipline which characterize the brittle fracture processes and developing practical assessing and checking methods, in order to conclude upon the imperfections of a material. The presence of the imperfections makes the difference in fracture mechanics comparing with strength of material field which starts from the prerequisite that the material has no flaws (figure 2.1).

The classic theory is based on fact the presence of a crack in a structural element, leads to exceeding its load capacity.

The actual principle is *"Living with defects"* which means that the "*defect*" parameter exists and must be assessed.

Classical Theory

| Internal forces | ⇨ | Stress - yield limit |

Fracture Mechanics Theory

| Internal forces |
| Size of the defect | ⇨ | Fracture toughness of the material |
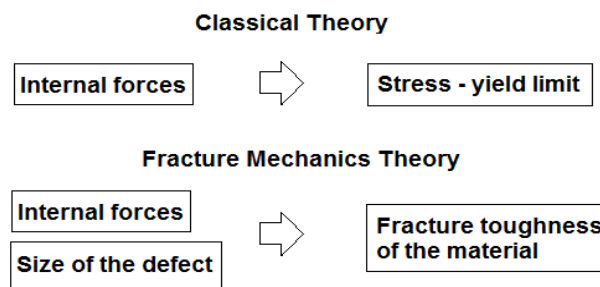
Fig.2.1. *Classical theory versus fracture mechanics theory*

The main characteristics of the fracture mechanics are: it is accepting the existence of the crack/defect, studies the appearance and the crack propagation speed and the remaining life in safe service state of the structural element.

First studies on fracture mechanics were done by Alan Arnold GRIFFITH, a British aeronautical engineer which became "*father of the science of fracture*" [2.1]. He clarified quantitatively the breaking strength of cracked material and realized that weakening of the material due to a crack can be treated as a matter of equilibrium, in which the strain energy reduction of a body containing a crack that propagates, could be equalized by surface energy increasing due to area growth. Griffith theory started from the assumption that brittle materials are containing elliptical micro cracks, which are inducing high levels of tension.

In 1920 Griffith founded a new concept for the extension of existing cracks based on a comparison of crack extension force and its critical value. He developed the first quantitative relationship between stress and crack propagation.

The large number of brittle fracture failures by vessels during the Second World War lead to in depth study of the phenomena by the engineers. Of the approximately 5,000 commercial vessels built by the Americans during the Second World War, more than 1,000 of them had sizeable cracks until 1946. Between 1942-

1952 more than 200 ships had serious cracks, and at least nine T2 tankers and 7 Liberty vessels were broken in half due to brittle fracture.

In 1955 arise concepts of "*fail safe*" and "*safe life*". The safe life design imposed that a structural component/element should be designed to last a predefined period of time. The fail safe design request that the failure of an element (designed component), must not jeopardise the safety of a structure, thus the structure can be safe for the people (e.g. occupants of a building). In practice the fail safe concept must contain a rigorous inspection plan in order to ensure that the cracks do not propagate to critical dimensions in the period of consecutive inspections. If a crack will propagate, the stress intensity in the other components of the structure, may increase; in this situation the result can be the total collapse of the structure, even if this component was designed to resist without the first damaged component.

At the end of 50th were done a number of several crack propagation experiments. First crack propagation basic theories are issued. Thus, at the mid 50th, George Irwin Rankine rediscovers the Griffith theories and he is replacing the energy-balance approach with the study of the stress at the crack opening tip, thus introducing the stress intensity factor *K*. The studies of Irwin were generally based on Westgaard solution which describes the stress intensity field nearby a crack with complex function.

Irwin discovers the *"fracture resistance",* thus giving birth to *linear elastic fracture mechanics (LEFM).* This approach is adopted in fatigue design field in 1962 with the *Paris law* publishing [2.15]. The law is linking the crack growth, resulted from the fatigue of the material in time of a stress cycle, to the stress intensity factor.

In 1968 Elber discovers that a crack exposed to high loads are closing before the stress is zero, effect which is named *crack closure effect.*

The theoretical development of fracture mechanics experienced new approaches in 60th, when Wells is introducing the *critical crack tip opening* concept (1966) and the studies of Rice lead to introducing a new parameter named *J integral* (1968).

In 1970, year in which the American norm ASTM-E 399 was published, are done the first tests in order to determine intensity factor at the crack tip K_{IC}. The testing is done on specimens containing sharp defects crack type (fatigue pre cracked). Similar testing standards were developed in 1977 by the British Standard Institute (BSI) and in 1996 by the International Standards Institute (ISO).

It is worth to mention that in 1978 ASTM association publishes tests procedures in order to determine the Fatigue Crack Growth and the Crack Tip Opening Displacement (CTOD).

In past years was done a vast research in the fracture mechanics field, converging to developing new application in different engineering domains.

2.2. Classic fracture mechanics theory – LEFM

2.2.1. Stress concentration and stresses at elliptical holes

The story of analysis of stress concentrations begins in 1898 with Ernst Gustav Kirsch's linear elastic solution for stresses around a hole in an infinite plate [2.2]. Kirsch's solution contains the factor-of-three stress concentration at the hole under uniaxial loading.
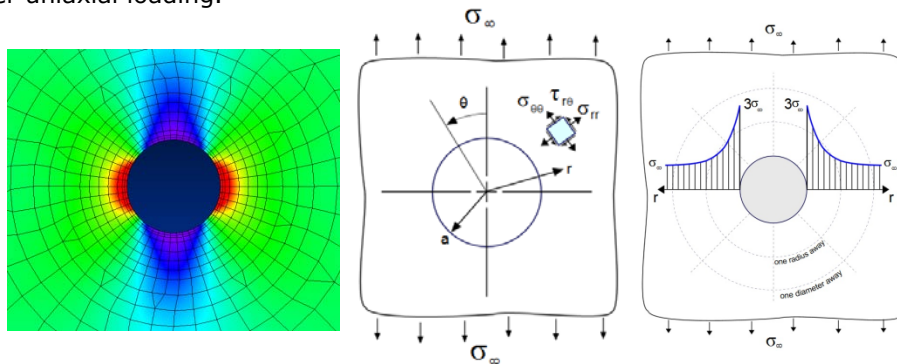
Fig.2.2. *Uniaxial loading – Kirsch's solution: stresses in the area of the hole, stress concentration factor $K_t=3$*

The solution for the stress state around a hole is:

$$\sigma_{rr} = \frac{\sigma_\infty}{2}\left(1-\left(\frac{a}{r}\right)^2\right) + \frac{\sigma_\infty}{2}\left(1-4\left(\frac{a}{r}\right)^2+3\left(\frac{a}{r}\right)^4\right)\cos 2\theta$$

$$\sigma_{\theta\theta} = \frac{\sigma_\infty}{2}\left(1+\left(\frac{a}{r}\right)^2\right) - \frac{\sigma_\infty}{2}\left(1+3\left(\frac{a}{r}\right)^4\right)\cos 2\theta \qquad \sigma_{rr} = \frac{\sigma_\infty}{2} \qquad (2.1.)$$

$$\tau_{r\theta} = -\frac{\sigma_\infty}{2}\left(1+2\left(\frac{a}{r}\right)^2-3\left(\frac{a}{r}\right)^4\right)\sin 2\theta$$

At $\theta = 90°$, the stress $\sigma_{\theta\theta}$ as a function of r, is having a factor of 3 immediately nearby the hole edge (r). The stress is decreasing as the calculation is done at a distance of $2r$. The figure 2.2 shows the factor-of-three concentration at the hole's edge and how it quickly dissipates away with increasing r. The stress concentration is small again at one diameter distance from the hole's edge, and is decreasing at two diameters distance.

In case of equibiaxial loading (equal tension in x and y directions), the effect of stress state can be determined through superposition principle of Kirsch solution.

It results a factor of two for the stress concentration which is applied over the complete circumference of the hole (figure 2.3.). As can be seen (equations 2.2), the stress state is independent of angle θ.

$$\sigma_{rr} = \sigma_\infty \left[1 - \left(\frac{a}{r} \right)^2 \right]$$

$$\sigma_{\theta\theta} = \sigma_\infty \left[1 + \left(\frac{a}{r} \right)^2 \right] \qquad (2.2.)$$

$$\tau_{r\theta} = 0$$
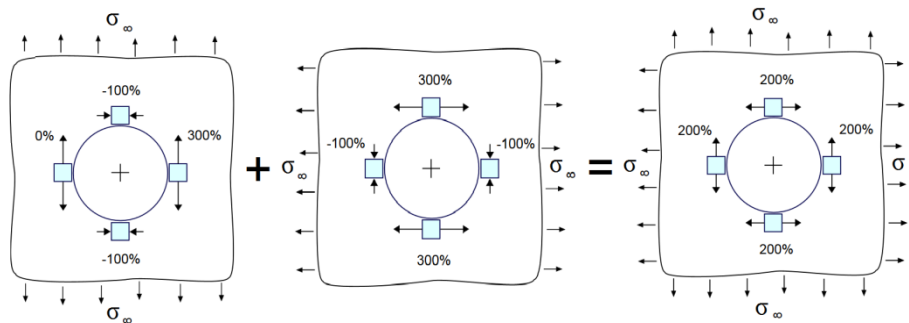
Fig.2.3. *Equibiaxial loading – Kirsch's solution: stresses in the area of the hole (superposition principle), stress concentration factor K_t=2*

In case of finite width plates, it is necessary to introduce an additional term – the nominal stress σ_{nom} which is defined as the average stress in the area of the hole due to the reduction of the cross section. Considering w the width of the plate, d the diameter of the hole and neglecting the thickness of the plate (figure 2.4.), the nominal stress σ_{nom} can be written function of stress σ_∞ as:

N (force) $= \sigma_\infty \cdot w = \sigma_{nom} \cdot (w\text{-}d)$

$$\sigma_{nom} = \frac{W}{W - d} \cdot \sigma_\infty \qquad (2.2.)$$
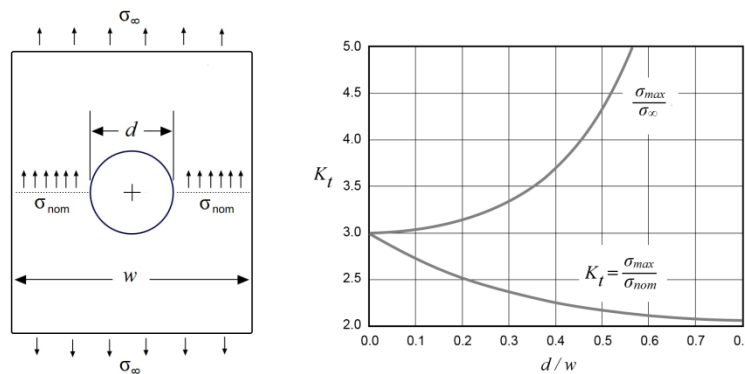
Fig.2.4. *Definition of σ_{nom} stress and the stress concentration factor K_t*

The **stress concentration factor** can be defined as the ratio between the maximum stress and the nominal one:

$$K_t = \frac{\sigma_{max}}{\sigma_{nom}} \qquad (2.3.)$$

In figure 2.4 there is presented a standard graph as a definition for stress concentration factor, showing the dependence of K_t on the ratio d / w. At $d/w=0$ (infinitely wide plate) the stress intensity factor is 3. The equation for the curve is:

$$K_t = 3 - 3{,}14\left(\frac{d}{W}\right) + 3{,}667\left(\frac{d}{W}\right)^2 - 1{,}527\left(\frac{d}{W}\right)^3 \qquad (2.4.)$$

The first major step in the development of the **Linear Elastic Fracture Mechanics** was done by Charles E. Inglis in 1913 [2.8]. Stress distribution in a shell element characterized by the presence of a defect and subjected to a uniform tensile stress is influenced by it. Thus the maximum tensile stresses on the edge defect are elliptical, with value:

$$\sigma_{max} = \sigma\left(1 + \frac{2a}{b}\right) \qquad (2.5)$$

$$\sigma_{max} = \sigma \cdot k_t \qquad (2.6)$$

Where $k_t = \sigma_{max} / \sigma$ is a stress concentration factor.

For a circular shape hole, where $a = b$, the value of the factor k_t will be 3, representing the local stress concentration value (as presented above). This stress concentration is much higher for an elliptical shape hole; it tends to infinity while semi-axis b tends to zero.
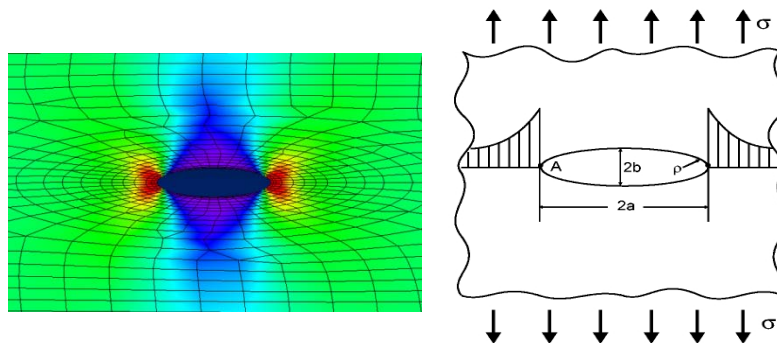
Fig.2.5. *Elliptical shape hole stress effect in a shell element*

Writing radius of curvature $\rho = b^2 / a$, solving for b and substituting into a/b ratio in (2.5) relation for the maximum stress will have the relation:

$$\sigma_{max} = \sigma\left(1 + 2\sqrt{\frac{a}{\rho}}\right) \qquad (2.7)$$

The relation 2.7 is considered a fundamental result because it relates the maximum stress at the tip of the ellipse to the distance to the tip, *a*, and the radius of curvature at the tip ρ.

In case a >> b, the relation is:

$$\sigma_{max} = 2\sigma\sqrt{\frac{a}{\rho}} \qquad (2.8)$$

Thus when $\rho \to 0 \quad \Leftrightarrow \quad \sigma_{max} \to \infty$

Inglis's solution shows that as the radius of curvature at the tip of a crack goes to zero, the stress goes to infinity, even for the slightest load. Nevertheless, a common characteristic of Linear Elastic Fracture Mechanics (LEFM) theory is that

stresses at crack tips are predicted to be infinite. Another aspect of Inglis's study is that through his analytical solution for the ellipse, he was the first to demonstrate that the stress concentration is proportional to $\sqrt{a}$ and that it goes to infinity as the ellipse squashes down to form a *crack*.

2.2.2. Griffith's energy release rate

Year 1920 is considered the birth year of fracture mechanics. In that time Alan Arnold Griffith issued the energy-based analysis of cracks [2.3]. The bases of the Griffith theory is the Inglis linear elastic solution for stresses around an elliptical hole. Inglis relation (2.8), being based on a linear elastic curvature of the material, shows that the stress tends to infinite when radius of curvature at the tip tends to zero, fact that prompted much discussions at the beginning of the 20 century. Thus Griffith changed the perspective and proposed an energy failure criterion approach. He used the *strain energy release* concept for a linear elastic material in uniaxial tension, starting from a bar pulled in tension by a stress σ for which its strain energy is

$$U = \frac{\sigma^2}{2E}V \qquad (2.9)$$

Griffith computed the strain energy release associated with crack growth using Inglis's case of an ellipse flattened to form a crack. He integrated the stress and strain field in order to obtain the strain energy as a function of crack length *a*:

$$U = \frac{\sigma^2}{2E}V - \frac{\sigma^2}{2E}B\pi a^2 \qquad (2.10)$$

where *B* is the thickness of the plate, *V* is the volume and *E* is the Young modulus.

Considering the atomic bonds energy as $E_{bond} = 2\gamma_s aB$, where γ_s is the energy required to break atomic bonds per unit surface area created by the crack, *a* is the crack length and *B* is the thickness, the total energy in the system can be written as the sum:

$$E_{total} = 2\gamma_s aB + \frac{\sigma^2}{2E}V - \frac{\sigma^2}{2E}B\pi a^2 \qquad (2.11)$$

In order to find the length at which the unstable crack growth (failure) can occur, the 2.11 equation is derivative to zero:

$$\frac{dE_{total}}{da} = 2\gamma_s B - \frac{\sigma^2}{E}B\pi a^2 = 0 \qquad (2.12)$$

Solving the 2.12 for σ, it results the failure stress:

$$\sigma_f = \sqrt{\frac{2\gamma_s E}{\pi a}} \qquad (2.13)$$

The $2 \cdot \gamma_s$ factor is named Griffith Critical Energy Release Rate [2.3] – G_c, denotation which transforms the 2.13 equation into:

$$\sigma_f = \sqrt{\frac{G_c E}{\pi a}} \qquad (2.14)$$

The shortcoming of the Griffith's criterion is the neglecting of energy associated with metal plasticity. The (2.14) equation can be applied only to brittle

materials - it is known that Griffith's theory tests were done on glass. The equation (2.11) only considers energy associated with atomic bond breaking. In steel elements there is more energy dissipation associated with plastic deformation, near the crack tip, than the atomic bond breaking. In 1948, Irwin [2.4] and Orowan [2.5] modified Griffith's equation by adding the energy due to plastic deformation at the crack tip per unit surface area created by crack propagation:

$$E_{bond} = 2(\gamma_s + \gamma_p)Ba \qquad (2.15)$$

In this case, Griffith's critical energy release rate becomes:

$$G_c = 2(\gamma_s + \gamma_p) \qquad (2.16)$$

Of course that the equation 2.14 remains the same.

2.2.3. **Westergaard's solution for stress field nearby cracks**

In 1939 Harold M. Westergaard analysed the stress field around a crack and developed a solution [2.6]. The approach was different from Inglis's solution, Westergaard solution being applied to cracks – not to an ellipse that become a crack at the limit. He also try to improve the mathematical approach by using complex numbers and a rectangular coordinates system.

Westergaard proposed an Airy stress function of complex numbers as a solution for the stress field in an infinite plate containing a crack. Thus naming $\overline{Z}$ the integral of $Z(x)$ complex function and $\overline{\overline{Z}}$ the integral of $\overline{Z}$ and the derivative of Z with Z', and expressing the Airy stress function Φ as Cauchy- Riemann equations:

$$\varphi = Re\,\overline{\overline{Z}} + y\,Im\,\overline{Z} \qquad (2.17)$$

the complete set of equations for the stress field is:

$$\sigma_{xx} = \frac{\partial^2 \varphi}{\partial y^2} = Re\,Z - y\,Im\,Z'$$

$$\sigma_{yy} = \frac{\partial^2 \varphi}{\partial x^2} = Re\,Z + y\,Im\,Z' \qquad (2.18)$$

$$\tau_{xy} = -\frac{\partial^2 \varphi}{\partial x \partial y} = -y\,Re\,Z'$$

where

$$Z(z) = \frac{\sigma_\infty}{\sqrt{1 - \left(\frac{a}{z}\right)^2}} \qquad (2.19)$$

where a is the crack length and $z=x+iy$.
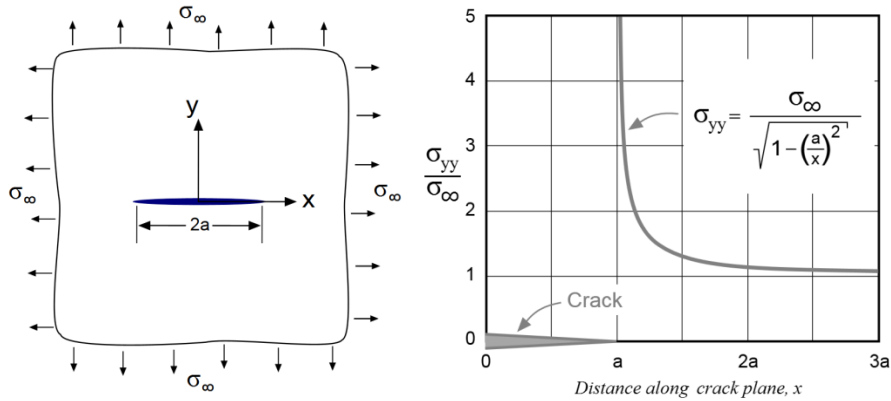
Fig.2.6. *Westergaard solution - graphical representation*

When *y=0* the equations 2.18 reduce to $\sigma_{xx} = Re\,Z$, $\sigma_{yy} = Re\,Z$ and $\tau_{xy} = 0$. The σ_{xx} and σ_{yy} stresses along y=0 and x>a are:

$$\sigma_{xx} = \sigma_{yy} = \frac{\sigma_\infty}{\sqrt{1 - \left(\dfrac{a}{x}\right)^2}}$$

(2.20)

Figure 2.6 shows the low value of the stress (dropping) from infinity at the crack tip for *y=0* – along the crack plane.

The computing of the stress at any other position (than for *y=0*) nearby the crack tip, requires a Taylor series of functions in order to separate the real and imaginary part.

2.2.4. Stress intensity factor „K"

In 1957 George Rakin Irwin developed a theory based on fundamental fracture mechanics analysis of stress and strain state at crack tip [2.7]. This theory shows that the stress area from the tip of a crack is determined by the factor *K* (as noted in honour of its employee Joseph Kies 1952-1954), known as the *stress intensity factor.*

Analysing the classic application and using Westergaard's theory of elasticity expressions, he characterized the elastic stress field in the proximity of a crack through the relations:

$$\sigma_x = \frac{\sigma_\infty \sqrt{\pi a}}{\sqrt{2\pi r}} cos\frac{\theta}{2}\left(1 - sin\frac{\theta}{2} sin\frac{3\theta}{2}\right)$$

$$\sigma_y = \frac{\sigma_\infty \sqrt{\pi a}}{\sqrt{2\pi r}} cos\frac{\theta}{2}\left(1 + sin\frac{\theta}{2} sin\frac{3\theta}{2}\right)$$

(2.21)

$$\tau_{xy} = \frac{\sigma_\infty \sqrt{\pi a}}{\sqrt{2\pi r}} cos\frac{\theta}{2}\left(sin\frac{\theta}{2} cos\frac{3\theta}{2}\right)$$

in which:

    r, θ - polar coordinates in x-y plane
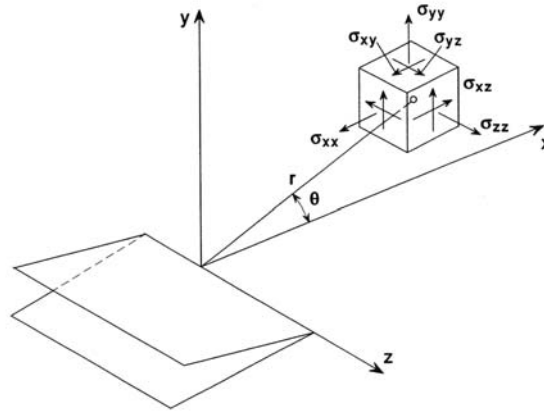
Fig.2.7. - Stress field in the proximity of a crack

    Irwin rephrased the Griffith criterion of energy release rate, by introducing the ***critical value of stress intensity factor – K_c***. According to Irwin all materials exhibit critical value of stress intensity factor K_c. When the critical value of stress intensity factor is achieved, crack can initiate to grow. Accordingly, the condition $K < K_C$, represent situation for *non growing crack existence*.

    Thus solving the Griffith equation (2.13) for G_c, it results

$$G_C = \frac{\sigma_f^2 \pi a}{E} \tag{2.22}$$

    Naming $K_C = \sigma_f \sqrt{\pi a}$, the Griffith equation becomes $G_C = \frac{K_C^2}{E}$ in plane stress and $G = \frac{K^2}{E}\left(1 - v^2\right)$ in plane strain.

    However, critical value of crack driving force, constant G_c, is very much greater than the surface energy of the material 2γ (equation 2.13). This suggests that the energy release in the specimens was to a large extent dissipated by producing plastic flow around the crack tip, so that the critical value at fracture was apparently much greater than 2γ. Therefore:

$$\sigma_{cr} = \sqrt{\frac{E\left(2\gamma + \gamma_p\right)}{\pi a}} \tag{2.23}$$

It was found experimentally that $(\gamma_p + 2\gamma)$ is much greater than 2γ, so the above equation can be rewritten

$$\sigma_{cr} = \sqrt{\frac{E\gamma_p}{\pi a}} \tag{2.24}$$

and values of γ_p could then be determined directly from the fracture stresses of specimens containing cracks of known lengths.

By introducing the elastic crack, in plane stress, the plastic zone of total extent $2r_Y = K^2 / \pi\sigma_Y^2$ produces crack of half-length $(a + r_Y)$. The failure stress is then given by:

$$\sigma_{cr} = \sqrt{\frac{EG_C}{\pi(a + r_Y)}} = \sqrt{\frac{EG_C}{\pi\left(a + \sigma_{cr}^2 a / 2\sigma_Y^2\right)}} \qquad (2.25)$$

or, in terms of the critical stress intensity:

$$K_C = \sigma_{cr}\sqrt{\pi a\left(1 + \frac{\sigma_{cr}^2}{\sigma_Y^2}\right)} \qquad (2.26)$$

A more in depth analysis of the crack plasticity will be done in chapter 2.3.

The use of stress intensity factors became much more popular than energy release rates for linear elastic problems.
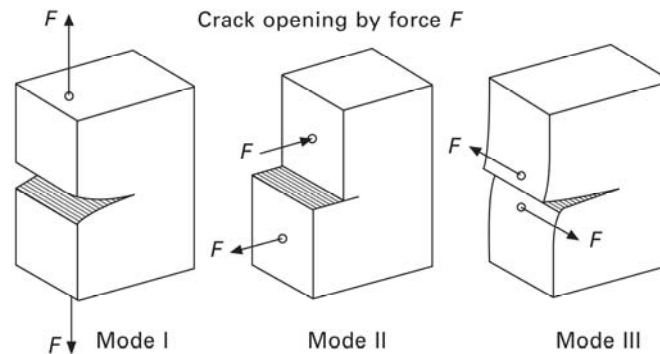
Fig.2.8. *Different crack opening modes (mode I – Opening; mode II – In-Plane Shear; mode III – Out-of-Plane Shear)*

Irwin, [2.7], had shown that there are three basic shapes of displacement of one crack surface relative to the other, and that they describe the behaviour of cracks in all stress states. In figure 2.8. are shown the basic shapes of displacement of elements which include the crack tip. Displacement shapes of a crack tip which lies in the x-z plane, can be described as follows:
- Mode I - crack propagation by cleaving, characterized by moving of crack surfaces in a way that they open symmetrically relative to the initial crack plane.
- Mode II - crack propagation by sliding, related to local deformation during which one surface slides along the other in the same plane, but in opposite directions.
- Mode III - crack propagation by shearing represents a case of local strain, during which surfaces slide along each other in the direction of the crack so that the points within the material, which were initially in the same vertical plane, are distributed along different vertical planes after crack propagation.

Most important is the crack opening mode I. The other modes and their combinations, the mixed mode loadings, are of minor significance. There is only a two-dimensional stress state at the surface of the plate, the so-called plane stress condition. Deeper inside a thick plate, a three dimensional stress state (*plane strain*)

develops because of the restrained contraction in the thickness direction. Under this condition, the critical resistance of a material to fracture K_{Ic} is lowest. It is a material property called **fracture toughness** K_{mat}, which depends on the material, temperature and, to some extent, the rate of loading. In materials testing for fracture toughness, a minimum wall thickness of the specimens must be present in order to ensure the plane strain state.

The **main check in fracture mechanics** is given by the relation:

$$K_{apl} \leq K_{crit} = K_{Ic} \tag{2.27}$$

where K_{apl} is the stress intensity factor which depends on the applied stress intensity and on the dimensions and geometry of the crack and K_{crit} is the critical value of the stress intensity factor (toughness) which is a material characteristic (is determined by tests).

In other terms, the loading of a crack tip in terms of SIF must exceed the material resistance against fracture, i.e. fracture toughness. This is strictly true for brittle materials. In ductile materials, a plastic zone around the crack tip develops. If this plastic zone is small in comparison to the dimensions of the crack, the assessment can be done in the same way without a major error.

The basic relationship for mode I (figure 2.8) crack growth between stress intensity factor ahead the crack front (K_I), crack length (a) and applied stress (σ) is derived in term of coordinate (x) in crack surface direction

Introducing the K_I in 2.20 equation, for mode I of crack opening, in polar coordinates (r, θ), the stress field equations in the proximity of a crack becomes:

$$\sigma_x = \frac{K_I}{\sqrt{2\pi r}} cos\frac{\theta}{2}\left(1 - sin\frac{\theta}{2}sin\frac{3\theta}{2}\right)$$

$$\sigma_y = \frac{K_I}{\sqrt{2\pi r}} cos\frac{\theta}{2}\left(1 + sin\frac{\theta}{2}sin\frac{3\theta}{2}\right) \tag{2.28}$$

$$\tau_{xy} = \frac{K_I}{\sqrt{2\pi r}} cos\frac{\theta}{2}\left(sin\frac{\theta}{2}cos\frac{3\theta}{2}\right)$$

All three expressions of stresses have the square root of r in the denominator, which underlines the dependence of stress to the distance from the crack tip and reflects the singularity at $r=0$.

The expression of σ_{yy} when y=0 is presented in the equation 2.21 (Westergaard). In crack plane, Irwin approximation (with $\theta=0$) is:

$$\sigma_{yy} = \frac{\sigma_\infty \sqrt{\pi a}}{\sqrt{2\pi r}} \tag{2.29}$$

The two equations differences are shown in the figure 2.9.
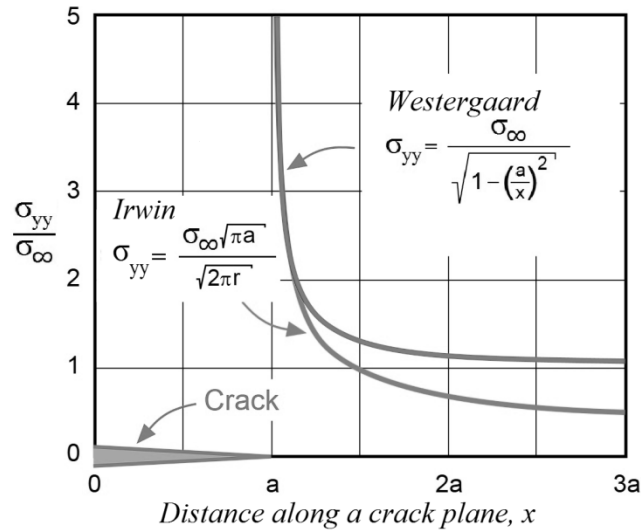
Fig.2.9. *Irwin's and Westergaard's nearby crack stress expressions*

In order to simplify, considering the plane strain, the principal stresses are given by:

$$\sigma_1 = \frac{K_I}{\sqrt{2\pi r}} \cos\frac{\theta}{2}\left(1 + \sin\frac{\theta}{2}\right) \tag{2.30}$$

$$\sigma_2 = \frac{K_I}{\sqrt{2\pi r}} \cos\frac{\theta}{2}\left(1 - \sin\frac{\theta}{2}\right) \tag{2.31}$$

where *r* and *Θ* are defined in figure 2.7.

Considering the relations 2.30 and 2.31, it can be determines the elastic displacement fields near the crack tip [2.14]:

$$u = \frac{K_I}{2G}\sqrt{\frac{r}{2\pi}} \cos\frac{\theta}{2}\left[\kappa - 1 + 2\sin^2\left(\frac{\theta}{2}\right)\right] \tag{2.32}$$

$$v = \frac{K_I}{2G}\sqrt{\frac{r}{2\pi}} \sin\frac{\theta}{2}\left[\kappa - 1 + 2\cos^2\left(\frac{\theta}{2}\right)\right] \tag{2.33}$$

Where G is the shear modulus, $\kappa = 3 - 4v$ for plain strain and $\kappa = (3 - v)/(1 + v)$ for plane stress, and *v* is the Poisson's ratio

The approximate solution of Irwin is more useful comparing to Westergaard exact solution. The approximate solution is accurate at the crack tip – this is an important fact which differentiate the two approaches. In practice (analytical studies of the crack opening), is used Irwin solution considering that it can determine the speed of crack growth and in which direction grows.

2.2.5. Stress intensity factor calculation for different cases

In this paragraph there are presented design solution for K factor [2.9] [2.10] characteristic for crack opening mode I for some simple elements, cracks and loads.

- ***Plate with crack throughout the entire thickness – through thickness crack***

In case of an infinite plate which is containing a crack flaw with length of *2a*, (fig. xx1 a) and it's having a tension stress *σ*, the relation for the stress intensity factor will have the form:

$$K_I = \sigma\sqrt{\pi a} \qquad (2.34)$$

Note: the "infinite plate" denomination indicate that the crack/flow is very small comparing with the dimensions of the element (plate)

Analysing the relation (2.34) can be noticed that the value of the K_I parameter is direct proportional with the stresses *σ*, which characterizes the global behaviour of the plate.

a/b	Y
0,074	1,00
0,207	1,02
0,275	1,03
0,337	1,05
0,410	1,08
0,466	1,11
0,535	1,15
0,592	1,20

(a)   (b)   (c)
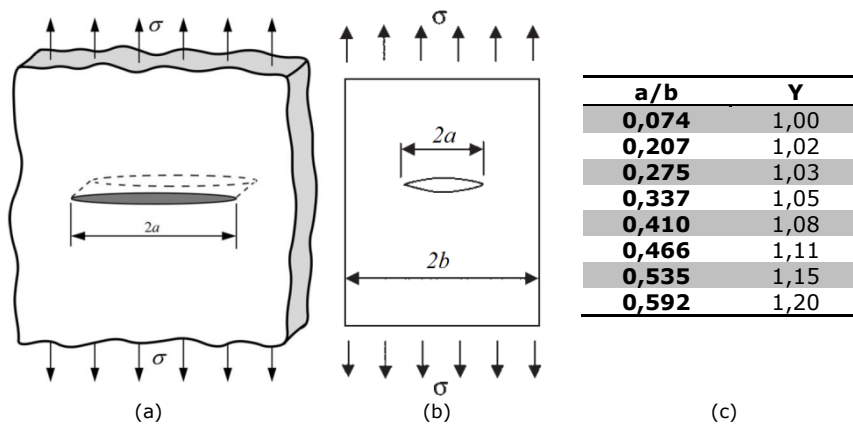
Fig.2.10. *Plate with through thickness crack: (a) Infinite plate; (b) finite plate; (c) correction factor Y for finite plate*

If it's taken a finite plate of *2b* width (figure 2.10 b), for the approximation of the stress intensity factor, it will be used the following relation:

$$K_I = \sigma\sqrt{\pi a}\left(\frac{2b}{\pi a}\tan\frac{\pi a}{2b}\right)^{1/2} \qquad (2.35)$$

relation in which was used a correction factor $y = \left(\dfrac{2b}{\pi a}\tan\dfrac{\pi a}{2b}\right)^{1/2}$

- ***Plate with crack at a side – single edge crack***

In case of an infinite plate under tension stresses which is containing a single edge crack with length of *a* and it's having a tension stress *σ*, the relation for the stress intensity factor will have the form:

$$K_I = 1,12\cdot\sigma\sqrt{\pi a} \qquad (2.36)$$

Note: In case of single edge crack, the K value increases with 12% - the edge crack tends to open different from the interior crack (figure 2.11).

$$K_I = \sigma\sqrt{\pi a} \qquad\qquad K_I = 1,12\sigma\sqrt{\pi a}$$
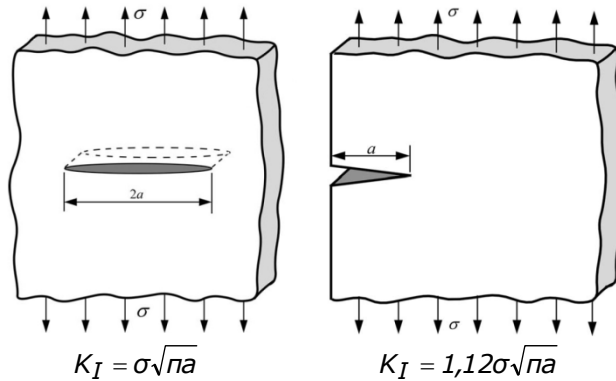
Fig.2.11. *K values for: (a) Plate with through thickness crack; (b) Plate with single edge crack*

In case of finite width plate with single edge crack, is needed to introduce in the relation of stress intensity factor a correction factor in order to consider the bending moment effort which appear due to the non-symmetric flaw. In this case the relation becomes:

$$K_I = 1,12 \cdot \sigma\sqrt{\pi a} \cdot k\left(\frac{a}{b}\right) \qquad\qquad (2.37)$$

The value of the correction factor $k\left(\dfrac{a}{b}\right) = Y$ is presented in figure 2.12.

a/b	Y
0,000	1,00
0,100	1,03
0,200	1,07
0,300	1,15
0,400	1,22
0,500	1,35
0,600	1,50
0,700	1,69
0,800	1,91
0,900	2,20
1,000	2,55
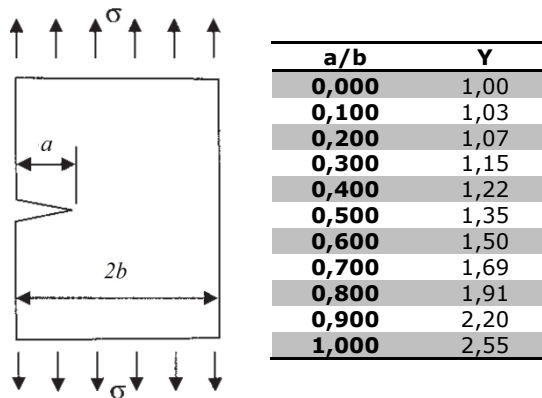
Fig.2.12. *Plate with single edge crack – correction factors Y*

- **Embedded circular or elliptical crack**

In case of an infinite plate under tension stresses which is containing an embedded circular or elliptical crack (figure 2.13) the relation for the stress intensity is:

$$K_I = \sigma \sqrt{n \frac{a}{Q}} \cdot g(\beta) \qquad (2.38)$$

where

$$g(\beta) = \left(sin^2\, \beta + \frac{a^2}{c^2} cos^2\, \beta \right)^{1/4} \qquad (2.39)$$
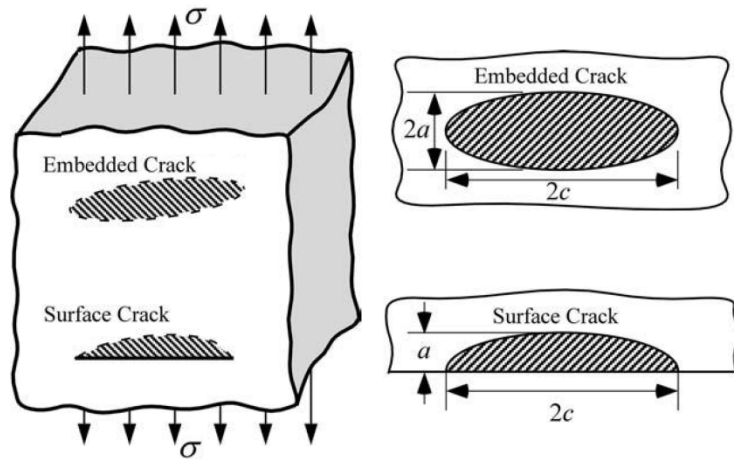
Fig.2.13. *Elliptical crack in infinite body*

Q is called flaw shape parameter and depends on the $\sigma\,/\,\sigma_y$ and $a\,/\,2c$ ratios (figure 2.14).
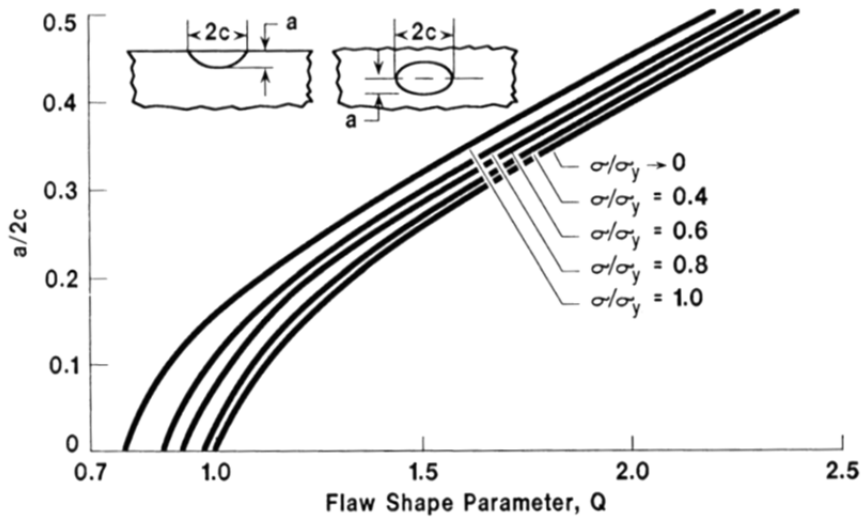
Fig.2.14. *Flaw shape parameter Q values*

Stress intensity factor K_I has the maximum value in case of embedded elliptical cracks – for $\beta = 90°$, thus having the formula:

$$K_I = \sigma \sqrt{\pi \frac{a}{Q}} \qquad (2.40)$$

For circular flaws, where $a=c$ and $Q=2,4$, stress intensity factor is having the following form:

$$K_I = 0,65 \cdot \sigma \sqrt{\pi a} \qquad (2.41)$$

- **Surface crack**

In case of surface crack, the stress intensity factor has the following form:

$$K_I = 1,12\sigma \sqrt{\pi \frac{a}{Q}} \cdot M_k \qquad (2.42)$$

where M_k can be approximate through the relation:

$$M_k = 1,0 + 1,2\left(\frac{a}{t} - 0,5\right) \qquad (2.43)$$

This presentation of the potential crack position and geometry does not deplete all the simple configurations for which the K value can be calculated. For more complex configurations, FEM type analysis can be used.

2.3. Elastic plastic fracture mechanics

Considering a cracked element (e.g. plate) that is under load reaching his limit resistance (failure), in figure 2.15 is presented a schematic graph of failure stress versus fracture toughness K_{IC}. For low toughness materials, the governing failure mechanism is *brittle fracture* (the variation of the stress is linear to fracture

$K_I = \sigma\sqrt{\pi a}$ - Irwin's stress intensity factor). At a high value of toughness the theory of linear elastic fracture mechanics is no longer valid. It can be said that NonLinear Facture Mechanics is a bridge between LEFM and failure.
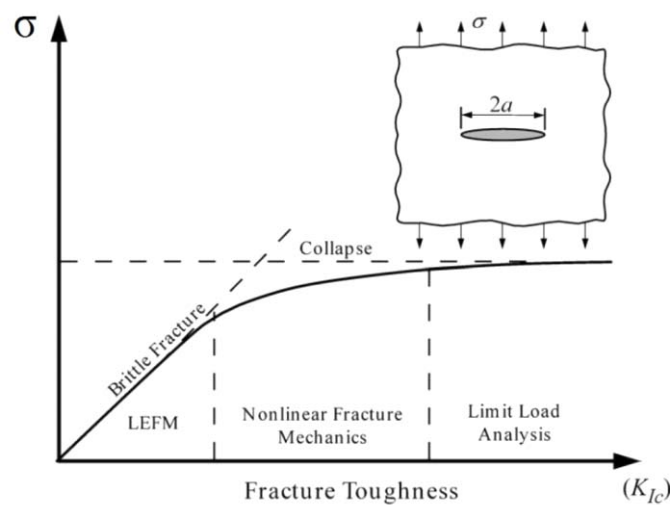
Fig.2.15. *Fracture toughness, LEFM and Elastic-Plastic Fracture Mechanics*

Linear elastic fracture mechanics (LEFM) is not valid any more when significant plastic deformation precedes failure (e.g. steel elements). As Griffith's criterion was put under question during his time, also in LEFM as entire part of the Fracture Mechanics field, was needed a change of perspective. In 1961 Wells [2.12] proposed the displacement of the crack faces as an alternative fracture criterion when significant plasticity precedes failure. The conclusion came as a result of his work applying LEFM to low- and medium strength structural steels. These materials were too ductile for LEFM to apply, but Wells noticed that the crack faces moved apart with plastic deformation before fracture occurs. This observation led to the development of the parameter now known as the ***crack-tip-opening displacement*** (CTOD) [2.11].

2.3.1. Crack tip opening displacement – CTOD

The elastic displacement fields near the crack tip described in Irwin's equations (2.32 and 2.33), are used in order to evaluate the displacement of a crack with length of $a+r_y$ where r_y is the radius of the Irwin's plastic zone at the tip of the crack (figure 2.16).
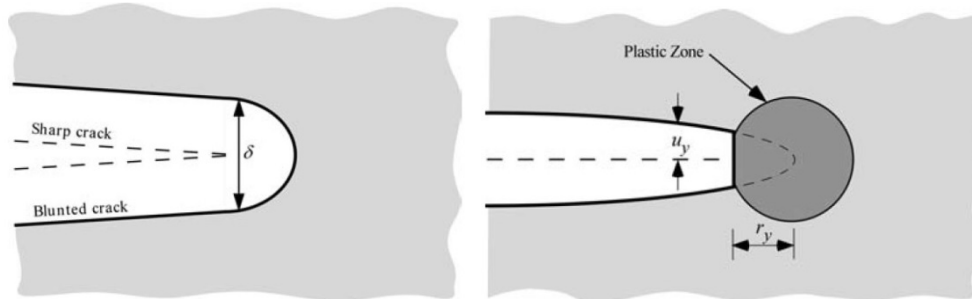
Fig. 2.16. *CTOD. (a) definition of displacement δ at the crack tip; (b) Irwin's plastic zone correction [2.11]*

For the given μ shear module, the displacement u_y (figure 2.16), considering the equation (2.32) is

$$u_y = \frac{\kappa + 1}{2\mu} K_I \sqrt{\frac{r_y}{2\pi}} = \frac{4}{E'} K_I \sqrt{\frac{r_y}{2\pi}} \qquad (2.44)$$

where $E' = \dfrac{E}{1 - v^2}$ (plain strain)

At Ch. 2.2.4. we found that $2r_Y = K^2 / \pi\sigma_Y^2$, meaning that:

$$r_y = \frac{1}{2\pi} \left(\frac{K_I}{\sigma_{YS}} \right)^2 \qquad (2.45)$$

where σ_{YS} is the yielding stress limit of the material.

Substituting the equation 2.45 into equation 2.44, it results δ – the CTOD:

$$\delta = 2u_y = \frac{4}{\pi} \frac{K_I^2}{\sigma_{YS}E} \qquad (2.46)$$

The **fracture criteria based on the critical crack opening** has the relation:

$$\delta_I \leq \delta_{crit} = \delta_{IC} \qquad (2.47)$$

The comparison values δ_{crit} are experiment determined, case in which it should be noticed that the validity of the obtained value is strictly limited to the thickness of the specimen on which the testing has been performed.

2.3.2. Rice's J contour integral

In 1968, Rice developed a parameter in order to characterize nonlinear behaviour of the material in the area of a crack [2.13]. By idealizing plastic deformation as nonlinear elastic, he provided the basis for extending fracture mechanics, determining the energy release rate to nonlinear materials. Rice showed

that this nonlinear energy release rate can be expressed as a line integral, which he called the **J integral**, evaluated along an arbitrary contour around the crack.

Rice's work has been put into active research due to the nuclear power industry in the U.S. in the early 1970s, where his studies were first applied. His work was used in order to determine the fracture toughness of nuclear pressure vessel steels where the use of LEFM has issues.

From 1971, researches use J integral in order to characterize the fracture toughness of the steels.

The value of J integral is equal to the energy release rate in a nonlinear elastic body that contains a crack.
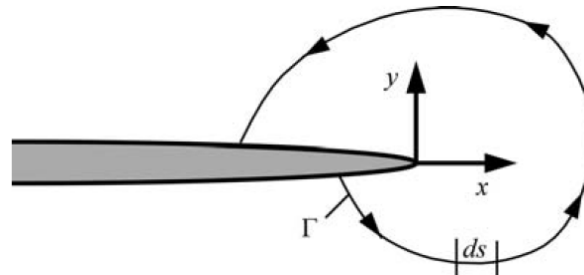
Fig. 2.17 *Arbitrary contour around the tip of a crack [2.11]*

Considering an arbitrary counter clockwise path (Γ) around the tip of a crack (figure 2.17), by definition J integral is given in following form:

$$J = \oint_{\Gamma} \left(W dy - T_i \frac{\partial u_i}{\partial x} ds \right) \tag{2.48}$$

with $W = \int \sigma_{ij} d\varepsilon_{ij}$ - strain energy density; Γ - integration path; ds - length increment along the contour Γ; $T_i = \sigma_{ij} n_j$ - traction vector on the contour; u_i - displacement vector, σ_{ij} - stress tensor and ε_{ij} - strain tensor.

As definition, the J integral is the mathematical expression of an integral which is calculated on the counter clock wise contour of the front of the crack, starting from one side to the other, in the cracked element (figure 2.17).

Rice has shown that J integral is path independent if necessary conditions are fulfilled. This is the prerequisite for its calculation along properly selected path, because its value is the same for the contours close to the crack tip, for contours outside plastic zone as well as for path along specimen sides.

J integral can also be presented as the energy, released on crack tip for unit area crack growth, *Bda*, by following expression

$$JBda = B \oint_{\Gamma} W dyda - B \oint_{\Gamma} T_i \frac{\partial u_i}{\partial x} dsda \tag{2.49}$$

where *B* is specimen thickness. The member $B \oint_{\Gamma} W dyda$ denotes the energy obtained

(and released) along the contour Γ for crack increase, *da*, supposing non-linear elasticity. Second member represents the work of traction forces on contour displacement for crack extension *da*. The value *JBda* is total energy at crack tip available for crack growth *Δa,* equal to the value *G*:

$$J = G = \frac{K^2}{E'} \quad E' = E \text{ for plane stress; } E' = \frac{E}{1 - v^2} \text{ for plane strain} \qquad (2.50)$$

In plastic region, *W* is not strain energy density, being dissipated inside the material, so *J* is not the energy at the crack, available for crack growth.

The ***fracture criteria based on the J integral*** has the relation:

$$J_I \leq J_{IC} \qquad (2.51)$$

Which means that the fracture occurs when the *J* integral value determined for the cracked element reaches the limit value of J_{IC}, value which represents the ***fracture toughness*** of the material.

2.3.3. J integral and CTOD relation

In the limit of small scale yielding,

$$J = m\sigma_{YS}\delta \qquad (2.52)$$

where m is a dimensionless constant that depends on the stress state and material properties.

If it is defined a contour Γ along the boundary of the strip yield area, the damage zone being long and slender (figure 2.18), meaning $\delta \gg d$, the first term in the *J* contour integral (equation 2.48) vanishes because $dy = 0$. Since the only surface tractions within δ are in the *y* direction, $n_y = 1$ and $n_x = n_z = 0$. Thus the *J* integral is given by

$$J = 2\int_0^\rho \sigma_{yy}(X)\left(\frac{du_y(X)}{dX}\right)dX = \int_0^\delta \sigma_{yy}(\delta)d\delta \qquad (2.53)$$

where $\delta = 2u_y (X= \rho)$. Since the strip-yield model assumes $\sigma_{yy} = \sigma_{YS}$ within the plastic zone, the integral *J* and crack tip opening displacement relation is given by:

$$J = \sigma_{YS}\delta \qquad (2.54)$$
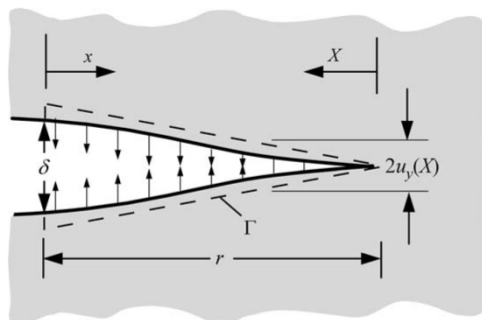
Fig. 2.18 *Contour along the boundary of the strip-yield zone ahead of a crack tip*

Many materials with high toughness do not fail catastrophically at a particular value of *J* or at a value of crack opening displacement.

Rather, these materials display a rising *R* curve, where *J* and CTOD increase with crack growth. Figure 2.19 schematically illustrates a typical *J* resistance curve for a ductile material. In the initial stages of deformation, the curve is nearly vertical; there is a small amount of apparent crack growth due to blunting. As *J* increases, the material at the crack tip fails locally and the crack advances further.

One measure of fracture toughness J_{Ic} is defined near the initiation of stable crack growth. The precise point at which crack growth begins is usually ill-defined.
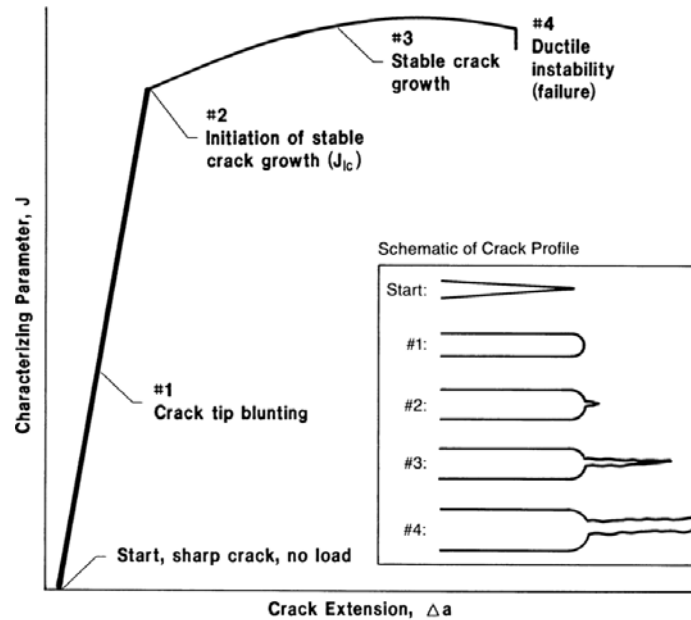
Fig. 2.19. *Schematic J resistance curve for a ductile material [2.11]*

The slope of the *R* curve at a given amount of crack extension is indicative of the relative stability of the crack growth - a material with a steep curve is less likely to experience unstable crack propagation. For *J* resistance curves, the slope is usually quantified by a dimensionless *tearing modulus*:

$$T_R = \frac{E}{\sigma_0^2} \frac{dJ_R}{da}$$

(2.55)

where the subscript *R* indicates a value of *J* on the resistance curve.

2.4. Fatigue

During service lifetime, steel structures elements under cyclic loads, can produce failure/rupture at stress values lower than the static loading yielding resistance. This phenomena can appear to structures like off shore structures, steel bridges, cranes, wind turbines towers or other structures under variable loads.

In a general form, structures under variable loads can develop a different behaviour comparing with structures subjected to static loading. The phenomena is known as *fatigue*, which is translated as a loss of strength during service life time. The fatigued element is subject to a damage which can evolve in time.

The fundamental equation for the fatigue cyclic loads was issued for the first time by Wöhler in 1847. The knowledge in the fatigue field evolved from a deterministic design, used in the beginning of 20 century, to a complex assessment procedure based on the damage accumulation produce by the high loads that action on the structure.

Wöhler imagined a diagram in which he showed that as the cyclic loads number is increasing, the failure is produced at lower values of stresses and the curve is asymptotic to σ_R (fatigue stress). Based on the experimental results, he postulate that the stress amplitude has the higher influence on the service life of a structure. He proposed higher safety factors for the design of the fatigued structures.

In 1924 Palmgreen observed for the first time the damage accumulation phenomena and around 1940 Miner develops an experimental program on fatigue with variable amplitude cycles. Both, but independently one of the other, have put the bases of the linear damage accumulation equation.

Fracture following fatigue is completely different from the static loads failure due to the possibility of failure at lower stresses, lower than the yield strength, without producing plastic deformations. Following this reason the fatigue cracks can be hardly visually noticed in the initial phase – crack initiation phase. Most of the fatigue cracks, which are producing the element failure, are starting in the proximity of the visible discontinuities which are the place for stress concentration. Types of discontinuities can be holes, section changing, welding, etc.

On the other side is wrong to consider that the fatigue fracture risk are exclusively attached to elements which are presenting macroscopic discontinuities. A shell type element which is presenting no visible flaw, under cyclic loading with constant amplitudes, may support damage from a level and then to fail at a precise number of cyclic loading.

Description of a characteristic fatigue fracture has in general the following three phases:
- o Crack initiation
- o Dominant crack propagation
- o Fracture

The fatigue phenomena can appear in following load cycling types:
- o High Cycle Fatigue (HCF) – considers that fatigue appears in a number of cyclic loads higher than 10^5, the repetitive stresses which are producing fracture, being under yielding strength, without plastic deformation appearance;
- o Low Cycle Fatigue (LCF) – named also the oligo-cyclic fatigue which appears at a number of cyclic loads lower that 10^4, under variable loading with stress peaks which determines accumulation of high

o local plastic deformations. This domain is important for the steel structure elements under seismic loads.

The low cycle fatigue is translated in principal through the damage which is affecting a structural element at a reduced number of cycles.

At the present time there are more types of approaches regarding the checking for fatigue:

(a) Fracture mechanics approach, using SIF of the stress and the crack propagation analytic formulae;
(b) Local deformation approach, based on specific deformation $\Delta\varepsilon$ in nonlinear domain;
(c) *S-N* curves approach.

2.4.1. Fatigue loading

Fatigue fracture of an element is defined as the fracture under repetitive loads for stresses lower than the ultimate strength of the material determined in static load conditions ($\sigma_{max} < \sigma_r$, and $\tau_{max} < \tau_r$). The phenomena is named fatigue of the material. Stress variation during a *T* period forms a cycle. For simplicity, the real variation of the stresses is replaced with a sinusoidal cycle (figure 2.20).
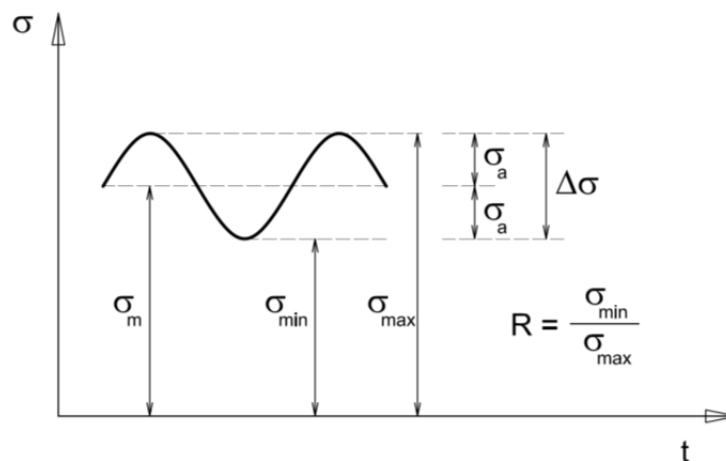
Fig.2.20. *Stress parameters used to define constant amplitude loading*

The following six parameters are used to define a constant amplitude stress cycle (figure 2.20)

σ_{max} – maximum stress in the cycle
σ_{min} – minimum stress in the cycle
σ_m – mean stress in the cycle; $\sigma_m = (\sigma_{max} + \sigma_{min})/2$
σ_a – stress amplitude; $\sigma_a = (\sigma_{max} - \sigma_{min})/2$
$\Delta\sigma$ – stress range; $\Delta\sigma = \sigma_{max} - \sigma_{min} = 2\sigma_a$
R – stress ratio; $R = \sigma_{min}/\sigma_{max}$

The loads can be grouped in function of the time variation as following:

o *Random load* – no variation rule;

o   *Periodical* – which is identical repeated at regular time intervals. These are divided in: stationary (the stress variates between a upper limit σ_{max} and a lower limit σ_{min} during a period *T* of time; nonstationary (the stresses is variating as amplitude in time of a period)

In figure 2.21 there are presented stress cycles with different mean stresses and R-ratios.
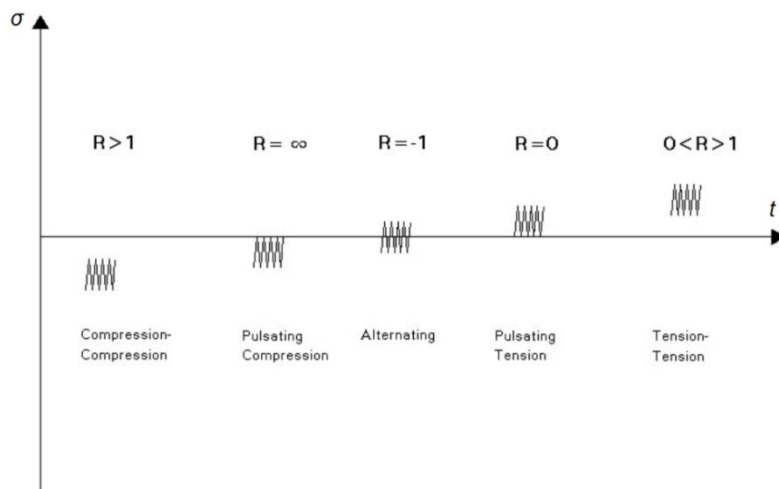
Fig.2.21. *Stress cycles with different mean stresses and R-ratios.*

Following figure 2.20 there are different types of cycles:
o   *Oscillating cycles* – if the stresses have the same sign
o   *Alternating cycles* – if the stresses are having different signs
o   *Pulsating cycles* – if the minimum stress is zero
Following the asymmetric coefficient R (figure 2.20), the cycles can be:

o   *Symmetrical cycles* $\left|\sigma_{max}\right| = \left|\sigma_{min}\right|$, $\sigma_m = 0$, $\sigma_A = \sigma_{max}$, R=-1

o   *Asymmetrical cycles* $\left|\sigma_{max}\right| > \left|\sigma_{min}\right|$, R≠-1

If the amplitude of the fatigue loading (σ_A) is having a low value, $\sigma_{max} = \sigma_{min} = \sigma_m$, R=1, it will be considered that the loading is static.

In case of wind loading applied on steel shell structures, several types of loading is needed to be taken into account:
a) Wind load as cyclic applied load which represent the wind load itself with varying values of speed
b) Wind load as a stochastic occurrence load which represent the extreme wind load with speeds values measured in short time of a turbulence or a gust. Types of stochastic wind loads are presented below:
- *Extreme wind* speeds are very high, sustained winds which will probably occur, but only rarely. Two extreme wind speeds are defined by the frequency with which they are expected to recur: the 50-year extreme wind, and the 1-year

extreme wind. They are based on the reference wind according to the design normative EN 1991-1-4 [2.34].

- An *extreme gust* is a sharp increase and then decrease in wind speed which occurs over a short period of time. The gust is also assumed to rise and fall over a period of 10 seconds. An illustration of an extreme operating gust is shown in figure 2.21 [2.35]

- *Extreme direction changes* are defined in an analogous manner to extreme gusts. In a typical example, the wind direction may change by 64 degrees over six seconds.

c) Resonance-induced loads which represents cyclic loads that result from the dynamic response of some part of the shell element or the entire structure (e.g. billboard tower), the structure being excited at one of its natural frequencies

The Eurocode [2.34] normative is considering in the design all three of the loads types through the load evaluation process. A detailed description of the wind load evaluation is done in the Annex 1 to the present thesis.
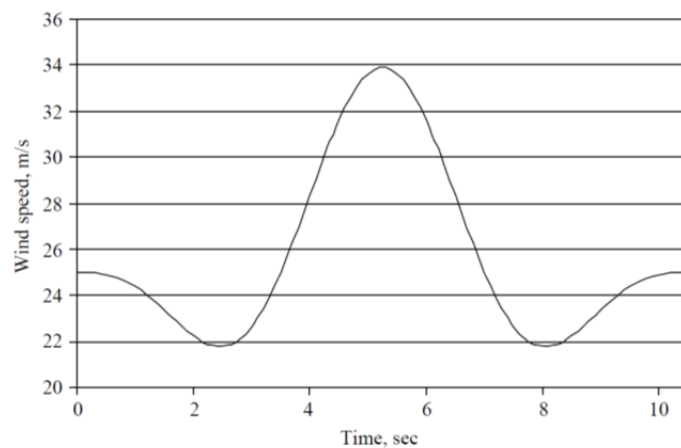
Fig.2.22. *Sample - extreme operating wind gust*

2.4.2. Fatigue strength of steel

The fatigue strength resistance under service loads can be defined as the fatigue of a structural element taken into account the following:

- *Irregular sequence of the loading cycles* with different values and different sequences (load spectrum)
- *Maximal values of the stresses* which rarely appear
- *Maximum allowable stresses* determined following life service structural element

The first structural fatigue accidents occurred at railway axles in 1843. After a number of kilometres, was noticed the inexplicable fracture of the railway axles, this element being under alternant load cycle. The moment is capture in history as the Versailles accident – derailment and fire of the train at Meudon caused by the locomotive one axle broke due to the fatigue.

The large number of brittle fracture failures by vessels during the Second World War lead to in depth study of the phenomena by the engineers. Of the approximately 5,000 commercial vessels built by the Americans during the Second World War, more than 1,000 of them had sizeable cracks until 1946. Between 1942-

1952 more than 200 ships had serious cracks, and at least nine T2 tankers and 7 Liberty vessels were broken in half due to brittle fracture.

All these events underlined that the known steel as a ductile material in normal conditions, became fragile in some conditions of loading.

In 1858 the German railway engineer Whöler made a series of testing on specimens made of same steel with same geometry. The specimens were tested under alternant cyclic loading. The results were presented graphically, each of the stress σ_i having correspondence a number of cycles N_i. The Whöler curve was obtained by linking the different points (σ_i, N_i) (figure 2.23)
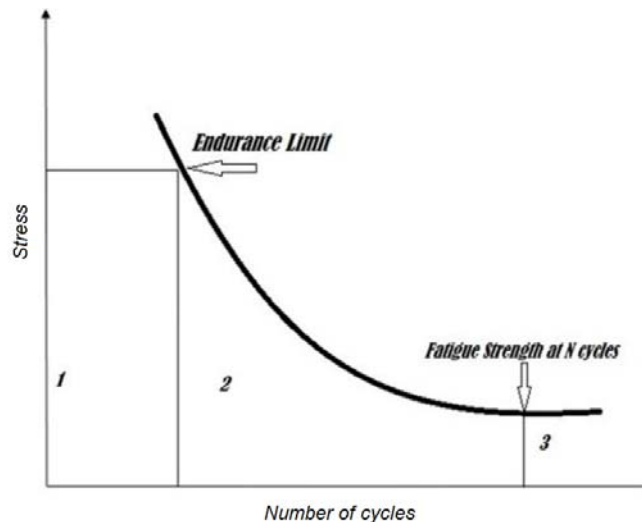
Fig.2.23. *S-N curve - Whöler curve*

Finding the fatigue strength throughout Whöler diagram can be laborious; the testing must be repeated for every asymmetry coefficient (*R*) of the cycle, for each curve fitting being necessary at least 9-11 specimens.

The main factors which are influencing the fatigue strength:
a) Loading
- o   loading cycles / stresses and deformations;
- o   the order of stresses application
- o   frequency
- o   the medium stresses
- o   the residual stresses

The cycling loading which are taken into account for the steel structures fatigue design, are producing in the structure effects which are differentiating from the element to element through the type, number and amplitude of these loading type. These loadings are determined by the service loadings which are acting on the structure throughout the entire life time.

According to EN 1993-1-9 [2.21], the fatigue loading is taken into account for a minimum $n = 2 \cdot 10^6$ cycles.

High Cycle Fatigue (**HCF**) is producing the fatigue of the material in variable loadings in which the maximum stress is having lower values compared to the static resistance of the material

Low Cycles Fatigue (**LCF**) is producing the fatigue of the material in loading conditions characterized by peaks of high stresses which are producing local elastic-plastic deformations.

These fatigue loads can integrate different loading cycles defined by complete sequences, occurrence frequency and size.

In case of steel shell structures, the wind load is producing a LCF cyclic loading type which determines the fatigue occurrence. The wind load is characterize by the load spectrum which depends on the location of the structure and topography of the site.

A detailed description of the wind loading force is done in chapter 3.3.

For the fatigue calculation (assessment of the flaws) will be used data from Romanian National Institute of Meteorology – recorded wind speed values. The distribution range of the values was done using Probability Density Functions (PDF) - Weibull distribution type detailed in the chapter 2.4.3.1. The stress ranges are considered following a rainflow algorithm, thus having the stresses linked to the loads and in the end the cycling loadings. It resulted the annually frequencies (cycles) to the stress range ($\Delta\sigma$) connection.

b) Material properties
- o   Material stress-deformation behavior
- o   Dimension and shape of the steel grains
- o   Hardness
- o   Chemical composition
- o   Microstructural homogeneity- microstructural inclusions, dislocations
- o   Welding process
- o   Thermic treatment applied to the welding

Fatigue strength of the steel depends on the microstructural state of it, on the chemical composition, thus, in order to achieve an alloy with optimal behaviour, must be take into consideration metallurgical methods.

Using a High Steel Strength delivers a fatigue strength improvement and higher ultimate limit strength for HCF.

However, for the with flaws structural elements, the behaviour is different. The weaken cross section of the structural elements (e.g. bolts holes, for maintenance cut outs, welding HAZ etc.), surface flaws or corrosion are reducing the fatigue strength throughout the reducing of the number fatigue loading cycles. This fact is having a major importance, considering that the speed of crack growth is (in great measure) independent of the tension resistance of the material.

The researches have proved that the fatigue strength of the different steel types, for elements which are having the same flaw type, is almost equal.

c) Geometry
- o   Global geometry of the structural element
- o   Local geometry of the element – local flaws
- o   Naked eye visible discontinuities: welding flaws, streaks, surface tweaks, nonlinearities etc.

The shape of the structural element represents the most important factor which is influencing the fatigue behaviour.

It is known that every cross section change can produce considerable stress concentrators – peak of local high stress. These stress concentrators can produce

micro cracks initiation which can produce failure of the structural element at lower stresses compared to the designed ones.

Eurocode 1993-1-9 [2.21] is presenting requirements for the different notch types and classification of the details into a fatigue design curve. A detailed presentation of the EN procedure is presented in chapter 2.4.6.

An optimal steel structures fatigue design must take into account followings prescriptions:

- o Respecting the neutral axis position for different details which are changing the stress values;
- o Applying notches type details in areas where the bending moment has minimum values;
- o Avoiding nonlinearities – avoiding secondary stresses;
- o Avoiding stress concentration compounds in same areas (e.g. welding in weaken cross section);
- o Applying notches details in area characterized by compression stresses;
- o Avoiding the peak stresses – efforts concentrators (e.g. respecting geometrical disposal of the welded elements)

d) Environment
- o Corrosion;
- o Temperature;
- o Humidity;
- o Radiation etc.

The severe corrosion of parts of surfaces of structural elements is a flaw that can drive to a considerable reduction of the structure under cyclic loads. The corrosion can be considered a surface flaw / notch type, which is minimising the material fatigue resistance. Also can be the situation of forming additional stress concentrators. Thus, the steel structure elements should have an adequate corrosion protection like: multiple layers of paint, zinc coating, different type of details (closing all the penetrating openings - e.g. end cap plate).

2.4.3. Loading history – loading spectrum

Throughout on structural elements measurements during the service time, it can be obtained graphical representations of the loading history – time / loading (or directly stress).

The *remaining lifetime of a structure* (or an element of a structure) can be determined in following ways:
- - Exactly loading simulations (used in aeronautic and automobile industry)
- - Throughout developed Wohler curves (with constant amplitudes) and then applying the damaging cumulation law.

In order to determine the number and sizes of the cycles, it must be adopted a numbering method.

Cycle counting methods are algorithms that identify fatigue cycles by combining and extrapolating information from extrema (maxima and minima) in a time series. These algorithms are used together with damage accumulation rules, which calculate the total damage as a summation of increments. The most popular method among the counting methods is the so-called rainflow counting (RFC) method, jointly with the Palmgreen-Miner rule of linear damage accumulation to

calculate the expected damage. Other cycle counting methods include: peak-valley counting (PVC), level-crossing counting (LCC), range counting (RC), and range-pairs counting (RPC);

2.4.3.1 Statistical analysis of wind load data - Probability Density Functions

Statistical analysis can be used to determine the wind of a given site and to estimate the wind load history. If time series measured data are available at the desired location and height, there may be little need for a data analysis in terms of probability distributions and statistical techniques. On the other hand, if projection of measured data from one location to another is required, or when only summary data are available, then there are distinct advantages to the use of analytical representations for the probability distribution of wind speed.

For statistical analysis, *a probability distribution is a term that describes the likelihood that certain values of a random variable (such as wind speed) will occur*. As discussed next, probability distributions are typically characterized by a probability density function or a cumulative density function.

The frequency of occurrence of wind speeds may be described by the probability density function, *p(U),* of wind speed. The probability density function (PDF) may be used to express the probability of a wind speed occurring between U_a and U_b:

$$p(U_a \leq U \leq U_b) = \int_{U_a}^{U_b} p(U)dU \tag{2.56}$$

Also, the total area under the probability density curve is given by:

$$\int_0^\infty p(U)dU = 1 \tag{2.57}$$

If *p(U)* is known, the following parameters can be calculated:
- *Mean wind speed,* $\overline{U}$:

$$\overline{U} = \int_0^\infty U p(U)dU \tag{2.58}$$

- *Standard deviation of wind speed,* σ_U :

$$\sigma_U = \sqrt{\int_0^\infty (U - \overline{U})^2 p(U)dU} \tag{2.59}$$

- *Mean available wind power density,* $\overline{P}/A$:

$$\overline{P}/A = \frac{1}{2} \cdot \rho \cdot \int_0^\infty U^3 p(U)dU = \frac{1}{2} \cdot \rho \cdot \overline{U}^3 \tag{2.60}$$

where $\overline{U}^3$ is the expected value for the cube of the wind speed.

It should also be noted that the probability density function can be superimposed on a wind velocity histogram by scaling it to the area of the histogram.

Two probability distributions are commonly used in wind data analysis: (1) the Rayleigh and (2) the Weibull. The Rayleigh distribution uses one parameter: the mean wind speed. The Weibull distribution is based on two parameters and, thus, can better represent a wider variety of wind regimes. Both the Rayleigh and Weibull distributions are called '*skew*' distributions in that they are defined only for values greater than 0.
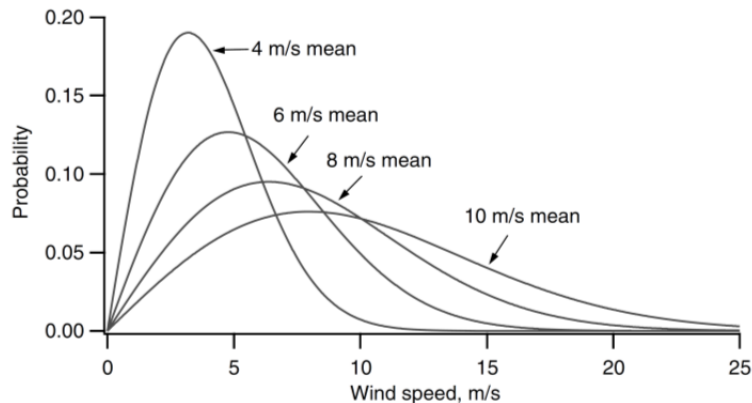
Fig. 2.24. *Example of Rayleigh probability density function*

Rayleigh Distribution

This is the simplest velocity probability distribution to represent the wind resource since it requires only a knowledge of the mean wind speed, $\overline{U}$. The probability density function and the cumulative distribution function are given by:

$$p(U) = \frac{\pi}{2}\left(\frac{U}{\overline{U}^2}\right)exp\left[-\frac{\pi}{4}\left(\frac{U}{\overline{U}}\right)^2\right] \tag{2.61}$$

$$F(U) = 1 - exp\left[-\frac{\pi}{4}\left(\frac{U}{\overline{U}}\right)^2\right] \tag{2.62}$$

Figure 2.24 illustrates a Rayleigh probability density function for different mean wind speeds. As shown, a larger value of the mean wind speed gives a higher probability of higher wind speeds.

Weibull Distribution

Use of the Weibull probability density function requires knowledge of two parameters: *k*, a shape factor, and *c*, a scale factor. Both of these parameters are functions of $\overline{U}$ and σ_U. The Weibull probability density function and the cumulative distribution function are given by:

$$p(U) = \left(\frac{k}{c}\right)\left(\frac{U}{c}\right)^{k-1} exp\left[-\left(\frac{U}{c}\right)^k\right] \tag{2.63}$$

$$F(U) = 1 - exp\left[-\left(\frac{U}{c}\right)^k\right] \tag{2.64}$$

Examples of a *Weibull* probability density function, for various values of k, are given in figure 2.25. As shown, as the value of k increases, the curve has a sharper peak, indicating that there is less wind speed variation. Methods to determine k and c from U and σ_U are presented below.
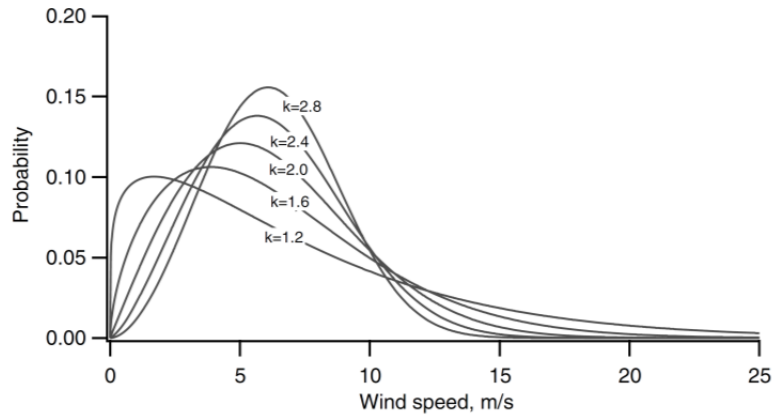
Fig. 2.25. *Example of Weibull probability density function* for $\overline{U}$ = 6 m/s

Using Equation (2.63) for the Weibull distribution, it is possible to determine the average velocity as follows:

$$\overline{U} = c \cdot \Gamma\left(1 + \frac{1}{k}\right) \tag{2.65}$$

where $\Gamma(x)$ = gamma function = $\displaystyle\int_0^\infty e^{-t} t^{x-1} dt$

It can also be shown that for the Weibull distribution:

$$\sigma_u^2 = \overline{U}^2 \left[\frac{\Gamma(1+2/k)}{\Gamma^2(1+2/k)} - 1\right] \tag{2.66}$$

Using the Weibull distribution and assuming that c and k are known, the expected value of the cube of the wind speed, $\overline{U^3}$, may be found as follows:

$$\overline{U^3} = \int_0^\infty U^3 p(U) dU = c^3 \Gamma(1+3/k) \tag{2.67}$$

One should note that normalized values of $\overline{U^3}$ depend only on the shape factor k. For example, the energy pattern factor, K_e (defined as the total amount of power available in the wind divided by the power calculated from cubing the average wind speed) is given by:

$$K_e = \frac{\overline{U^3}}{(U)^3} = \frac{\Gamma(1+3/k)}{\Gamma^3(1+1/k)} \tag{2.68}$$

Examples of some parameters of interest are given in Table 2.1.

It should also be noted that a Weibull distribution for which $k=2$ is a special case of the Weibull distribution. It equals the Rayleigh distribution.

Table 2.1. *Variation of parameters with Weibull k shape factor*

k	$\sigma_U/\overline{U}$	K_e
1,2	0,837	3,99
2	0,523	1,91
3	0,363	1,40
5	0,229	1,15

2.4.3.2 Calculating the number of fatigue cycles - Rainflow counting method

A technique known as rainflow cycle counting has been developed [2.22] [2.23] to identify alternating stress cycles and mean stresses from time series of randomly applied loads. Once the mean and alternating stress data have been found, they can be converted to zero mean alternating stresses and the total damage estimated using Miner's Rule.

Local highs and lows in the data are identified as '*peaks*' or '*valleys*'. The range between every peak and valley and between every valley and every peak are all considered to be '*half cycles*'. The algorithm then pairs the half cycles to find complete cycles, and associates them with a mean.
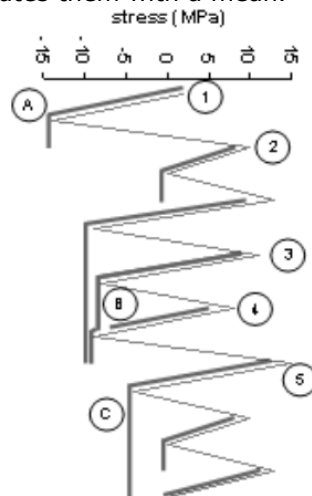
Fig. 2.26. *Example of Rainflow algorithm [2.42]*

The term '*rainflow*' derives from an aspect of the method, in which the completion of a cycle resembles rain water dripping from a roof (a peak) and meeting water flowing along another roof (from a valley below). In this view of the method, the peak–valley history is imagined to be oriented vertically so that the '*rain*' descends with increasing time. An example of a complete cycle is shown in figure 2.26 and the steps of the algorithm are described below:

1. Reduce the time history to a sequence of (tensile) peaks and (compressive) valleys.
2. Imagine that the time history is a template for a rigid sheet (pagoda roof).
3. Turn the sheet clockwise 90° (earliest time to the top).

4. Each *tensile peak* is imagined as a source of water that "drips" down the pagoda.
5. Count the number of half-cycles by looking for terminations in the flow occurring when either:
   o It reaches the end of the time history;
   o It merges with a flow that started at an earlier *tensile peak*; or
   o It flows when an opposite *tensile peak* has greater magnitude.
6. Repeat step 5 for *compressive valleys*.
7. Assign a magnitude to each half-cycle equal to the stress difference between its start and termination.
8. Pair up half-cycles of identical magnitude (but opposite sense) to count the number of complete cycles. Typically, there are some residual half-cycles.

2.4.4. Wöhler curves – fatigue resistance curves

A first step in determining the lifetime of the steel shell element structures, consists in establishing the fatigue resistance curves - Wöhler curves.

Obtaining the fatigue resistance curves, included in the design provisions, are derived from a large number of testing on samples, generally under tension cycle loading with constant variation. The curves are established through statistical analysis of the experimental data results associated to a probabilistic criteria.

The test results are presented in a double logarithmic system – the Wöhler curve becoming linear. Through linear regression it is obtained the Wöhler median curve with a 50% survival probability.

The Wöhler curve equation is under the following form:

$$N_i = \left(\frac{\Delta\sigma_R}{\Delta\sigma_i} \right)^k \cdot N_R \qquad (2.69)$$

or

$$N_i = C \cdot \Delta\sigma_i^{-k} \text{ , where } C = N_R \cdot \Delta\sigma_R^k \qquad (2.70)$$

or

$$log\, N_i = log\left(N_R \cdot \Delta\sigma_R^k \right) - K \cdot log\, \Delta\sigma_i \qquad (2.71)$$

where
$\Delta\sigma_i$ - stress range from the loading history

N_i - number of loading cycles corresponding to the stress range of $\Delta\sigma_i$ ($\Delta\sigma_1$, $\Delta\sigma_2$ …)

N_R - 2 x 10^6 cycles

$\Delta\sigma_R$ - fatigue resistance for N_R cycles

k - curve slope
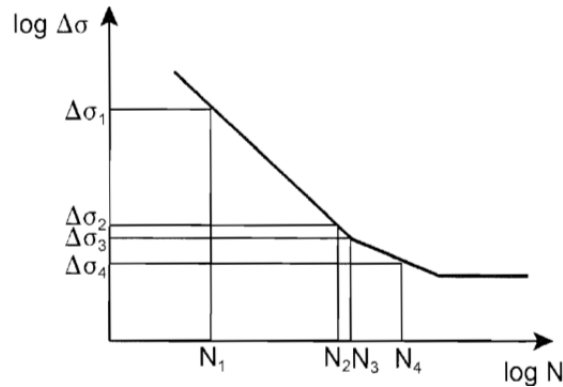
Fig. 2.27. *Eurocode 1993-1-9 – Fatigue resistance curve [2.21]*

Design fatigue calculation Wöhler curves can be as following:
- Singular slope curves – it is considered that also the lower stress ranges has impact on the fatigue resistance
- Singular slope and a plateau in the breaking point curves – the stress ranges after the breaking point are not producing fatigue
- Two slopes and a plateau – the Eurocode curves (figure 2.27)

2.4.5. Damage summation – Palmgreen-Langer-Miner rule

In order to consider the real loading which is acting on the structure, having variable amplitude, Palmgreen (1924) [2.38], Langer (1937) [2.39] and Miner (1945) [2.40] proposed a linear cumulative principle of the damages to a give structure.

According to this principle, if a testing probe is under level σ_1 (figure 2.28), failure will occurred after N_1 cycles, when the damage is total, meaning that at a lower
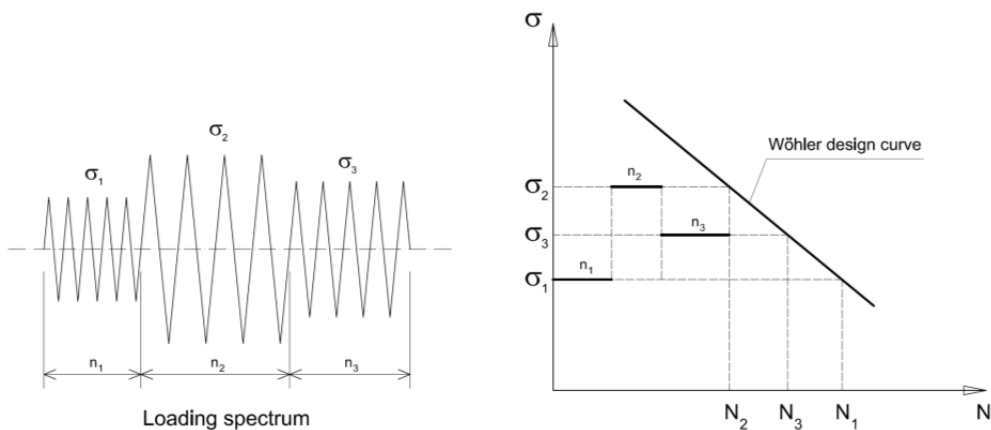
Fig. 2.28. *Schematic representation of the linear damaging cumulation principle*

number of cycles $n_1 < N_1$, the damage is produced only in (*100 · n_1/N_1)%*. Loading the testing probe at another level $\sigma_2 > \sigma_1$ with a number of $n_2 < N_2$ (N_2 being the number of cycles which is producing the failure at a σ_2 level), it will be added the damage (*100 · n_2/N_2)%*. Same for the level 3 of loading.

In the end the damage produced at different stress levels σ_i repeated for a number of n_i cycles, the failure will occurred at total damage of D = 1.

$$D = \frac{n_1}{N_1} + \frac{n_2}{N_2} + \frac{n_3}{N_3} + ... + \frac{n_k}{N_k} = \sum_{i=1}^{k} \frac{n_i}{N_i} \tag{2.72}$$

The Palmgree-Langer-Miner rule is not considers the history of loading and its nonlinear form, the order of the terms in the D relation being indifferent.

The Miner principle can determine the lifetime of a structure (fact which is detailed in chapter 2.7.

Palmgreen-Langer-Miner rule applied to the wind load structures

Fatigue failure results from an accumulation of damage due to fluctuating loads. For this kind of macroscopic view of fatigue, there is general agreement that an increment of damage results from each hysteresis cycle displayed in the local stress-strain diagram. Thus, each local maximum of the load time history is paired with the local minimum that completes a full cycle (rain-flow cycle counting [2.22], [2.23]). Each of these cycles is characterized by the paired extreme values (or equivalently by the range and midpoint values, i.e. the difference between and the mean of the two paired cycle extremes). If the damage accumulates linearly and independently for each cycle [2.24] then the total damage, *D*, will be given by:

$$D = \sum_{i} \frac{1}{N(S_i)} \tag{2.73}$$

where *Si* is the load range for the ith cycle, and $N(S_i \cdot)$ is the number of cycles to failure for a constant amplitude loading with the range given by the argument (i.e. the S-N curve). In this expression, it has been further assumed that the local stress at the failure location is linearly related to the loading. Typically, for fatigue analysis the S-N curve selected for design is associated with a given survival probability (often 95 %) and level of confidence (often 95 %) in determining the curve from materials data. Thus, the desired minimum level of reliability may be expected when the damage sums to unity.

For the life of a wind loaded structure, there will be many cycles of varying sizes resulting from a broad range of wind conditions. Therefore, for design purposes, a load spectrum must be estimated. The largest cycles for this spectrum will be estimated from a smooth fit to the data obtained from simulations or testing of a duration that is significantly shorter than the structure lifetime. For each wind condition, it may be assumed that the load is modelled by a stationary random process. Thus, the expected damage for a given wind speed, *V*, and a specific time period, *T*, will be given by:

$$E\langle D|V,T \rangle = \int_{0}^{\infty} \frac{n_{ST}(S|V,T)}{N(S)} dS \tag{2.74}$$

where $(S|V,T)$ is the short term load spectrum defined as a density function for the number of cycles. In this case, the expected number of cycles in any load range interval (S_A, S_B) during the time period *T* is given by:

$$\int\limits_{S_A}^{S_B} n_{ST}(S|V,T)dS \tag{2.75}$$

The expected damage from normal all loads for the whole structure life is then given by extending the time interval to the full lifetime and integrating over the range of operating wind speeds, so that

$$E\langle D\rangle = \frac{Lifetime}{T}\int\limits_{V_{in}}^{V_{out}} E\langle D|V,T\rangle p(V)dV = \frac{Lifetime}{T}\int\limits_{V_{in}}^{V_{out}}\int\limits_0^\infty \frac{n_{ST}(S|V,T)}{N(S)}p(V)dSdV \tag{2.76}$$

where $p(V)$ is the *probability density function* for the wind speed.

Defining the long-term load spectrum,

$$n_{LT}(S) = \frac{Lifetime}{T}\int\limits_{V_{in}}^{V_{out}} n_{ST}(S|V,T)p(V)dV \tag{2.77}$$

then gives:

$$E\langle D\rangle = \int\limits_0^\infty \frac{n_{LT}(S)}{N(S)}dS \tag{2.78}$$

In many cases, it is convenient, for practical purposes, to divide the ranges of load and wind speed values into discrete bins. In this case, the expected damage can be approximated by:

$$E\langle D\rangle \approx \sum\limits_{j,k} \frac{n_{jk}}{N(S_k)} \tag{2.79}$$

where n_{jk} is the expected number of lifetime load cycles in the jth wind speed and the kth load bins, and S_k is the center value for the kth load bin. Thus, from the above definition,

$$n_{jk} = \frac{Lifetime}{T}\int\limits_{V_j-\Delta V_j/2}^{V_j+\Delta V_j/2}\int\limits_{S_k-\Delta S_k/2}^{S_k+\Delta S_k/2} n_{ST}(S|V,T)p(V)dSdV \tag{2.80}$$

where ΔV_j is the width of the jth wind speed bin and ΔS_k is the width of the kth load bin.

Using these results, the limit state relation for fatigue analysis becomes:

$$\int\limits_0^\infty \frac{n_{LT}(S)}{N(\gamma S)}dS \le 1 \tag{2.81}$$

where $\gamma = \gamma_f\gamma_m\gamma_n$ is the product of all three general partial safety factors for load, materials, and consequences of failure, respectively. In discrete terms this equation results in:

$$\sum\limits_{j,k} \frac{n_{jk}}{N(\gamma S_k)} \le 1 \tag{2.82}$$

Also, for larger range values, the local stress or strain may transition from a compression-compression or tension-tension dominated case to a tension-compression case, which could have a different analytical S-N curve representation. It is important to utilize the proper S-N relation in determining the equivalent cyclic range. For a given load time history, the rain flow cycles are first identified. Then a set of equivalent constant-midpoint cycles is computed considering the proper S-N relation for each cycle. The distribution of these equivalent cycles is then estimated giving a new short-term equivalent load spectrum. This new spectrum is then used to define the number of cycles used for the damage fraction for each load and wind speed bin. The main advantage of using this method is that the estimation of the equivalent spectrum is statistically more robust than tracking the midpoint levels as an independent variable. This advantage results because many more load cycles are counted from typical time series load data for each load and wind speed bin than when midpoint bins are also tracked separately.

An additional practical issue that arises in determining the short-term load spectrum is the large number of small cycles determined by the rain-flow method. These small cycles can often occur at nearby points in time and may therefore be correlated. The small cycles can also distort the shape of analytical approximations to the tail of the distribution. It is therefore recommended to only consider cycles above a threshold when approximating the tail of the short-term distribution. A threshold value of at least the 95th percentile typically works well in practice. Lower threshold values may be appropriate if the small cycles have been eliminated or if the increased number of data points used for the fitting process is expected to yield significant additional statistical reliability.

For practical wind load structures design applications, it is necessary to estimate the short-term equivalent load spectrum from dynamic simulation data and then compute the lifetime damage. One method of accomplishing this task is given by the following procedure:

- select the reference midpoint level as the mean load level considering all wind speeds;
- from the simulation data for a given wind speed, extract the sequence of local maxima and minima. The sequences of local maxima and minima from multiple time series for the same wind conditions may be concatenated into a single series;
- use the rain flow method to identify the midpoint and range for each simulated load cycle;
- determine the equivalent range for each load cycle in relation to the selected reference midpoint level;
- determine an analytical fit for the short-term probability distribution of equivalent load cycles, $F_{ST}(S|V,T)$ for the data above the selected threshold.
- determine the expected number of lifetime cycles in each bin using the data when the load bin is below the threshold and the fitted load distribution when the load bin is above the threshold. This results in

$$n_{jk} \approx \left(\frac{Lifetime}{T}\right)P_j \begin{cases} m_{jk} & \text{if } S_k \text{ is below the } j^{th} \text{ threshold} \\ M_j\left(F\left(S_k + \frac{\Delta S_k}{2}|V_j,T\right) - F\left(S_k - \frac{\Delta S_k}{2}|V_j,T\right)\right) & \text{if } S_k \text{ is above the } j^{th} \text{ threshold} \end{cases} \qquad (2.83)$$

where m_{jk} is the number of simulation fatigue cycles counted in the data for the jth wind speed bin and k^{th} load bin below the threshold, M_j is the number of fatigue cycles counted in the simulation above the threshold, and

$$P_j = e^{-\pi\left(\frac{V_j - \Delta V_j/2}{2V_{ave}}\right)} - e^{-\pi\left(\frac{V_j + \Delta V_j/2}{2V_{ave}}\right)} \qquad (2.84)$$

is the fraction of time the wind speed is in bin j for the assumed Rayleigh wind speed distribution.

- Sum the damage using the left hand side of equation (2.82)
- Sum the total lifetime damage from all fatigue load cases.

In using this procedure, care must be taken that
  o the resolution of the wind speed and load range bins is sufficient for the desired numerical precision, and
  o sufficiently large values of load range are used to adequately represent the tail of the long-term load distribution.

The first issue may be addressed by approximating the error as half the difference between results computed by two different bin resolutions skipping data from every other wind speed or load range. An alternative would be to compute the damage summation using the endpoints for the bin values instead of the central values to bound the result.

The second issue may be addressed by progressively increasing the highest load range bin value until a negligible increase in the lifetime damage is observed. Note because the ratio $\frac{Lifetime}{T}$ is a large number, the largest required load bin may be significantly larger than the largest cycle observed in the simulation data. This results because the total simulated load time history is much smaller than the turbine lifetime, and statistical extrapolation is required to accurately estimate damage from the tail of the long-term load distribution.

2.4.6. Eurocode 1993-1-6 fatigue design requirements

The European Norm – Eurocode 1993-1-9 – Design of the steel structure – Fatigue design [2.21], is proposing the following assessment methods:
-    *damage tolerant method*
The damage tolerant method should provide an acceptable reliability that a structure will perform satisfactorily for its design life, provided that a prescribed inspection and maintenance regime for detecting and correcting fatigue damage is implemented throughout the design life of the structure.
-    *safe life method*
The safe life method should provide an acceptable level of reliability that a structure will perform satisfactorily for its design life without the need for regular in-service inspection for fatigue damage. The safe life method should be applied in cases where local formation of cracks in one component could rapidly lead to failure of the structural clement or structure.

Fatigue strengths are determined by considering the structural detail together with its metallurgical and geometric notch effects. In the fatigue details presented in this part the probable site of crack initiation is also indicated.

However the design for the shell elements must respect also the EN 1993-1-6 – Steel structure design - steel shell element design. Thus the design values of the actions for each load case should be taken as the varying parts of the total action representing the anticipated action spectrum throughout the design life of the structure.

In each verification of the limit state, the design value of the fatigue stress should be taken as the larger stress range $\Delta\sigma$ of the values on the two surfaces of the shell, and based on the sum of the primary and the secondary stresses.

The geometric stress range takes into account only the overall geometry of the joint, excluding local stresses due to the weld geometry and internal weld effects.

The fatigue strength for nominal stress ranges is represented by a series of (log $\Delta\sigma_R$) – (log N) curves and (log $\Delta\tau_R$) – (log N) curves (S-N curves), which correspond to typical detail categories. Each detail category is designated by a number which represents, in N/mm^2, the reference value $\Delta\sigma_C$ and $\Delta\tau_C$ for the fatigue strength at 2 million cycles (10^6).

For constant amplitude nominal stress ranges, the fatigue strength can be obtained as follows:

$$\Delta\sigma_R^m N_R = \Delta\sigma_C^m \, 2x10^6 \text{ with m=3 for N} \leq 5 \times 10^6 \text{ (figure 2.29)} \qquad (2.85)$$
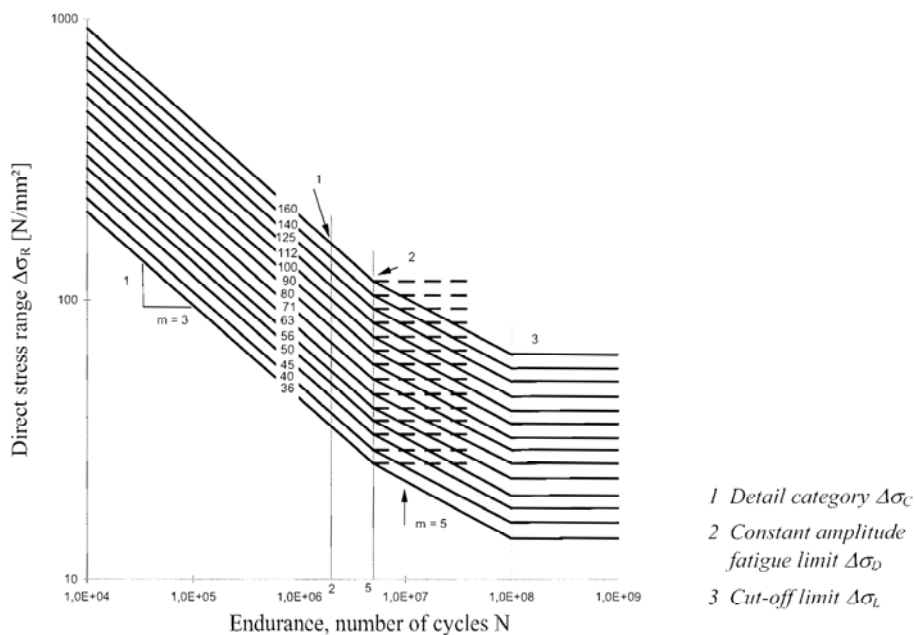
Fig.2.29. *Fatigue strength curves for direct stress ranges*

$$\Delta\tau_R^m N_R = \Delta\tau_C^m \, 2x10^6 \text{ with m=5 for N} \leq 5 \times 10^8 \text{ (figure 2.30)} \qquad (2.86)$$
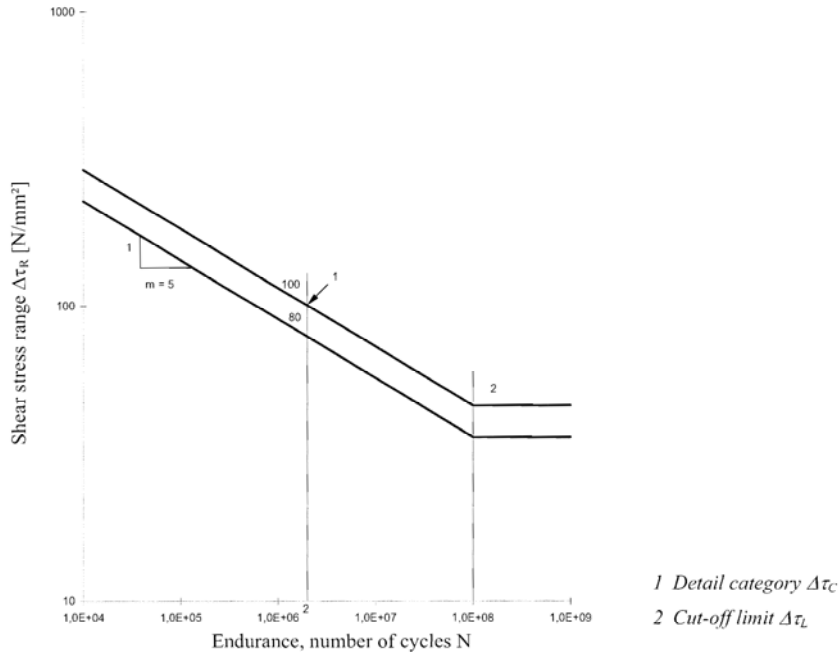
Fig.2.30. *Fatigue strength curves for shear stress ranges*

In order to ensure that non conservative conditions are avoided, such details an alternative assessment may increase the classification of such details by one detail category provided that the constant amplitude fatigue limit $\Delta\sigma_D$ is defined as the fatigue strength at 10^7 cycles for m=3 (figure 2.31)
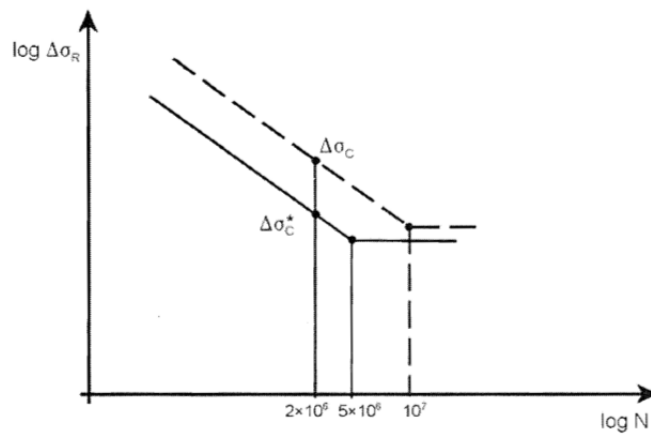
Fig.2.31. *Alternative fatigue strength* $\Delta\sigma_D$

For verification nominal, modified nominal or geometric stress ranges due to frequent loads should not exceed
$\Delta\sigma \leq 1,5\ f_y$ for direct stress ranges

$\Delta\tau \leq 1{,}5\, f_y /\sqrt{3}$ for shear stress ranges

where f_y represents the yielding strength of the steel.

The lifetime assessment of the structure according with Eurocode is done with Palmgreen-Langer-Miner rule presented at the previous subchapter.

A schematic representation of the phases of the fatigue design according with the European norm is presented in the figure 2.32.

a) Loading sequence: Typical load cycle (repeated n-times in the design life)	
b) Stress history at detail	
c) Cycle counting (e.g. reservoir method)	
d) Stress range spectrum	

e) Cycles to failure	
f) Damage summation (PaImgreen-Miner rule)	$$D = \frac{n_1}{N_1} + \frac{n_2}{N_2} + \frac{n_3}{N_3} + \ldots + \frac{n_k}{N_k} = \sum_{i=1}^{k} \frac{n_i}{N_i} < D_L$$
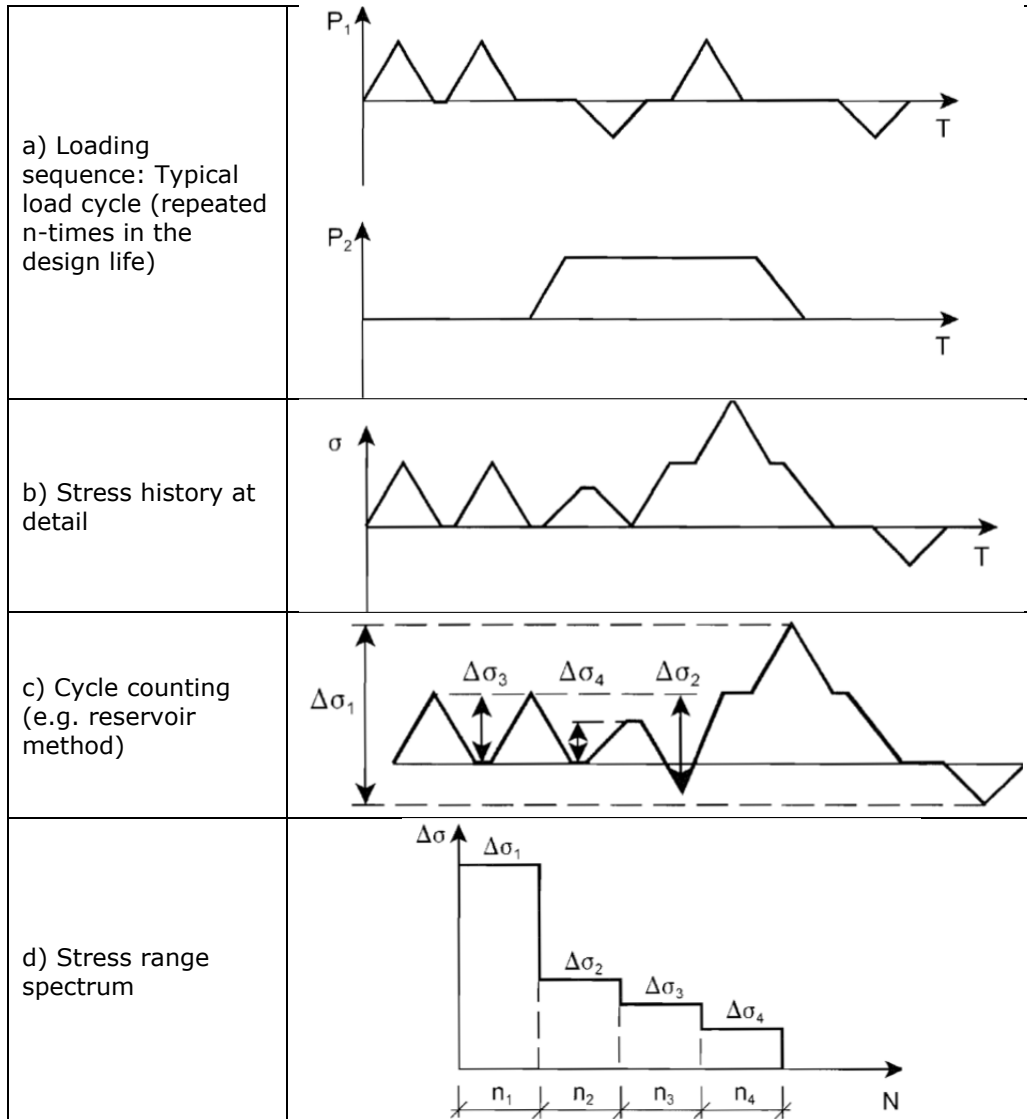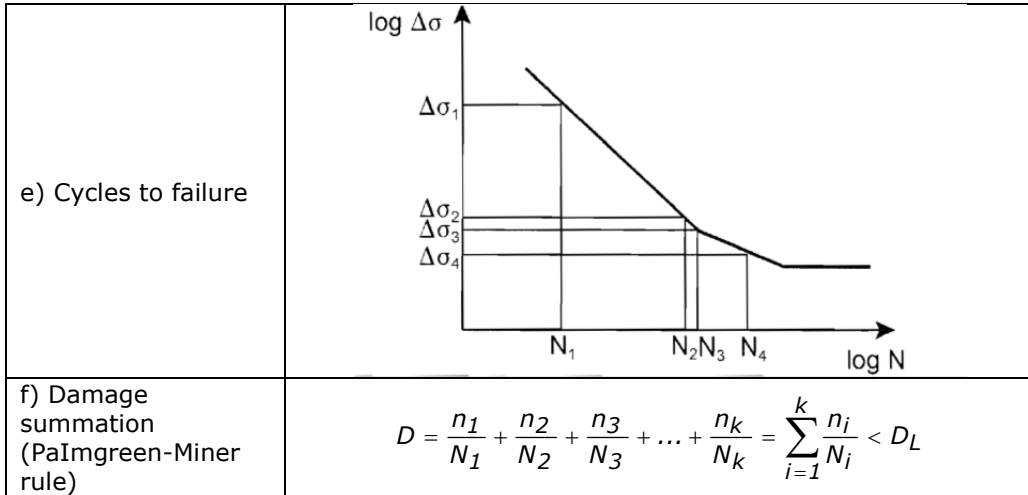
Fig.2.32. *Cumulative damage method [2.21]*

2.5.   Standard   methods   for   fracture   toughness determination

The material fracture toughness is defined, in a generic term, through the measurement of the crack propagation strength. In general the fracture toughness of the materials is associated with the fracture mechanics proposed methods.

In order to apply the fracture criteria, is absolutely necessary to know the critical values of the material toughness K, J and δ.

The first proposals of standards for determining fracture toughness in plane strain have published by American Society for Testing and Materials - ASTM (ASTM E399-70T) and British Standard Institution – BSI (DD 3). There are many common features in experimental determination of fracture mechanics parameters, especially in measuring their critical values and material properties.

The ASTM methodology which must be followed in a fracture mechanics testing, contains the following steps:

- o   Chosen the testing type and choosing of the materials
- o   Selection and processing of the specimen
- o   Acquirement of the equipment and testing instruments
- o   Introducing of the defect in the specimen
- o   Testing according with the procedure
- o   Assessing of the testing results
- o   Validation of the results
- o   Testing report

In the figure 2.33 there are presented the types of the fracture mechanics specimens for fracture toughness testing.
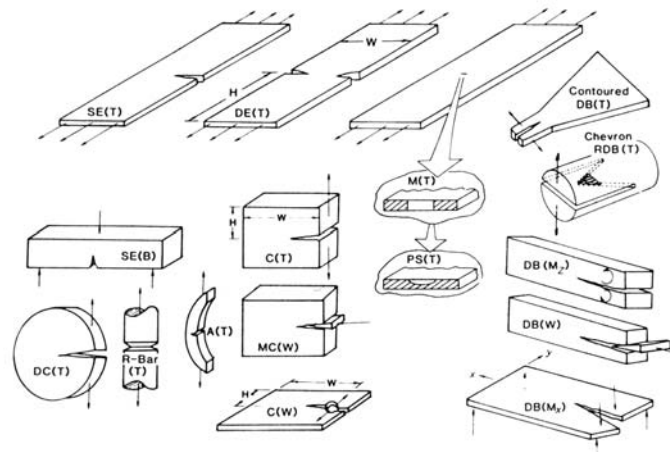
Fig.2.33. *Specimen examples specific to fracture mechanics testing*

As a general characteristic it should be noticed that the fracture mechanics specimens are having a *mechanical induced notch* below which is introduced a sharp crack type flaw – fatigue pre-crack.

At the beginning of the fracture mechanics developing, the fracture toughness determination testing started with a linear elastic methodology using the stress intensity factor at the crack tip, *K*. The extensions of this parameter into elastic plastic domain, are *J* integral, crack tip opening and the resistance *R* curve.

It should be noticed that K_{Ic} is determined directly by definition, and the standard methods of measuring *CTOD* and *J* integral are based on the indirect, approximate relations.

According to the ASTM standards, following testing equipment and auxiliary materials must be used:

Testing machinery

The testing of the specimens will be done on a testing machinery (figure 2.34) which permits the loading according with the specimen type and has the possibility to record the force signal applied to the specimen. The testing should respect the increasing control of the force with ±2%.

Fig.2.34. *Fracture toughness testing machinery assembly*

Fasteners devices

The specimens should be fasten in order to minimize the results errors – minimizing the friction effects (figure 2.35), allowing only the rotation of the supports and displacement only vertical in the testing. The materials used for supports should be made of high hardness (higher than 40 HRC).
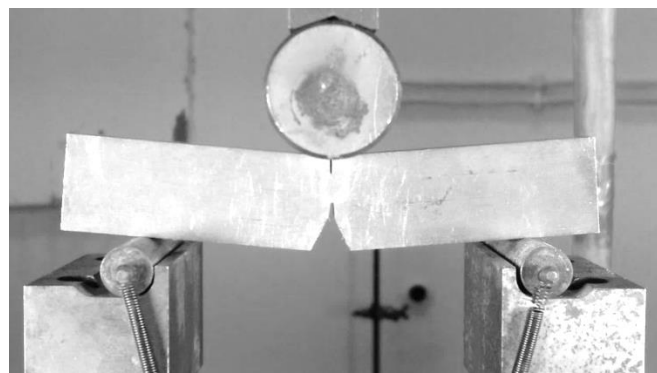
Fig.2.35. *Fracture toughness testing fastener devices*

Displacement transducers/gauges

The measurement of the crack opening is measured with a displacement transducer, composed of two high strength steel integral knife edges (elastic blades) [2.17]. The positioning of the transducer (figure 2.36) onto the specimen is having a critical importance for the correctness of the testing results.
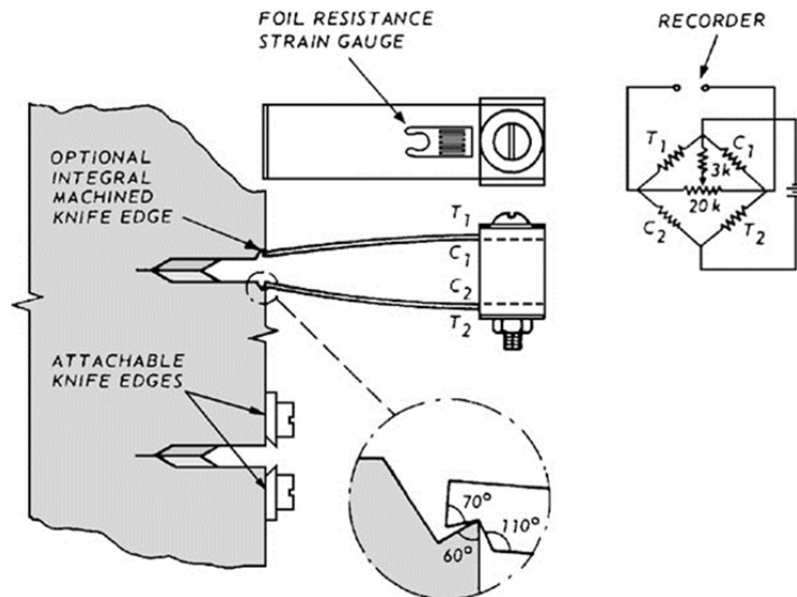
Fig.2.36. *Clip gauge and its attachment to the specimen [2.17]*

Specimens

The specimens are having standard configurations and geometry.

The first step in planning an experimental determination of fracture toughness in plane strain, K_{Ic}, is the choice of test specimens.

ASTM standard accepts four types of specimens: SEB, CT, AT and DCT [2.18] with specific geometry:

o   Three point bending rectangle type specimen – SE(B)
o   Three point bending square type specimen – SE(B)
o   Tension single notch type specimen – C(T)
o   Tension in steps single notch specimen – C(T)
o   Arc form tension type specimen – A(T)
o   Arc form bending type specimen – A(B)
o   Disc tension type specimen – DC (T)

Figure 2.37 shows standard single edge notched bend specimen, and figure 2.38 shows compact tension specimen [2.18].
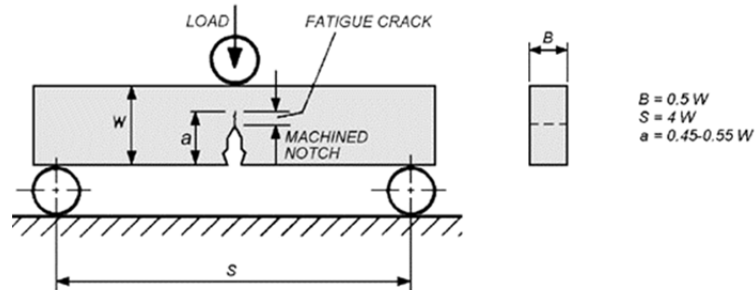
Fig.2.37. *ASTM Standard Single Edge notched Bend (SENB) Specimen*
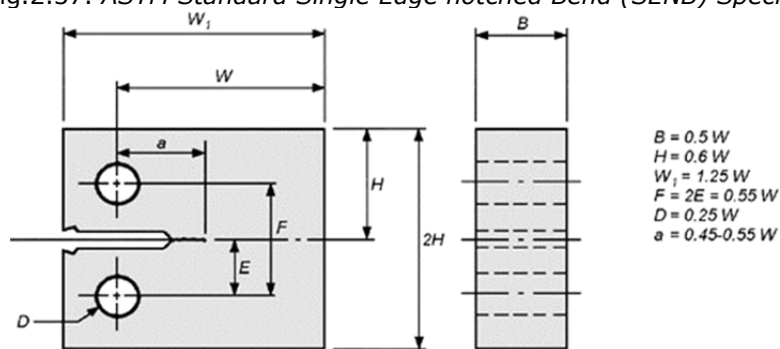
Fig.2.38. *ASTM Standard Compact Tension (CT) Specimen*

Fracture plane and direction according with the element geometry

This identification is done following a code in which the first letter represents the normal direction from the crack plane and the second letter represents the expected direction of crack propagation.

These codes appear in figure 2.39 and 2.40 depending on the position – parent material (base material) or welded joints:

- L - The main deformation direction – longitudinal
- T - The ultimate deformation direction – transversal
- S – Third direction of deformation – thickness of the element.
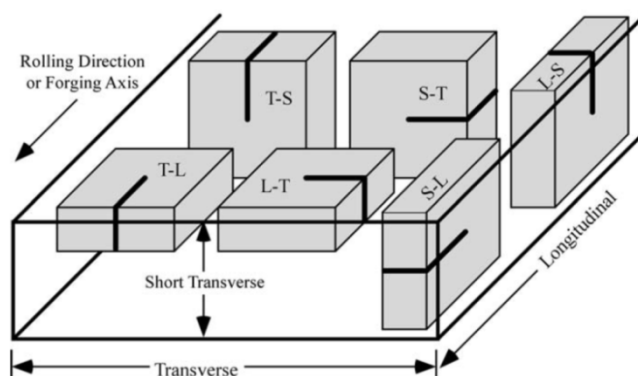
Fig. 2.39. *ASTM notation for specimens extracted from rolled plate and forgings [2.19]*
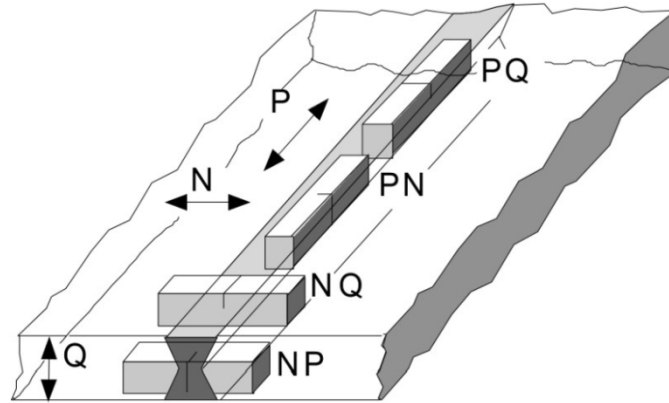
Fig. 2.40. *ISO 15653 standard – notation for specimen extracted from welded joints [2.20]*

Pre cracking of the specimens – notch type

All the specimens will be pre cracked through fatigue. A pre cracking can be obtained through cyclic loading of the specimen with number of loadings which are usually between 10^4 and 10^6, depending on the specimen dimension, flaw type and the intensity level of the stress.

In order to facilitate the fatigue crack at low value loads, the curvature radius at the base of the notch in V shape, must be lower than 0,08mm.

In order to determine the *J* and *CTOD*, the total length of the crack (the propagation of the crack length and the length of the pre cracking) must be 0,45 x *W* to 0,70 x *W*. In order to determine the *K* value, the total crack length must be limited to 0,45 x *W* to 0,55 x *W*.

The fatigue cracking equipment must be chosen thus to have an uniform distribution of the stress in whole thickness of the specimen, otherwise the results can be error affected.

Before testing it is calculated the maximum fatigue force in order to achieve 1,3mm total crack length:

a) For bending testing

$$P_f = 0,8 \frac{B(W - a_0)}{S} R_{p0,2} \qquad (2.87)$$

b) For tension testing

$$P_f = 0,6 \frac{B(W - a_0)^2}{(2W + a_0)} R_{p0,2} \qquad (2.88)$$

where *B*, *W* are the thickness and the width of the specimen, a_0 is the initial crack length (mechanical flaw, notch + pre cracking), $R_{p0,2}$ is the yielding strength of the material at the pre cracking processing temperature.

2.5.1. Testing methods for K_{IC}

When a material behaves in a linear elastic manner prior to fracture, such that the plastic zone is small compared to the specimen dimension, a critical value of the mode I stress intensity factor K_{IC} may be an appropriate fracture parameter.

ASTM-399 [2.17] was the first standard test method for K_{IC} testing, other K_{IC} testing was British Standard 5447 are generally based on ASTM-399 [2.17].

As presented in the previous chapters, K_{IC} is considered a limit value of toughness, which can be used for determining the relation between fracture stress and the dimension of the crack in case of an in service element.

The method serves for the following scopes:
- In research in order to establish, in quantitative terms, the internal composition of steel – different metallurgic variables, different manufacturing processes (welding or laminating), to the existing or new material fracture toughness.
- In service assessment, in order to choose the material for an application in which are described the loading conditions ant to which can be establish the maximum dimension of the crack/flaw;
- For different acceptance requirements – manufacturing quality control, in this case existing the need to specify the minimum value of $K_{IC.}$

The method specimens can be SE(B), C(T), A(T) and DC(T) type.

The pre cracking of the specimens must respect the ASTM 399 standard; in case of SE(B) type specimens, this operation will be done with a maximum fatigue force of:

$$P_f = 0,5 \frac{B \cdot b_0^2 \cdot \sigma_Y}{S} \tag{2.89}$$

In case of C(T) specimens, the maximum fatigue force is:

$$P_f = 0,4 \frac{B \cdot b_0^2 \cdot \sigma_Y}{(2W + a_0)} \tag{2.90}$$

Displacement and load are monitored during the test of pre cracked specimen until the fracture of specimen. The critical load P_Q is defined in several ways depending on the type of curve:
- Curve I, load-displacement behaviour is smooth and deviates slightly from linearity, this non-linearity could be caused by plasticity, or subcritical crack growth, or both.
- Curve II, small amount of unstable crack growth occurs before the curve deviates from non- linearity.
- Curve III, behaviour fails completely before achieving 5% of non-linearity.

In order to calculate the fracture toughness, following procedure is applied:
a. It is determined through graphic, the value of the P_Q force from the recorded $P=f(v)$ diagram. It is constructed the secant line (figure 2.41) with a slope of $(P/v)_5=0.95(P/v)_0$, where $(P/v)_0$ is the tangent OA slope to the initial recorded data. The start recording nonlinearity can be ignored. It is crucial to identify with precision the slope of the recorded data.
b. The P_Q force is defined as: if the force from each recorded point of the test which is before P_5 is P_5 then P_5 is P_Q – type I curve; if there is a maximum load which is before P_5 and with over P_5, then the maximum load became P_Q – type II and III curve.
c. The P_Q value is used for the K_Q critical value determining. It is used the relation:

$$K = \frac{P}{B\sqrt{W}} f(a/W)$$ (2.91)

where P is the applied force, B is the thickness and W is the width of the specimen. $f(a/W)$ is a calibration function which depends on the crack length / crack width and which is presented in the standard.
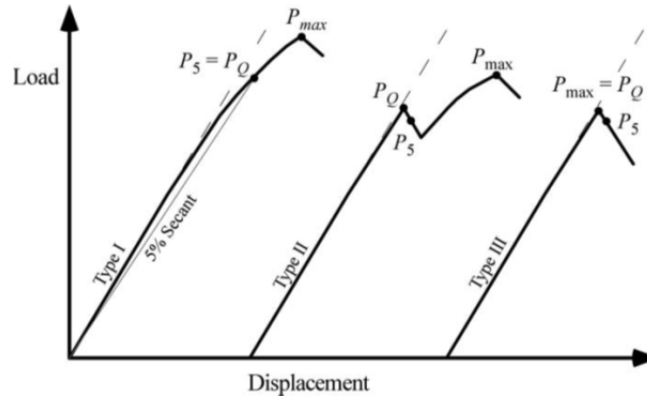
Fig.2.41. *Three types of load- displacement behaviour in K_{IC} test [2.17]*

d. The value of KQ becomes the value KIC if the validity conditions are satisfied. Thus the most important requirement is the checking of the P_{max}/P_Q ratio which must respect:

$$\frac{P_{max}}{P_Q} \le 1,10$$ (2.x.)

e. The second validity condition is:

$$a, B \ge 2,5\left(\frac{K_Q}{\sigma_{YS}}\right)$$ (2.x)

In which $\sigma_{YS} = R_{p0,2}$ is the yielding strength limit.

f. Calculation of the KQ – fracture toughness of the material. For the SE(B) specimen the following relations are valid:

$$K_{(i)} = \left[\frac{P_i S}{(BB_N)^{1/2} W^{1/2}}\right] f(a_i/W)$$ (2.92)

where:

$$f(a_i/W) = \frac{3(a_i/W)^{1/2}\left[1,99 - (a_i/W)(1 - a_i/W)\cdot(2,15 - 3,93(a_i/W) + 2,7(a_i/W)^2)\right]}{2(1 + 1a_iW)(1 - a_i/W)^{3/2}}$$ (2.93)

2.5.2. Testing methods for J_{IC}

One of the first methods for determining the material fracture toughness in elastic – plastic conditions was the determining of the J_{IC} parameter, method described in ASTM E 813 standard.

The main objective of the method consist in developing the initial portion of the *J-R curve*, portion which is having the values of *J* integral at a measured series of specimen cracks, and to determine the value of *J* integral needed in order to produce a lower number of stable crack increasing values.

The specimens are similar with the one presented at the K_{IC} determination – SE(B) and C(T) type.

In order to have error free results is good that the thickness of the specimen to be in equal thickness with the base material.

All the specimens must have induced the pre crack type flaw following fatigue. The pre cracking must be done with fatigue at a force equal with:

$$P_L = \left[\left(\frac{4}{3}\right)\left(\frac{B \cdot b_0^2 \cdot \sigma_Y}{S}\right)\right] \text{ for the SE(B) type specimens}$$
(2.94)

and

$$P_L = \left[\frac{B \cdot b_0^2 \cdot \sigma_Y}{(2W + a)}\right] \text{ for C(T) type specimens.}$$
(2.95)

The base result of the testing is the plotting of the J curve in relation with the crack extension Δa. In order to obtain this diagram, during testing will be made testing measurements of the force, displacement and the crack length.

The measurement technique is based on a complete recording of J points in relation with the crack extension Δa. For this procedure is needed to monitor the crack extension thorough the elastic unloading compliance method. The crack length is measured at regular time intervals during the test through partial unloading of the specimen in order to determine the elastic slope. The measurement of the elastic slope needs only a displacement transducer. The method is called compliance method (figure 2.42)
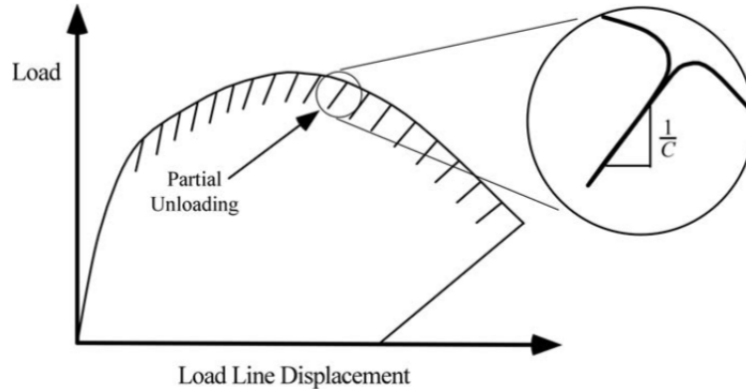
Fig. 2.42. *Compliance method for J curve*

Based on the force – displacement recording, it is determined the J value. This is calculated with the relation:

$$J = J_{el} + J_{pl} = \frac{K^2(1 - v^2)}{E} + \frac{\eta_{pl}}{Bb}\int_0^{v_{pl}} P dv_{pl}$$
(2.96)

where K is the stress intensity factor, E is the elastic module, v is the Poisson module, P is the load, v_{pl} is the plastic deformation, η is a coefficient (=2 for SE(B) specimens and =2+0,522b/W for C(T) specimens), B is the specimen thickness and $b=W-a$ where W is the width of the specimen.

The J function of Δa curve is part of resistance curve J-R which constitutes the base method for J_{IC} determination.

The method is complex and is described in ASTM standard. In principal, the pair of values J and Δa are assessed in order to determine which are on the prescribed interval.

2.5.3. Testing methods for *CTOD*

The method propose the material toughness point assessing, point which indicates a brittle fracture. Another way of the method is to determine the safety point in case of plastic fracture failure.

The results of the applied test is the critical displacement at the tip of the crack for one or more crack extensions.

The specimens are pre fatigued and pre cracked, three point bending type SE(B) or C(T).

The thickness of the specimens must be equal with the thickness of the base material.

The pre cracking must be done with fatigue at a force equal with:

$$P_f = 0,5 \frac{B \cdot b_0^2 \cdot \sigma_y}{S} \qquad \text{for SE(B) specimen type} \tag{2.97}$$

In case of C(T) specimens, the maximum fatigue force is:

$$P_f = 0,4 \frac{B \cdot b_0^2 \cdot \sigma_y}{(2W + a_0)} \quad \text{for C(T) specimens type} \tag{2.98}$$

The method require the displacement measurement during testing. The design values of δ uses a combination of elastic and plastic components (equation 2.97). Thus the calculation of *CTOD* for SE(B) specimens type is done with the relation:

$$\delta = \frac{K^2(1-v^2)}{2\sigma_{YS}E} + \frac{r_p(W-a_0)v_{pl}}{[r_p(W-a_0)+a_0+z]} \tag{2.99}$$

where a_0 is the initial crack length, K is the stress intensity factor, E is the elastic module, v is the Poisson module, σ_{YS} is the yielding stress value, v_{pl} is the plastic deformation, W is the width of the specimen and r_p is the plastic rotation factor (=0,44).

It can be noticed that the elastic component of δ has an equivalent K factor coefficient.

2.6. Fatigue crack growth

The ability to predict the onset of widespread fatigue damage in steel elements, requires methodologies that predict *fatigue crack initiation*, *crack growth*, and *residual strength*. Valid analytical methodology to predict the onset of widespread fatigue damage of the structure must be based on actual observations of the physical behaviour of crack initiation, crack growth, and fracture [2.11].

Cyclic fatigue involves the microstructural damage and failure of materials under cyclically varying loads, (figure 2.43). Fatigue crack growth of most alloyed metals is predominantly a cycle-dependent damage process. Structural steel, however, is rarely designed with compositions and microstructures optimized for fatigue resistance.

Fatigue crack growth behaviour of steel, have received increasing attention in the past several decades because the results of failure analyses indicate that fatigue is one of the major causes of failure in engineering structures, and the fatigue life of structures is determined by the initiation and the propagation behaviour of the cracks.

In year 1960, [2.15] Paris demonstrated that fracture mechanics is a useful tool for characterizing crack growth by fatigue. Considering a growing crack in the presence of a constant amplitude cyclic stress intensity (figure 2.43), a cyclic plastic area forms at the crack tip, and the growing crack leaves behind a plastic wake.
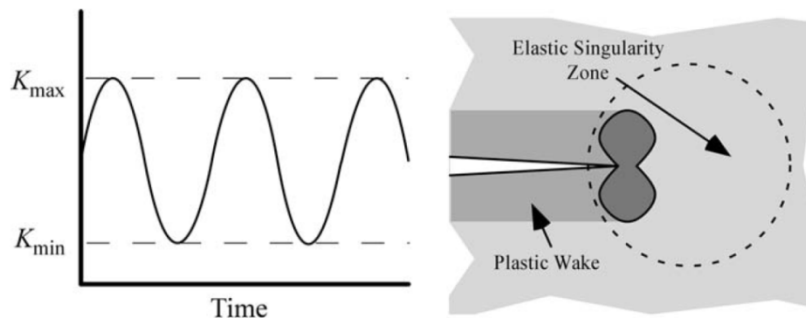
Fig.2.43. *Constant amplitude fatigue crack growth under small-scale yielding conditions*

If the plastic area is sufficiently small that it is embedded within an elastic singularity zone, the conditions at the crack tip are uniquely defined by the current K value, and the crack growth rate, is characterized by K_{min} and K_{max}. It is convenient to express the functional relationship for crack growth in the following form:

$$\frac{da}{dN} = f_1(\varDelta K, R) \tag{2.100}$$

where:

da/*dN*	is the crack growth per one loading cycle
ΔK	$= K_{max} - K_{min}$
R	$= \sigma_{min}/\sigma_{max}$

The influence of the plastic zone and plastic wake on crack growth is implicit in equation (2.100), since the size of the plastic zone depends only on K_{min} and K_{max}. Equation (2.100) can be integrated to estimate fatigue life. The number of cycles required to propagate a crack from an initial length a_o to a final length a_f is given by

$$N = \int_{a_o}^{a_f} \frac{da}{f_1(\Delta K, R)} \qquad (2.101)$$

If K_{max} or K_{min} varies during cyclic loading, the crack growth in a given cycle may depend on the loading history as well as the current values of K_{min} and K_{max}. Thus:

$$\frac{da}{dN} = f_2(\Delta K, R, H) \qquad (2.102)$$

Where H is a term that indicates the history dependence, which results from prior plastic deformation.

Fatigue crack growth analyses become considerably more complicated when prior loading history is taken into account.

Crack propagation data are usually represented as stress intensity factor range log ΔK vs. crack propagation rate log da/dN. Figure 2.44 is a representation crack growth which illustrates typical fatigue crack growth behaviour in metals. The sigmoidal curve contains three distinct regions. At intermediate ΔK values, the curve is linear, but the crack growth rate deviates from the linear trend at high and low ΔK levels. At the low end, da/dN approaches zero at a threshold ΔK, below which the crack will not grow. This is called as **fatigue threshold - ΔK_{th}**. In some materials, the observed growth rate increases rapidly at high ΔK values.
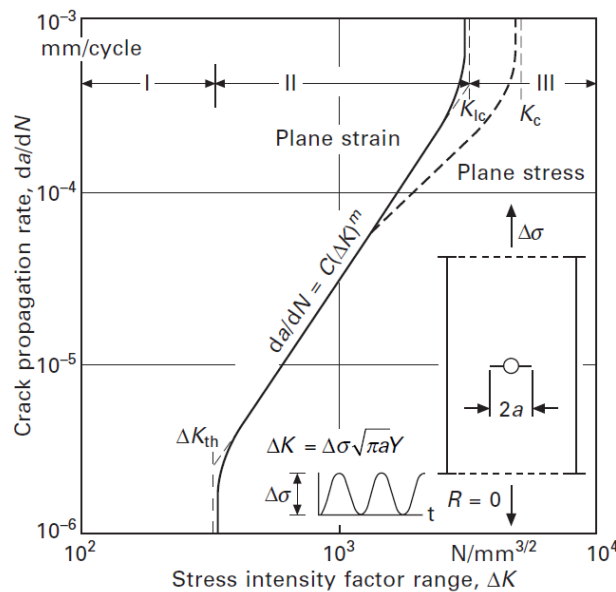
Fig.2.44. *Typical fatigue crack growth behaviour in metals.*

The linear region of the plot in figure 2.44 can be described by a power law:

$$\frac{da}{dN} = C\Delta K^m \qquad (2.103)$$

where C and m are material constants that are determined experimentally. According to equation (2.103), the fatigue crack growth rate depends only on ΔK; da/dN is insensitive to the R ratio in Region II.

Equation 2.103 is valid only for region I and II for $\Delta K_{th} \leq \Delta K \leq K_{mat}$ where ΔK_{th} is the threshold level range (which depends on the stress ration R), ΔK is the SIF and ΔK_{mat} is the fracture toughness in pane strain or plain stress.

Paris and Erdogan [2.16] were apparently the first to discover the power-law relationship for fatigue crack growth in Region II. Studies over the past three decades, however, have shown that m can range from 2 to 4 for most metals in the absence of a corrosive environment. Equation 2.103 has become widely known as the **Paris Law.**

During cyclic loading, a crack can be closed in the lower stress part of a cycle. This crack closure is considered by the introduction of an effective stress intensity factor range, which is smaller than that calculated from the exterior loads, $\Delta K_{eff} < \Delta K$.

The SIF range ΔK, can be expressed as following:

$$\Delta K = K_{max} - K_{min} = Y \cdot \left(\sigma_{max} - \sigma_{min} \right) \cdot \sqrt{\pi a} \qquad (2.104)$$

where Y represents a correction factor which corresponds to the geometry and dimension of the flaw.

The Paris – Erdogan relation can be applied with good results for determining the number of loading cycles until fracture of a with flaw/crack structural element.

2.7. Measuring and applying the fatigue crack growth data for steel shell structures lifetime assessment

Based on the presentation done in the previous subchapter, can be concluded that the safe service lifetime of a structure is based on the crack/flaw initiation phase and the stabile crack/flaw growth phase. If there are taken structural elements or structures that are presenting large cracks/flaws (macro-cracks), resulted from service of the structure, then the lifetime of the structure can be determined based on Paris Law, integrating the following relation:

$$N = \int_0^N dN = \int_{a_0}^{a_{crit}} \frac{da}{C \cdot \Delta K^m} \qquad (2.105)$$

where:

N – number of loading cycles needed for the crack/flaw to grow (extend) from the initial value (a_0) to the critical value (a_{crit}), value at which the fracture is occurring;

a – dimension of the crack (flaw)

C, m – material constants from the crack growth relation

ΔK – stress intensity factor range

This integral can be numerical calculated, taken into account the critical flaw, knowing the initial flaw and the critical flaw dimensions, based on the following relation:

$$N = \int_{a_0}^{a_{crit}} \frac{da}{C \cdot \Delta \sigma^m \cdot Y^m \cdot (\pi a)^{-m/2}} \qquad (2.106)$$

The number of cycles N_{ij} obtained with this relation represents the *remaining lifetime* of the structure for the considered flaw, starting from the initial dimension of the flaw (a_0) to the critical dimension (length, height) (a_{crit}), admitting a stable crack growth (linear variation of the Paris law).

The critical value of the crack can be calculated based on stress intensity factor criteria – K, with the following relation:

$$a_{crit} = \frac{K_{Ic}^2}{\pi \cdot Y^2 \cdot \sigma_{max}^2} \qquad (2.107)$$

The material constants C and m are determined experimentally, based on fracture mechanics testing (on testing probes which are presenting an induced flaw trough a fatigue cycle).

In chapter 5 there is presented an experimental research, following which there are determined the material constants C and m together with the material fracture toughness.

In chapter 6, there is presented a detailed assessment of different types of flaws for the streel shell structures. There are presented steps in fatigue assessment procedures with determination of the critical flaw dimensions and the calculation of the fatigue crack growth, thus resulting the lifetime assessment of the structure.

2.8. In service structure safety assessment

Establishing the remaining lifetime of a structure or an element of a structure, usually is made on *damage cumulation principle*. Theoretically, the fracture is produced when the damage is total.

Presents of cracks/flaws in the structural elements, is changing essentially the structure fatigue behaviour. The fracture itself is a continuous process of cracks/flaws extension under exterior loading and this process is influenced by the
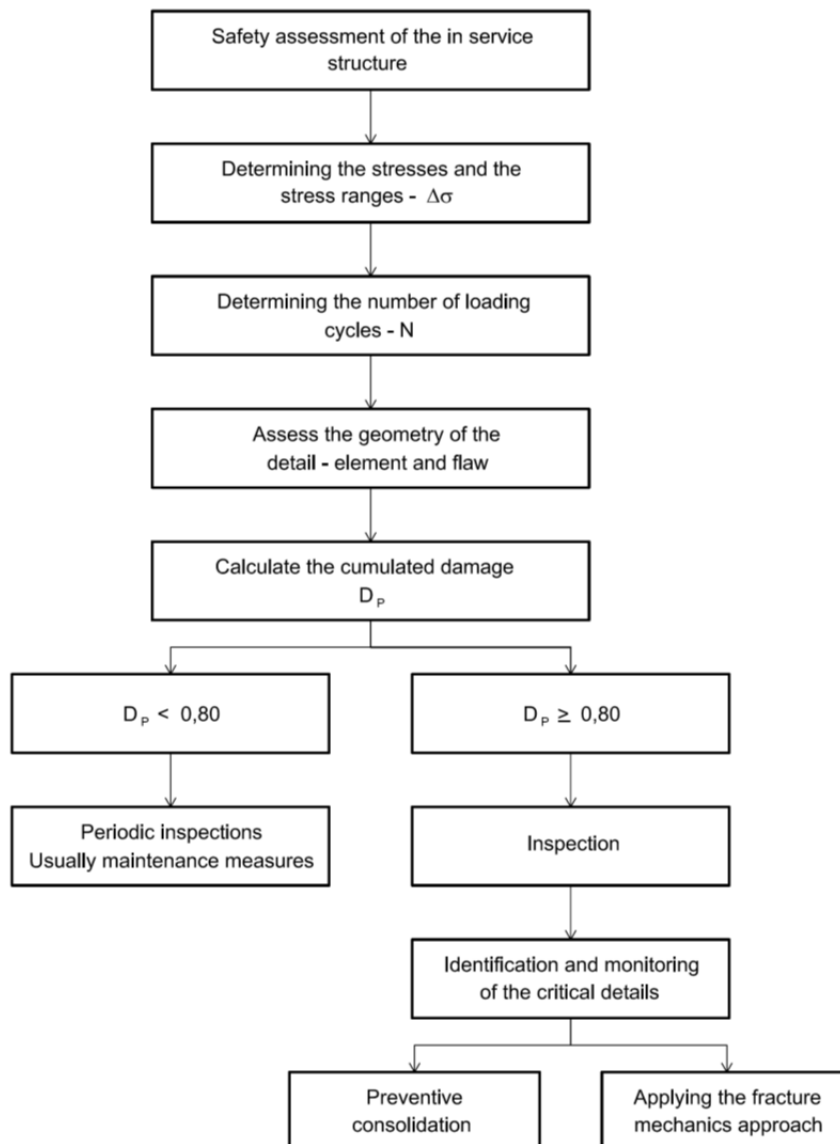
Fig.2.45. *In service structure safety assessment*

ductility of the material. Generally speaking, the fracture can be ductile or fragile (brittle fracture). A presentation of this matter was done in chapter 1. It is underlined that the fracture of an element is determined by the fracture toughness of the material (intrinsic characteristic), stress in relation with the geometry of the defect (flaw/crack), element thickness, loading speed and temperature.

In consequence, an assessment of the structure lifetime can be made through a fracture mechanics approach.

Fracture mechanics allows taken into consideration the acceleration effect of the damage growth. Together with the flaws growth dimension and lower stress ranges, the damage cumulation process is contributing to fatigue of the material.

The main safety assessment for in service structures are presented in figure 2.45.

In order to apply the lifetime assessment methodology for the existing structures, based on fracture mechanics approach, following steps must be respected [2.25]:

- o   information regarding the structure and the loading
- o   identification of the elements and the critical details
- o   information about the material / steel – chemical analysis, metallography analysis, mechanical properties tests results, tension testing results, Charpy V notch type testing results for fracture toughness.
- o   Loading history and loading evaluation based on measurements
- o   Calculation of the stress in the structure and the critical details areas
- o   Establishing the flaws geometry and dimensions (height, length) throughout non destructive testing
- o   Determining of the fracture toughness (fracture mechanics testing for determining the K_{crit}, J_{crit} and δ_{crit})
- o   Evaluation of the flaws admissibility detected in the structure, procedure done based on failure assessment diagrams - FAD-1 or/and FAD-2 (see chapter 6)
- o   Determining the critical flaw dimension
- o   Fatigue assessment – determining the remaining lifetime of the structure trough the crack growth assumption.

Applying the additional method for lifetime assessment and the in service safety assessment based on fracture mechanics principles, allows establishing inspection time period for the existing structures in which were detected flaws/cracks from fatigue loading.

The safety inspection time period can be calculated following the relation:

$$\Delta T_{insp} = \frac{N_{RFL}}{N_{\Delta a}}$$
(2.108)

in which:

N_{RFL} - remaining lifetime of the assessed structure (structural element)

$N_{\Delta a}$ - the number of cycles calculated for an extension of the crack with 5mm

Reference

[2.1] Masateru Ohnami "*Fracture and Society*", IOS Press, Inc. 1992

[2.2] Kirsch, E.G., "*Die Theorie der Elastizität und die Bedürfnisse der Festigkeitslehr*e," Zeitschrift des Vereines deutscher Ingenieure, Vol. 42, pp. 797-807, 1898.

[2.3] Griffith, A.A., "*The Phenomena of Rupture and Flow in Solids*," Philosophical Transactions, Series A, Vol. 221, pp. 163-198, 1920.

[2.4] Irwin, G.R., "*Fracture Dynamics*," Fracturing of Metals, American Society for Metals, Cleveland, OH, pp. 147-166, 1948.

[2.5] Orowan, E., "*Fracture and Strength of Solids*," Reports on Progress in Physics, Vol. XII, p. 185, 1948.

[2.6] Westergaard, H.M., "*Bearing Pressures and Cracks*," Journal of Applied Mechanics, Vol. 6, pp. A49-53, 1939.

[2.7] Irwin, G.R., "*Analysis of Stresses and Strains Near the End of a Crack Traversing a Plate*," Journal of Applied Mechanics, Vol. 24, pp. 361-364, 1957.

[2.8] Inglis, C.E., "*Stresses in Plates Due to the Presence of Cracks and Sharp Corners*," Transactions of the Institute of Naval Architects, Vol. 55, pp. 219-241, 1913.

[2.9] Barsom, J.M., Rolfe, S.T., "*Fracture and fatigue control in structures. Application of the structure mechanics*", Prentice Hall Inc., Third Edition, Philadelphia 1999

[2.10] Tada H., Paris P.C., Irwin G.R., "*Stress analysis of Cracks Handbook*", Del Research Corporation, St. Louis, 1985

[2.11] Anderson, T. L. "*Fracture Mechanics: Fundamentals and Applications*", Third Edition. CRC Press , 2005

[2.12] Wells, A.A., "U*nstable Crack Propagation in Metals: Cleavage and Fast Fracture*" Proceedings of the Crack Propagation Symposium*,* Vol. 1, Paper 84, Cranfield, UK, 1961.

[2.13] Rice, J.R., "*A Path Independent Integral and the Approximate Analysis of Strain Concentration by Notches and Cracks*." Journal of Applied Mechanics*,* Vol. 35, 1968, pp. 379–386.

[2.14] Ashok Saxena, "*Nonlinear Fracture Mechanics for Engineers*", CRC Press; 1 edition (March 31, 1998)

[2.15] Paris, P.C., Gomez, M.P., and Anderson, W.P., "*A Rational Analytic Theory of Fatigue*" The Trend in Engineering, Vol. 13, 1961, pp. 9–14.

[2.16] Paris, P.C. and Erdogan, F., "*A Critical Analysis of Crack Propagation Laws*" Journal of Basic Engineering, Vol. 85, 1960, pp. 528–534

[2.17] ***, ASTM E 399-1983, "*Test Methods for Plane-Strain Fracture Toughness of Metallic Materials"*

[2.18] ***, ASTM E 616-1989, "*Standard Methodology Relating to Fracture Mechanics Testing"*, ASTM - American Society for Testing and Materials handbook 1989

[2.19] ***, ASTM E 1823 - 96, ''*Standard Terminology Relating to Fatigue Fracture Testing''* American Society for Testing and Materials, Philadelphia, PA, 1996 (Reapproved 2002)

[2.20] ***, ISO 15653:2010, „*Metallic materials - Method of test for the determination of quasistatic fracture toughness of welds*"

[2.21] ***, EN-1993:2006, *Steel structures design. Part 1-9: Fatigue design*, CEN – European Committee for Standardization

[2.22] Matsuishi, M. and Endo, T., *Fatigue of Metals Subjected to Varying Stress*, Proc. Japan Soc. of Mech. Engrs., n. 68-2, 1968, pp. 37-40.

[2.23] Dowling, N.E., *Fatigue Failure Predictions for Complicated Stress-strain Histories*, J. of Materials, v.7, n.1, Mar., 1972, pp. 71-87.

[2.24] Palmgren, A. , *Die Lebensdauer von Kugellagern*, Zeitschrift der Vereines Deutscher Ingenieure, v. 68, n. 14, 1924, pp. 339-341.

[2.25] Petzek, E, "*Elaborarea de instrucțiuni pentru aplicarea principiilor mecanicii ruperii la stabilirea siguranței în exploatare și a duratei de viața rămasă a podurilor metalice existente*", Editura Orizonturi Universitare, Timișoara 2006

[2.26] Dumitru, I., Marșavina, L., "*Introducere în mecanica ruperii*", Ed. Mirton, Timișoara 2001

[2.27] Johnson, H.H, Paris, P.C., Subcritical Flaw Growth", Engineering fracture mechanics, 3/1968

[2.28] Pană. T., "*Aplicații inginerești ale mecanicii ruperii*", Editura Tehnică București 1974

[2.29] Rakin, M., Cvijovic, Z., Sedmak, A., Sedmak, S., "*Analysis of the transferability of micromechanical parameters of damage of steel under the conditions of ductile-fracture initiation*", Materials Science, Vol. 38 (1), pp. 104-113, 2002

[2.30] Dobrojević, M., et al, Sedmak, A., „*Micromechanical analysis of constraint effect on fracture initiation in strength mismatched welded joints*", Materials Science Forum 555, pp. 571-576, 2007

[2.31] Milović, Lj., Sedmak, A., et al, „*Numerical and analytical modeling of elastic-plastic fracture mechanics parameters*", Materials Science Forum 555, pp. 565-570, 2007

[2.32] Rakin, M., Gubeljak, N., Dobrojević, M., Sedmak, A. "*Modelling of ductile fracture initiation in strength mismatched welded joint*" Engineering Fracture Mechanics Vol. 75 (11), pp. 3499-3510 2008

[2.33] Sedmak, S., Sedmak, A. "*Fracture mechanics and non-destructive testing for structural integrity assessment*" Key Engineering Materials, Vol. 399, pp. 27-36 2009

[2.34] ***, EN 1991 *Action on structures – Part 1-4 – Wind load*, CEN – European Committee for Standardization

[2.35] ***, IEC 61400-1, *Wind turbines. Part 1 – Design requirements,* International Electrotechnical Commission

[2.37] Maddox, S.J., "*Fatigue Strength of Welded Structures*", Cambridge, Abington Publishing 1991

[2.38] Palmgren, A.G. (1924): *Die Lebensdauer von Kugellagern* (Life Length of Roller Bearings. In German). Zeitschrift des Vereines Deutscher Ingenieure (VDI Zeitschrift), ISSN 0341-7255, Vol 68, No 14, April 1924, pp. 339–341

[2.39] B. F. Langer: *Fatigue failure from stress cycles of varying amplitude*. In: *Journal of Applied Mechanics*. Band 59, 1937, S. A160–A162.

[2.40] M. A. Miner: *Cumulative damage in fatigue*. In: *Journal of applied mechanics*. Band 12, Nr. 3, 1945, S. 159–164.

[2.41] http://www.fracturemechanics.org

[2.42] http://en.wikipedia.org/wiki/Rainflow-counting_algorithm

3. DESIGN OF THE CYLINDRICAL STEEL SHELL ELEMENTS

Cylindrical shell structures are often subjected to compressive stresses in the direction of the cylinder axis, which can be either uniform or varying throughout the cylinder.

Structural members subjected to compression are susceptible to Euler buckling, and the Euler buckling stress of a given quantity of material is at its greatest when all the material is placed as far as possible from the axis. This makes the thin cylindrical tube or shell the most efficient form for compression members. However, as the tube wall becomes thinner, other local forms of buckling intervene, and these shell buckling modes control the strength of steel shell cylinders. Compression members of this form include aircraft, spacecraft and terrestrial vehicles, as well as components of bridges, offshore platforms and other civil engineered structures.

Shell structures are also very efficient for containment of fluids and solids, with thin walled vessels being commonly used for both tanks and silos. The low resistance to shell buckling of shells means that buckling is a primary design concern.

Axial compression in a cylinder arises from different causes in different structures: in a tower, the weight of the structure may provide a relatively uniform compression. In both towers and chimneys (figure 3.1), the transverse loading of wind or earthquake leads to compressive stresses on one side, increasing down the length of the structure, and sometimes in a more complex pattern than that predicted by engineering bending theory. In storage tanks with the cylinder axis vertical, loads on the roof cause axial compression in the shell walls (figure 3.2), and also the stored solid exerts a normal pressure against the wall, but also applies a frictional drag (figure 3.2) which accumulates into a substantial axial compression.

Fig.3.1. *Example of steel shell structures [3.19]*
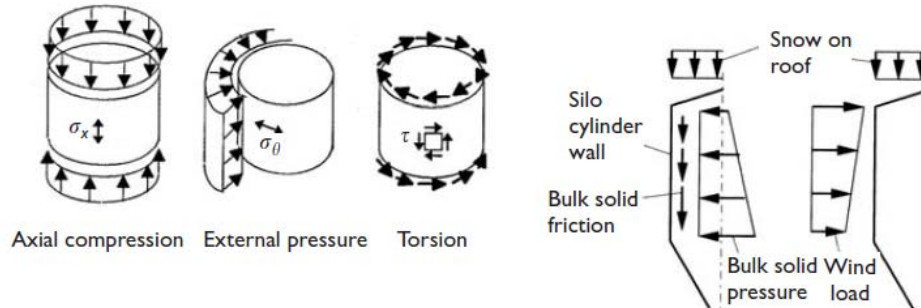
Fig.3.2. *Load and example of combined loading simple cases*

There have been many structural failures in thin shells, and the commonest failure mode is probably buckling under axial compression (figure 3.3).

Due to the geometrical configuration, the most important parameter in the design of steel shell elements is the *buckling strength*.

3.1. Buckling strength

The buckling strength of an isotropic axially compressed cylindrical shell depends on its geometry (radius r, thickness t and length L), its elastic modulus E and yield stress σ_Y, the amplitudes and forms of minor imperfections in its geometry, the end boundary conditions and the pattern of loading. If the shell has ring stiffeners or changes of plate thickness within it, then these generally act as boundaries between one shell segment and another, separating the shell into zones which can often be considered independent.

Fig.3.3. *Cylindrical shell structure – buckling failure [3.5]*

As it buckles, the surface of a shell suddenly and dramatically changes from the initial shape into a wave-form which is termed the buckling mode. The mode may be symmetric with respect to the axis, forming a single bulge around the circumference, but this only occurs under special circumstances. Most commonly, the buckling mode involves alternately inward and outward displacements of the shell wall, termed an asymmetric or non-symmetric buckle (Fig. 3.3) [3.10]

The wavelength of the buckles in both the axial and circumferential directions may vary without significantly altering the buckling load. This leads to a multiplicity of possible modes at closely spaced loads, and jumps usually occur from one mode to another as the buckling progresses into the post buckling region [3.5]. This rich potential for many different modes of buckling is also implicated in the sensitivity of the buckling strength to geometric imperfections.

As a result, buckling is "*commonly a sudden, dramatic, unpredictable event leading to a substantial loss of load-carrying capacity*". [3.10]

As a structural failure mode, it deserves special attention in design and a certain caution if stresses approaching a potential buckling condition may occur.

3.1.1. Bifurcation and post-buckling

Generally buckling may be defined as the sudden failure, or instability, of a structural member subject to compression load. This instability occurs at a maximum point on the load-deflection curve at which point instability may fall into one of two categories: *Bifurcation of Equilibrium* or *Limit Load Buckling.*

If a perfect member is subject to an external load and initially deforms in one configuration, then at a critical load the deformation of this structure changes to another pattern (referred to as the buckling mode), the instability is said to be **bifurcation buckling**, it occurs when two (or more) equilibrium paths pass through the same point. Taken for instance a column subject to axial loading; initially the column will shorten, then at a critical load the column will begin to bend.

In figure 3.4 is shown the classic elastic buckling of a compressed cylinder. The element is axially compressed and the pre buckling path is finished with the point where the shell bifurcates into a non symmetric. When buckling occurs, the axial load is decreased very fast (*y* axis) and can be seen that the cylinder is increasing length as the displacement to the normal surface increases. As the axial load is decreasing, bifurcation after bifurcation occurs and the buckling modes switches from one to another wave number *n.*

This type of buckling can be found in structures such as axially compressed columns, plates and cylindrical shells and may be further broken down based on post buckling behaviour to *stable post buckling* or *unstable post buckling*.

In a *stable post buckling*, the load required to keep the structure in a deformed configuration increases as the deformation increases in magnitude. For example, an axially compressed plate will develop tensile membrane stresses as it deforms which will result in an increase of stiffness.

In an *unstable post buckling* the external load required to maintain equilibrium decreases as the post buckling deformation increases, e.g. an axially compressed cylindrical shell.
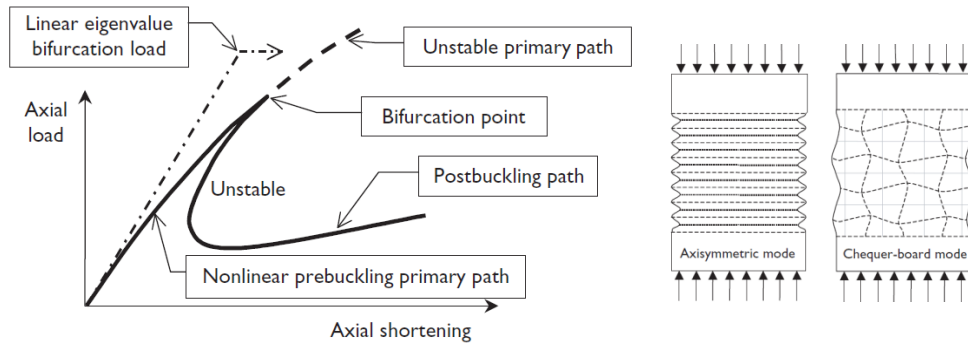
Fig. 3.4. *Load-end shortening relation for an axially compressed cylinder [3.10]*

In the case of **limit load buckling**, when the initially stable shape loses its stability at the limit point of the system, and there is a sudden change from a non equilibrium state to a stable shape, this is known as the limit load.
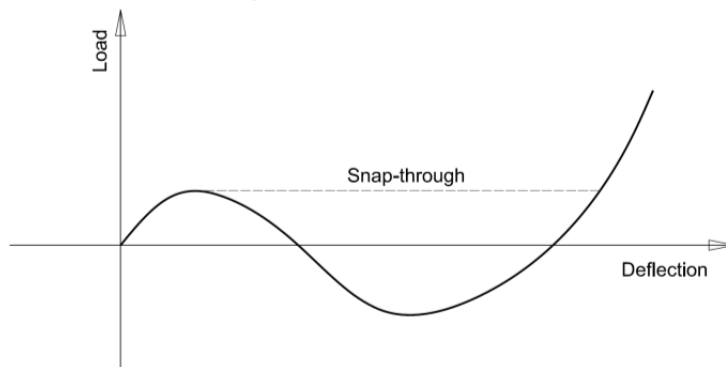
Fig. 3.5. *Limit load buckling [3.10]*

3.1.2. Steel plate and steel shell structural elements

A plated structure as defined by Eurocode EN 1993-1-5 is "*a structure built up from nominally flat plates which are connected together (where) the plates may be stiffened or unstiffened*" and a stiffener is defined as a plate or section attached to the plate to resist buckling or to strengthen the plate. Structural plates and panels are very common in the fields of civil engineering and also in other disciplines such as marine and offshore engineering. In typical civil engineering structures they are often seen as elements in built up sections, such as plate girders or columns which primarily function as beams, but due to their geometrical aspects must be considered as plates.

It is important to note that mathematically we can define three different types of plates: (1) thin plates with small deflections, (2) thin plates with large deflections and (3) thick plates, each with their own theory and conditions.

Eurocode EN 1993-1-6 Strength and Stability of Shell Structures [3.2] defines a shell panel as "*an incomplete shell of revolution*", or more explicitly that "*the shell form is defined by a rotation of the generator about the axis through less than 2 radians*." The main suppositions of the theory of thin plates also form the

basis for the usual theory of thin shells. There exists, however, a substantial difference in the behaviour of plates and shells under the action of external loading. The static equilibrium of a *plate element* under a lateral load is only possible by action of bending and twisting moments, usually accompanied by shearing forces, while a *shell*, in general, is able to transmit the surface load by "*membrane*" stresses which act parallel to the tangential plane at a given point of the middle surface and are distributed uniformly over the thickness of the shell. "*This property of shells makes them, as a rule, a much more rigid and a more economical structure than a plate would be under the same conditions*" [3.7].

As an example of the ease of calculation throughout introducing the curvature, it is taken two elements – a steel plate with thickness of 5mm, height of 1000mm and an length of 1570,8 mm, and a steel shell element (curved panel) with same geometric properties. The panel and the shell are both considered simply supported on all four edges and are loaded on an edge with a distributed force (1N over the short edge).

Steel plate element

The buckling strength of a flat plate in plane loaded, which has the supports on sides is [3.8]:

$$\sigma_c = k \frac{\pi^2 E}{12\left(1 - v^2\right)\left(b / t\right)^2} \tag{3.1}$$

where:
  a is the length of the plate,
  b is the width of the plate,
  t is the thickness of the plate,
  E is the modulus of elasticity of the material,
  v is Poisson's ratio

and

$$k = \left(\frac{b}{a} + \frac{a}{b}\right)^2 = 4,873 \tag{3.2}$$

Thus the buckling strength is:

$$\sigma_c = 4,873 \frac{\pi^2 \cdot \left(2 \cdot 10^5\right)}{12\left(1 - 0,3^2\right)\left(1570,8 / 5\right)^2} = 8,92N / mm^2$$

The result is compared with the FEM analysis (Abaqus) (figure 3.6). The buckling strength in this case it results σ_c = 7,9761 MPa, lower with almost 11% than the manual calculation.
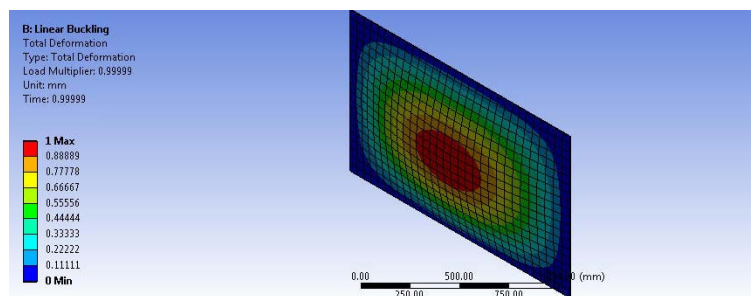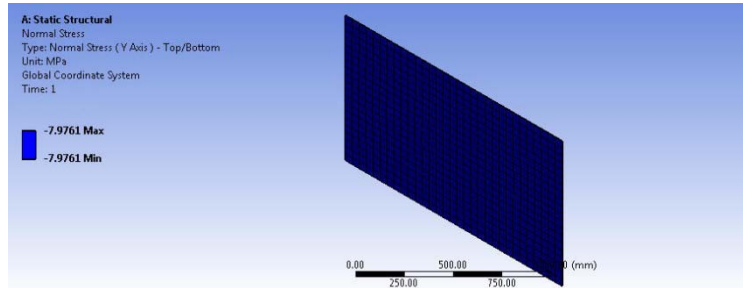
Fig. 3.6. *First buckling mode flat plate - deformed shape and buckling stress*

Steel shell element

It is taken the same plate (geometrically identical) and it is applied a curvature with a radius of 500mm, thus forming a semi circular shape.

By adapting the theory for at plates the compressive buckling coefficient [3.9] is changed to:

$$k = \frac{\left(n^2 + \beta^2\right)^2}{\beta^2} + \frac{12z_b^2\beta^2}{\pi^4\left(n^2 + \beta^2\right)^2}$$

(3.3)

where $z_b = \left(b^2 \,/\, rt\right)\left(1 - v^2\right)^{1/2}$

and $\beta = b/\lambda$, where $\lambda = (\pi \cdot r)/n$

This equation for k is minimised to determine n, the wave number in the circumferential direction of cylinders and singly curved plates.

This gives a value of $k=269.06$ which results in a critical buckling stress for the curved plate of $\sigma_{cr} = 1.215,9$ MPa.

Throughout FEM analysis (figure 3.7), the buckling force multiplier is $9.6783 \cdot 10^6$, giving a buckling force of $N_{cr} = 9.6783 \cdot 10^6$ x N over an area of Area = $\pi \cdot r \cdot t = 7.854$ mm^2, resulting a bucking stress of $\sigma_{cr} = 1.232,3$ MPa.
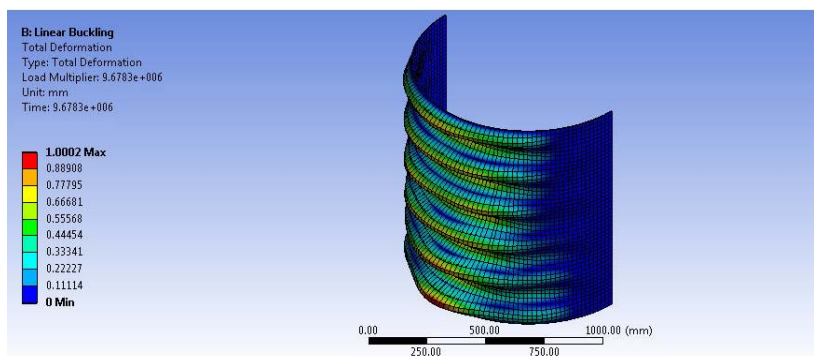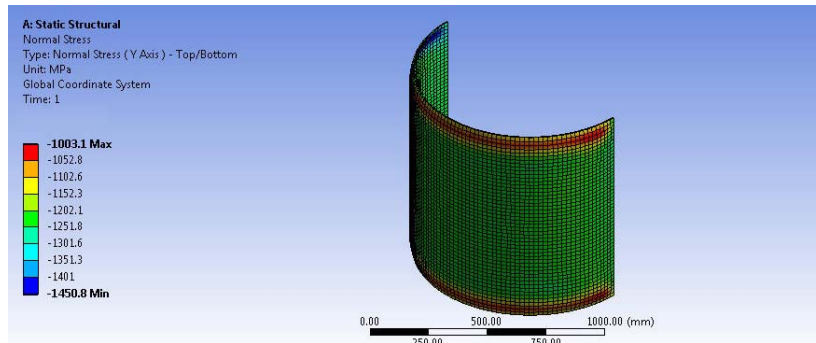
Fig. 3.7. *First buckling mode of curved plate/shell element - deformed shape and buckling stress*

It can be noticed that if the same dimensions are used but a large curvature is introduced, the buckling strength of the plate increases significantly.

3.1.3. Buckling stresses

For the steel shell elements with stiffeners, the buckling modes of ring- and/or stringer-stiffened cylindrical shells can be described as presented in the figure 3.8. These categories of buckling are of particular interest for shell structures and can be described as follows:

- o Local shell or curved panel buckling (i.e., buckling of the shell between adjacent stiffeners).
- o Bay buckling (i.e., buckling of the shell plating together with the stringers (if present) between adjacent ring stiffeners). The ring stiffeners and the ends of the cylindrical shells remain round.
- o General buckling, (i.e., buckling of one or more ring stiffeners together with the attached shell plus stringers, if present).
- o Local stiffener buckling (i.e., torsional/flexural buckling of stiffeners, ring or stringer, or local buckling of the web and flange). The shell remains undeformed.
- o Column buckling (i.e., buckling of cylindrical shell as a column).

For the unstiffened cylindrical shells, the EN 1993-1-6 defines the buckling modes according to the direction of the buckling relative to cylindrical axis. The norm [3.2] is defining the critical buckling stresses as – ***meridional buckling***, ***circumferential buckling*** and ***shear buckling***.

Considering the analytical calculation, for the buckling limit state (defined as Limit State 3 – LS3), [3.2] is defining the boundary conditions for the cylindrical shell elements – table 3.1.

A direct example to the buckling boundary conditions may be found in the figure 3.10 [3.2], in direct correspondence with boundary conditions code presented in table 3.1. For the buckling limit state, special attentions should be paid to the boundary conditions which are relevant to the incremental displacements of buckling.
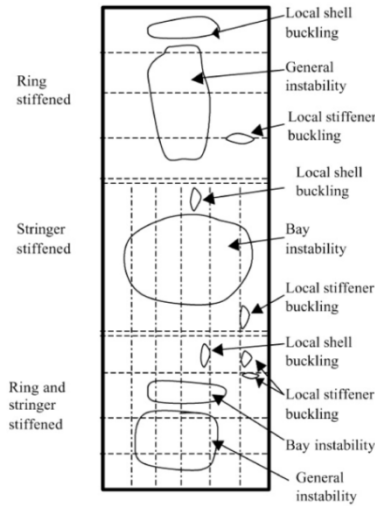
Fig. 3.8. *Buckling modes of stiffened cylindrical shells [3.6]*

l - cylinder length between defined boundaries
r – radius of cylinder middle surface
t – thickness of shell
Δw_k – characteristic imperfection amplitude
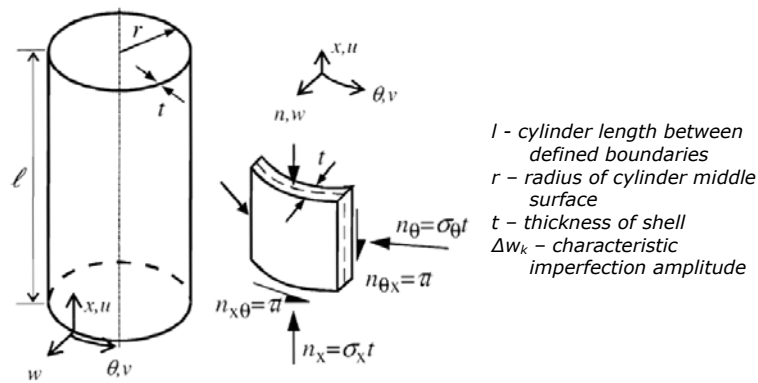
Fig. 3.9 *Cylinder geometry, membrane stresses and stress resultants [3.2]*

Table 3.1. *Eurocode defined buckling boundary conditions [3.2]*

Boundary condition code	Simple term	Description	Normal displacemen	Meridional displacements	Meridional rotation
BC1r	Clamped	radially restrained meridionally restrained rotation restrained	w=0	u=0	$\beta_\varphi = 0$
BC1f		radially restrained meridionally restrained rotation free	w=0	u=0	$\beta_\varphi = 0$
BC2r		radially restrained meridionally free rotation restrained	w=0	u ≠ 0	$\beta_\varphi = 0$
BC2f	Pinned	radially restrained meridionally free rotation free	w=0	u ≠ 0	$\beta_\varphi = 0$
BC3	Free edge	radially free meridionally free rotation free	w ≠ 0	u ≠ 0	$\beta_\varphi = 0$
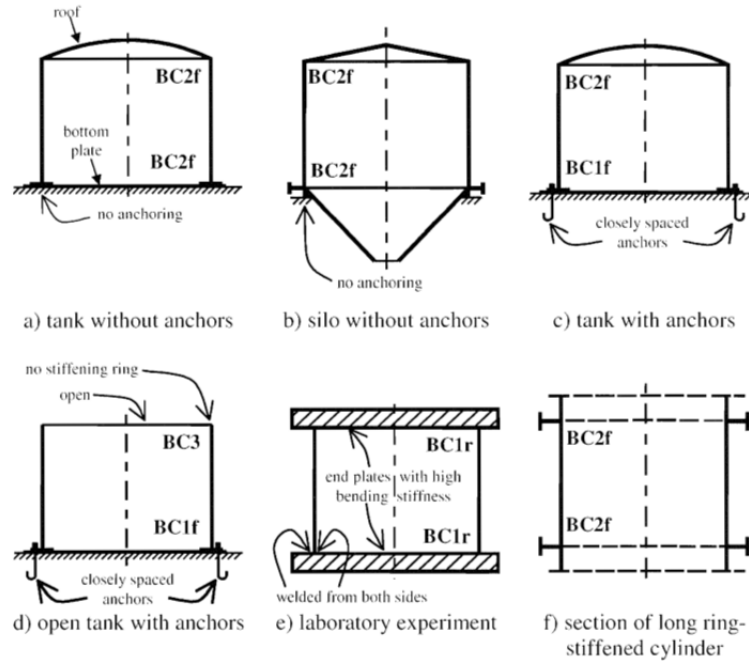
Fig. 3.10. *Schematic examples of boundary conditions for buckling design [3.2]*

According with EN 1993-1-6 Ch. 8.5 & Annex D, considering the length parameter (ω) which is $\omega = \dfrac{l}{r}\sqrt{\dfrac{r}{t}} = \dfrac{l}{\sqrt{r \cdot t}}$, the ***critical meridional buckling stress***, using a value of c_x should be obtained from

$$\sigma_{x,Rcr} = 0,605 \cdot E \cdot c_x \cdot \frac{t}{r} \qquad (3.4)$$

where

$$c_x = \begin{vmatrix} 1, if\, 1,7 \leq \omega \leq 0,5 \cdot \dfrac{r}{t} \\[2mm] \left(1,36 - \dfrac{1,83}{\omega} + \dfrac{2,07}{\omega^2}\right), if\, \omega \leq 1,7 \\[2mm] max\left[0,6,1 + \dfrac{0,2}{c_{xb}} \cdot \left(1 - 2 \cdot \omega \cdot \dfrac{t}{r}\right)\right], if\, \omega > 0,5 \end{vmatrix} \qquad (3.5)$$

the different values of c_x being in correlation with the length of the cylinder (short ($\omega < 1,7$), medium and long($\omega > 0,5\,r/t$)). The c_{xb} is the parameter for the effect of boundary conditions on critical meridional buckling stress in long cylinders (table 3.2)

Table 3.2. *Parameter c_{xb} for effect of boundary conditions [3.2]*

Case	Cylinder end	Boundary condition	C_{xb}
1	end 1	BC 1	6
	end 2	BC 1	
2	end 1	BC 1	3
	end 2	BC 2	
3	end 1	BC 2	1
	end 2	BC 2	

The meridional elastic imperfection factor should be obtained from:

$$a_x = \frac{0,62}{1 + 1,91 \cdot \left(\frac{\Delta w_k}{t}\right)^{1,44}} ,$$ where $\Delta w_k = \frac{1}{Q} \cdot \sqrt{\frac{r}{t}} \cdot t$ is the characteristic imperfection

amplitude and Q is the meridional compression fabrication quality parameter (table 3.3.)

Table 3.3. *Values of fabrication quality parameter Q [3.2]*

Fabrication Quality Class	Description	Q
Class A	Excellent	40
Class B	High	25
Class C	Normal	16

The ***critical circumferential buckling*** *stress* for long cylinders (for $\frac{\omega}{c_\theta} > 1,63 \frac{r}{t}$) should be obtained

$$\sigma_{\theta,Rcr} = \left[E \cdot \left(\frac{t}{r}\right)^2 \cdot \left[0,275 + 2,03 \cdot \left(\frac{c_\theta}{\omega} \cdot \frac{r}{t}\right)^4\right]\right] \tag{3.6}$$

The circumferential elastic imperfection reduction factor should be taken from table 3.4 for the specified fabrication tolerance quality class.

Table 3.4. *Values of a_θ based on fabrication quality [3.2]*

Fabrication Quality Class	Description	α_θ
Class A	Excellent	0,75
Class B	High	0,65
Class C	Normal	0,50

For boundary conditions except BC3. At both edges, the ***critical shear buckling*** stress for cylindrical steel shell elements, is obtained according with [3.2], and is:

$$\tau_{x\theta,Rcr} = 0,75 \cdot E \cdot c_T \cdot \sqrt{\frac{1}{\omega}} \cdot \left(\frac{t}{r}\right) \tag{3.7}$$

For long cylinders ($\omega > 8,7\,r/t$), the factor c_T can be obtain from $c_T = \left(\dfrac{1}{3}\cdot\sqrt{\omega\cdot\dfrac{t}{r}}\right)$. The shear elastic imperfection reduction factor a_T should be taken from table 3.5.

Table 3.5. *Values of a_τ based on fabrication quality [3.2]*

Fabrication Quality Class	Description	a_τ
Class A	Excellent	0,75
Class B	High	0,65
Class C	Normal	0,50

The presented fabrication quality class classes are in connection with the fabrication tolerance quality; choosing a class (A, B or C) must be in accordance with imperfections of the structure – revealed following an assessment of the structure/elements of the structure.

3.1.4. Imperfections and geometrical tolerances

The buckling strength depends very much on the shape and amplitude of the imperfection, the shell geometry and boundary conditions. Many imperfection forms do not have a very harmful effect, and the strength reduction caused by an imperfection cannot be easily deduced from the depth of dents in the shell surface. In addition, imperfections of the loading (loss of concentricity, non-uniformity of the applied stress), of the boundary conditions (especially local variations in axial restraint), and residual stresses in the shell due to fabrication processes can all have significant additional impacts on its strength.

Each shell element structure imperfection must be asseses and taken as possible into account (advanced analysis). The characteristic buckling stresses determined according with [3.2] – analytically, include imperfections that are based on the amplitudes and forms of geometric tolerances that are expected to met during execution of the steel shell element.

The tolerances defined by [3.2] for the cylindrical shell element are in accordance with EN1090 execution standard, the norm [3.2], giving the correlation between the imperfections/tolerances and evaluated resistance.

Types of imperfections – tolerances:
- Out of roundness tolerance
- Eccentricity tolerance
- Dimple tolerance

Out of roundness tolerance

The out of roundness imperfection can be assessed in term of the parameter U_r (figure 3.11) given by:

$$U_r = \frac{d_{max} - d_{min}}{d_{nom}} \tag{3.8}$$

where d_{max} is the maximum measured internal diameter; d_{min} is the minimum measured internal diameter and d_{nom} is the nominal internal diameter.

The U_r value should not exceed $U_{r,max}$, as presented in the table 3.6.

a) flattening   b) unsymmetrical
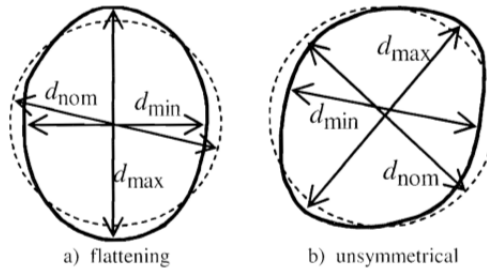
Fig.3.11. *Measurement of diameters for assessment of the out-of-roundness*

Table 3.6 *Recommended values for out of roundness tolerance parameter ($U_{r,max}$)*

	Diameter range	$d[m] \leq 0,50m$	$0,50m < d[m] < 1,25m$	$1,25m \leq d[m]$
Fabrication tolerance quality class	Description	Recommended value of $U_{r,max}$		
Class A	Excellent	0,014	0,007+0,0093(1,25-d)	0,007
Class B	High	0,020	0,010+0,0133(1,25-d)	0,010
Class C	Normal	0,030	0,015+0,0200(1,25-d)	0,015

Eccentricity tolerance

At joints in shell walls perpendicular to membrane compression forces, the eccentricity should be evaluated from the measurable total eccentricity e_{tot} and the intended offset e_{int}:

$$e_a = e_{tot} - e_{int} \qquad (3.9)$$

where e_{tot} is the eccentricity between the middle surface of the jointed plates, e_{int} is the intended offset between the middle surfaces of the jointed pates and e_a is the non intended eccentricity between the middle surfaces of the joined plates (figure 3.12)
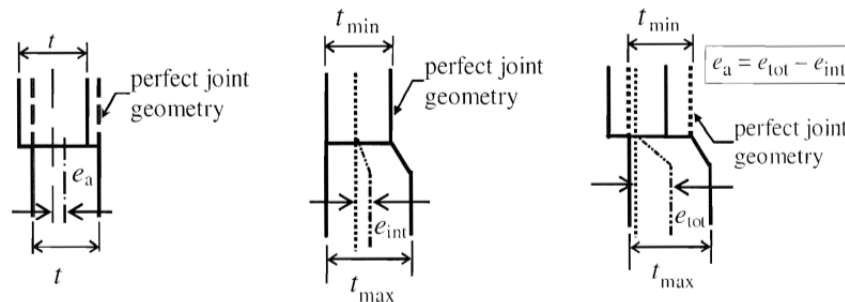
Fig.3.12. *Non intended eccentricity and intended offset at a joint: a) non intended eccentricity when there is no change of the plate thickness; b) intended offset at a change of plate thickness without non intended eccentricity ; c) total eccentricity (non intended plus intended) at a change if plate thickness*

The non intended eccentricity e_a should be less that the maximum permitted non intended eccentricity $e_{a,max}$ for the relevant fabrication tolerance quality class (table 3.7)

Table 3.7. *Recommended values for maximum permitted non intended eccentricity*

Fabrication tolerance quality class	Description	Recommended values for maximum permitted AC₁ non − intended AC₁ eccentricity $e_{a.max}$
Class A	Excellent	2 mm
Class B	High	3 mm
Class C	Normal	4 mm

Dimple tolerances

The dimple measurements (figure 3.13) must be done both meridional and circumferential directions. The meridional gauge should be straight but gauge for circumferential direction should have a curvature equals to the intended radius of the curvature r of the middle surface of the shell.
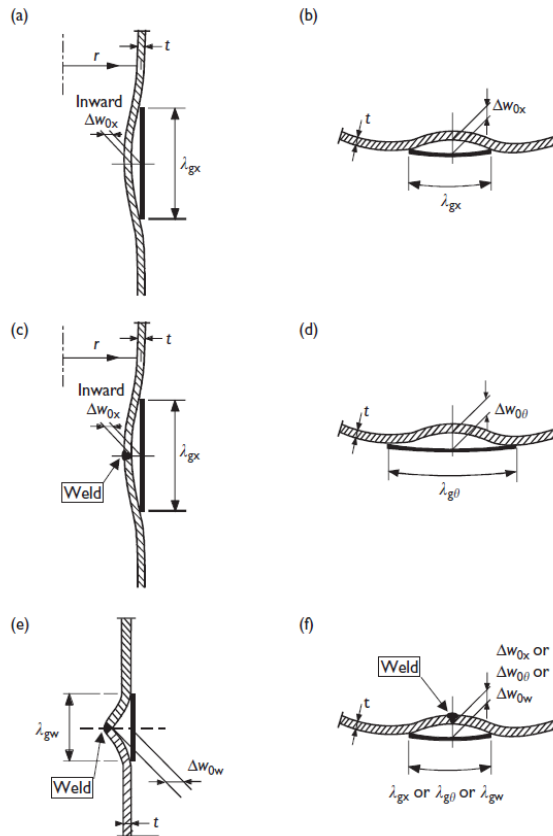
Fig.3.13. *Dimple imperfection measurements required by [3.2] (a) Measurement on a meridian. (b) First measurement on a circumferential circle. (c) First measurement across a weld. (d) Second measurement on circumferential circle. (e) Second measurement across a weld using a special gauge. (f) Measurements on circumferential circle across weld. [3.10]*

For the meridional direction, the gauge length must be equal with $\lambda_{gx} = 4\sqrt{r \cdot t}$. For the circumferential direction, the gauge length should be $\lambda_{g\theta} = 2,3 \cdot (l^2 \cdot r \cdot t)^{0,25}$.

Additional across welds, in both directions (circumferential and meridional), the gauge length must be $\lambda_{gw} = 2,5 \cdot t$ or $\lambda_{gw} = 25 \cdot t_{min}$ with $\lambda_{gw} < 500mm$, where t_{min} is the thickness of the thinnest plate at the welded joint.

The depth of the initial dimples should be assessed in terms of the dimple parameters U_{0x}, $U_{0\theta}$ and U_{0w}.

$$U_{0x} = \Delta w_{0x} / l_{gx} \qquad U_{0\theta} = \Delta w_{0\theta} / l_{g\theta} \qquad U_{0w} = \Delta w_{0w} / l_{gw} \qquad (3.10)$$

The value for the dimple parameters U_{0x}, $U_{0\theta}$ and U_{0w} should satisfy the conditions:

$$U_{0x} \leq U_{0.max} \qquad U_{0\theta} \leq U_{0.max} \qquad U_{0w} \leq U_{0.max} \qquad (3.11)$$

where $U_{o,max}$ is the dimple tolerance parameter for the relevant fabrication tolerance quality class.

Table 3.8. *Recommended values for dimple tolerance parameter $U_{o,max}$*

Fabrication tolerance quality class	Description	Recommended value of $U_{0.max}$
Class A	Excellent	0,006
Class B	High	0,010
Class C	Normal	0,016

3.2. Eurocode approach in design of steel shell elements

3.2.1. Global analysis and limit states

For designing of shell steel structures simplified or complex analysis methods can be used. Simplified methods are based on analytical formulae for determining the bifurcation critic load, plastic limit capacity, sensitivity to imperfections, elastic-plastic interaction and the combining mode of efforts. Advanced step is to find the bifurcation critical force of the plastic limit capacity using finite element method.

The most complete approach, and more complex, is based on the numerical evaluation (using FEM software) of the parameters that are involved in dimensioning of the element: determining the critical bifurcation load following a stability analysis and determining of the plastic capacity of the element following a non-linear analysis. Thus, according with [1,2], for designing thin shell structures, are four limit states (LS): **_LS1 – plastic limit_**_, _**_LS2 – cyclic plasticity_**_, _**_LS3 – Stability_**_ and _**_LS4 – fatigue._**

The EN normative, [3.2], is presenting the following designing possibilities for shell structures: using and comparing the stresses with the von Misses equivalent stress in the most strained point; through direct designing using the normative analytical relations; using a global numerical analysis through a FEM software.

Thus the design should be based on one or more types of analysis: membrane theory of shells (membrane equilibrium), linear elastic shell analysis (LA) (linear bending and stretching), linear elastic bifurcation analysis (LBA) (linear bending and stretching), geometrically non-linear elastic analysis (GNA) (non-linear), materially non-linear analysis (MNA) (linear), geometrically and materially non-linear analysis (GMNA) (non-linear), geometrically non-linear elastic analysis with imperfections (GNIA) (non-linear), geometrically and materially non-linear analysis with imperfections (GMNIA) (non-linear). In table 3.9. is presented the types of shell analysis [3.2].

Table 3.9. *Types of shell analysis [3.2]*

Abbreviations	Type of analysis	Shell theory	Mateial law	Shell geometry
÷	Membane theory of shells	Membrane equilibrium	Not applicable	Perfect
LA	Linear elastic shell analysis	Linear bending and stretching	Linear	Perfect
GNA	Geometrically nonlinear elastic analysis	Nonlinear	Linear	Perfect
MNA	Materially nonlinear analysis	Linear	Nonlinear	Perfect
GMNA	Geometrically and materially nonlinear analysis	Nonlinear	Nonlinear	Perfect
GNIA	Geometrically nonlinear elastic analysis with imperfections	Nonlinear	Linear	Imperfect
GMNIA	Geometrically and materially nonlinear analysis with imperfections	Nonlinear	Nonlinear	Imperfect

The linear elastic shell analysis (LA) is considering a linear elastic material and the linear small deflection theory. Small deflection theory implies that the assumed geometry remains after the deformation of the structure.
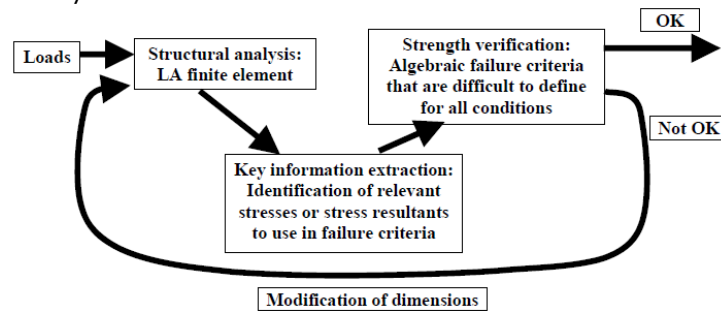
Fig. 3.14. *Linear elastic computational analysis (LA) procedure:*
all parts of the structure can be modified as the dimensions are changed [3.11]

Where a linear elastic analysis (LA) is used, the extensive results must be examined to find the key information needed for a strength verification process (figure 3.14). The focus of failure criteria on a single point in the structure is generally very conservative, and if both bending and membrane stresses are used (i.e. first surface yield or Ilyushin), the criteria of failure become very conservative for membrane type shells. However, in bending situations, such as transversely loaded plates omission of the bending stresses leads to serious over-estimates of strength.

The linear elastic bifurcation analysis (LBA) obtains the lowest eigenvalue at which the shell buckles into a different deformation mode, assuming no change of geometry, no change in the direction of action of the loads and no material degradation. Imperfections of all kind are neglected. The analysis provides the elastic critical buckling resistance r_{Rcr} which has importance for LS3 limit state.

A geometrically nonlinear elastic analysis (GNA) delivers the elastic buckling load of the perfect structure, including changes in the geometry that may be needed in checking the limit state LS3.

The materially nonlinear analysis (MNA) gives the plastic limit load, which can be interpreted as a load amplification factor $r_{R,pl}$ on the design value of the loads F_{Ed}. This type of analysis may be used to verify the limit states LS1 and LS3.

The MNA/LBA numerical method allows the determination of the buckling resistance of simple structures under load conditions not covered by the classical theory.

The results of geometrically and materially nonlinear analysis (GMNA) gives the geometrically nonlinear plastic limit load of the perfect structure and the plastic strain increment, that may be used for checking the limit states LS1 and LS2. Where compression or shear stresses are predominant in some part of the shell structure, a GMNA analysis gives the elasto-plastic buckling load of the perfect structure, that may be of assistance in checking the limit state LS3.

The geometrically nonlinear elastic analysis with imperfections included (GNIA) is used in cases where compression or shear stresses dominate in the shell. It delivers elastic buckling loads of the imperfect structure for checking in the LS3 limit state.

The geometrically and materially nonlinear analysis with imperfections included (GMNIA) analysis is the most complex analysis and it delivers elasto-plastic

buckling loads (the realistic buckling resistance) for the real imperfect structure (LS3 checking). The disadvantage of this method is that is time consuming – determining the imperfections.
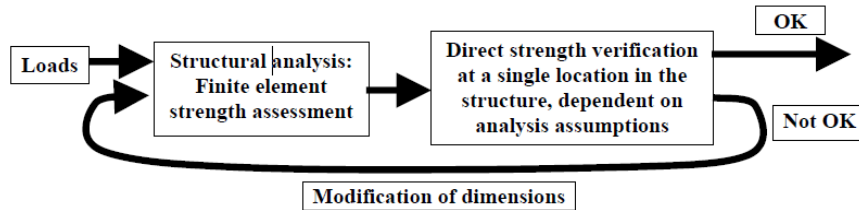
Fig. 3.15. *Dimensioning and design assessment processes using strength assessment FE analysis (LBA, MNA, GMNA, GMNIA) [3.11]*

The design buckling resistance is determined from the amplification factor r_{Rd} applied to the design values F_{Ed} of the combination of actions for the relevant load case. Thus $F_{Rd} = r_{Rd} \cdot F_{Ed}$. F_{Rd} is obtained from the plastic reference resistance $F_{Rpl} = r_{Rpl} \cdot F_{Ed}$ and the elastic critical buckling resistance $F_{cr} = r_{Rcr} \cdot F_{Ed}$, combining these to find the characteristic buckling resistance $F_{Rk} = r_{Rck} \cdot F_{Ed}$.

The plastic reference resistance ratio r_{Rpl} (figure 3.16) should be obtained by materially nonlinear analysis (MNA) as the plastic limit load under the applied combination of actions. This load ratio r_{Rpl} may be taken as the largest value attained in the analysis, ignoring the effect of strain hardening.

Where it is not possible to undertake a materially non-linear analysis, the plastic reference resistance ratio r_{Rpl} may be conservatively estimated from linear shell analysis (LA) conducted using the design values of the applied combination of actions. Thus the evaluated membrane stress resultants $n_{x,Ed}$, $n_{\theta,Ed}$ and $n_{x\theta,Ed}$ at any point in the shell should be used to estimate the plastic reference resistance:

$$r_{Rpl} = \frac{t \cdot f_{yk}}{\sqrt{n_{x,Ed}^2 - n_{x,Ed} \cdot n_{\theta,Ed} + n_{\theta,Ed}^2 + n_{x\theta,Ed}^2}} \qquad (3.12)$$
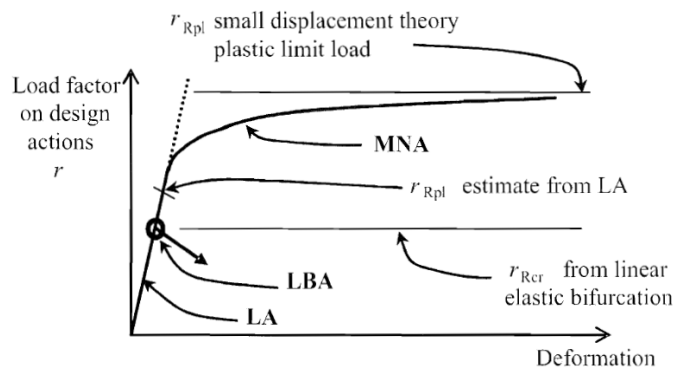
Fig. 3.16. *Definition of plastic reference resistance ratio r_{Rpl} and critical buckling resistance ratio r_{Rcr} derived from global MNA and LBA analyses*

The lowest value of plastic resistance ratio so calculated will be taken as the estimate of the plastic reference resistance ratio r_{Rpl}. The relation will be verified in the three points in which the stresses reach highest values.

The elastic critical buckling resistance ratio r_{Rcr} should be determined from an eigenvalue analysis (LBA) applied to the linear elastic calculated stress state in the geometrically perfect shell (LA) under the design values of the load combination. The lowest eigenvalue (bifurcation load factor) should be taken as the elastic critical buckling resistance ratio r_{Rcr} (figure 3.16).
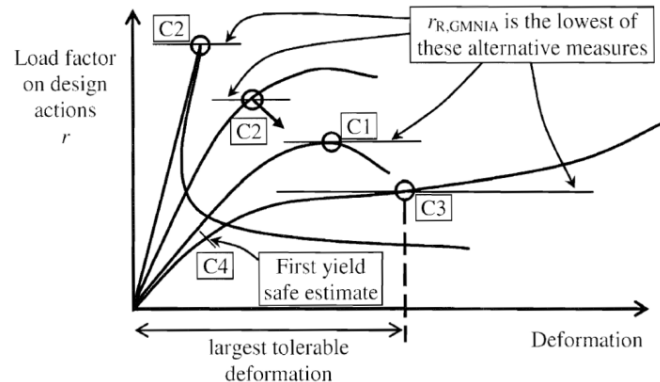
Fig. 3.17. *Definition of buckling resistance from global GMNIA analysis*

The imperfect elastic-plastic buckling resistance ratio $r_{R,GMNIA}$ should be found as the lowest load factor r_R obtained from the three following criteria CI , C2 and C3 (figure 3.17):

- o   *Criterion C1*: The maximum load factor on the load-deformation-curve (limit load);
- o   *Criterion C2*: The bifurcation load factor, where this occurs during the loading path before reaching the limit point of the load-deformation-curve;
- o   *Criterion C3*: The largest tolerable deformation, where this occurs during the loading path before reaching a bifurcation load or a limit load.

   A conservative assessment of the imperfect elastic-plastic buckling resistance ratio $r_{R,GMNIA}$ may be obtained using a GNIA analysis of the geometrically imperfect shell under the applied combination of actions. In this case, the following criterion should be used to determine the lowest load factor r_R.

- o   *Criterion C4:* The load factor at which the equivalent stress at the most highly stressed point on the shell surface reaches the design value of the yield stress $f_{yd}=f_{yk}/\gamma M_0$ (figure 3.17).

In formulating the GMNIA (or GNIA) analysis, appropriate allowances should be incorporated to cover the effects of imperfections that cannot be avoided in practice, including: a) geometric imperfections, such as: deviations from the nominal geometric shape (pre-deformations, out-of roundness); irregularities at and near welds (minor eccentricities, shrinkage depressions, rolling curvature errors); deviations from nominal thickness; lack of evenness of supports. b) material imperfections, such as: residual stresses caused by rolling, pressing, welding, straightening.

The imperfections should generally be introduced by means of equivalent geometric imperfections in the form of initial shape deviations perpendicular to the middle surface of the perfect shell, unless a better technique is used. The middle surface of the geometrically imperfect shell will be obtained by superposition of the equivalent geometric imperfections on the perfect shell geometry.

The correctness of the imperfect elastic-plastic buckling resistance ratio r_R, GMNIA, numerically determined, must be validated throughout numerical analysis considering the same procedures and parameters and comparing the numerical models and experimental results.

3.2.2. Stress design in plastic limit state

For the plastic limit state (limit state 1 - LS1), the designing [3.2] is done by determining the stress design values. Although stress design is based on an elastic analysis and therefore cannot accurately predict the plastic limit state, it may be used, on the basis of the lower bound theorem, to provide a conservative assessment of the plastic collapse resistance which is used to represent the plastic limit state.

In this case Ilyushin yield criterion is used – rather conservative criterion, mainly because it only considers yield at a single point – not an incremental mechanism. Thus at each point in the structure the design value of the stress $\sigma_{eq,Ed}$ should be taken as the highest primary stress determined in a structural analysis that considers the laws of equilibrium between imposed design load and internal forces and moments.

Using a membrane theory analysis, the resulting two-dimensional field of stress resultants $n_{x,Ed}$, $n_{\theta,Ed}$ and $n_{x\theta,Ed}$ may be represented by the equivalent design stress $\sigma_{eq,Ed}$ obtained from:

$$\sigma_{eq,Ed} = \frac{1}{t}\sqrt{n^2_{x,Ed} + n^2_{\theta,Ed} - n_{x,Ed} \cdot n_{\theta,Ed} + 3n^2_{x\theta,Ed}} \qquad (3.13)$$

where an LA or GNA analysis is used, the resulting two dimensional field of primary stresses may be represented by the von Misses equivalent design stress:

$$\sigma_{eq,Ed} = \sqrt{\sigma^2_{x,Ed} + \sigma^2_{\theta,Ed} - \sigma_{x,Ed} \cdot \sigma_{\theta,Ed} + 3\left(\tau^2_{x,\theta,Ed} + \tau^2_{xn,Ed} + \tau^2_{\theta n,Ed}\right)} \qquad (3.14)$$

in which:

$$\sigma_{x,Ed} = -\frac{N_{Ed}}{2 \cdot \pi \cdot r \cdot t} + \frac{M_{y,Ed}}{\pi \cdot r^2 \cdot t} \pm \frac{M_{z,Ed}}{\pi \cdot r^2 \cdot t} \qquad (3.15)$$

$$\sigma_{\theta,Ed} = \left(q_{eq} + q_s\right) \cdot \left(\frac{r}{t}\right) \qquad (3.16)$$

$$\tau_{x,\theta,Ed} = \frac{M_{t,Ed}}{2 \cdot \pi \cdot r^2 \cdot t} \pm \frac{V_{z,Ed}}{\pi \cdot r \cdot t} \qquad (3.17)$$

and $\tau_{x,n,Ed} = \dfrac{q_{xn,Ed}}{t}$ $\tau_{\theta,n,Ed} = \dfrac{q_{\theta n,Ed}}{t}$ (due to the low value, these stresses can be ignored).

The q_{eq} is the equivalent distribution of the wind load onto the cylinder surface (figure 3.18).
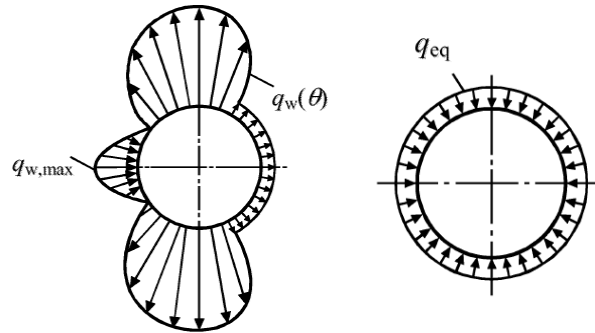
Fig.3.18 *Transformation of the wind pressure distribution - (a) Wind pressure distributed around the shell circumference; (b) equivalent axial symmetric pressure distribution*

The stresses will be limited to: $\sigma_{eq,Rd} \leq f_{eq,Rd}$, where $f_{eq,Rd}=f_{yk}/\gamma_{Mo}$. For LS3 limit state, the buckling resistance is represented by the design buckling stresses, which are obtained from relations: $\sigma_{x,Rd} = \sigma_{x,Rk} / \gamma_{M1}$, $\sigma_{\theta,Rd} = \sigma_{\theta,Rk} / \gamma_{M1}$, $\tau_{x\theta,Rd} = \tau_{x\theta,Rk} / \gamma_{M1}$

The characteristic buckling stresses should be obtained by multiplying the characteristic yield strength by the buckling reduction factors χ: The stresses will be limited to the design stresses.

3.3. Wind load on steel shell type tall structures

Assuming initially the construction fixed and non-deformable, wind (V) is exerting on the construction as a whole and on its individual elements components, a system of aerodynamic actions F_s, functions of form, orientation and size of the wind loaded structure.

Admitting that the structure is subjected to displacements caused by the wind, but these movements are so small that the system status can be identified at the initial configuration, the response R can be determined with the classical methods of structural analysis; this response is dynamic type for flexible structures and / or little damped. Figure 3.19 illustrates the chain of steps that transform the speed of the wind V to the structure response R.
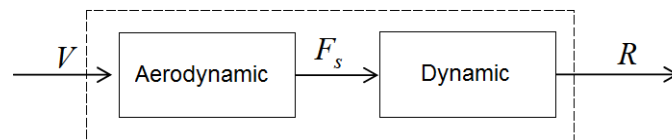
Fig.3.19. *Structural response of the wind loaded structures*

In reality the structures are characterized by a sensible aerodynamic shape. Following the wind load action appear aero – elastic interaction wind-structure phenomenon which modifies the wind load V, the aero dynamic force F_w and the structural response R. In this case the wind is producing to the structure a total force $F = F_w + F_a$ where F_w is the wind force and the F_a is the aero elastic force generated from the structure movement.
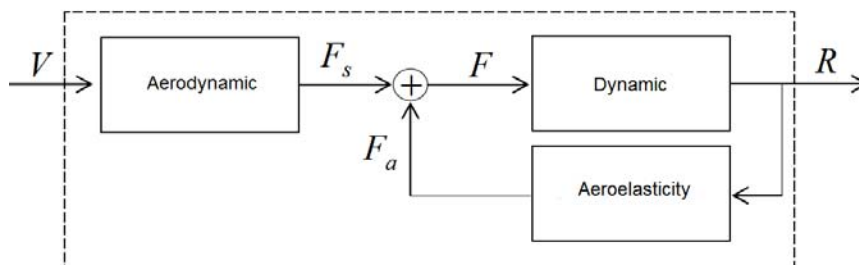
Fig.3.20. *Structural response and aero elastic interaction*

3.3.1. Aerodynamics of the structures

Considering a fixed, non-deformable body immersed in the wind, can be identified two linked effects, on the one hand the body changes the flow by altering the local configuration; the other, on surface of the body arises a pressure P different from the static pressure P_0 of the undisturbed flow.

The body surface is therefore subjected to aerodynamic action linked, as a whole, the pressure change on its surface, $p = P-P_0$. The representation of the physical phenomenon changes depending on whether the fluid has typically three-dimensional properties (figure 3.21), or can be attributed, at least away from the

edge areas, in a two-dimensional scheme (figure 3.22) (in the plane of the cross section).
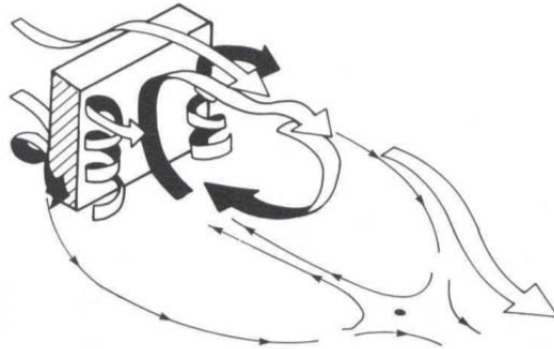
Fig.3.21. *Three dimensional body in a wind field*
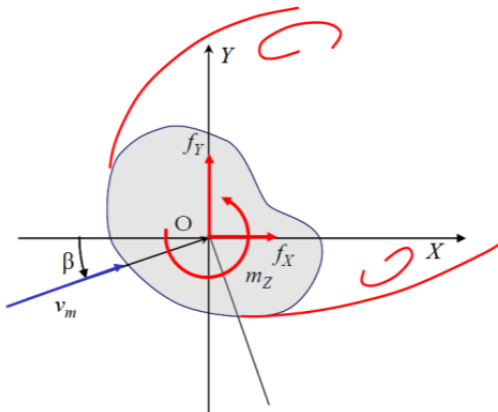
Fig.3.22. *Bi dimensional body in a wind field [3.12]*

In both cases, on the surface of the body exposed to the incident flux it is provided a thin layer laminar or turbulent nature limit (Figure 3.23), as a function of Reynolds number *Re*, and the surface roughness of the body.

(a)   (b)
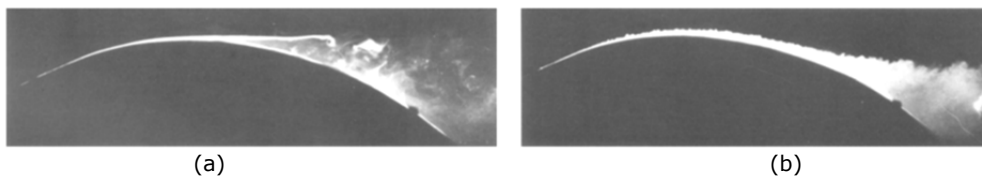
Fig.3.23. *Laminar boundary layer (a) and turbulent (b) [3.12]*

When the boundary layer is subjected to a negative pressure gradient in the wind direction, that is when the flow tends to accelerate to the Bernoulli principle, the boundary layer is increasing in thickness. It tends to decrease and the vorticity in its interior is transported towards the surface; in other words, the boundary layer tends to further squeeze against the surface.

The opposite phenomenon implements when the boundary layer is the seat of a positive pressure gradient, said gradient adverse pressure; in this circumstance the boundary layer thickness increases, and the vorticity is transported from the surface of the body towards the outside, giving rise to the phenomenon of the boundary layer separation.

To downstream of this separation, the external flux to the boundary layer is removed from the surface; therefore, the vorticity is no longer confined in a thin adhering to the surface area, but occupies a large area of flow. This flow area is called trail vortex, and plays an essential role in behavior construction subjected to the action of the wind.

The onset of an adverse pressure gradient has different aspects depending on whether the surface of the body is rounded or have sharp edges.

In the case of bodies with rounded surfaces, the physical phenomenon depends, apart from the shape of the body, to the Reynolds number and the roughness of the surface. Figure 3.24 shows the classic case of a smooth cylinder of infinite length and circular section, surrounded by a laminar wind field, that is, free from turbulence. For *Re <1*, the boundary layer is laminar and is kept attached to the cylinder along the perimeter (figure 3.24a). For *1 <Re <30*, the boundary layer remains laminar, but is separated from the cylinder giving rise to two symmetrical vortices in stationary laminar structure (figure 3.24b). For *30 <Re <10000*, the boundary layer is still laminar but the vortices, while retaining laminar structure, come off alternately from the cylinder creating a trail of *Von Karman* (figure 3.24c). To *10000 < Re < 200000*, the boundary layer remains laminar, but the vortices present in turbulent predominating structure with swirling layers difficult to detect (Figure 3.24d). For *Re> 200,000*, the boundary layer is turbulent, the separation points move to the valley and the trail, still turbulent, become closer (figure 3.24e). The increase of the surface roughness causes the transition regime is realized for Reynolds numbers less.

(a) $Re \sim 1$ (b) $Re \sim 20$

(c) $30 < Re < 10000$

(d) $10000 < Re < 200000$ (e) $Re > 200000$
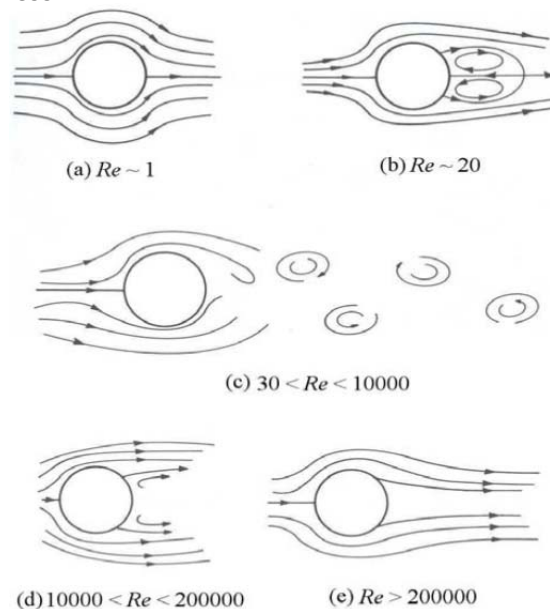
Fig.3.24 *Cylinder of indefinite length and circular section immersed in a flow field*

In Eurocode provisions (EN1991-1-4) is presented a detailed description of the wind load on cylinders type structures (figure 3.25)
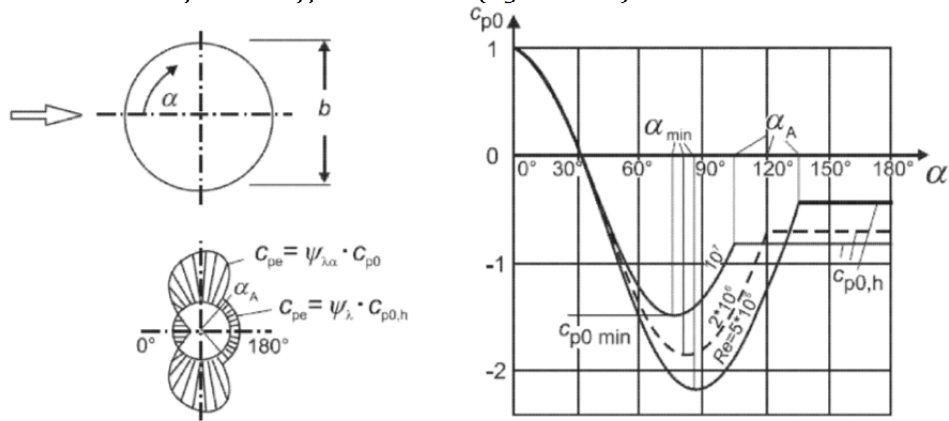
Fig.3.25. *EN1991-1-4 wind load distribution for different Reynolds number values*

A design calculation – loads evaluation EN approach is presented in Annex 1 to the present thesis.

The situation radically changes in the bodies with sharp edges. In this case there is a separation of the boundary layer because, if the flow was able to wrap around the edge, the external speed to the layer limit would be very high and with very little pressure. Immediately after the corner would therefore be adverse gradient so high as to be unsustainable pressure without separation. The figure 3.26a shows the flow in the proximity of a body of square section, where the separation is done at the edges of the front face. The flow configuration is thus independent from the Reynolds number and the roughness of the surface.

Can be notice that the elongated bodies in direction of flow often give rise, after separation from the front edges, the formation of separation curves (figure 3.26b); downstream of these the flow tends to reattach to the side walls of the body, then it is separated again at the corners in the rear-body. The wind resistance of the body is greater as the wider is the vortex trail.
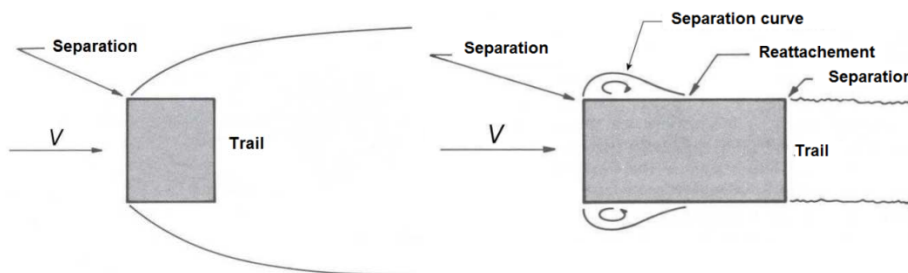
Fig.3.26. *Separation of the flow from the bodies with sharp edges.*

Based on these principles, the aerodynamic action of the wind on the fixed and non-deformable bodies depend, in a different way, on the *incident flux* and the *vortex trail*. The first acts through the average speed and its fluctuation. The second

generates actions related to the turbulence produced by the body. The wind engineering is used to quantify these actions through dimensionless parameters called *aerodynamic coefficients*. They include the *pressure coefficients*, the *overall pressure ratios*, the *force coefficients* and the *resulting moment*, the coefficients of force and moment per unit length, and *the friction coefficients*. It is defined the pressure coefficient parameter as:

$$c_p = \frac{p}{\frac{1}{2} \cdot \rho \cdot V^2} \tag{3.18}$$

where *V* is an average value or peak of speed, so independent of time, characteristic of flow undisturbed and rated to a conventional reference dimension.

When *p> 0 (P > P₀)*, c_p is positive indicating pressure; such a situation is typical of the front surfaces exposed to the incident wind, and more generally, of the areas where the boundary layer remains attached to the body surface. On the other hand, if *p <0 (P < P₀)*, c_p is negative and the pressure is defined as vacuum or suction; such a situation is typical of the side surfaces.

It is defined as the external pressure *p* acting on the external faces of the body; in this case the coefficient c_p is called *external pressure* coefficient and is denoted by the symbol c_{pe}. It is defined also p_i pressure which acts on the inner faces of the body; in this case the coefficient c_p and it is called *internal pressure* coefficient and is indicated with the symbol c_{pi}.

The overall pressure p_n exerted by the wind on a surface is the resultant of the pressures p_1 and p_2 applied by the wind, respectively, on the faces 1 and 2 of the surface. Assuming p_n concordant with the wind pressure applied on face 1, $p_n = p_1 - p_2$. It is defined the overall pressure ratio parameter:

$$c_{pm} = \frac{p_n}{\frac{1}{2} \cdot \rho \cdot V^2} = \frac{p_1 - p_2}{\frac{1}{2} \cdot \rho \cdot V^2} \tag{3.19}$$

The pressure coefficients and the total pressure coefficients are generally used in order to represent the distribution of the pressure *p* on the three-dimensional bodies of extended surfaces. In the case of compact three-dimensional bodies, it is often sufficient to know the three components of the resultant force, F_X, F_Y and F_Z, and the resulting moment, M_X, M_Y and M_Z, with respect to a cartesian reference system X, Y, Z are defined as coefficients of strength, C_{FX}, C_{FY} and C_{FZ}, and moment coefficients, C_{MX}, C_{MY}, and C_{MZ}, the six parameters:

$$c_{Fa} = \frac{F_a}{\frac{1}{2} \cdot \rho \cdot V^2 \cdot L^2} \; ; \; c_{Ma} = \frac{M_a}{\frac{1}{2} \cdot \rho \cdot V^2 \cdot L^3} \quad (a = X, Y, Z) \tag{3.20}$$

Where *L* is the characteristic dimension of the building.

The knowledge of atmospheric parameters, *ρ* and *V*, the characteristic dimensions of the body, *L* and *l*, and the aerodynamic coefficients, provides through equations (3.19)-(3.20) the aerodynamic actions.

In particular, identifying *V* with average wind speed, $V = v_m$, can be identified the average values of the aerodynamic actions. For example, starting from eq. (3.20) the average force of the wind in the *X* direction per unit length is given by the equation:

$$f_{Xm} = \frac{1}{2} \cdot \rho \cdot v_m^2 \cdot l \cdot c_{fX} \tag{3.21}$$

3.3.2. **Dynamic response of the structures due to wind loads**

Taken into consideration a construction in a two-dimensional diagram (Figure 3.27), admitting that the displacements caused by the wind are small, the aerodynamic actions can be assessed by considering the structure as fixed and immovable. These actions are shown schematically (per unit length) by means of a longitudinal force F_D (D = drag, resistance, in x direction), a transverse force F_L (L = lift, lift, in the y direction) and a torque (M, around to the z axis). Due to these actions the body manifests three forms of response, defined as longitudinal (D), transversal (L) and torsional (M). The longitudinal and the transversal response are expressed, respectively, in planes x, z and y, z; the torsional rotation is about the z axis.
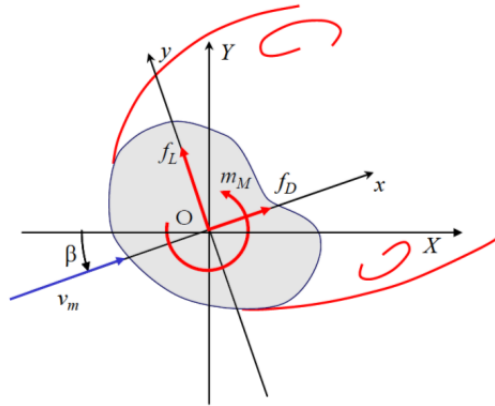
Fig.3.27. *Longitudinal, lateral and torsional response*

Assuming that the structure possesses a linear elastic behavior, the equation of motion of the degree of longitudinal freedom $x(t)$ takes the form:

$$\ddot{x}(t) + 2 \cdot \xi_D \cdot (2\pi \cdot n_D) \cdot \dot{x}(t) + (2\pi \cdot n_D)^2 \cdot x(t) = \frac{1}{m} \cdot f_D(t) \tag{3.22}$$

where m, n_D and ξ_D are the mass, the fundamental frequency and the damping ratio in the longitudinal direction. Like the wind velocity, also the aerodynamic f_D and dynamic response are expressed in the form x:

$$f_D(t) = f_{Dm} + f_D'(t) \tag{3.23}$$

$$x(t) = x_m + x'(t) \tag{3.24}$$

where f_{Dm} and f_D' are, respectively, the average value and the variable part of f_D; x_m and x' are, respectively, the average value and the variable part of x.

In particular (assuming little atmospheric turbulence), similarly to the speed, also the aerodynamic load and response are stationary Gaussian random processes. Therefore, the peak value of x is given by the relations:

$$x_p = x_m + g_D \cdot \sigma_x = x_m + g_D \cdot \sqrt{\sigma_{Bx}^2 + \sigma_{Rx}^2} = x_m \cdot G_D \tag{3.25}$$

$$G_D = 1 + g_D \cdot \frac{\sigma_x}{x_m} = 1 + 2 \cdot g_D \cdot I_v \cdot \sqrt{B^2 + R_D^2} \tag{3.26}$$

where σ_x and g_D are, respectively, the standard deviation and x peak factor; σ_{Bx} and σ_{Rx} are, respectively, the quasi-static part and the resonant part of the standard

deviation of the response; G_D is the gust factor longitudinal dynamic response; B and R_D are two defined coefficients, respectively, the response factor almost-static and resonant response factor.

The quasi-static response factor B is a coefficient that takes into account the partial correlation of wind pressures on the surface area A exposed to the wind. When A is so small as to tend to a point (A tending to 0), $B = 1$; to growing of A, because of non-simultaneity of pressure peaks, B progressively decreases up to tend to 0 for A that tends to infinity (figure 3.28).

The resonant response factor R_D is a coefficient depending on the area exposed to the wind, the fundamental frequency n_D and damping ratio of the structure ξ_D. Similarly to B, it decreases with the increase of A by virtue of the non-simultaneity of pressure peaks. In addition, as part of the common values of the fundamental frequency, it is lower the more rigid is the structure (Figure 3.28b). Finally, R_D decreases with increasing damping.
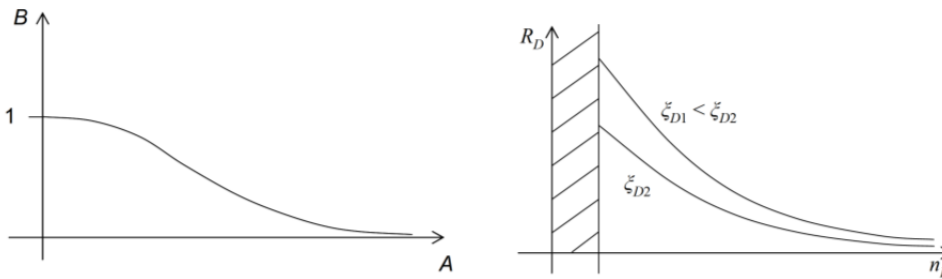
Fig. 3.28. *Factor of almost-static response B (a) and resonant R_D (b)*

Therefore it can be said that the gust factor G_D depends on the size, stiffness and the damping of the structure. It is great if the structure is small and slender, flexible and / or slightly damped; It is small if the structure is large, rigid and highly damped.

Table 3.10. *The gust factor G_D*

Frequency n_D and damping ξ_D	Exposed to wind surface *A*		
	Very small surface (B→1)	Medium surfaces (0<B<1)	Extended surfaces (B→0)
$R_D \gg B$	$G_D = 1 + 2g_D I_v R_D$	$G_D = 1 + 2g_D I_v R_D$	-
$R_D > 0$	$G_D = 1 + 2g_D I_v \sqrt{1 + R_D^2}$	$G_D = 1 + 2g_D I_v \sqrt{B^2 + R_D^2}$	$G_D = 1 + 2g_D I_v R_D$
$R_D \to 0$	$G_D = 1 + 2g_D I_v$	$G_D = 1 + 2g_D I_v B$	1

Considering equation (3.24), can be written

$$f_{Dse} = f_{Dm} \cdot G_D \qquad (3.27)$$

where G_D is the gust factor.

Alternatively Eq. (3.27), the equivalent static action can be expressed by the relation

$$f_{Dse} = f_{Dp} \cdot c_{dD} \qquad (3.28)$$

where $f_{Dp} = f_{Dm}(1 + 2g_v I_v)$ is the aerodynamic load peak and C_{dD} is the dynamic coefficient given by the equation:

$$c_{dD} = \frac{G_D}{1 + 2 \cdot g_v \cdot I_v} = \frac{1 + 2 \cdot g_D \cdot I_v \cdot \sqrt{B^2 + R_D^2}}{1 + 2 \cdot g_v \cdot I_v} \qquad (3.29)$$

Unlike G_D gust factor, the dynamic coefficient c_{dD} may be greater than, less than or equal to 1. The condition $c_{dD} > 1$ corresponds to $G_D > 1 + 2g_v I_v$ and leads to equivalent static actions more aerodynamic peak actions; it is typical of small structures, flexible and a little damped. The condition $c_{dD} < 1$ corresponds to $G_D < 1 + 2g_v I_v$ and leads to equivalent static actions minor aerodynamic peak actions; it is typical of large structures, rigid and very damped. Table 3.11 provides a summary diagram of the values assumed by c_{dD}, having placed $g_D = g_v = 3.5$; $g_D = 3.5$ represents an average value representative of the peak coefficient of longitudinal response; $g_v = 3.5$ is the conventional value attributed to the coefficient of peak speed.

Table 3.11. *The dynamic coefficient c_{dD}*

Frequency n_D and damping ξ_D	Exposed to wind surface *A*		
	Very small surface (B→1)	Medium surfaces (0<B<1)	Extended surfaces (B→0)
$R_D \gg B$	$C_{dD} = \dfrac{1 + 7 I_v R_D}{1 + 7 I_v}$	$C_{dD} = \dfrac{1 + 7 I_v R_D}{1 + 7 I_v}$	-
$R_D > 0$	$G_D = 1 + 2 g_D I_v \sqrt{1 + R_D^2}$	$G_D = 1 + 2 g_D I_v \sqrt{B^2 + R_D^2}$	$C_{dD} = \dfrac{1 + 7 I_v R_D}{1 + 7 I_v}$
$R_D \to 0$	$C_{dD} = 1$	$C_{dD} = \dfrac{1 + 7 I_v B}{1 + 7 I_v}$	$C_{dD} = \dfrac{1}{1 + 7 I_v}$

Structural factor – $c_s c_d$

The wind actions and the lack of simultaneously appearing of peak wind pressures onto the surface of the building/structures is defined by the Eurocode EN1991-1-4 as a coefficient – c_s. The same normative is taken into account the structure vibration effect due to turbulence – c_d.
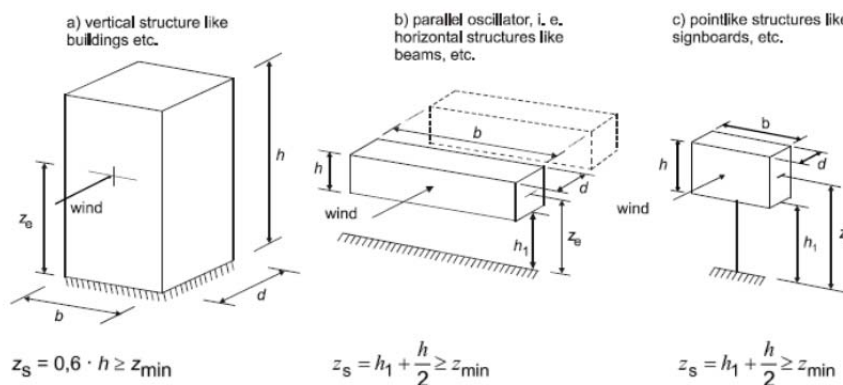
Fig. 3.29. *Types of tall structures and notation according with EN1991-1-4*

This factor $c_s c_d$ is neglected for the relative low height buildings (lower than 15m) and must be calculated according with Eurocode for other structures.

$$c_s c_d = \frac{1 + 2 \cdot k_p I_v(z_s) \cdot \sqrt{B^2 + R^2}}{1 + 7 \cdot I_v(z_s)} \qquad (3.30)$$

Where z_s - reference height for determining the structural factor,

k_p - peak factor defined as a ratio from maximal value of the variable structure response and the standard deviation of this response;

I_v - turbulence intensity

B^2 - cvasi static response factor which takes into account the lack of complete correlation of the wind pressure onto the structure surface,

R^2 - the resonant response factor.

Independently, the c_s factor, which takes into account the lack of simultaneously appearing of peak wind pressures onto the surface of the structure, can be taken as:

$$c_s = \frac{1 + 7 \cdot I_v\left(z_s \cdot \sqrt{B^2}\right)}{1 + 7 \cdot I_v(z_s)} \qquad (3.31)$$

Also the cd factor is taken into account the structure vibration effect due to turbulence, can be considered as:

$$c_d = \frac{1 + 2 \cdot k_p \cdot I_v(z_s) \cdot \sqrt{B^2 + R^2}}{1 + 7 \cdot I_v(z_s) \cdot \sqrt{B^2}} \qquad (3.32)$$

3.3.3. Wind loads

Reference wind velocity

The reference wind velocity is defined as the 10 minutes mean wind velocity at 10m above ground of terrain category II (open field with obstacles at a distance of 20 times height of the obstacle),

With a roughness length of 0,03m having an annual exceeding probability of 0.02 (commonly referred to as having a mean return period af 50 years).

The reference wind speed is to be calculated as following:

$$v_b = c_{dir} \cdot c_{season} \cdot v_{b.0} \qquad (3.33)$$

where v_b is the reference wind velocity following the wind direction and season at a height of 10m above ground for a terrain of type II, v_{b0} is the fundamental value of the wind speed, c_{dir} is the direction coefficient, c_{season} is the season factor.

Mediation wind speed for a period of 10 minutes leads to a stable wind speed for an area greater than that of the construction and for a period of time sufficient for the development of the dynamic response of the structure.

For open ground it is recommended the following conversion relations between averaged wind speeds over different time intervals:

$$1{,}05 \cdot v_b^{1h} = v_b^{10\,min} = 0{,}84 \cdot v_b^{1min} = 0{,}67 \cdot v_b^{3s} \qquad (3.34)$$

The reference value of the wind speed, having an exceeding probability of 2%, can be determined from statistical analysis of the maximum values of the average wind speed. In the statistical analysis the number of years for which there are meteorological records it is recommended to be compared with the average recurrence interval related to reference wind speed (50 years). For zoning the wind action it is recommended to use the same type of probability repartition of the extreme values. In this way the (SR EN 1991-1-4) recommends using ***Gumbel***

repartition for the extreme values. The maximal annual average wind speed, having the probability of not exceeding, *p*=0.98 is

$$v_{0,98} = m_1 \cdot (1 + 2{,}593 \cdot V_1) \tag{3.35}$$

Where m_1 and V_1 are the average and the variation coefficient of the annual maximal wind speed.

The variation coefficient of the wind speed annual maximal values, in Romania is in generally lower than 0,35.

The maximal value of the average wind speed, having the probability of not exceed in one year, p can be established as following, relation valid in Gumbel repartition of the maximal annual wind speed values

$$v_{prob} = \frac{1 - \left[0{,}45 + \dfrac{ln(-ln\ p)}{1{,}282}\right] \cdot V_1}{1 + 2{,}593 \cdot V_1} \cdot v_{0,98} \tag{3.36}$$

The average wind velocity

The average wind velocity $v_m(z)$ at a height *z* above the ground, depends on the terrain roughness and orography and on the reference wind speed v_b:

$$v_m(z) = c_r(z) \cdot c_0(z) \cdot v_b \tag{3.37}$$

Where $c_r(z)$ is the roughness factor and $c_0(z)$ is the orographic factor.

Peak wind velocity

The peak wind speed vp is the expected value of the maximum speed of the wind during a time interval *T* = 10 minutes, averaged over a much smaller time interval *τ* of *T*. It depends on the height z on the ground, from wind of the area in question , the design return period, and the local characteristics of the site where the building is located.

In the absence of specific analyzes that take into account the direction of the wind and the effective roughness and topography of the land in the area of the structure, for heights above ground not greater than *z* = 200 m, the peak wind speed it is provided by the relation:

$$v_p(z) = v_m(z) \cdot G_v(z) \tag{3.38}$$

Where $v_m(z)$ is the average wind velocity; G_v is the wind gust factor, expressed by the formula:

$$G_v(z) = 1 + g_v(z) \cdot I_v(z) \cdot P_v(z) \tag{3.39}$$

where g_v is factor for the peak wind speed, I_v is the intensity of the turbulence and P_v is a coefficient which considers the reduction of the turbulence intensity due to the time period *τ* on which is mediated the wind speed.

The g_v and P_v coefficients are in the following relations:

$$g_v(z) = \sqrt{2 \cdot ln[u_v(z) \cdot T]} + \frac{0{,}5772}{\sqrt{2 \cdot ln[u_v(z) \cdot T]}} \tag{3.40}$$

$$u_v(z) = 0{,}032 \frac{v_m(z)}{L_v(z)} \cdot \left[\frac{L_v(z)}{\tau \cdot v_m(z)}\right]^{1{,}44} \tag{3.41}$$

$$P_v(z) = \cfrac{1}{1 + 0.56 \cdot \left[\cfrac{T \cdot v_m(z)}{L_v(z)}\right]^{0.74}} \tag{3.42}$$

where u_v is the frequency of the turbulence and L_v is the integral scale of the turbulence.

Following the provision recommendations, it shall be taken $G_v=1.5$, thus the wind pressure associated with the wind speed is given be the relation:

$$q_p(z) = \frac{1}{2} \cdot \rho \cdot v_m^2(z) \cdot \left[1 + 2 \cdot g_v(z) \cdot I_v(z) \cdot P_v(z) + g_v^2(z) \cdot I_v^2(z) \cdot P_v^2(z)\right] \tag{3.43}$$

in which ρ is the air density.

With approximations given by the provisions (EN1991-1-4), the general form of the wind pressure is:

$$q_p(z) = \frac{1}{2} \cdot \rho \cdot v_m^2(z) \cdot \left[1 + 7 \cdot I_v(z)\right] \tag{3.44}$$

In annex 1 is presented the wind load evaluation for the specific shell type structure.

In following chapter is presented a brief loads evaluation and design of a billboard tower – steel shell type.

3.4. Design of steel shell type billboard tower

The case study presents the global analysis and the simplified designing of 30 m height tower elements – only the pillar [3.20].

The structure has two components: the column which is a 1680 mm diameter S355J0 steel quality tube and the head of the tower where the billboard is fixed. The head is made of a truss system in order to undertake the dead and wind loads and to transmit them directly to the pillar (figure 3.30).

Due to the triangular shape of the billboard area structure, and the size of the billboard (21 m length), the wind loads evaluation must be in depth evaluated. It was used the EN 1991-1-4 norm [3.3], considering the National Annexes for RO.

The pillar is made of four sections – from the base to the top: Tube 1680 x 20 mm – 7 m, Tube 1680 x16 mm – 8 m, Tube 1680 x 12 – 7 m and Tube 1680 x 10 – 8 m. The sections are joined by bolted endplate connections.

For the model was considered self weight, dead load, live load (for maintenance), wind load and a geometric imperfection. The imperfection was taken into account as presented in EN1993-3-2 [3.4] – Chimneys:

$$\Delta = \frac{h}{500}\sqrt{1 + \frac{50}{h}} = \frac{30,00}{500}\sqrt{1 + \frac{50}{30,00}} = 0,0979m \qquad (3.45)$$

The wind load was evaluated as concentrated forces and as radial pressure onto the column surface and onto the billboard. In table 3.12, the forces on the tower from the wind action are presented. Following a dynamic analysis of the structure (see annex 1), results a frequency of η_{1x} = 0,69 Hz, thus the calculated coefficient c_{scd} = 0,984.

The wind on the billboard area was considered according with [3.3] Ch. 7.4.3:

$$F_w = c_s \cdot c_d \cdot c_f \cdot q_p(ze) \cdot A_{ref} \qquad (3.46)$$

thus resulting F_w=146,664 kN.

According to [3.3], Ch.7.9.1, the pressure onto the cylinder (tower) was determined. The pressure coefficients depend on the Reynolds number Re, defined by:

$$Re = \frac{b \cdot v(z_e)}{v} \qquad (3.47)$$

with v= $15 \cdot 10^{-6}$ m^2/s (cinematic viscosity of the air) and b = 1,68 m (diameter of the pillar).

Table 3.12. *Wind load forces at different heights*

h [m]	$q_p(z)$ [kN/m^2]
2.00	0.782
6.00	0.631
8.00	0.711
12.00	0.830
14.00	0.878
16.00	0.919
18.00	0.957
20.00	0.991
22.00	1.022
24.00	1.050
26.00	1.077
28.00	1.102
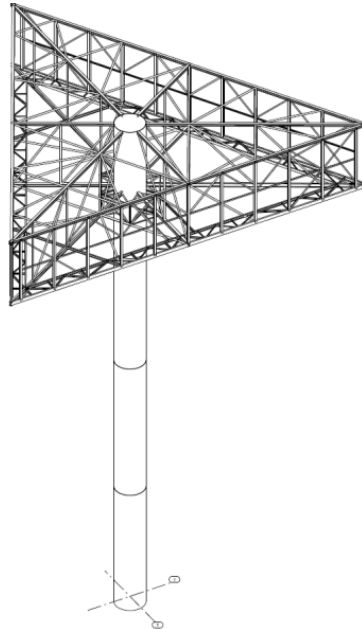
Fig.3.30. *The billboard tower geometry - view*

$$v(z_e) = \sqrt{\frac{2 \cdot q_p(z_e)}{\rho}} - 39{,}403 \ m/s \qquad (3.48)$$

Through interpolation (figure 3.31), the pressure coefficients for different positions - a values (table 3.13).
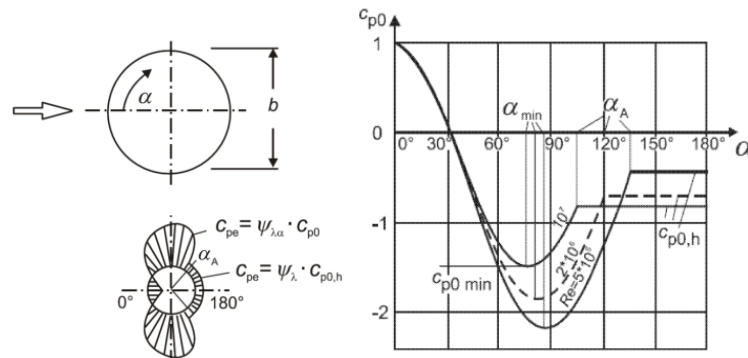
Fig.3.31. *Pressure distribution for cylinders for different Reynolds number values.*

Table 3.13 *Wind pressure coefficients*

α	c_{p0}	$\psi_{\lambda\alpha}$	c_{pe}	w_e
0°	1	1,00	1	0,95
30°	0,1	1,00	0,1	0,095
60°	-1,25	1,00	-1,25	-1,187
90°	-1,65	0,968	-1,597	-1,517
120°	-0,75	0,720	-0,540	-0,513

In order to assess the concentrated wind load, it was done the calculation of the force coefficients $c_f = c_{f,0} \cdot \psi_\lambda = 0{,}562$. The concentrated wind load is $F_w = c_s \cdot c_d \cdot c_f \cdot q_p(z_e) \cdot A_{ref}$. In table 3.14 the wind load forces are presented.

Table 3.14. *Wind load forces on the tower*

z_e	l	A_{ref}	$q_p(z_e)$	F_w	F_w/l
2.00	2.00	3.36	0.352	0.665	0.333
5.00	3.00	5.04	0.541	1.532	0.511
9.00	4.00	6.72	0.676	2.555	0.639
13.00	4.00	6.72	0.767	2.897	0.724
17.00	4.00	6.72	0.836	3.157	0.789
21.00	4.00	6.72	0.892	3.368	0.842
24.00	3.00	5.04	0.928	2.628	0.876
26.00	2.00	3.36	0.950	1.794	0.897

A detailed loads evaluation is presented in annex 1.

Following the structural analysis it results in the internal forces, presented in table 3.15.

Table 3.15. *Internal forces on each section of the tower*

Height (from-to) (m)	Cross section (D x t) (mm)	N_{ed} (kN)	$V_{y,Ed}$ (kN)	$V_{z,Ed}$ (kN)	$M_{t,Ed}$ (kNm)	$M_{y,Ed}$ (kNm)	$M_{z,Ed}$ (kNm)
22-30	1680x10	372	130	224	1120	1430	673
15-22	1680x12	418	136	235	1110	3052	1611
7 - 15	1680x16	488	142	247	1111	4997	2731
0 - 15	1680x20	566	147	255	1111	6772	3749

Determining the critical stresses, the meridian and circumferential stress, is done using annex D ([3.1]) – buckling design of the unstiffened shell element. The design of the stresses which appear in the walls of the tube pillar is done using annex A2 ([3.1]) using shell theory (figure 3.32). In case of circumferential stress following the wind load, is considered an equivalent pressure (q_{eq}) which is uniformly onto the surface of the cylinder – $k_w = 0{,}165$ ([3.1], D.1.3.2 chapter).

a) Axial uniform load; b) Axial load from global bending; c) internal pressure
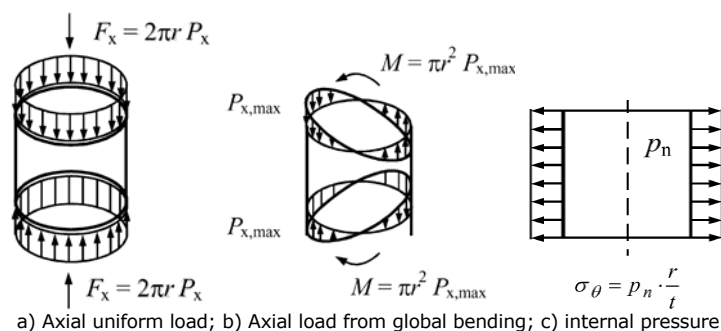
Fig. 3.32. *Membrane theory stresses in unstiffened cylindrical shells*

The designing results are presented in table 3.16 for each limit state design – LS1 and LS3.

The extended/detailed design for each segment of the steel shell tower element is presented in Annex 2.

It can be noticed that the circumferential design buckling stress has low values ($\sigma_{\theta,Rd}$) in comparison with other design stresses, the dimensioning stress being the meridional design buckling stress ($\sigma_{x,Rd}$). The capacity of the elements (segments of the tower) is not exceeded, the maximum utilization factor being 0,94.

Table 3.16. *Design results – stress values and ratio of the elements*

Height (m)	Cross section (Dxt) mm	$\sigma_{x,Ed}$ (MPa)	$\sigma_{\theta,Ed}$ (MPa)	$\tau_{x\theta,Ed}$ (MPa)
22 - 30	1680x10	103,18	0,0552	33,909
15 - 22	1680x12	184,51	0,043	28,67
7 - 15	1680x16	227,98	0,032	21,88
0 - 15	1680x20	248,51	0,026	17,74

LS1 – limit state – values of the stresses and ratio

Height (m)	Cross section (Dxt) mm	$\sigma_{eq,Ed}$ (MPa)	RATIO $\sigma_{eq,Rd}$ / $\sigma_{eq,Ed}$
22 - 30	1680x10	118,7	0,334
15 - 22	1680x12	191,06	0,538
7 - 15	1680x16	231,09	0,651
0 - 15	1680x20	250,39	0,705

LS3 – limit state – values of the stresses and ratio

Height (m)	Cross section (Dxt) mm	$\sigma_{x,Rd}$ (MPa)	$\sigma_{\theta,Rd}$ (MPa)	$\tau_{x\theta,Rd}$ (MPa)	RATIO
22 - 30	1680x10	207,96	3,78	47,31	0,848
15 - 22	1680x12	226,44	5,45	59,48	0,96
7 - 15	1680x16	250,43	9,72	85,96	0,921
0 - 15	1680x20	265,54	15,25	107,26	0,936

The presented design calculation results will be used in the fracture mechanics and fatigue assessment in chapter 6.

References

[3.1] ***, Eurocode 1993 - *Design of steel structures, part 1–1: General rules*, European Committee for Standardisation (CEN), Brussels, 2006

[3.2] ***, Eurocode 1993 - *Design of steel structures, part 1-6: Strength and Stability of Shell Structures*, European Committee for Standardisation (CEN), Brussels, 2006

[3.3] ***, Eurocode 1991 - *Action on structures, part 1-4: Wind load*, European Committee for Standardisation (CEN), Brussels, 2006

[3.4] ***, Eurocode 1993 - *Design of steel structures, part 1–8: Joints design*, European Committee for Standardisation (CEN)., Brussels; 2006

[3.5] ***, ECCS – European Conventions for Constructional Steelwork, "Buckling of Steel Shells – European Design Recommendations", 2013

[3.6] Das, P., Thavalingam, A. and Bai, Y., "*Buckling and ultimate strength criteria of stiffened shells under combined loading for reliability analysis*", Thin-walled structures 41(1): 69-88, 2003

[3.7] Timoshenko, S. and Woinowsky-Krieger, S., "*Theory of plates and shells"*, Vol. 2, McGraw-hill New York, 1959

[3.8] Timoshenko, S. and Gere, J., "*Theory of elastic stability*", McGraw-hill New York, 1961

[3.9] Gerard, G. and Becker, H. (1957). "*Handbook of structural stability part III: buckling of curved plates and shells*" Technical note, 3783.

[3.10] J.G. Teng, J.M. Rotter – "*Buckling of thin metal shell*" – Spon Press (2001)

[3.11] Rotter, J.M., "*Shell buckling design and assessment – the LBA-MNA methodology*", Stahlbau – October 2011 (pp. 791-803)

[3.12] CNR-DT 207/2008 "*Istruzioni per la valutazione delle azioni e degli effetti del vento sulle costruzioni"*, Consiglio Nazionale delle Ricerche, Roma CNR 2009

[3.13] D.Radu, A. Sedmak, "*Welding joints failure assessment – Fracture mechanics approach*", Bulletin of the Transilvania University of Brasov, Vol.x.-2016, Series I: Engineering Sciences

[3.14] D. Radu, A. Sedmak, "*Failure modes and designing procedures of the tubular truss beams welded joints according with EN 1993-1-8*", Proceedings of The International Scientific Conference CIBv 2014,

[3.15] Bancila R., Feier A., Radu D., "*Rehabilitation of existing steel structures, an integral part of the sustainable development*", Proceedings of The International Scientific Conference CIBv 2014,

[3.16] D. Radu, TF. Galatanu, "*Aspects on designing the truss elements welded joints*", Transilvania University Press Brasov, Proceedings of The International Scientific Conference CIBv 2015

[3.17] Radu D., „*Manufacturing imperfections importance in rectangular hollow section welded joints behaviour*", SGEM2015 Conference Proceedings, ISBN 978-619-7105-33-9 / ISSN 1314-2704, June 18-24, 2015, Book1 Vol. 3, 895-902 pp

[3.19] Enercon E-126 - the world's tallest wind turbine. Image: Armin Kübelbeck / Wikimedia Commons. https:// www.asme.org/ engineering-topics/articles/renewable-energy/wind-turbines-get-bigger-smarter; http://www.rajansteelfabricators.com/mild-steel-chimney.html

[3.20] D.Radu, A. Sedmak, "*Design of cylindrical shell steel structures with billboard tower as the case study*", TEAM2015 Conference, Belgrade 2015.

4. FINITE ELEMENTS ANALYSIS OF THE CYLINDRICAL STEEL SHELL STRUCTURES

4.1. Introduction

Finite element method, or finite element analysis, represents a numerical methods used for solving of complex geometry problems, for which obtaining of an analytical solution is extremely difficult. FEM is a method based on discretization of complex geometrical domains into much smaller and simpler ones, wherein field variables can be interpolated using shape functions. Such domains are referred to as elements. The field of variables within a finite element is described by approximative functions, whereas terms of this function are defined based on the values of variables in the nodes.

Points in which adjacent elements are connected are called node points, or nodes. Each nodes has the property that the displacement of all adjacent elements in that node is the same. In this way, the behavior of a part of the structure can be described through a common node, i.e. the behavior of the structure as a whole can be described by the nodes of the model. Based on the node displacement field, strain and stresses can be determined for finite elements, and consequently, the structure as a whole.

Stress analysis is of great significance, since if the stresses are known, it is possible to calculate the strain within a body, and determine whether the component can withstand the given load. FEM enables the simulation of mechanical behavior of individual parts subjected to external load, assuming that the geometry and material properties are known. The result of this method is the verification of a specific design, assuming it meets the defined requirements and specification.

4.2. An overview of finite element method

First papers in the field of finite element method were written during the 1940s. In 1941, Hrenikof was solving problems related to structural and stress analysis of a solid body. Due to the need to discretize the model into finite elements, further development advanced towards topology and geometric properties. Soon afterwards, finite element method found its application in the aircraft industry. The founders of the method, who have defined its basic concepts, were Kloug, Martin, Top and Tarner. First papers on the matrix concept were published by Argyris et al. These papers were printed in 1960, in a book where the term finite element was used for the first time. First university textbook was written by Cook in 1974, at a time when the method was already widely accepted and significantly developed.

Variation principles of continuum mechanics were of great significance in FEM development, giving it a general approach. Static approach to FEM was established in 1960. In the mid-sixties, White and Friedrich solved partial differential equations by using a mesh of triangular elements and variation principles. After that, Helinger and Reisner established a mixed finite element model, which combined both forces and strain as unknown quantities.

Nowadays, finite element method is widely used in solving of various problems. Despite this, this method is still being developed and new possibilities for its application are being researched.

Basic steps in finite element method

There are two basic approaches in finite element method. First one is the force, or flexibility method. Within this method, forces are the basic unknown quantities in a problem that is being analyzed. In order to obtain structural equations, equilibrium equations need to be set up first. This results in a system of algebraic equations, wherein unknown quantities are the forces determined from these equations. In order to achieve compatibility conditions during the solving of specific problems, the elements must be connected by nodes, along sides or surfaces. Basic structural equations are related to node displacement, and equilibrium equations and relations between forces and displacements are also used. Of the two method mentioned here, the second one is far more commonly used.

Finite element method uses structural models which consist of mutually connected finite elements. A displacement function is assigned to each element. All elements are connected directly, or indirectly including nodes and/or common boundary lines/surfaces of elements. Based on known stress and strain values in a node, these values can be determined for any other nodes and elements within the considered structure, assuming its material properties and the applied load are already known. The total number of structural equations describes the behavior of all nodes and represents a system of algebraic equations, which are best represented in matrix form.

Domain discretization and selection of element type

Finite element method is based on physical discretization of an observed domain (figure 4.1). The base of the structural analysis is the subdomain, a part of the structure (domain), called the finite element. A finite element is not of differentially small dimensions, but instead has finite dimensions, and hence its name. Due to this, the equations which describe the state in individual finite elements are of algebraic nature. The first step in structural analysis, i.e. in determining of stresses and strain, is the discretization of the domain (model). It is performed by dividing the domain with lines into subdomains, or finite elements. The selection of finite element size determines the accuracy of obtained results, and the time needed for the analysis.
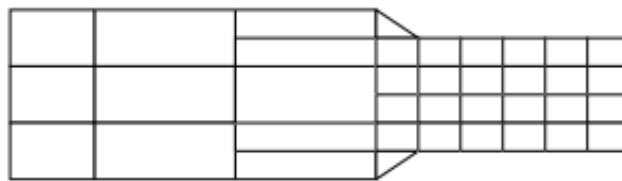
Figure 4.1. Discretization of domain into finite elements

The selection of elements used in FEM analysis depends on the domain geometry. If the domain is planar, two-dimensional plane elements are used, and for spatial domains, three-dimensional elements are used (figure 4.2).
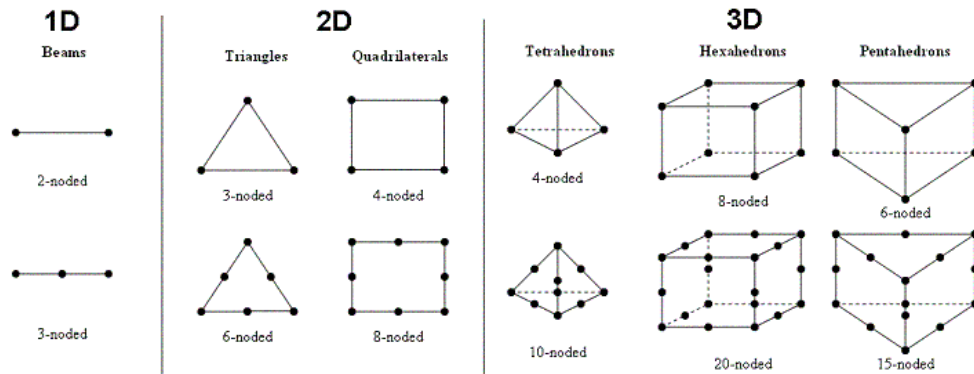
Figure 4.2. Types of finite elements

Selection of displacement functions

The selection of displacement functions is performed for every element. The function is defined within the element and uses values calculated in nodes. Linear, quadratic or cubic polynomials are typically selected as displacement functions. Functions in nodes are unknown quantities. Functions are selected in a way that ensures that FEM can be used to achieve displacement continuity within the body, i.e. between all elements in nodes, along sides and surfaces. Upon selecting the displacement function, the relationship between strain and displacement is established, along with the relationship between stress and strain.

Defining of relationships between strain and displacement and stress and strain

For every finite element, equations must be set up. If the problem is one-dimensional, i.e. strain only occurs in one direction, for example the x direction (it is related to displacement "u"), then axial strain is defined by the following expression:

$$\varepsilon_h = \frac{du}{dx} \tag{4.1}$$

This equation holds for small strain. Stresses and strain are also related by the so-called constitutive relations. Hooke's Law is one of them. For a one-dimensional problem, the relationship between stress and strain is given by:

$$\sigma_h = E \cdot \varepsilon_h \tag{4.2}$$

where σ_h is the stress in x direction and E is the elasticity modulus. Once the relationships have been established, the stiffness matrix is set up.

Stiffness matrix

There are several methods for determining stiffness matrices.
a) Direct equilibrium method - Stiffness matrix relates the forces in element nodes to the nodes. It is obtained from the force equilibrium conditions for each element considered.
b) Variation methods **-** based on the stationary principle. Unlike the direct method, it can be applied to more complex elements.
c) Weight residual method - is based on differential equations for the considered problems. Galerkin method is the most famous one. Based on residual methods,

equations are obtained which describe the behaviour of elements. In matrix form, this can be written as:

$$\begin{Bmatrix} f_1 \\ f_2 \\ \vdots \\ f_n \end{Bmatrix} = \begin{bmatrix} k_{11} & k_{12} & k_{13} & \cdots & k_{1n} \\ k_{21} & k_{22} & k_{23} & \cdots & k_{2n} \\ k_{n1} & k_{n2} & k_{n3} & \cdots & k_{nn} \end{bmatrix} \begin{Bmatrix} d_1 \\ d_2 \\ \vdots \\ d_n \end{Bmatrix} \tag{4.3}$$

$$\{f\} = [k] \cdot [d] \tag{4.4}$$

where $\{f\}$ is the force vector in element nodes; $[d]$ is the nodal displacement vector and $[k]$ is the element stiffness matrix.

d) Energy balance method - based on the balance of various types of energy. It is used in thermostatic and thermodynamic continuum analysis.

The stiffness matrix and equations for individual finite elements are obtained using one of the aforementioned methods. By using the direct method and superposition, individual element matrices can be summed. Herein the concept of continuity or compatibility, according to which the structure must be continuous, must be satisfied. Global structural equation in matrix form is:

$$\{F\} = [K] \cdot [d] \tag{4.5}$$

where $\{F\}$ is the force vector in a global coordinate system; $[d]$ is the vector of known and unknown displacement of all nodes within the structure and $[K]$ is the global stiffness matrix.

Global stiffness matrix $[K]$ is a singular matrix, since its determinant is equal to zero. The singularity problem is solved by introducing adequate boundary conditions.

Determining of displacement of the whole structure

Matrix equation of the structure, wherein the boundary conditions are defined, represents a system of algebraic equations in the following form:

$$\begin{Bmatrix} F_1 \\ F_2 \\ \vdots \\ F_n \end{Bmatrix} = \begin{bmatrix} K_{11} & K_{12} & K_{13} & \cdots & K_{1n} \\ K_{21} & K_{22} & K_{23} & \cdots & K_{2n} \\ K_{n1} & K_{n2} & K_{n3} & \cdots & K_{nn} \end{bmatrix} \begin{Bmatrix} d_1 \\ d_2 \\ \vdots \\ d_n \end{Bmatrix} \tag{4.6}$$

where *n* is the total number of unknown degrees of freedom.

Based on the equations mentioned above, stresses and strain are determined. The conclusion of each analysis is reduced to determining of the correct location where highest stresses and strain occur.

4.3. Finite element method application in steel shell elements

In this thesis, the application of FEM in designing of steel shell elements – a billboard type structure will be considered. This method can be divided into three basic steps:

- Pre-processing
- Processing
- Post-processing

Two type of analysis were done – analysis of the entire structure – Linear elastic analysis, and an analysis of the segment joint area.

4.3.1. Entire structure FEM analysis

The model consist in a truss type structure for the upper part of the billboard tower (head) and a shell type structure for the column. The head is made of a truss system in order to undertake the dead and wind loads and to transmit them directly to the pillar (figure 4.3.).
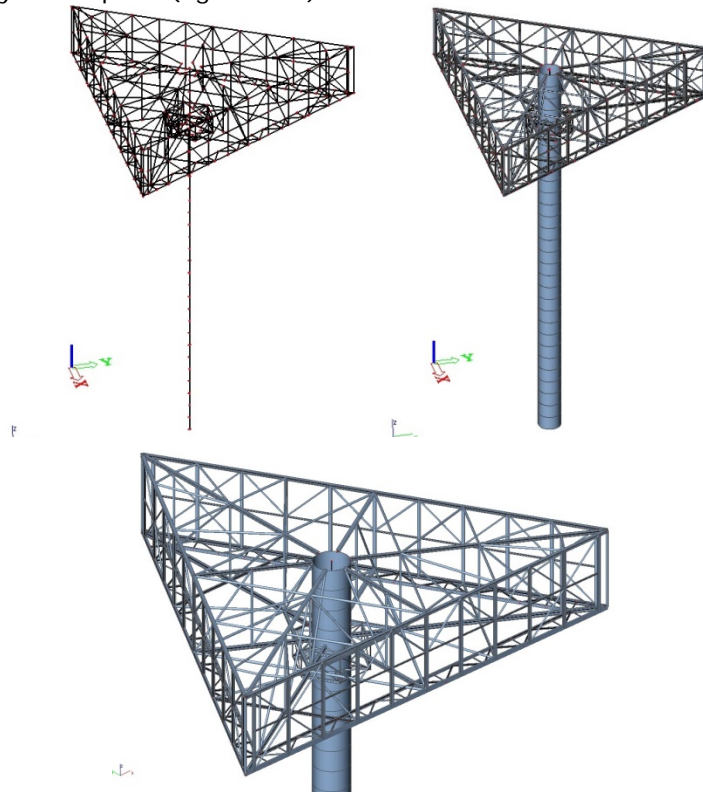
Fig.4.3. *Different views of the FEM model – entire structure*

The upper part structure is a triangular shape layout with a side length of 21,00m. The height of the head is 3,80m.

The column is 30m height and is having a circular cross section with a diameter of 1680mm and is mate of four segments - from the base to the top: Tube

1680 x 20 mm – 7 m, Tube 1680 x16 mm – 8 m, Tube 1680 x 12 – 7 m and Tube 1680 x 10 – 8 m (figure 5). The sections are joined by bolted endplate connections with the bolts into the interior of the cylinder. In FEM analysis, the segments are considered as division of the element for the possibility of having results in the area of the segment connection.

All the elements are made of S355J0 steel type.

Due to the triangular shape of the billboard area structure, and the size of the billboard (21 m length), the wind loads were in depth evaluated (annex 1). Were taken into account also: self weight of the structure and dead load of the additional elements (e.g. billboard itself, lightning cables etc.), live load (for maintenance) and snow/ice load.

Following the linear structural analysis (LA) it resulted the internal forces, presented in table 4.1. and stresses presented in figure 4.4.

Table 4.1. *Internal forces on each section of the tower*

Height (from-to) (m)	Cross section (D x t) (mm)	N_{ed} (kN)	$V_{y,Ed}$ (kN)	$V_{z,Ed}$ (kN)	$M_{t,Ed}$ (kNm)	$M_{y,Ed}$ (kNm)	$M_{z,Ed}$ (kNm)
22-30	1680x10	372	130	224	1120	1430	673
15-22	1680x12	418	136	235	1110	3052	1611
7 - 15	1680x16	488	142	247	1111	4997	2731
0 - 7	1680x20	566	147	255	1111	6772	3749

(a)   (b)
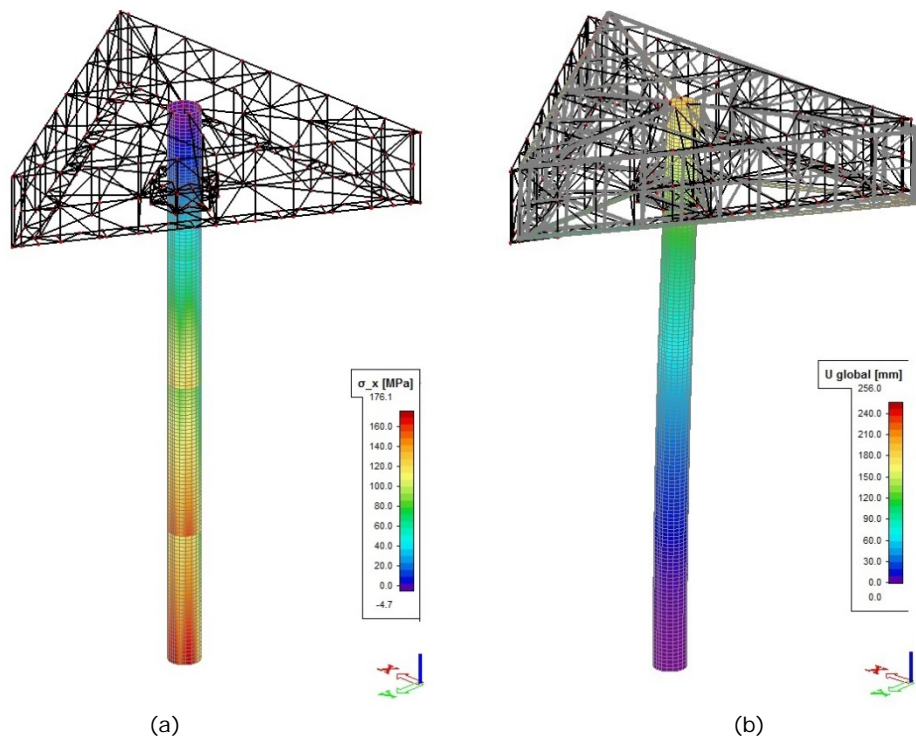
Fig.4.4. *Results from FEM linear analysis (LA) (entire structure) – (a) Von Mises stresses (max=177 MPa); (b) Displacements (max=256mm)*

Following the linear analysis (LA), the buckling design forces must be analytical calculated [4.2]. Determining the critical stresses, the meridian and circumferential stress, is done using annex D ([4.2]) – buckling design of the unstiffened shell element. The design of the stresses which appear in the walls of the tube pillar is done using annex A2 ([4.2]) using shell theory (figure 4.5.). In case of circumferential stress following the wind load, an equivalent pressure (q_{eq}) is considered which is uniformly distributed onto the surface of the cylinder – $k_w = 0,165$ ([4.2], D.1.3.2 chapter).

a) Axial uniform load;   b) Axial load from global bending;   c) Internal pressure
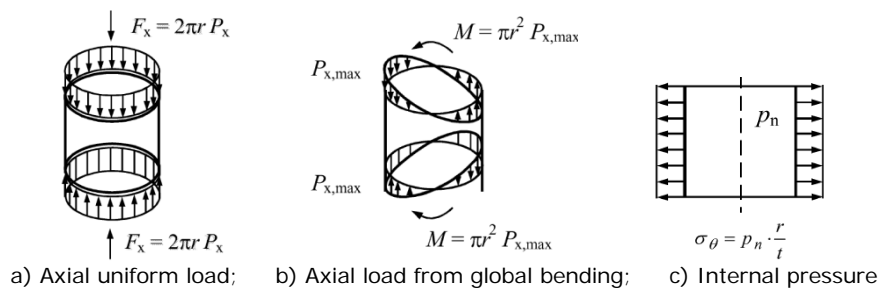
Fig.4.5. *Membrane theory stresses in unstiffened cylindrical shells*

The design results are presented in table 4.2 for each limit state design – LS1 and LS3.

It can be noticed that the circumferential design bucking stress has low values ($\sigma_{\theta,Rd}$) in comparison with other design stresses, the dimensioning stress being the meridional design buckling stress ($\sigma_{x,Rd}$). The capacity of the elements (segments of the tower) is not exceeded, the maximum utilization factor being 0.94 (buckling checking).

Table 4.2. *Design results – stress values and ratio of the elements following analytic design [4.2] – LA and buckling design stresses*

Height (m)	Cross section (*D* x *t*) mm	$\sigma_{x,Ed}$ (MPa)	$\sigma_{\theta,Ed}$ (MPa)	$\tau_{x\theta,Ed}$ (MPa)
22 - 30	1680x10	103,18	0,0552	33,909
15 - 22	1680x12	184,51	0,043	28,67
7 - 15	1680x16	227,98	0,032	21,88
0 - 7	1680x20	248,51	0,026	17,74

Height (m)	Cross section (*D* x *t*) mm	LS1	
		$\sigma_{eq,Ed}$ (MPa)	RATIO $\sigma_{eq,Rd}$ / $\sigma_{eq,Ed}$
22 - 30	1680x10	118,7	0,334
15 - 22	1680x12	191,06	0,538
7 - 15	1680x16	231,09	0,651
0 - 7	1680x20	250,39	0,705

Height (m)	Cross section (*D* x *t*) mm	LS3			
		$\sigma_{x,Rd}$ (MPa)	$\sigma_{\theta,Rd}$ (MPa)	$\tau_{x\theta,Rd}$ (MPa)	RATIO
22 - 30	1680x10	207,96	3,78	47,31	0,848
15 - 22	1680x12	226,44	5,45	59,48	0,96
7 - 15	1680x16	250,43	9,72	85,96	0,921
0 - 7	1680x20	265,54	15,25	107,26	0,936

4.3.2. Segment joint FEM analysis

According with [4.2] an advanced FEM analysis was done. With Abaqus FEM software the model of three segments was designed, jointed together with endplate bolted joints (figure 4.7). In order to evaluate the stresses around the joints, the model consist in one segment, two flange joints and extended with 1,00m on bottom and top with additional segments (figure 4.6.).
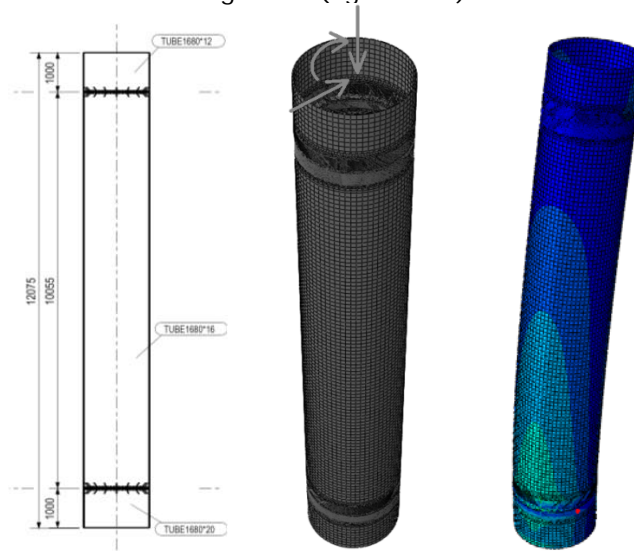
Fig.4.6. *Geometry and the finite element model (unloaded and loaded) and loading values*
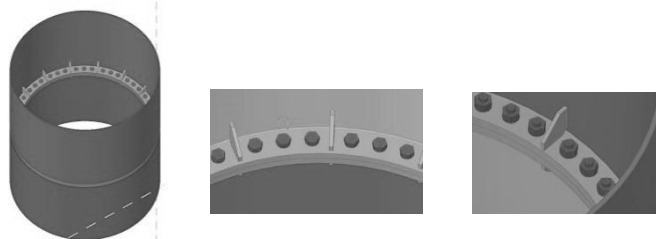
Fig. 4.7. *Joint of the tower segments*

The segment model with joints was loaded with forces determined from LA analysis (table 4.3). The forces were taken from the section from 1,00m from the joint of the 12mm thick segment and applied onto the top of the model. At the bottom (section -1,00m from the 20 to 16 mm segments joint), the model was considered fixed.

Table 4.3. *Loads on the top of the segment with joints model.*

N	V_y	V_z	M_x	M_y	M_z
[kN]	[kN]	[kN]	[kNm]	[kNm]	[kNm]
-412.04	135.55	-234.21	1110.89	2815.83	-1475.2

Following the design, it was noticed that the stress concentration is around joints elements (figure 4.8). The values of the stresses are close to the values taken from the linear elastic analysis, thus the model was verified. (table 4.4).

Table 4.4. *Von Mises Maximum stress values comparison between LA entire model analysis and the three segments FEM analysis*

Cross section (Dxt) mm	LA analysis of the entire model (MPa)	FEM segments analysis (LA) (MPa)
1680x12	184,51	178,20
1680x16	227,98	204,10
1680x20	248,51	221,11
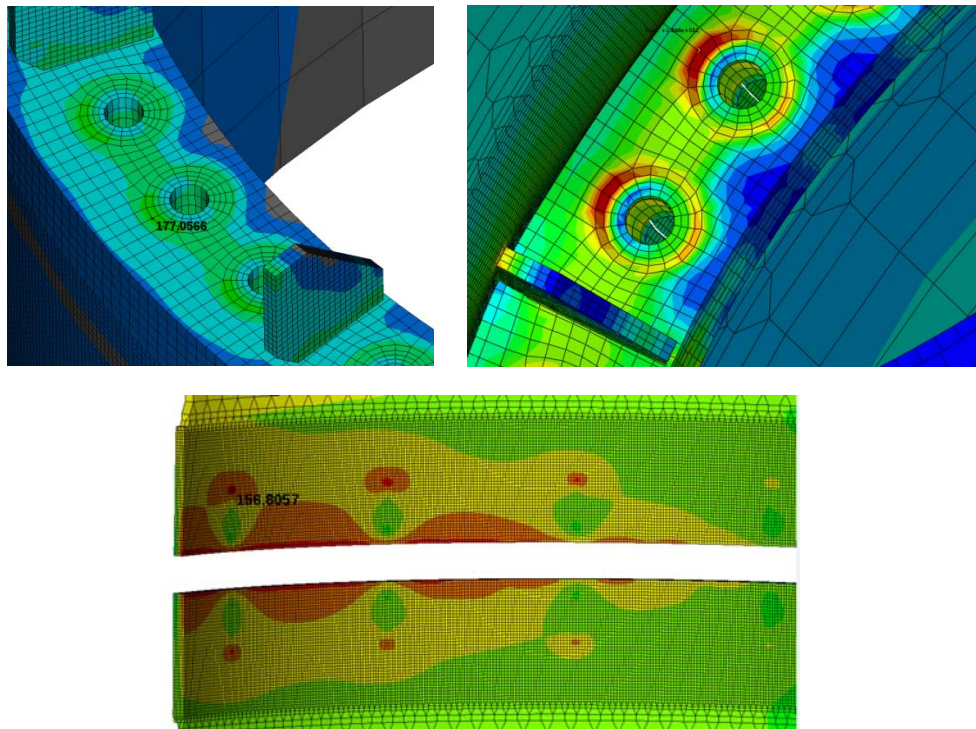
Fig.4.8. *Stress results (Von Misses - MPa) following segments FEM analysis. Concentration of the stresses in the joint area*

Following the analytical results, using the internal forces, stresses in the shell element are determined in the joint area, [4.2]:

$$\sigma_{x,Ed,1} = -\frac{N_{Ed}}{2 \cdot \pi \cdot r \cdot t} + \frac{M_{y,Ed}}{\pi \cdot r^2 \cdot t} + \frac{M_{z,Ed}}{\pi \cdot r^2 \cdot t} = 216 \text{ MPa} \tag{4.7}$$

$$\sigma_{x,Ed,2} = -\frac{N_{Ed}}{2 \cdot \pi \cdot r \cdot t} - \frac{M_{y,Ed}}{\pi \cdot r^2 \cdot t} - \frac{M_{z,Ed}}{\pi \cdot r^2 \cdot t} = -228 \text{ MPa} \tag{4.8}$$

$$\sigma_{x,Ed} = max\left(\left|\sigma_{x,Ed,1}\right|, \left|\sigma_{x,Ed,2}\right|\right) = 228 \text{ MPa} \tag{4.9}$$

The other stresses: $\sigma_{\theta,Ed}$, $\tau_{x,\theta,Ed,1}$, $\tau_{x,\theta,Ed,2}$, $\tau_{x,\theta,Ed}$, $\tau_{x,n,Ed}$ and $\tau_{\theta,n,Ed}$, having very low value, were neglected.

Advanced LBA analysis

A linear buckling analysis (LBA) was performed to the perfect shell for the extreme wind load combination (taken from the Linear Analysis 1,35 x SelfWeight + 1,35 x DeadLoad + 1,50 x WindLoad X).

The elastic critical buckling resistance ratio r_{Rcr} is determined from an eigenvalue analysis (LBA) applied to the linear elastic calculated stress state in the geometrically perfect shell (LA) under the design values of the load combination.

The first ten buckling eigenvalues were calculated, as presented in Figure 4.9. and Table 4.5. The linear buckling eigenvalues represent the factors r_{Rcr} by the expression $r_{Rcr} = F_{Rk}/F_{Ed}$, where F_{Ed} represent the design loads and F_{Rk} the characteristic buckling resistance, at the bifurcation point.
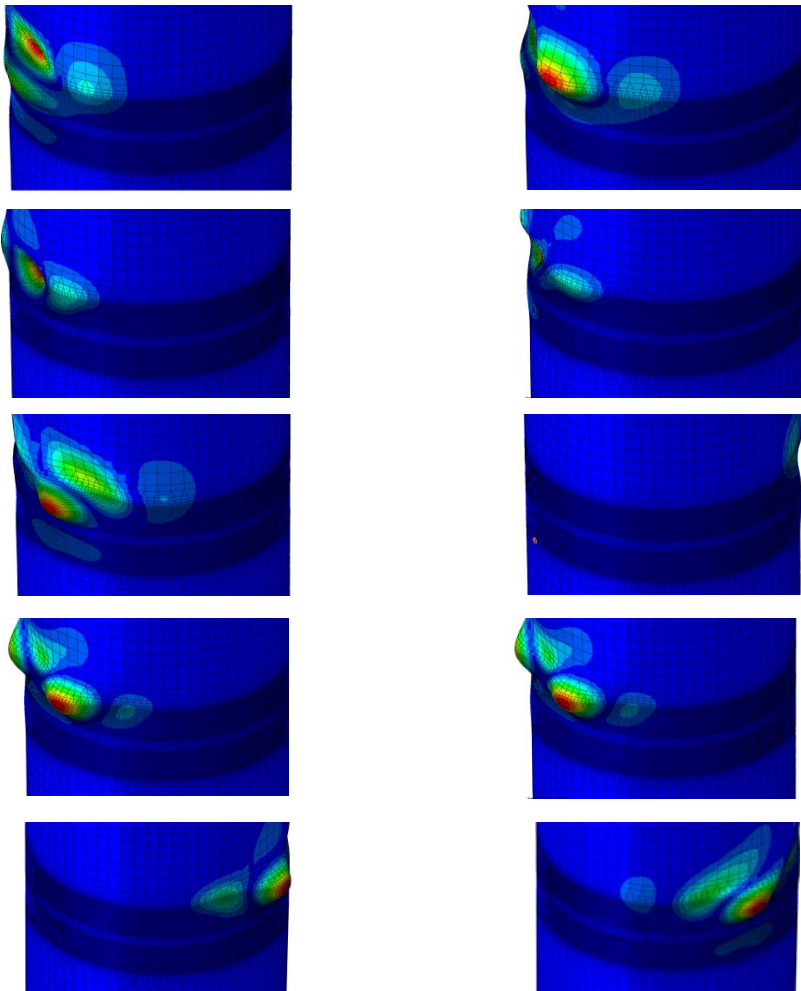
Fig.4.9. *Buckling deformed shapes for each eigenmode (1 to 10 from left to right)*

Table 4.5. *Design results – buckling eigenvalues r_{Rcr}*

Eigenmode	[1]	[2]	[3]	[4]	[5]
Eigenvalues r_{Rcr}	1.154	1.021	1.199	1.010	1.240

Eigenmode	[6]	[7]	[8]	[9]	[10]
Eigenvalues r_{Rcr}	1.154	1.215	1.008	1.204	1.001

All buckling eigenmodes present deformed shapes (buckling) at the lower part of the 16 mm thickness segment – nearby the joint area (immediately to the joint stiffeners)

The bifurcation load factor was taken as the first eigenmode corresponding value - critical buckling resistance ratio $r_{Rcr} = 1.154$ (figure 4.10).
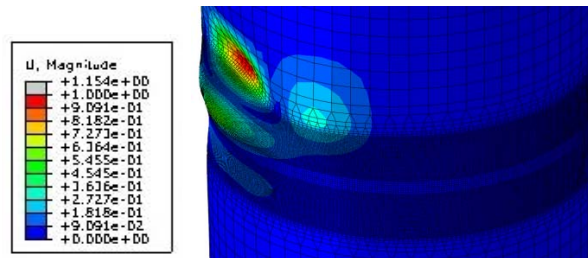
Fig.4.10. *Buckling resistance ratio r_{Rcr} for first eigenmode*

The results of the stress values is presented in table 4.6. – comparison between stress values (Von Mises) calculated analytically [4.2] and the ones calculated with FEM LBA analysis – taken into account the critical buckling resistance value $r_{Rcr} = 1.154$, value used as a multiplication factor for the elastic loads ($F_{Rk} = r_{Rcr} \cdot F_{Ed}$).

Table 4.6. *Von Mises Maximum stress values comparison between LA entire model analysis and the three segments FEM analysis*

Cross section (Dxt) mm	Analytically calculated stresses (LS3-buckling) (MPa)	LBA resulting stress values (Von Mises) (MPa)
1680x12	226,44	178,20
1680x16	250,43	204,10
1680x20	265,54	221,11

As a first overlook, the conclusion is that the LS3 ultimate limit state design (buckling) [4.2] analytical calculated stresses are presenting higher stress values than the FEM analysis, which means that the Eurocode [4.2] is presenting a conservative.

4.4. Application of FEM in analysis of behaviour of steel elements and welded joints with cracks

Modelling of fracture mechanics problems requires an adequate treatment of displacement and stress field singularity around the crack tip, wherein the biggest problem is reflected in drastic increase in discretization error, which occurs when using classic FE, such as the eight-node element. The most efficient solution is obtained by using the reduction technique (reducing the error to only 1%) or by applying special FE around the crack tip, which contains the strain field singularity, figure 4.11. First papers related to elements around the crack tip were written by Henshell and Shaw, 1975 [4.5], who have introduced quadrilateral elements, and Barsoum, 1974 [4.6], 1976 [4.7], who introduced triangular elements.
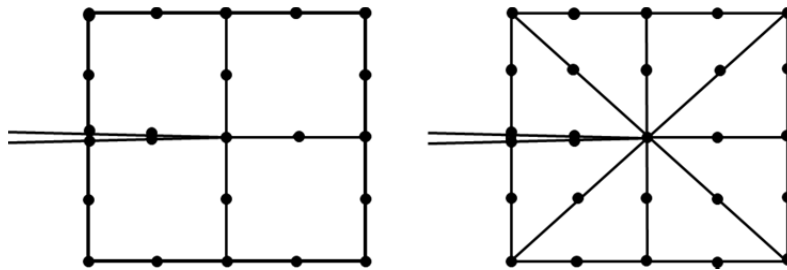
Fig. 4.11 *Special Crack Tip Elements, quarter-point elements*

Properties of an eight-nodded isoparametric element, shown in figure 4.12., are described by following equations:

$$N_1 = -\frac{1}{4}(1-\xi)(1-\eta)(1+\xi+\eta)$$

$$N_2 = -\frac{1}{4}(1+\xi)(1-\eta)(1-\xi+\eta)$$

$$N_3 = -\frac{1}{4}(1+\xi)(1+\eta)(1-\xi-\eta)$$

$$N_4 = -\frac{1}{4}(1-\xi)(1+\eta)(1+\xi-\eta)$$

(4.10)

$$N_5 = \frac{1}{2}\left(1-\xi^2\right)(1-\eta)$$

$$N_6 = \frac{1}{2}(1+\xi)\left(1-\eta^2\right)$$

$$N_7 = \frac{1}{2}\left(1-\xi^2\right)(1+\eta)$$

$$N_8 = \frac{1}{2}(1-\xi)\left(1-\eta^2\right)$$

(4.11)
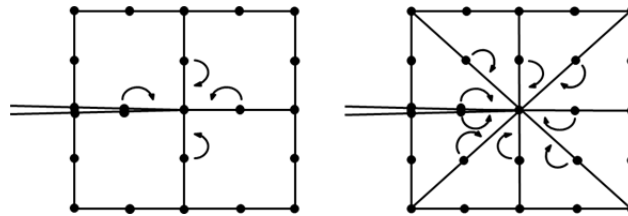
Fig. 4.12. *Eight-nodded isoparametric element*

Banks-Sills and Bortman (1984) [4.8] introduced the square-root singular element, figure 4.13.
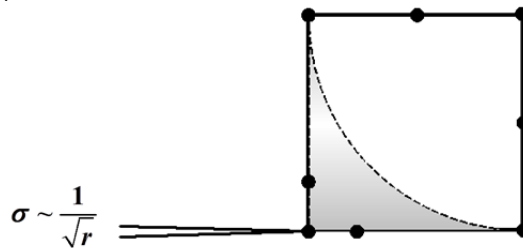
Fig. 4.13. *Square-root singular element*

When analyzing the stress state around the crack tip, it is recommended to use triangular isoparametric elements, since such elements, when subjected to load, gives a $1/\sqrt{r}$ strain singularity in the vicinity of the crack tip, and are displayed in nodes "shifted" by 1/4 of the side length. This region is modeled by placing elements in concentric circles, while ensuring that their size decreases as the approach the tip (figure 4.13). The area which suffers plastic strain must be accurately modeled using a larger number of FE, whereas elastic analysis of stress state does not require a particularly fine mesh, which is important in terms of calculation time.

By applying FEM in order to simulate the behavior of a material with a crack, it is necessary to emphasize that elements which define the elastic state, require special formulation within the software, whereas in the case of elements which define the plastic behavior, it is sufficient to place three nodes around the crack tip in an almost identical position.

Fracture mechanics parameters can be determined in a number of different methods, such us displacement extrapolation, J-Integral, stiffness derivative method, etc.
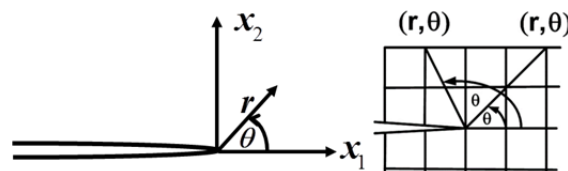
Fig. 4.14. *Displacement extrapolation method*

In the case of displacement extrapolation method, figure 4.14., when crack propagation simulation in the material is performed using polar coordinates, the following expressions can be defined for plane strain conditions:

$$v(r,\theta) = \frac{K_I}{2\mu} \sqrt{\frac{r}{2\pi}} \sin\frac{\theta}{2}\left(\kappa + 1 - 2\cos^2\frac{\theta}{2}\right) \tag{4.12}$$

$$\mu = \frac{E}{2(1+v)} \tag{4.13}$$

$$\kappa = \begin{cases} 3 - 4v & pl\varepsilon \\ (3-v)/(1+v) & pl\sigma \end{cases} \tag{4.14}$$

Equivalent coefficient is determined according to expression 4.15.

$$K_I^* = \frac{\sqrt{2\pi}}{2} \frac{E}{(1+v)} \frac{1}{\sin\frac{\theta}{2}\left[2(1-v)-\cos^2\frac{\theta}{2}\right]} \frac{v(r,\theta)}{\sqrt{r}} \tag{4.15}$$

If the angle $\theta = 0$, the following expression is obtained:

$$K_I^* = \frac{\sqrt{2\pi}}{2} \frac{E}{1-v^2} \frac{v(r,\pi)}{\sqrt{r}} \tag{4.16}$$

As shown in figure 4.15., $K_I = \lim\limits_{r\to\infty} K_I^*$.
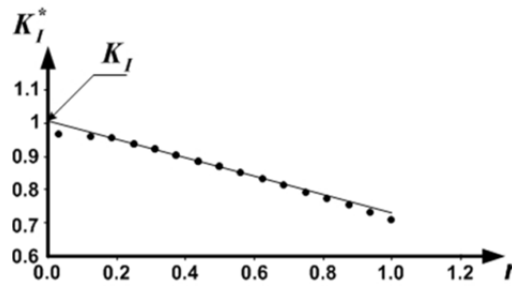
Fig.4.15. *Diagram of dependence of K_I and K_I^**

One of the commonly used methods is the *J* integral method, shown in figure 4.16., and in this case the *J* integral can be expressed by 4.17.
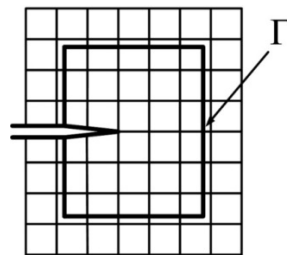
Fig. 4.16. *J – integral method*

$$J = \int_r \left\{ \frac{1}{2}\left[\sigma_{11}\frac{\partial u_1}{\partial x_1} + \sigma_{22}\frac{\partial u_2}{\partial x_2} + \sigma_{12}\left(\frac{\partial u_1}{\partial x_2} + \frac{\partial u_2}{\partial x_1}\right)\right]n_1 - \left[\left(\sigma_{11}\frac{\partial u_1}{\partial x_1} + \sigma_{12}\frac{\partial u_2}{\partial x_1}\right)n_1 + \left(\sigma_{12}\frac{\partial u_1}{\partial x_1} + \sigma_{22}\frac{\partial u_2}{\partial x_1}\right)n_2\right]\right\}ds \tag{4.17}$$

4.5 Application of XFEM method to crack growth simulation

In order to evaluate the influence of initial defects in material on strength and life of structures, finite element analysis is applied to cracks of various shapes, sizes and locations. In these analyses, FEM is limited, since changes in crack topology require additional generating of mesh domain. This represents a significant constraint and complicates crack growth simulation on complex geometries. Extended finite element method, X-FEM was developed in order to make calculations easier, which was required during positioning of arbitrary cracks within a finite element model.

Extended finite element method (XFEM) used enhancement functions as a means of displaying all forms of discontinuous behavior, such as crack displacement. Enhancement functions are introduced into the displacement approximation for only a small number of finite elements, relative to the size of the whole domain. Additional degrees of freedom are introduced for all elements where the discontinuity is present, and in some cases - depending on the type of the selected function - into adjacent elements, which are then referred to as mixed elements.

Displacement approximation can be expressed in the following way, by applying enhancement functions:

$$u^h(x) = \sum_i N_i(x)\left[u_i + \sum_j v^j(x)a_i^j\right] \tag{4.18}$$

The unity property is based on the fact that the sum of interpolation functions of finite elements equals one. Assuming that the unity property is fulfilled, additional enriching functions, i.e. improvement functions, can be given in displacement approximation. In this case, application of standard X-FEM displacement formulation approximate displacements as:

$$u(\xi,\eta,\zeta) = \sum_i N_i(\xi,\eta,\zeta)U_i + \sum_i N_i(\xi,\eta,\zeta)H(\xi,\eta,\zeta)b_i +$$
$$\sum_i N_i(\xi,\eta,\zeta)\left(\sum_j \psi_j(r,\theta)c_{ji}\right) \tag{4.19}$$

where $N_i(\xi,\eta,\zeta)$ are shape functions, $U_i \in R^3$ are node displacement parameters for all nodes of a hexahedron element: 1~8, $b_i \in R^3$ are parameters of jump function on jump nodes, and $c_{ji} \in R^3 \times R^4$ are parameters of the branching function for nodes at the crack tip.

It is necessary during calculation to determine which mesh elements were divided by the crack and in which element the crack tip is located, taking into account that X-FEM does not approximate the entire domain. In this sense, an unequivocal identification of elements uses two functions on the level of sets (LS functions), which are based on level set (LS) method.

Jump function H is defined as the sign of the level set φ:

$$H(\xi,\eta,\zeta) = \begin{cases} +1: & (\xi,\eta,\zeta) > 0 \\ -1: & (\xi,\eta,\zeta) < 0 \\ \pm 1 \div & (\xi,\eta,\zeta) = 0 \end{cases} \tag{4.20}$$

It should be noticed that function $H(\xi,\eta,\zeta)$ is not well defined when $\varphi(\xi,\eta,\zeta)=0$, $H(\xi,\eta,\zeta)=\pm 1$ merely represents a suitable way of calculating of the jump function in points which are located at the crack surface.

References

[4.1] ***, Eurocode 3. "*Design of steel structures, part 1–1: General rules*", European Committee for Standardisation (CEN). Brussels; 2006

[4.2] ***, Eurocode 3. "*Design of steel structures, part 1-6: Strength and Stability of Shell Structures*", European Committee for Standardisation (CEN)

[4.3] ***, Eurocode 1. *"Action on structures, part 1-4: Wind load",* European Committee for Standardisation (CEN).

[4.4] ***, Eurocode 3. "*Design of steel structures, part 1–8: Joints design*", European Committee for Standardisation (CEN). Brussels; 2006

[4.5] Henshell, R. D., Shaw, K.G., "*Crack tip finite elements are unnecessary*", International Journal for Numerical Methods in Engineering, Volume 9, Issue 3, Pages 495-507, 1975

[4.6] Barsoum, R. S. (1974). Application of Quadratic Isoparametric Finite Elements in Linear Fracture Mechanics. International Journal of Fracture, 10, 603-605.

[4.7] Barsoum, R. S. (1976). Application of Triangular Quarter-Point Elements as Crack Tip Elements of Power Law Hardening Material. International Journal of Fracture, 12, 463-466.

[4.8] Banks-Sills, L. and Bortman, Y. "*Reappraisal of the quarter-point quadrilateral element in linear elastic fracture mechanics*", International Journal of Fracture, 25, 169–180, 1984.

[4.9] Kundu, T., "*Fundamentals of Fracture Mechanics*", CRC Press, 2008

[4.10] Radu D., „*Manufacturing imperfections importance in rectangular hollow section welded joints behaviour*", SGEM2015 Conference Proceedings, ISBN 978-619-7105-33-9 / ISSN 1314-2704, June 18-24, 2015, Book1 Vol. 3, 895-902 pp

[4.11] Abaqus User Manual, Abaqus 6.7.-1, Dassault Systems, 2007

5. EXPERIMENTAL RESEARCH

5.1. Introduction

Steel shell elements are used in civil engineering commonly in the wind farming industry, steel towers, silos and other industrial applications.

The research program of this thesis is based on a steel shell element part of a billboard tower structure located in Brașov.

After erection in 2009, two inspections of the structure were performed by qualified personnel in order to assess the state of the structure. Following a visual investigation of the structural elements and the joints of the billboard tower, several cracks were discovered in the area of the segment joints of the tower.
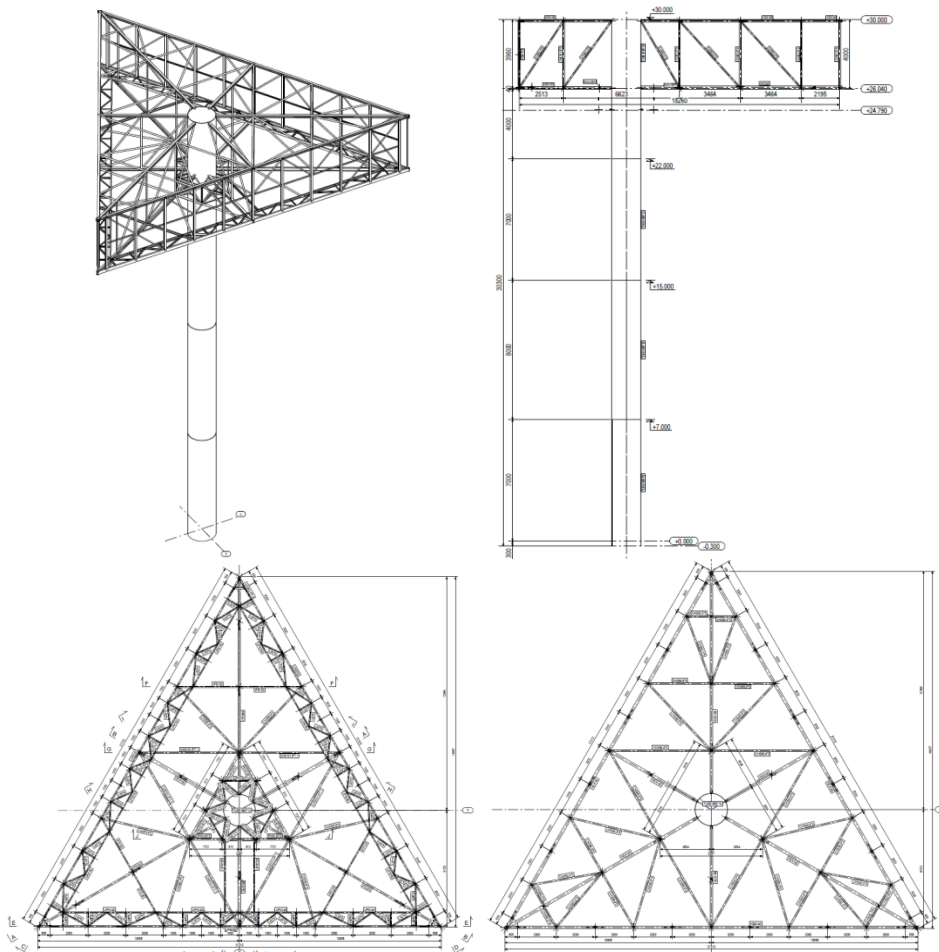
Fig. 5.1. *Geometry of the billboard tower*

Considering that the structure design project was applied by the owner of the tower (a multinational company), in different countries with respecting each country design requirements, an in depth assessing of the structure was needed in order to conclude about the structure reliability.

The structure has two components: the column which is a 1680 mm diameter S355J2 steel quality tube and the head of the tower where the billboard is fixed. The head is made of a truss system in order to undertake the dead and wind loads and to transmit them directly to the pillar (figure 5.1).

The pillar is made of four sections – from the base to the top: Tube 1680 x 20mm – 7m, Tube 1680 x16mm – 8,00m, Tube 1680 x 12 – 7,00m and Tube 1680 x 10 – 8,00m. The sections are connected by bolted endplate joints.

The main loads events of the tower consists in wind loads from august 2009 until august 2016. A detailed wind load data was provided by the National Institute of Meteorology and Hydrology (INMH).

Applying a methodology for assessing the safety for a structure requires the knowledge of the base material from which the structure was build.

The research program consist in:

- conventional testing: chemical analysis of the steel composition, traction tests , Charpy V-notch test, in order to determine the amount of energy absorbed by a material during fracture.

- fracture mechanics testing: determining the J integral curve, the fatigue crack growth

Following the test results complex fracture and fatigue calculations were done (chapter 6).

5.2. Laboratory tests and measurements

The laboratory testing and measurements were done at Faculty of Mechanical Engineering – University of Belgrade and also at the Technical University of Timișoara.

5.2.1. Samples of the base material

For these test different specimens were processed from the structure – areas with no major structural implication. The position of the specimen processing was at the middle and upper part of the tower – in the area of the billboard. Different reinforcement solution were applied after samples were taken – new steel plates welded onto contour in the area of the holes.

For testing purposes, four pieces of steel sheets were provided, figure 5.2:

o   Specimen with dimensions of 100 x 310 x 16 mm (Specimen A)

o   Specimen with dimensions of 115 x 320 x 10mm (Specimen B)

o   Specimen with dimensions of 100 x 280 x 10 mm (Specimen C)

o   Specimen with dimensions of 100 x 290 x 10 mm (Specimen D)
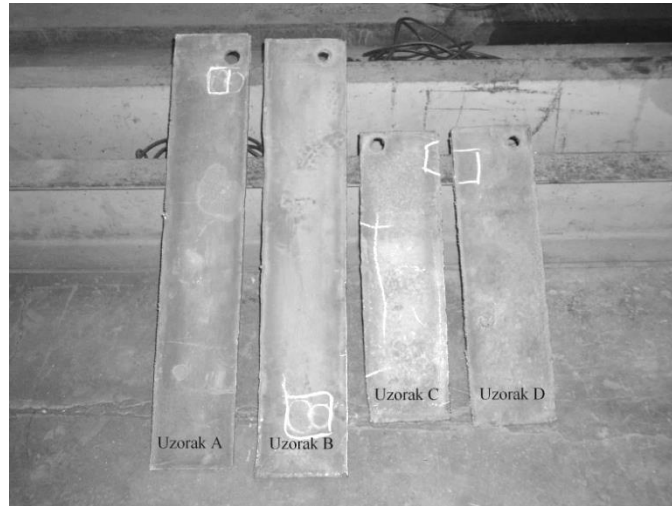
Fig.5.2. *Supplied steel sheet specimens from the tower*

5.2.2. **Determining of the chemical composition**

A plate with dimensions of 30x30x10 mm was cut from steel sheet specimen C, for the purpose of chemical analysis of the material. The specimen was prepared for analysis – the paint and rust stains were removed. The analysis were done at Mechanical Faculty of Belgrade, where spectral analysis were performed through modern investigation methods based on chemical aggressivity. The dimensions of the specimens did respected the equipment requirements.

Results of chemical composition tests are given in table 5.1.

Table 5.1. *Chemical composition of the supplied specimen and EN10025-2 requirements for max values*

Specimen	% mas.						
name	C	Si	Mn	P	S	N	Al
Specimen C in test	0.11	0.37	1.23	0.017	0.011	0.003	0.017
EN10025-2 max values	0.24	0.55	1.60	0.035	0.035	0.012	0.017

Conclusions of the results for the chemical composition of the material showed that the steel quality is in standards (EN10025-20).

5.2.3. **Determining of tensile properties**

Specimens for tensile tests were cut out of samples C and D. Tests were performed in order to determine the tensile properties of materials. The test procedure itself, as well as specimen geometry, figure 5.3, was defined by standard EN 10002-1.
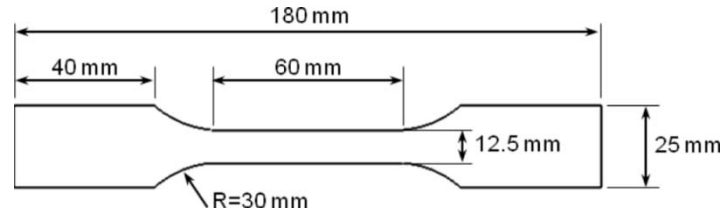
Fig. 5.3. *Specimen used for determining of tensile properties*

Tests were performed on a SCHENCK-TREBEL RM 100 electro-mechanical test machine in load control, figure 5.4. Elongation was registered using an extensometer with accuracy of $\pm0,001$ mm. Results of tensile properties determining obtained for specimens cut out of steel sheet samples are shown in tab 5.2.

Stress – elongation diagram, obtained by testing of *C - 1* specimen is shown in figure 5.5.

Table 5.2. *Results of tensile properties*

Specimen name	Upper yield stress, R_{eH}, MPa	Lower yield stress, R_{eL}, MPa	Tensile strength R_m, MPa	Elongation A, %
C - 1	328	319	425	34.6
C - 2	322	317	421	33.2
D - 3	335	322	431	31.7

The results of the tensile properties reveals the nonconformity of the steel type – the steel is not according to the requirements of the design project – S355J2 (minimum yield strength of 355 N/mm^2). This result was another reason for more in depth study of the existing structure behavior and for assessing of the fracture mechanics parameters.

Fig. 5.4. *Electro-mechanical test machine SCHENCK-TREBEL RM 100*
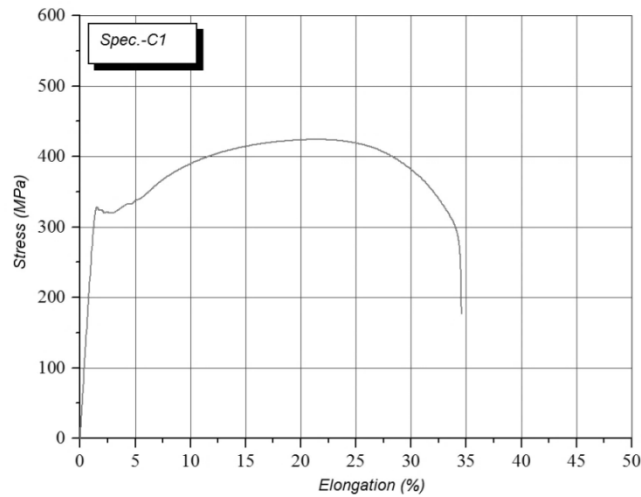
Fig. 5.5. *Stress – elongation diagram of specimen C - 1*

5.2.4. Impact tests

The test were performed in Faculty of Mechanical Engineering from Belgrade University and had the scope of assessing the material toughness in the presents of a notch type defect and its tendency to brittle fracture at low temperature

Specimens for impact tests were cut out of supplied steel sheet samples C and D. Impact tests were performed at room temperature, at -20°C and at -40°C in order to determine total impact energy, as well as crack initiation energy components and crack propagation crack. Testing procedures, along with specimen geometry, figure 5.7, were defined by standard EN 10045-1 [5.1], and ASTM E23-03 [5.2]. The test was performed on an instrumented Charpy pendulum 150/300 J, figure 5.6. Results of steel sheet specimen tests at room temperature and at -20°C are given in table 3.
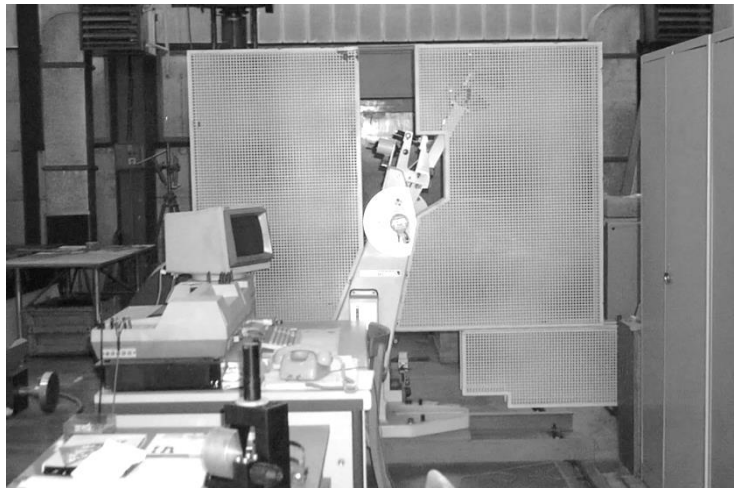
Fig. 5.6. *Instrumented Charpy pendulum SCHENCK TREBEL 150/300 J*

Force-time and energy-time diagrams were obtained by performing tests with the instrumented pendulum with an oscilloscope, which have enabled the analysis of the influence of temperature on total impact energy A_{tot}, and its components, crack initiation energy A_I and crack propagation energy A_P.
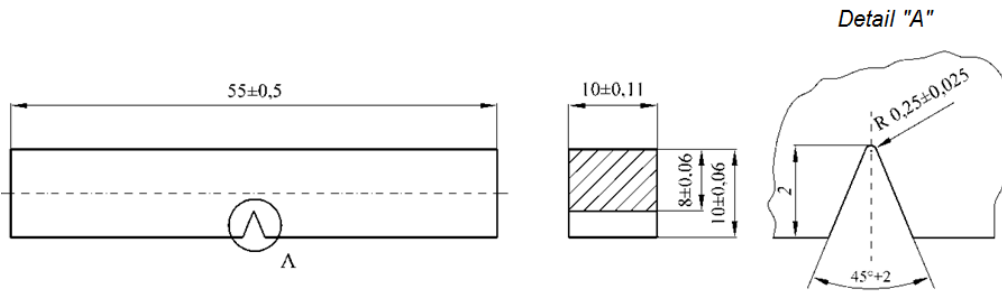
Fig. 5.7. *Shape and dimensions of a standard V-notched specimen for Charpy testing*

Typical force-time and energy-time diagrams, obtained by testing of Charpy specimens cut out of the supplied steel sheets are given in figure 5.8, for specimen 1A, at room temperature, in fig. 5.9 for specimen 1B at the temperature of -20°C, Remaining test diagrams are not shown, since they have shown similar behaviour.

Table 5.3. *Results of impact tests of the supplied steel sheet specimen*

Specimen name	Test temperature °C	Total impact energy, A_{uk}, J	Crack initiation energy, A_I, J	Crack propagation energy, A_P, J
1A	20	136	48	88
2A	20	116	44	72
3A	20	148	50	98
1B	-20	77	41	36
2B	-20	69	39	30
3B	-20	73	40	33
1C	-40	32	20	12
2C	-40	25	18	7
3C	-40	29	21	8

Following the tests results, there were different values of total impact energy results (table 5.3), denoting that the used steel came from same sources – for different types of thickness and specimen locations.

Following a crystal and fibrousness measurements of the after test edges of the specimens, were revealed rupture surfaces with crystal aspect (central part) and a marginal areas with dull aspect.

Can be concluded that the used steel for tower manufacturing is a ductile type with almost brittle fracture at temperature under -40°C. The S355J2 steel required by the design project met the tests expectancies for a EN 10025 standard requirements - the requested EN value regarding the minimum absorbed impact energy – 27 J, was considered achieved at temperature below -20°C.
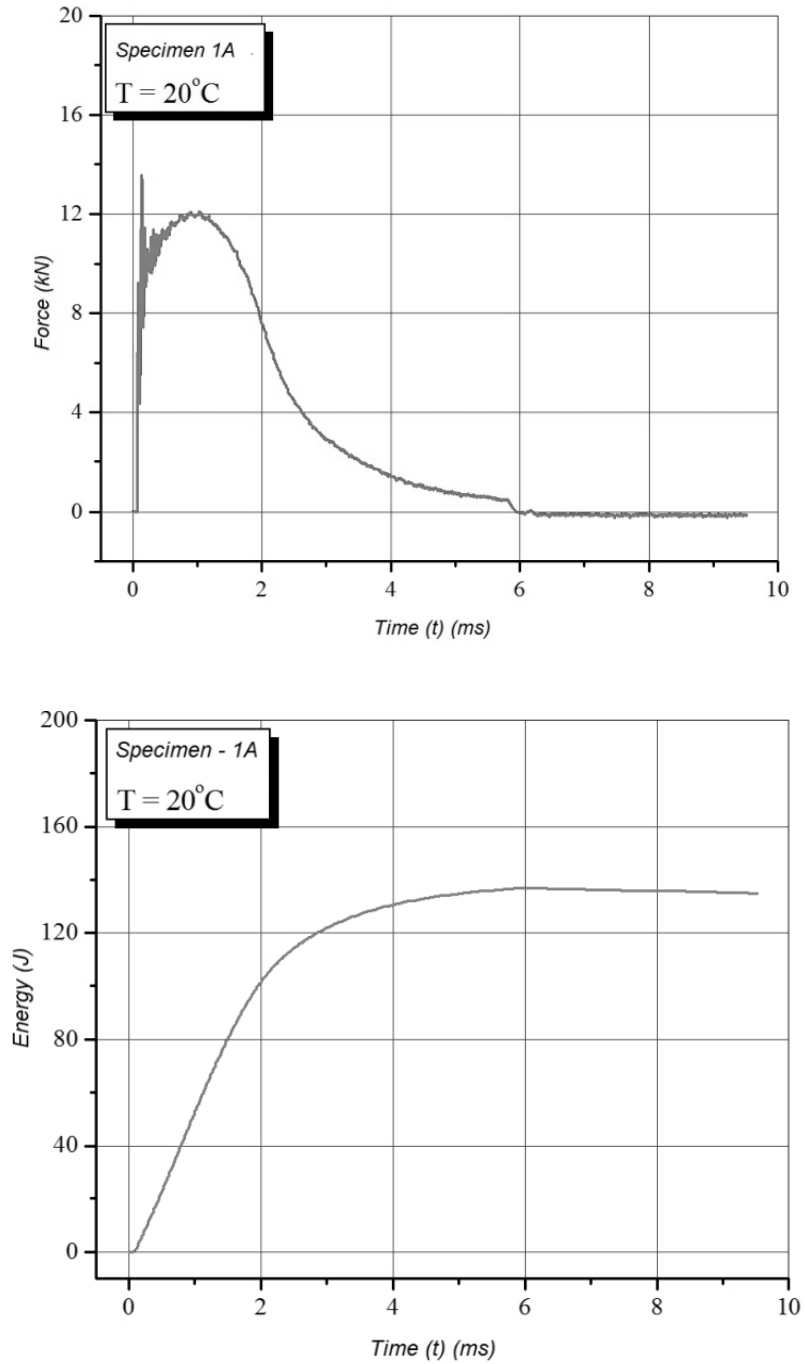
Fig. 5.8 *Diagrams obtained by impact testing of specimen 1A: (a) force – time; (b) energy – time*
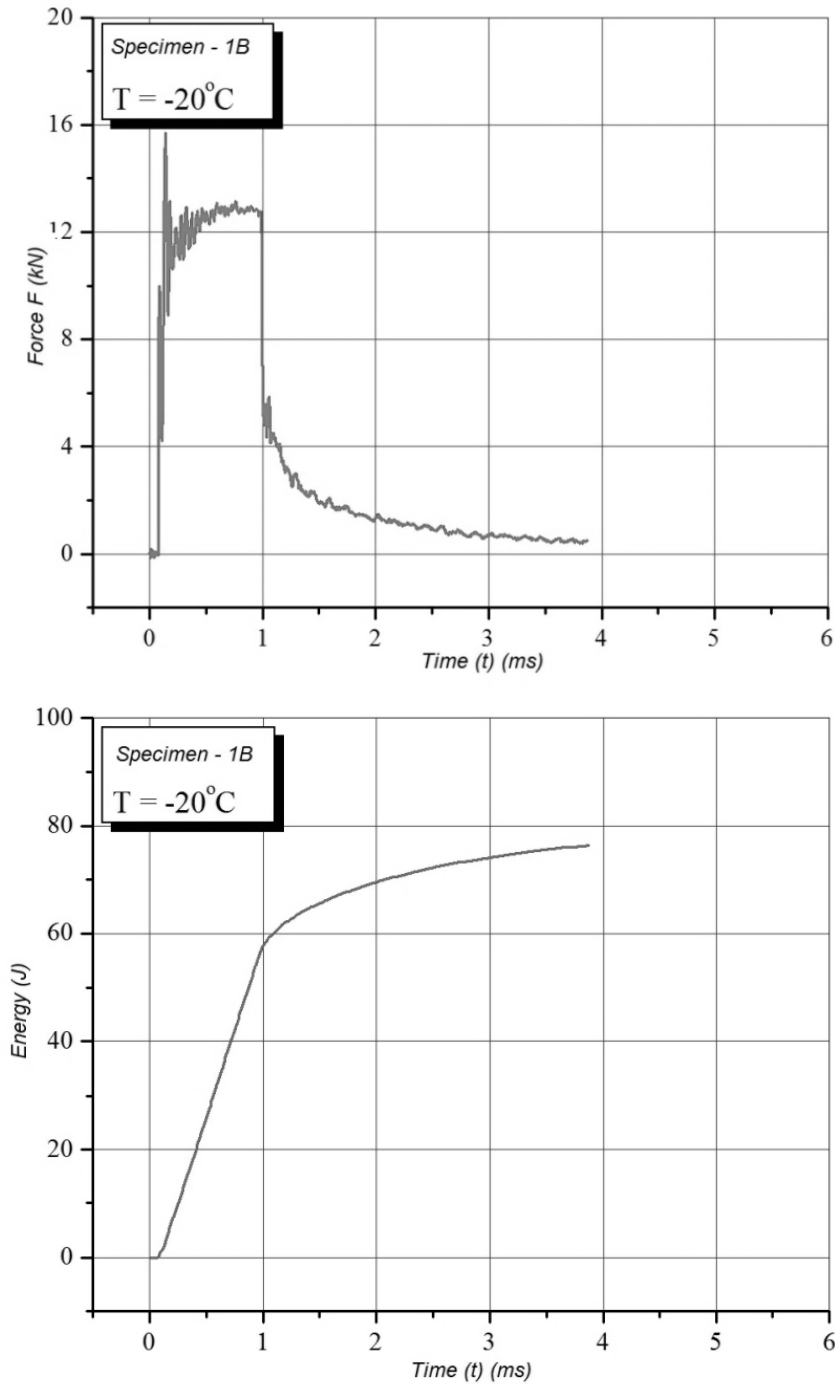
Fig.5.9 *Diagrams obtained by impact testing of specimen -1B: (a) force – time; (b) energy – time*

5.2.5. Variable load testing

Dynamic tests specimens, used for determining of the dynamic fatigue strength were cut out of supplied steel sheet samples A, B and C. Behaviour of supplied materials under the effect of variable load was tested on specimens whose geometry is shown in figure 5.10.

Specimens were shaped and dimensioned in accordance with standard ASTM E466 [5.3], and are meant for dynamic load tests for the purpose of obtaining points in the S-N diagram (constructing of Whöler curves) and determining of dynamic fatigue strength S_f. The test itself was performed on a high-frequency pulsator "AMSLER" at room temperature and 70% humidity.
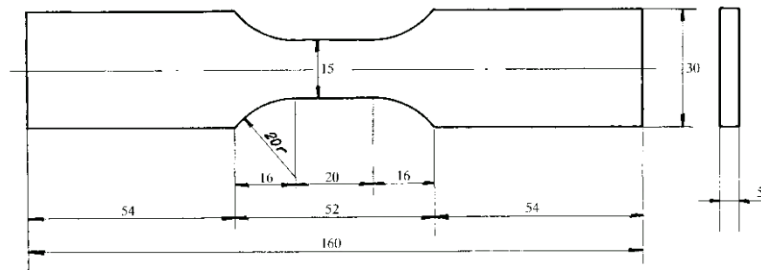
Fig.5.10. *Dynamic test specimen*

The high-frequency pulsator can achieve a sinusoidal one directional variable load range in from -100 to 100 kN. Mean load and amplitude were registered with an accuracy of ±50 N. Achieved frequency ranged from 180 to 190 Hz, depending on the load magnitude and the ratio between minimum and maximum load (ratio R). For the purpose of a more complete assessment of base material behavior under variable load, and taking into account specimen thickness, the most critical case of variable load was analyzed, with an alternating load R = -1 (tension – compression). Variable load scheme is shown in figure 5.11.
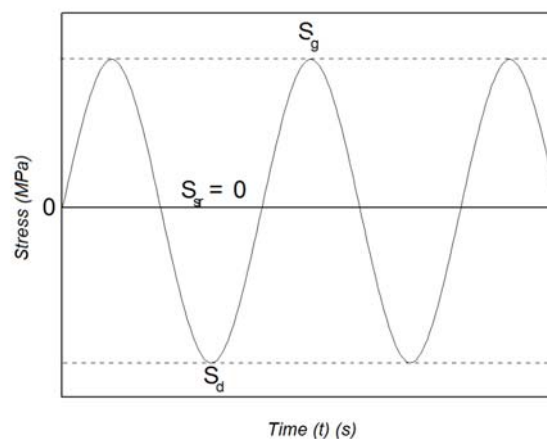
Fig.5.11 *Alternating variable load R = -1 scheme*

Results of variable load tests are presented graphically in S-N (Whöler) curve form in figure 5.12.
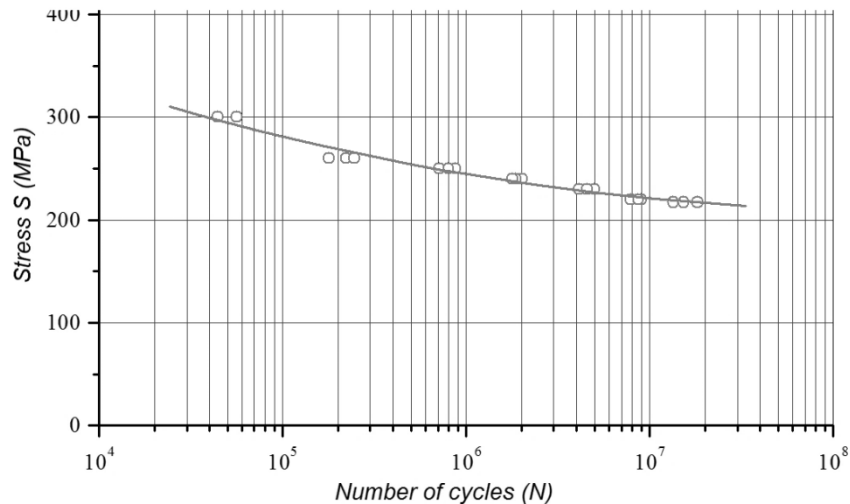
Fig.5.12. *S-N diagram for specimens cut out of supplied samples*

During these tests, it is typical to determine only the number of load variations until fracture, under the effects of constant range load, and the standard only requires the magnitude of stress for which fracture does not occur after a certain number of cycles (usually between 10^6 and 10^8 cycles). For steel materials, standard ASTM E468 defines the dynamic fatigue strength, S_f, after 10^7 cycles. Due to this, such tests are very expensive and justified when design data is necessary, related to fatigue and fracture mechanics; hence, in the case when parts that will be subjected to long-term variable load during the total designed exploitation life are designed.

5.2.6. Determining of fracture mechanics parameters

Testing of specimens with cracks had shown local material behaviour around the crack tip and was based on the assumption that the specimen material is sufficiently homogeneous, which means that local behaviour results can be treated as global, i.e. that they can be directly applied to a corresponding structure.

Fracture toughness under plain strain for specimens cut out of supplied specimens from the given tower structure was determined in order to evaluate the critical stress intensity factor, K_{Ic}, in the presence of crack type defect, as the most dangerous of all defects in structural materials.

For theses test, three point bending (3PB) specimens were used, whose geometry is defined according to standard ASTM E399 [5.5] and is given in figure 5.13. Three point bending specimen had turned out quite suitable in practice, hence it is the most commonly used type.

As defined by [5.5] standard, specimen preparation was performed first, i.e. a fatigue crack was introduced. Fatigue crack is necessary in order to achieve plain strain conditions, since the desired stress field around the fatigue crack tip can be achieved in

a reproductive way, but only in the case that the fatigue crack has provided adequate conditions.
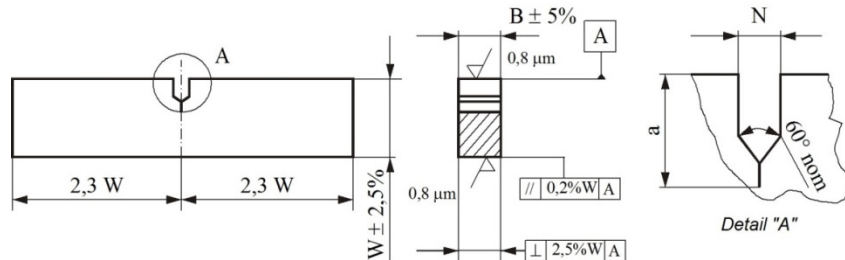
Fig. 5.13. *3PB specimen for fracture mechanics tests*

Determining of the nominal limit force F_L, i.e. the maximum force since the fatigue was initiated is defined by the following formula:

Compact tensile (CT) specimen:

$$F_L = \frac{0{,}2 \cdot B \cdot (W - a)^2 \cdot R_T}{(2W + a)} \qquad (5.1)$$

Three point bending (3PB) specimen:

$$F_L = \frac{B \cdot (W - a)^2 \cdot R_T}{2L} \qquad (5.2)$$

where: B   - specimen width, mm
      W   - specimen height, mm
      a   - crack length, mm
      L   - support span, mm, and
      R_T - effective yield stress, MPa, which is determined according to the following formula:

$$R_T = \frac{R_{p0{,}2} + R_m}{2} \qquad (5.3)$$

where: $R_{p0{,}2}$ – yield stress, MPa, and
      R_m – tensile strength, MPa.

Approximately 50% of total fatigue crack length was performed under maximum fatigue force $F_{max} = 0{,}4 \cdot F_L$. In both cases, the minimum force was $F_{min} = 0{,}1 \cdot F_{max}$.

Fatigue crack initiation was performed on a high-frequency pulsator "AMSLER".

Since the required condition for plain strain $B \geq 2{,}5 \cdot \left(\dfrac{K_{Ic}}{R_{p0{,}2}} \right)^2$ is not fulfilled,

elastic-plastic fracture mechanics, defined in accordance with ASTM E813 [5.7], ASTM E1152 [5.8], ASTM E1820 [5.9] and BS 7448 [5.6], was used instead of linear-elastic fracture mechanics,

The respected procedure was the one defined by [5.5] standard. The purpose of using elastic-plastic fracture mechanics was to determine the values of critical stress intensity factor K_{Ic}, indirectly via critical J integral, J_{Ic}, i.e. to monitor *crack propagation* in extreme plasticity conditions.

The experiments were performed by testing of a single specimen with successive partial unloading, i.e. the single specimen *yielding method*, as defined by [5.8] standard. The purpose of yield method with unloading is to register the magnitude of crack propagation, Δa, during the testing.

Description of the testing

The testing itself was performed at room temperature on an electro-mechanical test machine SCHENCK TREBEL RM 400.

The specimen equipped with a COD extensometer is placed on the three point bending tool for testing of 3PB specimens.

Load was introduced at a slow rate. In this case, load rate was 0.5 mm/min, thus testing of a single specimen lasted between 20 and 30 minutes.

Load was introduced with period unloading until significant plastic strain occurred or the specimen fractured, i.e. until the point where the strain was out of extensometer measuring range. During this time, data about load, displacement (deflection) and crack tip opening was gathered via an A/D converter.

Results

Based on data obtained from the test machine and COD sensor, force F – crack mouth opening displacement (CMOD) δ. The *F-δ* diagrams obtained by testing at room temperature, for a specimen cut from T-L direction and denoted by A-1 is given by figure 5.14, whereas the specimen cut from L-T direction was denoted by B-1 (figure 5.15)
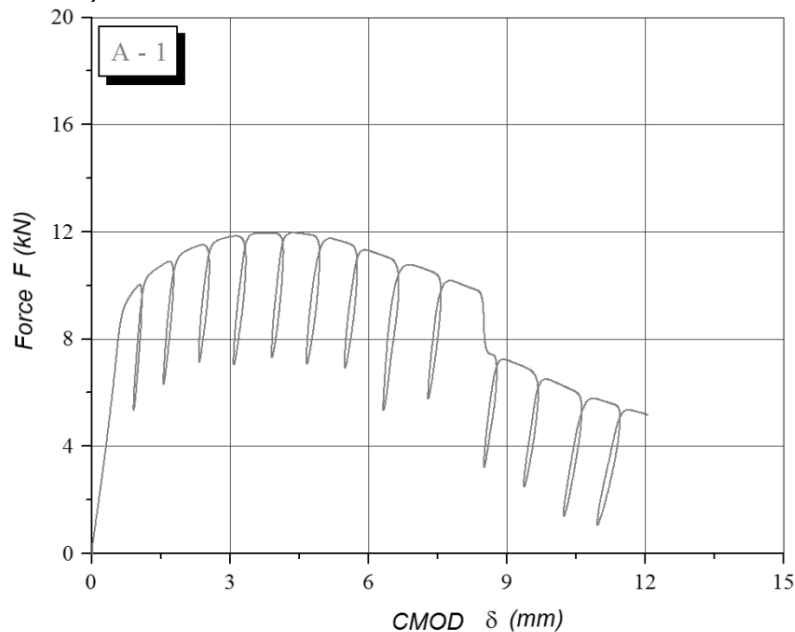
Fig.5.14. *F - δ diagram for specimen A-1*
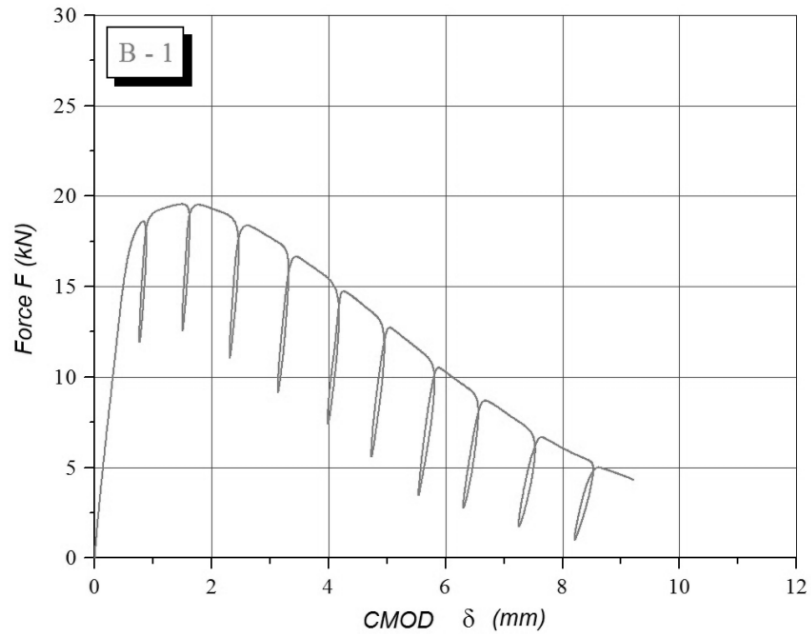
Fig. 5.15. *F - δ diagram for specimen B-1*

After the test is finished, specimens are fractured, so that initial (a_0) and final (a_f) crack length could be measured.

Taking into account that the crack front is not parallel to the specimen edge, measuring is performed along 3 to 5 parallel measuring lines, depending on specimen thickness and fatigue crack front regularity.
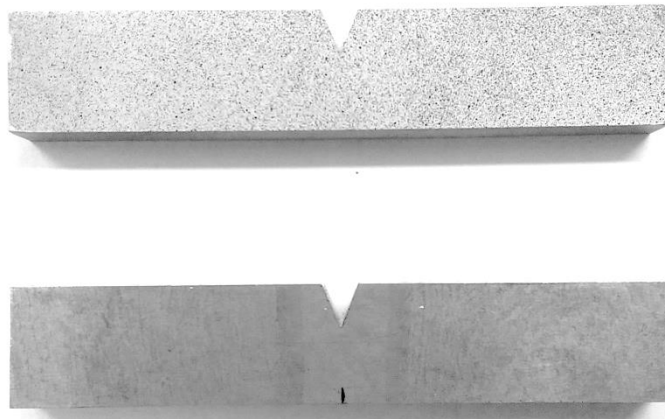
Fig.5.16. *Specimens A and B before testing*
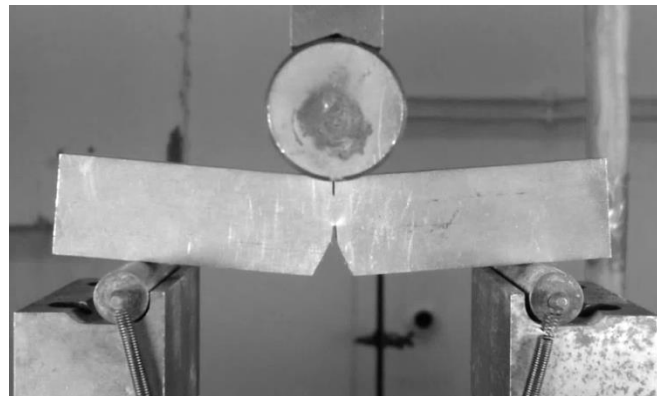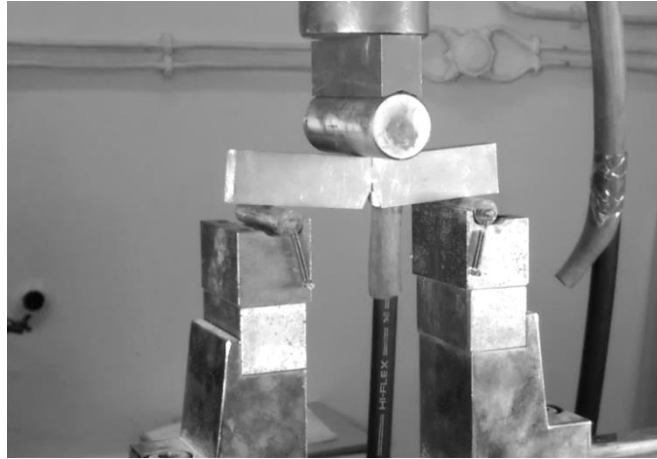
Fig.5.17. *Specimen B in test*
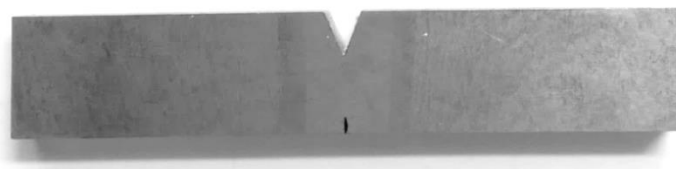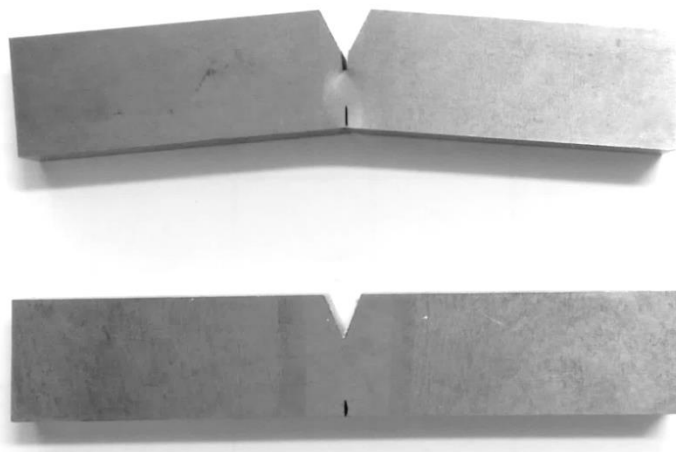
Fig.5.18. *Specimen B after test*
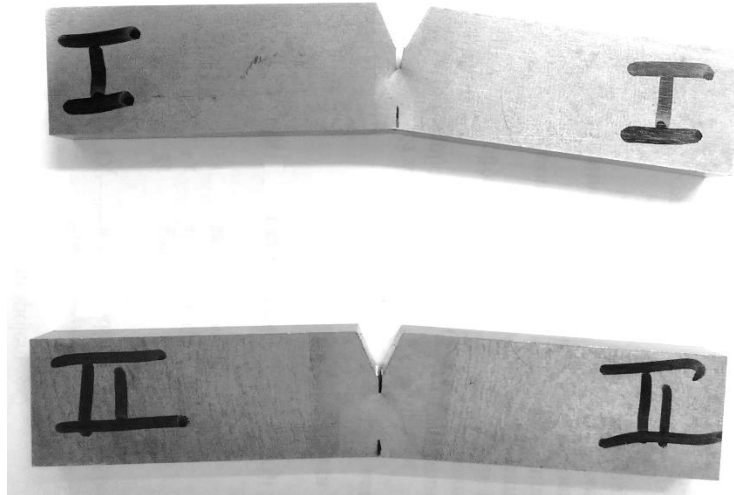
Fig.5.19. *Specimen A(I) and B(II) after test*

In this case, crack length measuring was performed with a special microscope with a cross-hair along 5 parallel lines.

Noticeable unloading on the force – crack opening displacement curve is used for determining the specimen yielding under three point bending for current crack length *a*. Based on yielding, represented by the ratio between the increment of δ and the increment of *F* at the unloading line, was possible to determine the critical crack length using the following expression:

$$\Delta a_i = \Delta a_{i-1} + \left(\frac{b_{i-1}}{2}\right) \cdot \left(\frac{C_{i-1} - C_i}{C_i}\right) \tag{5.4}$$

where: a_{i-1} - previous crack length.
        $C_i = tg\,\alpha_i$ - slope of the observed unloading line.
        $C_{i-1} = tg\,\alpha_{i-1}$ - slope of the previous unloading line.

J integral is equal to the sum of elastic and plastic components of the J integral:

$$J = J_{el} + J_{pl} \tag{5.5}$$

Elastic component of the J integral, i.e. energy, is calculated based on:

$$J_{el(i)} = \frac{K_i^2 \cdot \left(1 - v^2\right)}{E} \tag{5.6}$$

where K_i - stress intensity factor
        v - Poisson's ratio and
        E- Elasticity modulus.

Stress intensity factor is determined according to:

$$K_i = \frac{F_i \cdot S}{\left(B \cdot B_N\right)^{1/2} \cdot W^{3/2}} \cdot f(a_0 / W) \tag{5.7}$$

Value of the $f(a_0/W)$, is calculated according to the following equation:

$$f(a_0/W) = \frac{3(a_0/W)^{1/2}\left[1,99 - (a_0/W)\cdot(1 - a_0/W)\left(2,15 - 3,39(a_0/W) + 2,7(a_0/W)^2\right)\right]}{2(1 + 2a_0/W)(1 - a_0/W)^{3/2}}$$ (5.8)

Plastic component of the J-integral, i.e. energy, is calculated based on:

$$J_{pl(i)} = \frac{2 \cdot A_{pl}}{B_N \cdot b_i}$$ (5.9)

where: A_{pl} - plastic energy component,
B_N - net specimen width, in this case $B_N = B$ since the specimen was made without lateral notched.

J integral was calculated with the following relation:

$$J_i = \left[J_{i-1} + \left(\frac{2}{b}\right)\cdot\frac{A_i - A_{i-1}}{B}\right]\left[1 - \frac{a_i - a_{i-1}}{b_i}\right]$$ (5.10)

where: A - area underneath the curve.
B - specimen thickness.
b - ligament length.

Based on gathered data, a J - Δa curve is obtained, which includes a regression line according to ASTM E 1820. From the obtained regression line, critical J integral, J_{Ic}, is determined.

J-Δa dependence for the specimen denoted by A-1 is shown in figure 5.20, whereas for specimen denoted by B-1, it is given in figure 5.21.
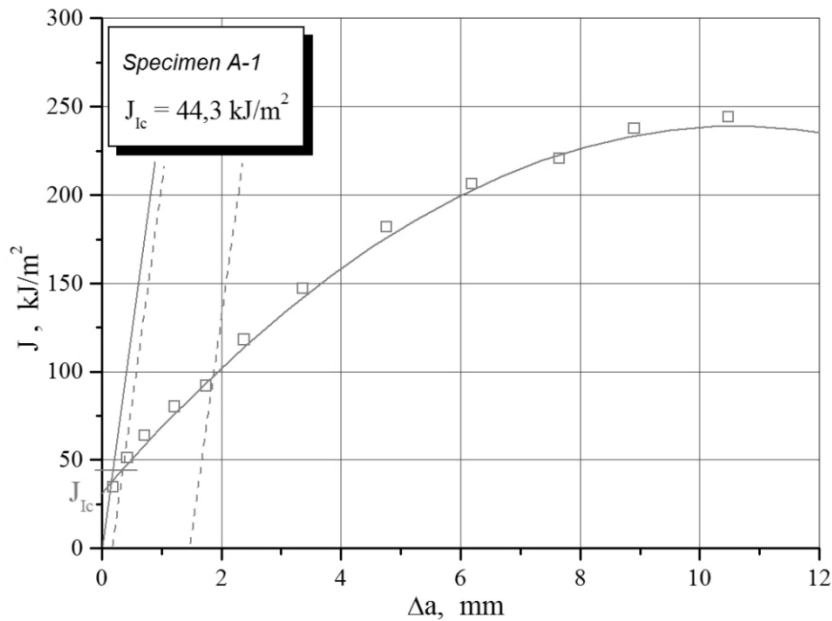
Fig. 5.20. *Diagram J - Δa for specimen A-1*
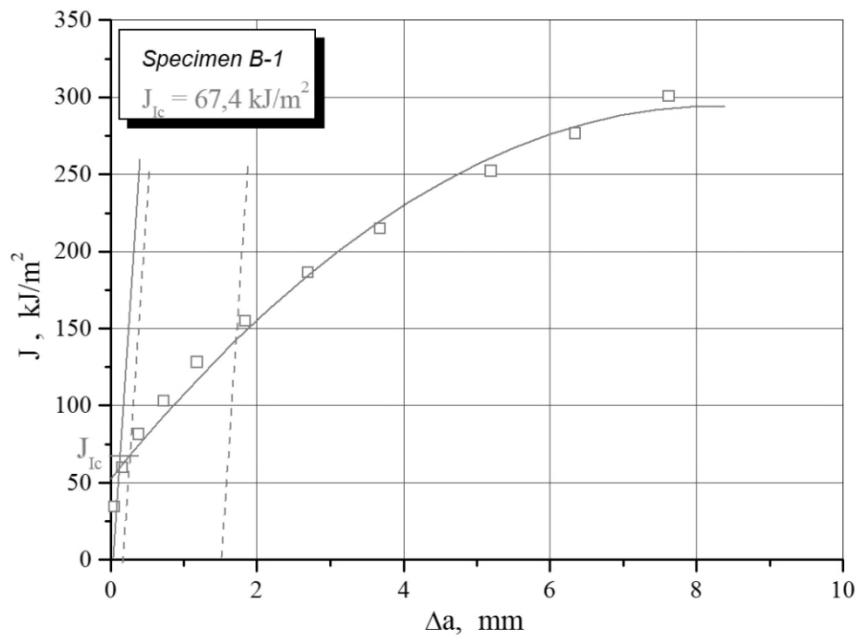
Fig. 5.21. *Diagram J - Δa for specimen B-1*

If the values of critical J_{Ic} integral are known, critical stress intensity factor values or plane strain fracture toughness K_{Ic}, can be determined using the following relation:

$$K_{Ic} = \sqrt{\frac{J_{Ic} \cdot E}{1 - v^2}}$$ (5.11)

Calculated values of plane strain fracture toughness, K_{Ic}, are given in tab. 5.4 for specimens A and B.

Table 5.4. *Fracture toughness values for specimens A and B*

Specimen designation	Critical J-integral J_{Ic}, kJ/m^2	Critical stress intensity factor, K_{Ic}, MPa m$^{1/2}$
A-1	44,3	99.9
A-2	36,4	90.6
A-2	29,7	81.8
B-1	67,4	123.2
B-2	58,5	114.8
B-2	64,2	120.3

By applying the formula for determining of stress intensity factor:

$$K_{Ic} = \sigma \cdot \sqrt{\pi \cdot a_c}$$ (5.12)

followed by introducing values for conventional yield stress $R_{p0,2} = \sigma$, which were obtained from tensile tests, approximate values for critical crack length, a_c, are calculated and shown in table 5.4.

For the purpose of safe crack detection before it reaches critical length, adequate non-destructive test procedures should be applied. It is of great

importance to note that calculated critical crack length values, a_c, is related to plane strain conditions, and that for every concrete case it must be corrected relative to real structure thickness.

In chapter 6 will be used the specimen A-2 value for K_{Ic} = 81.8 MPa m$^{1/2}$.

5.2.7. Fatigue crack growth

Assuming that, in the first approximation, it is adopted that Y does not depend on the crack length, expression 5.12 can be written in the following form:

$$\Delta N = \frac{1}{C_p[Y\Delta\sigma]^{m_p}} \int_{a_0}^{a_d} a^{-\frac{m_p}{2}} da \tag{5.13}$$

Thus, upon integration, a solution is obtained in closed form as:

$$\Delta N = \frac{1}{C_p[Y\Delta\sigma]^{m_p}} \cdot \frac{a_0^{\left(1-\frac{m_p}{2}\right)} - a_d^{\left(1-\frac{m_p}{2}\right)}}{\frac{m_p}{2} - 1} \tag{5.14}$$

It should be mentioned that this approximation results in a non-conservative solution, compared to solutions which take into account the fact that $Y = Y(a)$ and which must be determined via numerical methods.

A typical fatigue crack growth rate, *da/dN* vs. change in stress intensity factor range *ΔK*, diagram for specimens with the crack tip in the parent material (PM), denoted by -1, as well as with the crack tip in the weld material (WM) is shown in figures 5.22 and 5.23.
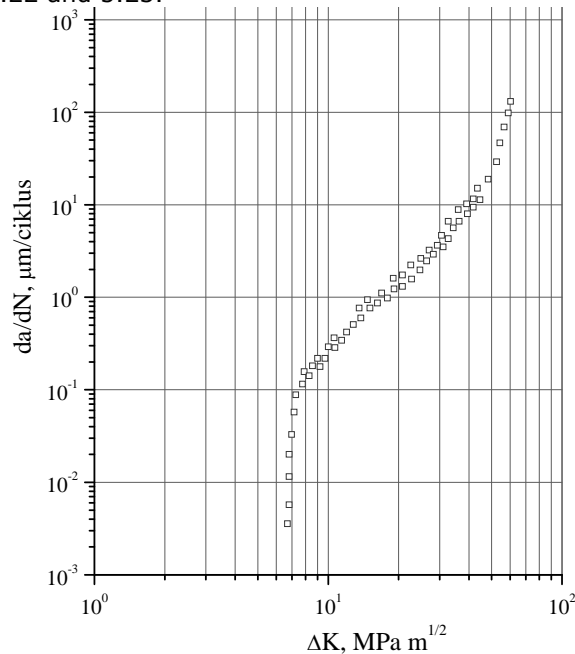
Fig. 5.22. *da/dN - ΔK diagram for specimen A-1*
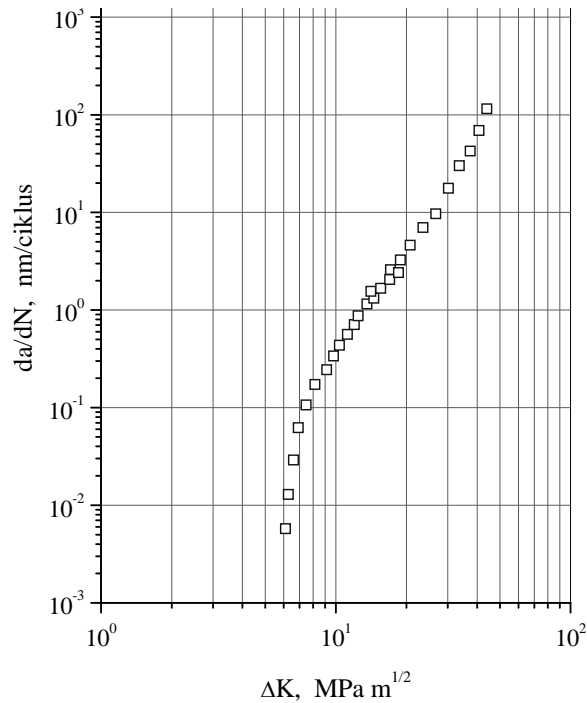
Fig. 5.23. *da/dN - ΔK diagram for WM – 1 specimen*

Obtained values of Paris equation parameters: coefficient *C* and exponent m, fatigue threshold ΔK_{th}, and fatigue crack growth rate, *da/dN*, for ΔK=15 MPa $m^{1/2}$, are given in table 5.5 for specimens with a notch in the PM.

Table 5.5. *Fatigue crack growth parameters for specimens with a notch in the PM*

Specimen designation	Fatigue threshold ΔK_{th}, MPa $m^{1/2}$	Coefficient C	Exponnet m	da/dN, μm/cycle, for ΔK=15 MPa $m^{1/2}$
PM – 1	6,6	$3,05 \cdot 10^{-12}$	3,01	$1,06 \cdot 10^{-8}$
PM – 2	6,8	$3,07 \cdot 10^{-12}$	3,04	$1,15 \cdot 10^{-8}$
PM – 3	6,5	$2,85 \cdot 10^{-12}$	3,09	$1,23 \cdot 10^{-8}$
WM – 1	6,1	$3,27 \cdot 10^{-12}$	3,34	$2,77 \cdot 10^{-8}$
WM – 2	6,2	$3,39 \cdot 10^{-12}$	3,31	$2,65 \cdot 10^{-8}$
WM – 3	6,1	$3,23 \cdot 10^{-12}$	3,42	$3,21 \cdot 10^{-8}$

Prediction of fatigue life for constant amplitude load, i.e. the number of cycles necessary for the crack to grow from initial (a_0) to critical (a_c) or allowed (a_d) crack length is determined according to the following formula:

$$\Delta N = \frac{1}{C_p [Y \Delta \sigma]^{m_p}} \cdot \frac{a_0^{\left(1-\frac{m_p}{2}\right)} - a_d^{\left(1-\frac{m_p}{2}\right)}}{\frac{m_p}{2} - 1}$$ (5.15)

Initial testing parameters include:
- o Initial crack length a_0, which can be detected by using non-destructive tests, with an average length of 2 mm.
- o Varying load, from the least favourable case, i.e. $R = R_{p0,2}$ for the tested material
- o Critical or allowed crack length will also be varied from 2 mm to critical crack length a_{cr}.
- o C_p and m_p represent Paris equation constants determined during the fatigue crack growth parameters testing
- o Coefficient Y is a geometry term which depends on the ratio between the crack length and air tank thickness, and is given in literature, for the case of a surface crack and for various a/W ratios.

Maximum allowed stress was adopted as the value of dynamic fatigue strength of this steel, obtained by testing of specimens cut from **Samples A**, **B and C** (217 MPa).

Detailed assessment of the structure is done in Chapter 6. For the given material properties and fracture parameters, the flaws were assessed – calculated the crack propagation.

Reference

[5.1] ***, EN10045 – 1 - *"Metallic materials — Charpy impact test, Part 1: Test method",* CEN

[5.2] ***, ASTM E23-03 – "*Charpy testing standard*"

[5.3] ***, ASTM E466 – "*Force Controller Constant Amplitude Axial Fatigue Testing of Metallic Materials"*

[5.4] ***, ASTM E468 – "*Standard Practice for Presentation of Constant Amplitude Fatigue Test Results for Metallic Materials"*

[5.5] ***, ASTM E399 – "Standard *Test Method for Linear-Elastic Plane-Strain Fracture Toughness K_{Ic} of Metallic Materials"*

[5.6] ***, BS 7448-1:1991 - *Fracture mechanics toughness tests. Method for determination of K_{Ic}, critical CTOD and critical J values of metallic materials"*

[5.7] ***, ASTM E813 – "*Test Method for JIC, A Measure of Fracture Toughness"*

[5.8] ***, ASTM E1152 – "*Test Method for Determining J-R Curves"*

[5.9] ***, ASTM E1820 – "*Standard Test Method for Measurement of Fracture Toughness"*

6. STRUCTURAL INTERGRITY AND LIFE ASSESSMENT OF CYLINDRICAL STEEL SHELL STRUCTURES

6.1. Engineering critical assessment (ECA)

Most welding fabrication codes specify maximum tolerable flaw sizes and minimum tolerable Charpy energy, based on good workmanship, i.e. what can reasonably be expected within normal working practices. These requirements tend to be somewhat arbitrary, and failure to achieve them does not necessarily mean that the structure is at risk of failure. An Engineering Critical Assessment (ECA) is an analysis, based on fracture mechanics principles, of whether or not a given flaw is safe from brittle fracture, fatigue, creep or plastic collapse under specified loading conditions. An ECA can therefore be used:

1. During design, to assist in the choice of welding procedure and/or inspection techniques.
2. During fabrication, to assess the significance of:
   a) known defects which are unacceptable to a given code [6.15], or
   b) a failure to meet the toughness requirements of a fabrication code.
3. During operation, to assess flaws found in service and to make decisions as to whether they can safely remain, or whether down-rating/repair are necessary.

The ECA concept (also termed 'fitness-for-purpose analysis') is widely accepted by a range of engineering industries.

For an analysis of a known flaw, the following information is needed:

- size, position and orientation of flaw,
- stresses acting on the region containing the flaw,
- toughness and tensile properties of the region containing the flaw,

The fact that knowledge of all these three aspects is necessary, implies a multidisciplinary approach, involving stress analysis, NDT expertise and materials engineering.

The analysis is carried out in accordance with the British Standard procedure BS 7910 ('Guide to methods for assessing the acceptability of flaws in metallic structures'). Although simplified analyses can be carried out based on code values of Charpy energy and maximum allowable stresses, it is usually necessary to carry out fracture-mechanics testing (critical K, $CTOD$ or J) in order to obtain an accurate measurement of the material toughness. Additional stress analysis (e.g. by hand calculation or Finite Element Analysis) may also be required.

For design purposes, or for analysis of weldments which fail to meet a toughness requirement the ECA is based on a hypothetical '*reference flaw*' which is highly unlikely to be missed during inspection.

An ECA can also be used to assess the significance of growing flaws, e.g. fatigue, creep or stress corrosion cracks, in order to make decisions on life extension and safe inspection intervals.

6.2. Determining the crack acceptability based on fracture toughness

6.2.1. Scope. Methodology

Elaboration of a methodology for determining the acceptability of detected cracks/flaws in a structure, has a major practical importance in the overall assessment and life integrity of a structure. The relation given by fracture mechanics links a parameter which describes the ***stress intensity at a crack tip*** to a material characteristic – ***fracture toughness***. This relation provides the possibility of assessing the fracture conditions of the structural elements with defects (cracks) [6.17].

This type of assessing can be done if the following elements are known:
- *material fracture toughness*
- *geometry and size of the crack*
- *resulted stresses from the applied forces*

The fracture mechanics based methodologies are permitting the following types of assessments:
- *Maximal crack dimension assessment* to which the structural element will not fail, named also the admissible crack dimension; for this type of assessing is needed the maximal stresses values and the value of the material fracture toughness;
- *Maximal stress value assessment* to which the structural element with a crack will not fail
- *Minimal fracture toughness value assessment* to the structural element with a crack; this assessment needs knowing the maximal stress value and the admissible crack dimensions.

Following the assessment procedures, can be determined a **life time assessment of the structure**. The methodology implies two phases:
- First phase in which it is determined the acceptability of the detected cracks in the structure (material and/or in welding seams)
- Second phase – fatigue assessment of the analysed structural elements based on loading events history.

Considering a simple case – a steel plate under tension (figure 6.1.), can be underlined the following types of fracture: *Brittle fracture* – controlled by the value of the applied tension force, dimension of the crack, material fracture toughness and geometry of the element; *Plastic fracture* – the net section in which the yielding phenomena appears, controlled by the applied tension force value, the yielding limit and the element geometry; *Rupture as a result of extended material yielding*, controlled by the applied tension force, crack size, material fracture toughness and the element geometry.
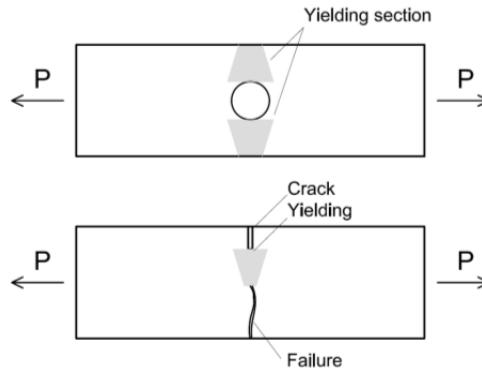
Fig. 6.1. *Describing fracture – plate under tension*

       The transition domain between these types of fracture is governed by the interaction between the *brittle fracture* and the *plastic failure*. This is expressed through a dependency relation of two parameters K_r and S_r. These parameters are defined based on the geometrical dimensions of the structural element, crack dimensions and geometry, stresses that appear in the cross section following the applied loads, taken into account the fracture toughness of the material K_{mat}.

       The **Failure Assessment Diagram** (FAD) describes the interaction between the brittle fracture and plastic failure through a $F_f = f(S_r)$ function.

       Structures using reasonably tough materials (high K_{Ic}) and having only small cracks (low K) will lie in the strength-of-materials regime. Conversely, if the material is brittle (low K_{Ic}) and strong S_r (high yield strength), the presence of even a small crack is likely to trigger fracture.

       Thus, the fracture mechanics assessment is a crucial one. The special circumstances that would be called into play in the upper right corner of figure 6.2 in this regime, a cracked structure would experience large-scale plastic deformation prior to crack extension.
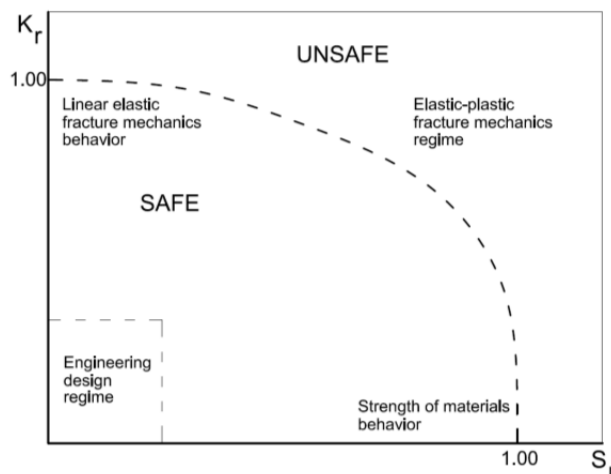
Fig.6.2. *General plot of the ratios of the toughness and stress showing the relationship between linear elastic fracture mechanics and strength of materials as it relates to fracture and structural integrity [6.2]*

Damage tolerance is the philosophy used for maintaining the safety of structures. The use of fracture mechanics and damage tolerance has evolved into the design program for structures that are damage tolerant, designed to operate with manufacturing and in-service-induced defects [6.5].

Damage tolerance evaluation has been interpreted in the past as a means to allow continued safe operation in the presence of known cracking. This interpretation was incorrect. The damage tolerance evaluation can be detailed as a procedure of providing an inspection program for a structure that is not expected to crack under normal circumstances but may crack in service due to inadvertent circumstances. If cracks are found in structure elements, they must be assessed Following the assessment can be concluded: the element of the structure needs to be repaired (the operation of the structure is forbidden n the actual circumstances), the element of the structure can operate until a time where a new assessment must be made . The only allowable exception is through an engineering evaluation, which must show that the strength of the structure will never be degraded below ultimate strength operations or in-service conditions.

FAD represents an assessing instrument of the acceptability of a detected crack in the structural elements. The procedure is simple and consist in determining the K_r and S_r parameters for the particular case of the analysed crack, then positioning of the points (K_r, S_r) in a diagram and comparing the position according with the evaluation line (dotted line presented in figure. 6.2).

$$K_r = K_I / K_{mat} \tag{6.1}$$

where K_I – stress intensity factor calculated for the given case and K_{mat} – the fracture toughness of the material.

If $K_r = 1$, the failure is through brittle fracture.

$$S_r = \sigma_n / \sigma_f \tag{6.2}$$

where σ_n is the effective stress (following the analysis); σ_f (f-flow) is the resistance stress calculated as arithmetic average from yielding stress and ultimate stress resistance of the material (ultimate tensile resistance):

$$\sigma_f = (f_y + f_u)/2 \tag{6.3}$$

where f_y is the yielding strength of the material and f_u is the ultimate limit strength.

If $S_r = 1$ then is resulting a plastic failure.
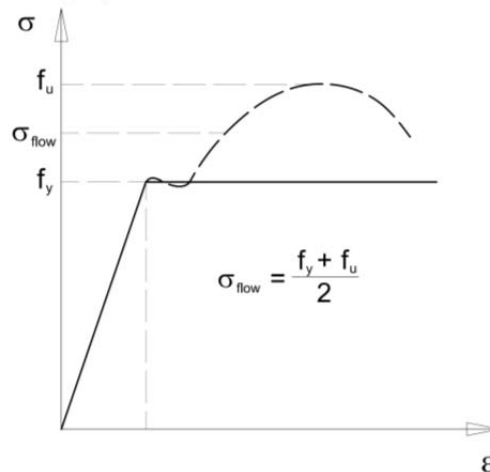
Fig.6.3. *Definition of the "flow resistance - σ_f"*

If the evaluation point (K_r, S_r) is situated in the domain (below the evaluation line), the dimension of the crack / flaw is considered acceptable. If the evaluation point is situated above the evaluation line, the defect is considered unacceptable.

The methodology can be used in a large spectrum of structures for assessing the defects and conclude upon the structural integrity.

The phases of the assessing of the known flaw can be considered as following:

1. Identification of the crack type;

2. Establishing the relevant data regarding the analyzed structure;

3. Determining the crack geometry;

4. Evaluation of the possible degradation mechanisms and the speed of the degradation;

5. Determining the crack maximum dimension for the failure modes;

6. Based on the speed of degradation, it is evaluated if the crack would grow to a maximal dimension in the remaining lifetime or is needed to have additional inspections in order to monitor the crack growth;

7. It is examined the failure consequences;

8. Maintaining the flaw under the maximal size, including the safety coefficients.

6.2.2. Stresses to be considered

The stresses to be considered in the assessment are those which would be calculated by a stress analysis of the unflawed structure. It can be used the actual stress distributions or the linearized stresses, as shown in figure 6.4.

The second method will normally provide overestimates but has the advantage that linearization does not need to be repeated with crack growth. It is essential that account is taken of the **primary membrane and bending stresses**, the **secondary stresses** and the **magnification of the primary stresses caused by local or gross discontinuities or by misalignment**.
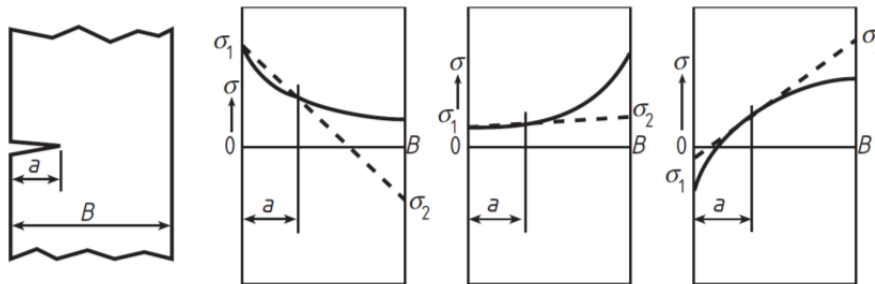
a) Examples of linearization of primary or secondary stress distributions for surface flaws
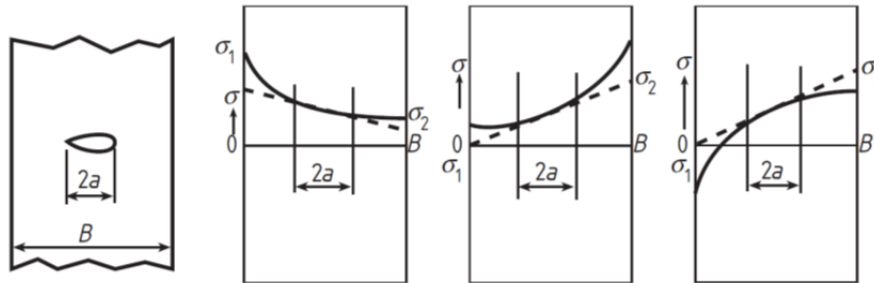
b) Examples of linearization of primary or secondary stress distributions for embedded flaws

P_m, Q_m and P_b, Q_b can be determined from the distribution in i) and ii) using the following equations:

$$P_m, Q_m = \frac{\sigma_1 + \sigma_2}{2} \qquad\qquad P_b, Q_b = \frac{\sigma_1 - \sigma_2}{2}$$

NOTE: Any linearized distribution of stress is acceptable provided that it is greater than or equal to the magnitude of the real distribution over the flaw surface.

i) Linearization of stress distributions in fracture assessments
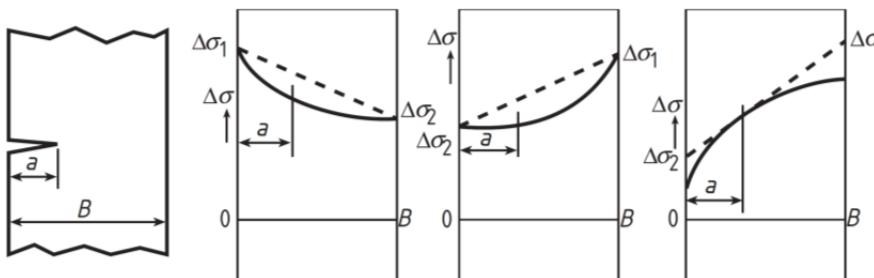
a) Examples of linearization of stress range distributions for surface flaws
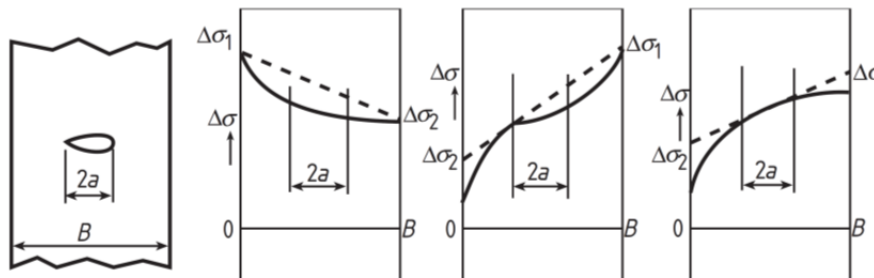
b) Examples of linearization of stress range distributions for embedded flaws

$\Delta\sigma_m$ and $\Delta\sigma_b$ can be determined from the distributions in i) and ii) using the equations:

$$\Delta\sigma_m = \frac{\Delta\sigma_1 + \Delta\sigma_2}{2} \qquad\qquad \Delta\sigma_b = \frac{\Delta\sigma_1 - \Delta\sigma_2}{2}$$

ii) Linearization of stress distributions in fatigue assessments

Fig. 6.4 - *Linearization of stress distributions [6.1]*

Typical schematic representations of these stresses are given in figure 6.5. In an assessment of the effect of a single or steady state applied load, it is important to distinguish between **primary** and **secondary** stresses, since only the former contribute to plastic collapse.

In a fatigue assessment, the important distinction is between **static** and **fluctuating** stresses and all fluctuating stresses are treated in the same way as primary stresses.

a) Primary membrane stress, P_m

b) Membrane stress multiplied by stress concentration factor, $k_{tm}P_m$

c) Primary bending stress, P_b

d) Bending stress multiplied by stress concentration factor $k_{tb}P_b$

e) Bending stress due to misalignment, k_mP_m

f) Secondary stress, Q

g) Total stress, $k_{tm}P_m + k_{tb}[P_b + (k_m - 1)P_m] + Q$
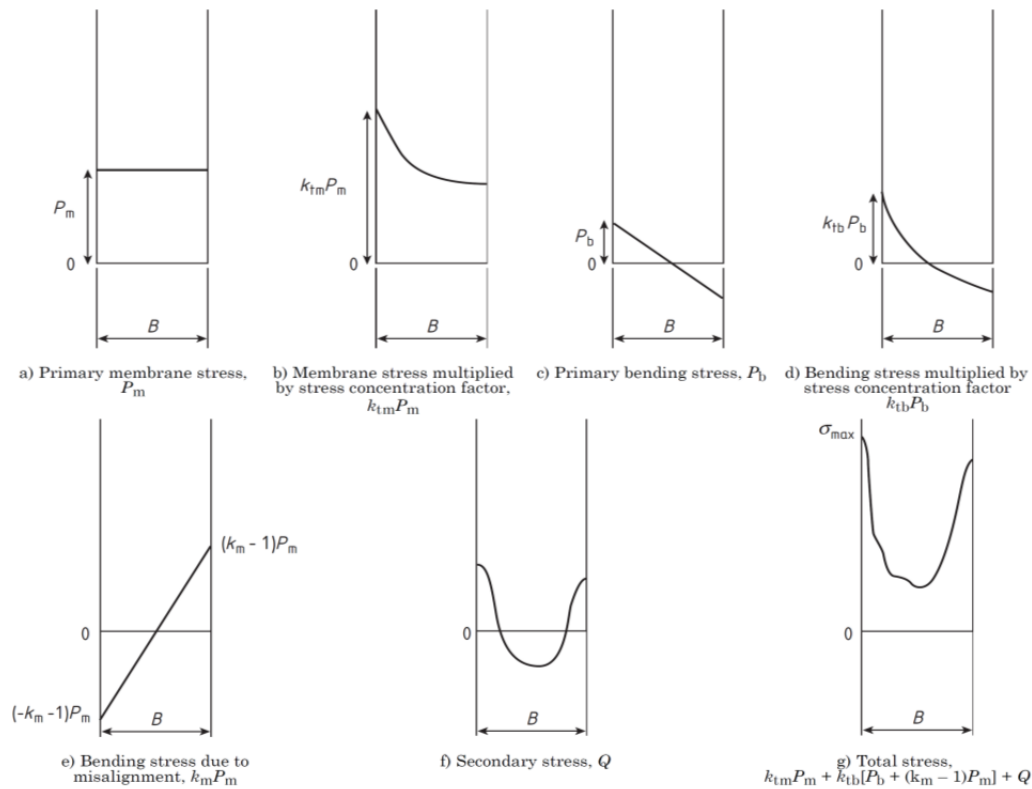
Fig.6.5. *Schematic representation of stress distribution across section [6.1]*

(1) *Primary stress (P)*

These are stresses that could (if sufficiently high) contribute to plastic collapse, as distinct from secondary stresses, which do not. They can also contribute to failure by fracture, fatigue, creep or stress corrosion cracking. They include all stresses arising from internal pressure and external loads.

The primary stresses are divided into membrane, P_m, and bending, P_b, components as follows.

a) **Membrane stress (P_m)** is the mean stress through the section thickness that is necessary to ensure the equilibrium of the component or structure.

b) **Bending stress (P_b)** is the component of stress due to imposed loading that varies linearly across the section thickness. The bending stresses are in equilibrium with the local bending moment applied to the component. For

the purpose of this document, P_b is regarded as a stress superimposed upon Pm.

(2) *Secondary stress (Q)*

The secondary stresses, Q, are self-equilibrating stresses necessary to satisfy compatibility in the structure. An alternative description is that they can be relieved by local yielding, heat treatment, etc.

The main reasons for this type of stress are: inhomogeneous cooling, constrained shrinking, solid plate phase transformations etc.

Thermal and residual stresses are usually secondary, although, in a fatigue assessment, fluctuating thermal stresses are treated as primary.

A significant feature of secondary stresses is that they do not cause plastic collapse, since they arise from strain/displacement limited phenomena. They contribute to the severity of local conditions at a crack tip. When it is necessary to include them in an assessment, they have to be included in calculations of K_I, δ_I and ΔK_I.

The thermal stresses (primary and secondary) should also be multiplied by appropriate stress concentration and misalignment factors, k_t and k_m.

The secondary stresses may be divided into membrane, Q_m, and bending, Q_b, components as for primary stresses.

(3) *Stresses at structural discontinuities*

All the stress increasing which sums to primary or secondary stresses are considered peak values of stress – stress concentrators. These stress concentrators are produced by structural discontinuities under applied primary or thermal stresses.
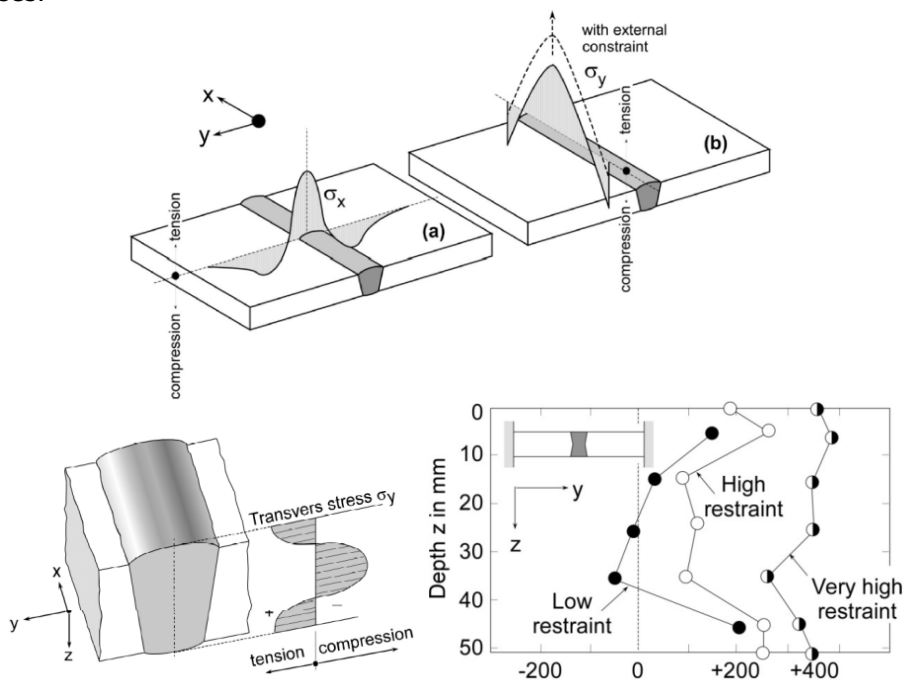
Fig. 6.6. *Welding residual stress. Transversal residual welding stress graph function of plate thickness following an external restrain [6.3]*

There are three basic categories of such discontinuities:
> — *gross discontinuities*;
> — *misalignment and deviation* from intended shape (figure 6.7)
> — *local discontinuities* such as welds, holes, notches, etc. (figure 6.6)

Their effects are quantified by calculating peak stresses at the discontinuities with SIF (stress intensity factor).
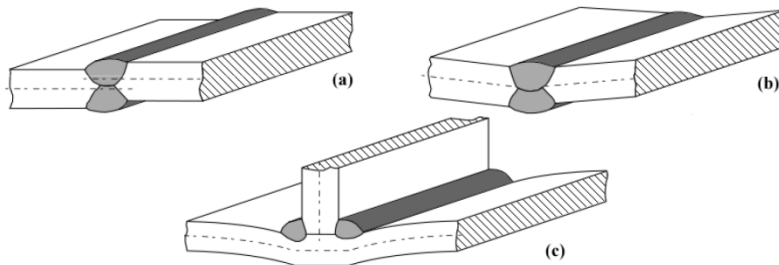
Fig.6.7. *Types of misalignment: a) Axial misalignment between flat plates, b) Angular misalignment between flat plates; c) Angular misalignment in a fillet welded joint*

6.3. Crack admissibility – assessment for fracture resistance

6.3.1. Generalities

There are three levels of fracture assessment:
a) *Level 1* is a simplified assessment method applicable when the information on materials properties is limited.
b) *Level 2* is the normal assessment route.
c) *Level 3* is appropriate for ductile materials and enables a tearing resistance analysis to be performed.

Assessment is generally made by means of a failure assessment diagram (FAD) based on the principles of fracture mechanics. The vertical axis of the FAD is a ratio of the applied conditions, in fracture mechanics terms, to the conditions required to cause fracture, measured in the same terms. The horizontal axis is the ratio of the applied load to that required to cause plastic collapse. An assessment line is plotted on the diagram. Calculations for a flaw provide either the co-ordinates of an assessment point or a locus of points.

6.3.2. Flaws types, dimensions and interaction

Planar flaws should be characterized by the height and length of their containment rectangles following the flaw type:
- ***through thickness flaws***
- ***surface flaws***
- ***embedded flaws***

These dimensions (figure 6.8. (a), (b) and (c)) are as follows: $2a$ for through thickness flaws; a and $2c$ for surface flaws; and $2a$ and $2c$ for embedded flaws.

a) Through thickness flaw
[Required dimensions: $2a$, B]

b) Embedded flaw
[Required dimensions: $2c$, p, $2a$, B]

c) Surface flaw
[Required dimensions: a, $2c$, B]

d) Flaw at toe of fillet weld
[Required dimensions: $2c$, a, B]

e) Flaw at hole
[Required dimensions: c, a, B]
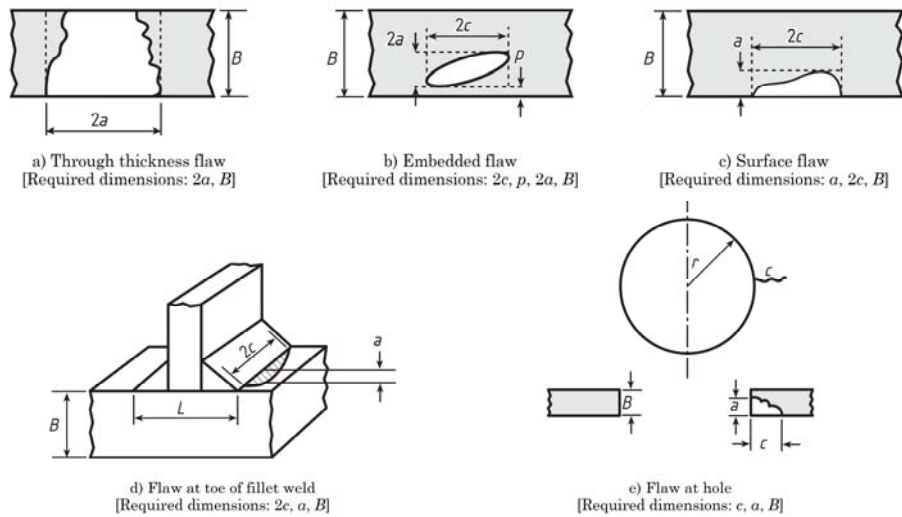
Fig.6.8. *Flaw types and dimensions [6.1]*

Multiple flaws on the same cross-section may lead to an interaction and to more severe effects than single flaws alone. Simple criteria for interaction are given in figure 6.9., together with the dimensions of the effective flaws after interaction.

If multiple flaws exist, each flaw should be checked for interaction with each of its neighbours using the original flaw dimensions in each case. It is not normally necessary to consider further interaction of effective flaws.

Schematic flaws	Criteria for interaction	Effective dimension after interaction
Coplanar surface flaws	$s \leq 2c_1$ for a_1 / c_1 or $a_2 / c_2 > 1$ $s=0$ for a_1 / c_1 and $a_2 / c_2 < 1$ $(c_1 < c_2)$	$a = max\{a_1, a_2\}$ $2c = 2c_1 + 2c_2 + s$
Coplanar embedded flaws (interaction in thickness direction)	$s \leq a_1 + a_2$	$2a = 2a_1 + 2a_2 + s$ $2c = max\{2c_1, 2c_2\}$
Coplanar embedded flaws (interaction in width direction)	$s \leq 2c_1$ for a_1 / c_1 or $a_2 / c_2 > 1$ $s=0$ for a_1 / c_1 and $a_2 / c_2 < 1$ $(c_1 < c_2)$	$2a = 2a_2$ $2c = 2c_1 + 2c_2 + s$
	$s \leq a_1 + a_2$	$a = 2a_1 + a_2 + s$ $2c = max\{2c_1, 2c_2\}$
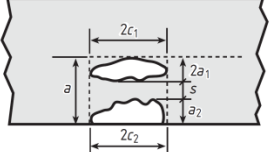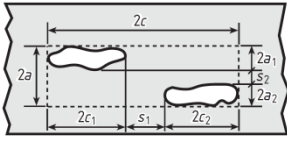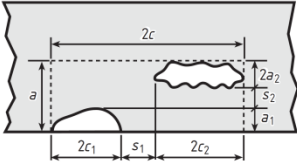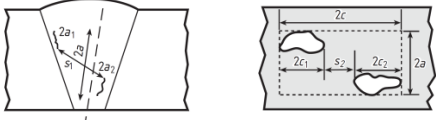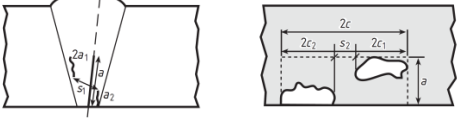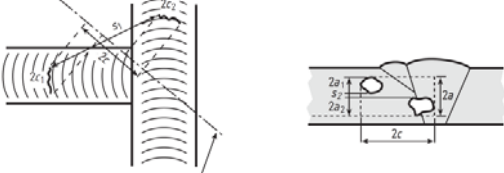
Figure	Condition	Result
Coplanar surface and embedded flaws (interaction in thickness direction)		
Coplanar embedded flaws (interaction in both thickness and width direction)	$s \leq 2c_1$ for a_1/c_1 or $a_2/c_2 > 1$ $s=0$ for a_1/c_1 and $a_2/c_2 < 1$ and $s_2 \leq a_1 + a_2$ $(c_1 < c_2)$	$2a = 2a_1 + 2a_2 + s_2$ $2c = 2c_1 + 2c_2 + s_1$
Coplanar surface and embedded flaws (interaction in both thickness and width direction)	$s \leq 2c_1$ for a_1/c_1 or $a_2/c_2 > 1$ $s=0$ for a_1/c_1 and $a_2/c_2 < 1$ and $s_2 \leq a_1 + a_2$ $(c_1 < c_2)$	$a = a_1 + 2a_2 + s_2$ $2c = 2c_1 + 2c_2 + s_1$
Principal plane normal to the maximum principal stress in weld — Projection of flaws onto the principal plane Adjacent **non – coplanar** embedded flaws	$s_1 \leq a_1 + a_2$ and $s_2 \leq 2c_1$ for a_1/c_1 or $a_2/c_2 > 1$ $s_2 = 0$ for a_1/c_1 or $a_2/c_2 < 1$ Where $c_1 < c_2$ ($2c_1$ and $2c_2$ are projected lengths)	2a is the minimum height of containment rectangle constructed on the plane normal to the maximum principal stress in the weld $2c = 2c_1 + 2c_2 + s_2$
Principal plane normal to the maximum principal stress in weld — Principal plane normal to the maximum principal stress in weld Adjacent **non – coplanar** surface and embedded flaws	$s_1 \leq a_1 + a_2$ and $s_2 \leq 2c_1$ for a_1/c_1 or $a_2/c_2 > 1$ $s_2 = 0$ for a_1/c_1 or $a_2/c_2 < 1$ Where $c_1 < c_2$ ($2c_1$ and $2c_2$ are projected lengths)	2a is the minimum height of containment rectangle constructed on the plane normal to the maximum principal stress in the weld $2c = 2c_1 + 2c_2 + s_2$
Principal plane normal to the maximum principal stress in weld — Projection of flaws onto the principal plane Adjacent **non-coplanar** embedded flaws in intersecting welds	$s_1 \leq 2c_1$ for a_1/c_1 or $a_2/c_2 > 1$ $s_1 = 0$ for a_1/c_1 or $a_2/c_2 < 1$ and $s_2 \leq a_1 + a_2$ Where $c_1 < c_2$ ($2a_1$ and $2a_2$ are projected lengths)	$2a = 2a_1 + 2a_2 + s_2$ 2c is the minimum height of containment rectangle constructed on the plane normal to the maximum principal stress in the weld

Fig.6.9. – *Flaw interaction [6.1]*

6.3.3. Simplified assessment method – Level 1 (FAD-1)

This method is applied in situations in which there are limited information regarding the material or/and the stresses.

Conservative estimates of applied stress, residual stress and fracture toughness are employed. Additional partial safety factors are not used.

The area bounded by the axes and by the assessment line is a rectangle.

The flaw is acceptable if K_r or δ_r is less than $1 / \sqrt{2}$ (i.e. 0.707) and S_r is less than 0.8.

A single FAD is used. If the assessment point lies in the area within the assessment line, *the flaw is acceptable*; if it lies on or outside the line, *the flaw is not acceptable*.
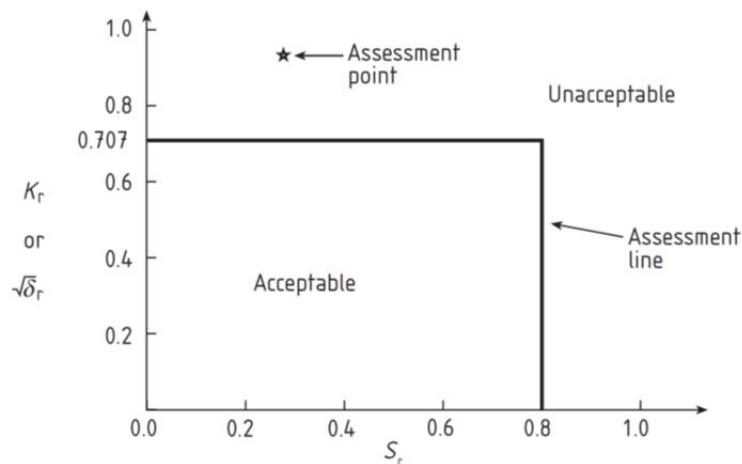
Fig. 6.10. *FAD-1 assessment [6.1]*

Where a measured fracture toughness (as given by K_{mat} or δ_{mat}) is not available, an estimate of K_{mat} determined from Charpy V-notch impact test data may be used. The BS 7910 / 2013 standard is proposing the following relation:

$$K_{mat} = \frac{12\sqrt{C_V} - 20}{(25 / B)^{1/4}} + 20 \qquad (6.4)$$

in which:
K_{mat} – represents the estimated inferior limit of fracture toughness [MPa·m$^{1/2}$]
B – the thickness of the material for which the estimation of K_{mat} is requested [mm]
C_v – Charpy energy determined at service temperature [J]

Values of K_{mat} derived from J or from "invalid" K tests may have to be adjusted to take account of the different constraint conditions in the test piece compared with those of plane strain.

The simplified level 1 assessment procedure which is needed to assess the *acceptability of a flaw for a steel shell element structures* (in base metal or in weld joint), has the following steps (presented schematic in the figure 6.11):
- Through a structural analysis it is calculated the maximum stress in the assessed element [6.16]. The used stress is the maximum tension stress

σ_{max} which is equal with sum of the stress components. There are used only the nominal membrane stresses S_{nom} (figure. 6.5) for which

$$\sigma_{max} = k_t \cdot S_{nom} + (k_m\text{-}1) \cdot S_{nom} + Q \tag{6.5}$$

where k_t – stress concentration factor and k_m – stress magnification factor due to misalignment)

- It is determined the fracture toughness throughout the K, J and δ parameters.

- It is determined the *fracture ratio (K_r or δ_r)*
  Can be applied two paths:
  - *Fracture ratio K_r* – the ratio of the stress intensity factor K_I, to the fracture toughness K_{mat} (6.6.) with the applied stress intensity factor, K_I general form presented in formula 6.7.

$$K_r = K_I / K_{mat} \tag{6.6}$$

where K_{mat} represents the fracture toughness of analysed element material determined for the in service temperature.
The stress intensity factor (SIF) – K_I is determined with the following relation:

$$K_I = (Y \cdot \sigma) \cdot (\pi \cdot a)^{1/2} \tag{6.7}$$

where $Y \cdot \sigma = M \cdot f_w \cdot M_n \cdot \sigma_{max}$ depends on flaw type (according to annex M – BS7910 / 2013), M and f_w are bulging correction and finite width correction factors respectively; σ_{max} is the maximum tensile stress and M_m is a stress intensity magnification factor.
  - *Fracture ratio δ_r* – the ratio of CTOD δ_I to the fracture toughness δ_{mat}. The square root of δ_r is calculated from the following equation:

$$\sqrt{\delta_r} = \sqrt{\delta_I/\delta_{mat}} \tag{6.8}$$

Where the CTOD δ_I is determined from K_I as follows:

$$\text{for } \sigma_{max}/\sigma_Y \leq 0,5, \quad \delta_I = K_I^2 /(\sigma_Y E) \tag{6.9}$$

$$\text{for } \sigma_{max}/\sigma_Y > 0,5, \quad \delta_I = \frac{K_I^2}{\sigma_Y E}\left(\frac{\sigma_Y}{\sigma_{max}}\right)^2\left(\frac{\sigma_{max}}{\sigma_Y} - 0.25\right) \tag{6.10}$$

- It is determined the *load ratio (S_r).*
  The load ratio, Sr, is calculated from the following equation:

$$S_r = \frac{\sigma_{ref}}{\sigma_f} \tag{6.11}$$

Where σ_{ref} is obtained from an appropriate reference stress solution given in Annex P of BS 7910/2013. The flow strength, σ_f, should be assumed to be
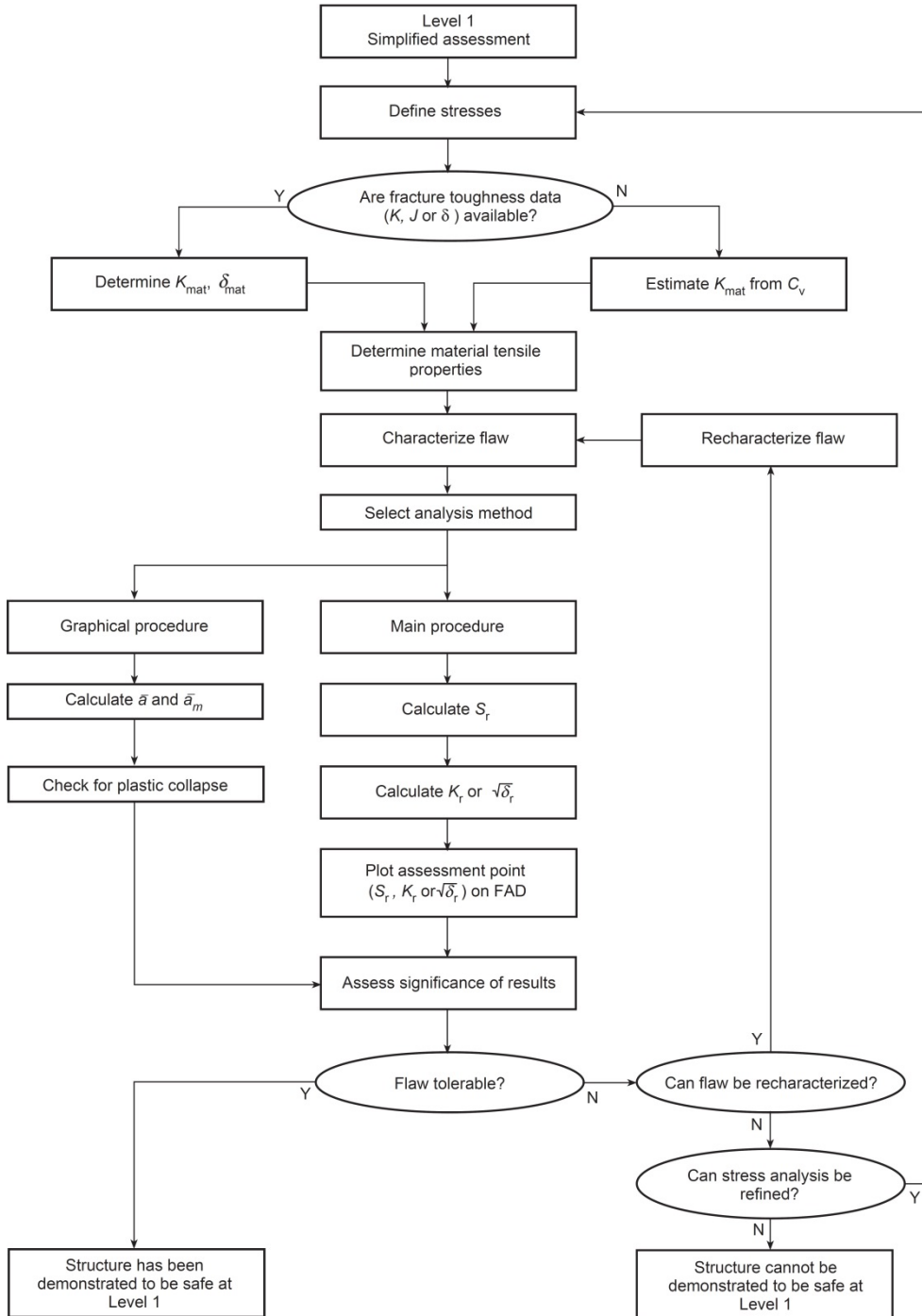
Fig.6.11. *Schematic algorithm for FAD-1 (level 1) [6.1]*

the arithmetic mean of the yield strength and the tensile strength up to a maximum of $1.2\sigma_Y$.

For study case presented in chapter 5, were done several assessments. For steel shell elements were chosen two types of flaws (figure 6.12 a and b):

- Flat plate through-thickness flaw
- Flat plate edge flaw

(a)

(b)
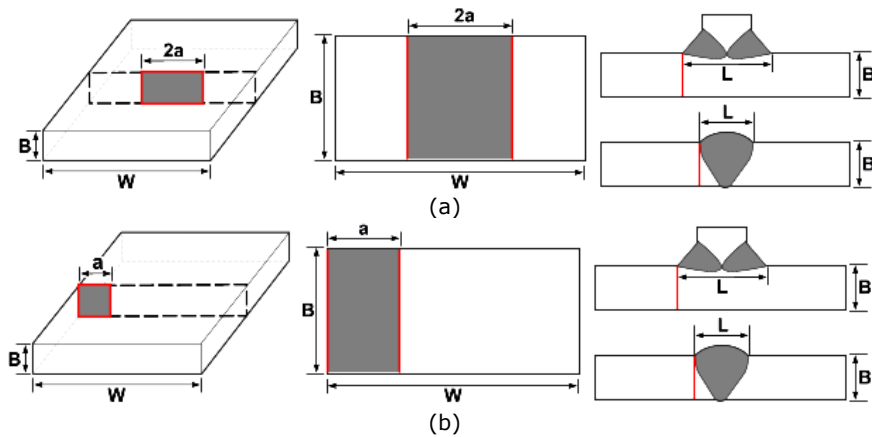
Fig. 6.12. *Idealizing of flaws for a flat plate – (a) through-thickness flaw
(b) edge flaw*

a) Case of flat plate through-thickness flaw

For the calculation of SIF, $K_I = (Y \cdot \sigma) \cdot (\pi \cdot a)^{1/2}$ where $Y \cdot \sigma = M \cdot f_w \cdot M_n \cdot \sigma_{max}$.
According with BS7910 / 2013 M.3.1:

$$M = M_m = M_b = 1 \tag{6.12}$$
$$f_w = [\sec(\pi a/W)]^{1/2} \tag{6.13}$$

In order to determine δ_r parameter – the fracture ratio, for assessment can be used a path based on CTOD values. In this case the fracture ratio has the relation (6.8).

Determining the ratio S_r based on relation $S_r = \sigma_{ref} / \sigma_f$, in which the reference stress is calculated according to BS7910 / 2013 P.3.1:

$$\sigma_{ref} = \frac{P_b + \left(P_b^2 + 9P_m^2\right)^{0.5}}{3\left[1 - \left(\dfrac{2a}{W}\right)\right]} \tag{6.14}$$

It is calculated the yielding stress σ_f according with relation (6.3) (*flow stress* – figure 6.3.), for which is needed the characteristics of the material (yielding and ultimate resistance). These can be determined following tests.

b) Case of flat plate edge flaw

According with BS7910 / 2013 M.3.5:
For $a/W < 0,6$

$$M = 1; f_w = 1 \tag{6.15}$$

$$Mm = Mb = 1{,}12 - 0{,}23(a/W) + 10{,}6(a/W)^2 - 21{,}7(a/W)^3 + 30{,}4(a/W)^4 \qquad (6.16)$$

Using CTOD path, the fracture ratio δ_r is calculated according with (6.8) relation.

Determining the ratio S_r based on relation $S_r = \sigma_{ref} / \sigma_f$, in which σ_f is calculated with the relation (6.3) and the reference stress is calculated according to BS7910 / 2013 P.3.5:

$$\sigma_{ref} = \frac{P_b + \left(P_b^2 + 9P_m^2\right)^{0.5}}{3\left[1 - \left(\dfrac{a}{W}\right)\right]} \qquad (6.17)$$

For both cases (through thickness and edge flow), the point of assessment S_r and K_r is represented on FAD. The conclusions can be made base on the position of the points (figure 6.10)

In case of assessment level 1 – FAD-1, there were done assessments on different flaws type and flaws positon for the in case – billboard tower presented at Chapter 4 – segment joint (figure 6.13). The toughness value of 81,8 MPa·m$^{1/2}$ was determined on the specimens (see Chapter 5) and was used in the assessment.

A primary stress of 251 MPa was determined following the structural analysis (see Chapter 4).
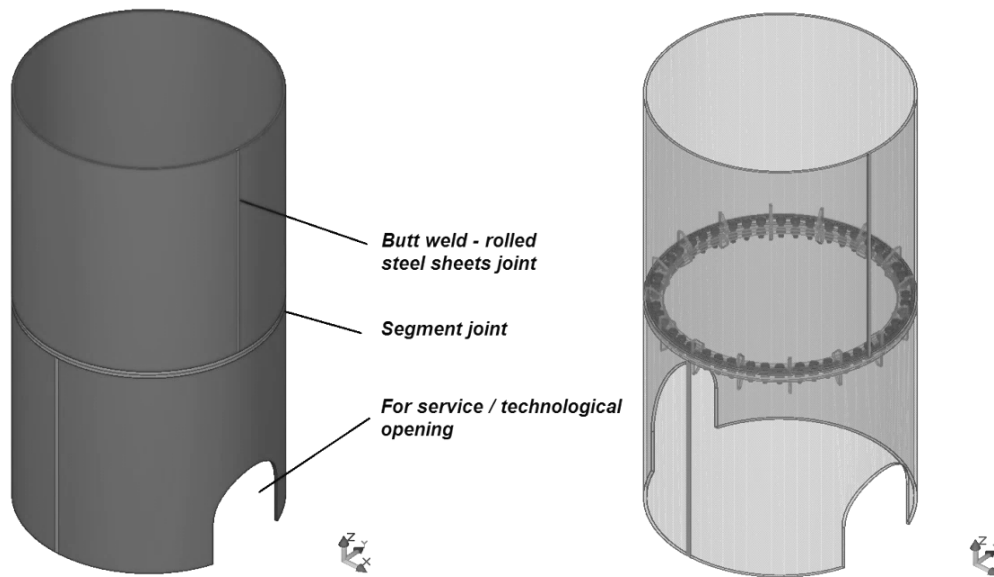
Fig. 6.13 *Shell steel element segment joint view*

Ten cases were assessed. These are presented in table 6.1. and figure 6.14.

Table 6.1 – *Flaw cases description*

Case no.	Name	Flaw type	Description of the flaw
Case 1	(TTF-1)	through thickness flaw	Crack in the tube wall in the proximity of the welded joint
Case 2	(TTF-2)	through thickness flaw	Crack in the welding longitudinal direction
Case 3	(TTF-3)	through thickness flaw	Crack in the welding transversal direction
Case 4	(TTF-4)	through thickness flaw	Crack in the flange of the segment joint in proximity of the welding longitudinal direction
Case 5	(TTF-5)	through thickness flaw	Crack in the flange of the segment joint in proximity of the welding transversal direction
Case 6	(EF-1)	edge flaw	Crack in the tube wall in the proximity of the welded joint
Case 7	(EF-2)	edge flaw	Crack in the welding longitudinal direction
Case 8	(EF-3)	edge flaw	Crack in the welding transversal direction
Case 9	(EF-4)	edge flaw	Crack in the flange of the segment joint in proximity of the welding longitudinal direction
Case 10	(EF-5)	edge flaw	Crack in the flange of the segment joint in proximity of the welding transversal direction
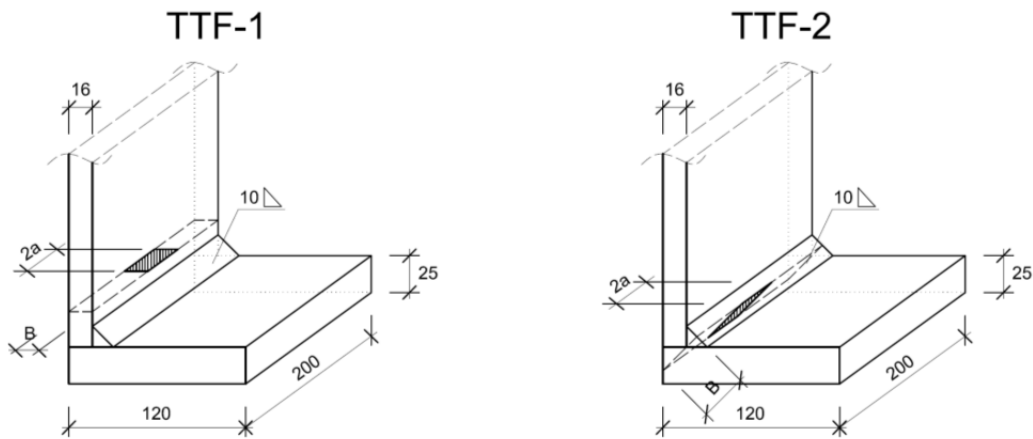
Fig. 6.14. *FAD – 1 assessed flaw types (continued on the next page)*
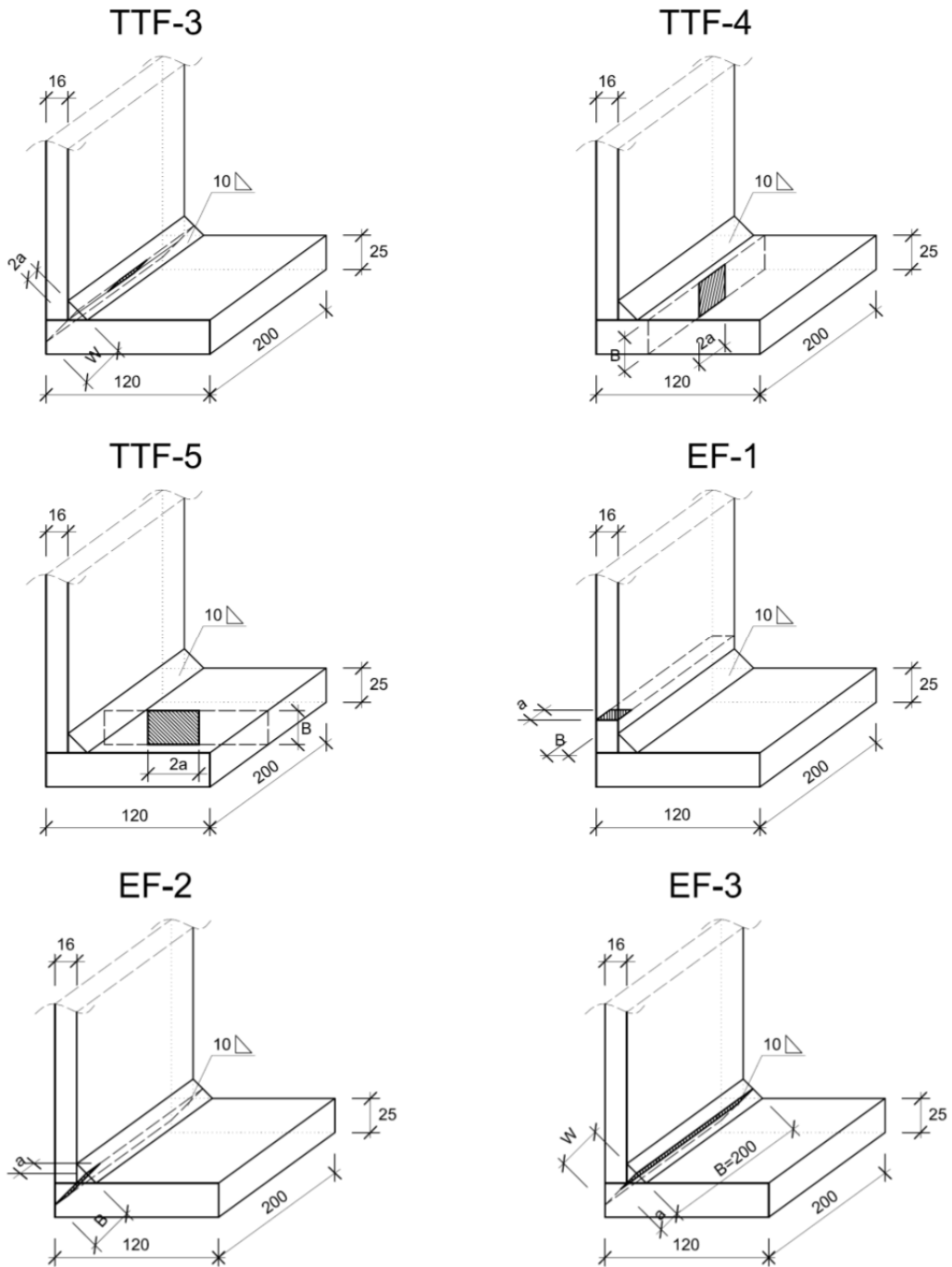
Fig. 6.14. *FAD – 1 assessed flaw types (continued on the next page)*
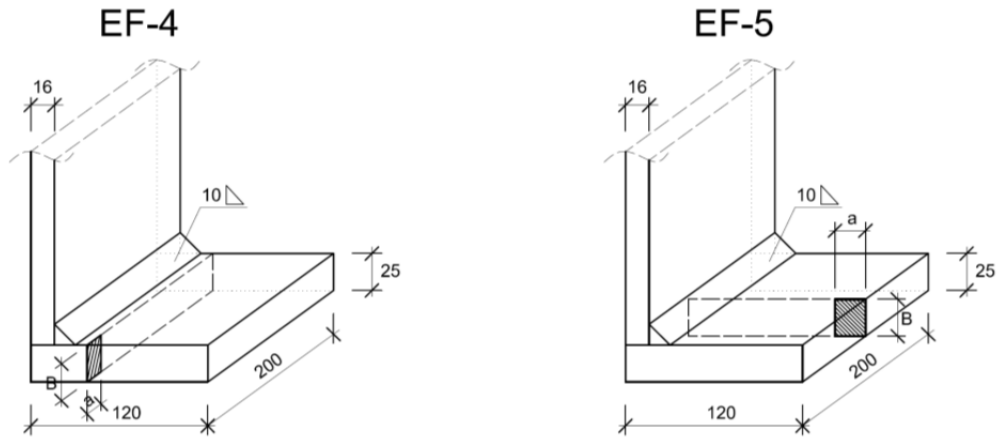
Fig. 6.14. *FAD – 1 assessed flaw types*

Following calculations according to the above presented procedure, the results are represented in tables 6.2, 6.3 and graphically in figure 6.15.

Table 6.2 - *FAD 1 – TTF type flaws - results*

Through thickness flaw									
Case	B	W	2a	P_b	P_m	σ_{ref}	σ_f	S_r	K_r
	mm	mm	mm	MPa	MPa	MPa	MPa		
TTF-1	16	200	30	0	251	295.29	432.50	0.68	0.6755
TTF-2	32.63	200	30	0	251	295.29	432.50	0.68	0.6755
TTF-3	200	32.63	10	0	251	361.91	432.50	0.84	0.4085
TTF-4	25	200	30	0	251	295.29	432.50	0.68	0.6755
TTF-5	25	120	30	0	251	334.67	432.50	0.77	0.6931

Table 6.3 - *FAD 1 – EF type flaws - results*

Edge flaw									
Case	B	W	a	P_b	P_m	σ_{ref}	σ_f	S_r	K_r
	mm	mm	mm	MPa	MPa	MPa	MPa		
EF-1	16	200	15	0	251	271.35	432.50	0.63	0.7688
EF-2	32.63	200	15	0	251	271.35	432.50	0.63	0.7688
EF-3	200	32.63	15	0	251	464.56	432.50	1.07	1.6678
EF-4	25	200	15	0	251	271.35	432.50	0.63	0.7688
EF-5	25	120	15	0	251	286.86	432.50	0.66	0.8139
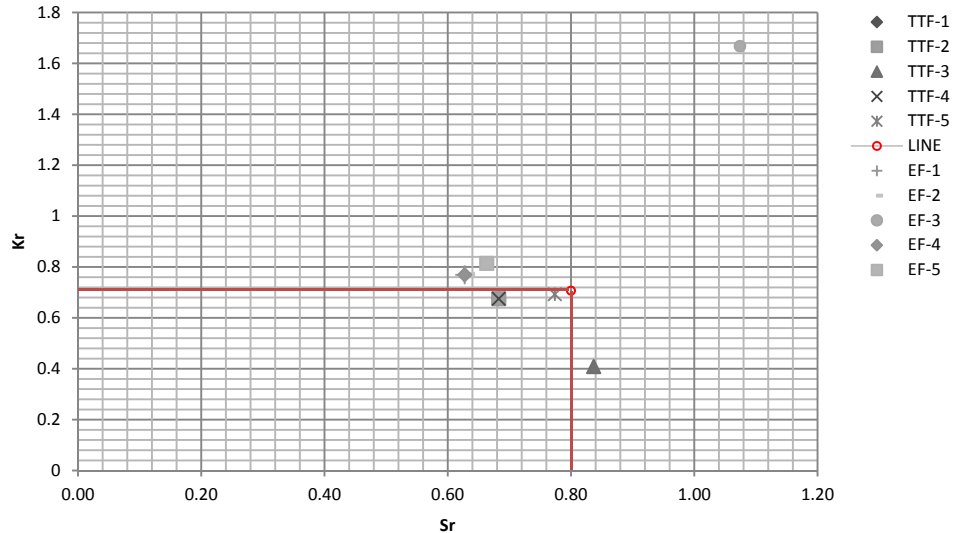
Fig. 6.15. *FAD – 1 plotted results*

From the analysis of the assessment, can be concluded the followings:

- In the assessed cases of thickness through flaw, for the given dimensions (geometry of the element and the crack), the structure is on the safe side according to the failure assessment diagrams level 1 – FAD-1, with one exception TTF-3 case. This is caused by the high value of S_r – the element (joint) is sensible in the area of the weld. High value of the main stress and the given crack size, makes the joint to fracture;
- It can be noticed an approach to the assessment line for TTF5 case – crack in the flange of the segment of the joint – K_r value is close to 0.707;
- The edge flaw type case are presenting different conclusions – the assessing FAD-1 reveals an over limit of all cases. The K_r fracture ratio is higher than 0.707 and in case EF-3 the S_r is also over limit;
- The flange of the segment joint is a critical part of the structure. This subassembly is subjected to high local stresses;
- The weld itself is not checking for edge flaws of 15mm which can be a common situation in the assessment of the joints;
- The engineering critical assessment (ECA) can conclude that there is a high risk of fracture for the given segment joint in the area of the flange;

6.3.4. Determining the critical dimension of the flaw – FAD 1

Another important problem can be solved following an analysis based on failure assessment diagrams (in this case FAD – 1 type), is the determination of the *critical dimension of the flaw*.

In case of shell steel structures, this value represents the critical dimension at which the element can fail (through fracture). This value is then *used in a fatigue assessment for determining the number of cycles needed for an initial crack (flaw)*

length, to propagate under the given loads and eventually to produce failure of the element.

Determining the critical value of the flaw is done based on parameters δ_{mat} and K_{mat} and using the fracture ratio $K_r = K_I / K_{mat}$, through an iterative procedure.

Thus, based on the limit of the fracture ratio:

$$K_r = 0{,}707 \rightarrow K_I^{Limit} \tag{6.18}$$

but, $K_I = (Y \cdot \sigma) \cdot \sqrt{\pi \cdot a}$, thus can be determined throughout iterations:

$$K_I^{a_c} = (Y \cdot \sigma_{max}) \cdot \sqrt{\pi \cdot a_i} \tag{6.19}$$

where Y – correction factor which depends on the type of the flaw

a_i – length of the flaw: $a_i = a_{crit}$ when $K_I^{a_c} = K_I^{Limit}$

Determining the admissible maximum length of the flaw can be done according with BS 7910 /2013 – annex N. Thus when toughness estimates are available in terms of K_{mat}, the maximal allowable flow dimension:

$$\bar{a}_m = \frac{1}{2\pi}\left(\frac{K_{mat}}{\sigma_{max}}\right)^2 \tag{6.20}$$

When toughness estimates are available in terms of δ_{mat}, $\bar{a}_m$ can be calculated with relation:

$$\bar{a}_m = \frac{\delta_{mat}E}{2\pi\left(\dfrac{\sigma_{max}}{\sigma_Y} - 0{.}25\right)\sigma_Y} \tag{6.21}$$

6.3.5. Level 2 assessment method – FAD-2

The level 2 assessment is the normal evaluation path for general application. The method is presenting an assessment line given by an equation of a curve and a cut-off line. If the assessment point is in the interior of the surface limited by the assessment line, the flaw is acceptable and if the assessment point is at the outside area, the flaw is considered unacceptable.

The equations which are describing the assessment line are:

$$\sqrt{\delta_r} \ or \ K_r = \left(1 - 0{,}14L_r^2\right)\left[0{,}30 + 0{,}70 \, exp(-0{.}65L_r^6)\right] \ for \ L_r \le L_{rmax} \tag{6.22}$$

$$\sqrt{\delta_r} \ or \ K_r = 0 \ for \ L_r > L_{rmax} \tag{6.23}$$

The cut-of line is fixed in point where $L_r = L_{rmax}$ where:

$$L_{r\,max} = (\sigma_Y + \sigma_u)/(2\sigma_Y) \tag{6.24}$$

in which:

σ_Y – the yielding resistance of the material

σ_u – the ultimate resistance of the material

The assessment procedure is presented in the figure 6.16. For the assessment on level 2 FAD is necessary to pass through the following phases (more or less similar with FAD-1):

- As presented at FAD-1, the stresses must be known – following a structural analysis, these can be determined. The assessments are considering the real distribution of the stresses in the proximity of the flaws – P_m, P_b, Q_m and Q_b.

- The fracture ratio K_r must be determined

$$K_r = K_I / K_{mat} \tag{6.25}$$

in which K_{mat} represents the fracture toughness of the assessed material, determined at the service temperature.
It will be used the minimum value of the fracture toughness.
The stress intensity factor (SIF) – K_I is determined with the following relation:

$$K_I = (Y{\cdot}\sigma){\cdot}(\pi{\cdot}a)^{1/2} \tag{6.26}$$

where for the level 2 the factor

$$Y{\cdot}\sigma = (Y{\cdot}\sigma)_P + (Y{\cdot}\sigma)_S \tag{6.27}$$

in which:
   $(Y{\cdot}\sigma)_P$ – contribution of the main stresses
   $(Y{\cdot}\sigma)_S$ – contribution of the secondary stresses

$$(Y{\cdot}\sigma)_P = M{\cdot}f_w{\cdot}\ \{k_{tm}{\cdot}M_{km}{\cdot}M_m{\cdot}P_m + k_{tb}{\cdot}M_{kb}{\cdot}M_b{\cdot}\ [P_b+(k_m-1)P_m]\} \tag{6.28}$$

$$(Y{\cdot}\sigma)_S = M_m{\cdot}Q_m + M_b{\cdot}Q_b \tag{6.29}$$

The correction factor Y is determined according to the level 1 relations function of the defect type [6.1] – relations (6.12) to (6.17).
As presented at level 1 method, can be chosen the fracture ratio $\sqrt{\delta_r}$.

- Determining the ratio of stress L_r according with:

$$L_r = \sigma_{ref} / \sigma_Y \tag{6.30}$$

in which σ_{ref} is obtain according with a relation specific with the flaw type (e.g. formula (6.14) and (6.17)) and σ_Y is the yielding strength of the material.

- The point/points of assessment are represented graphically in (K_r, L_r) coordinates on the FAD level 2.

- The evaluation of the position of the point is done according with the specifications done.
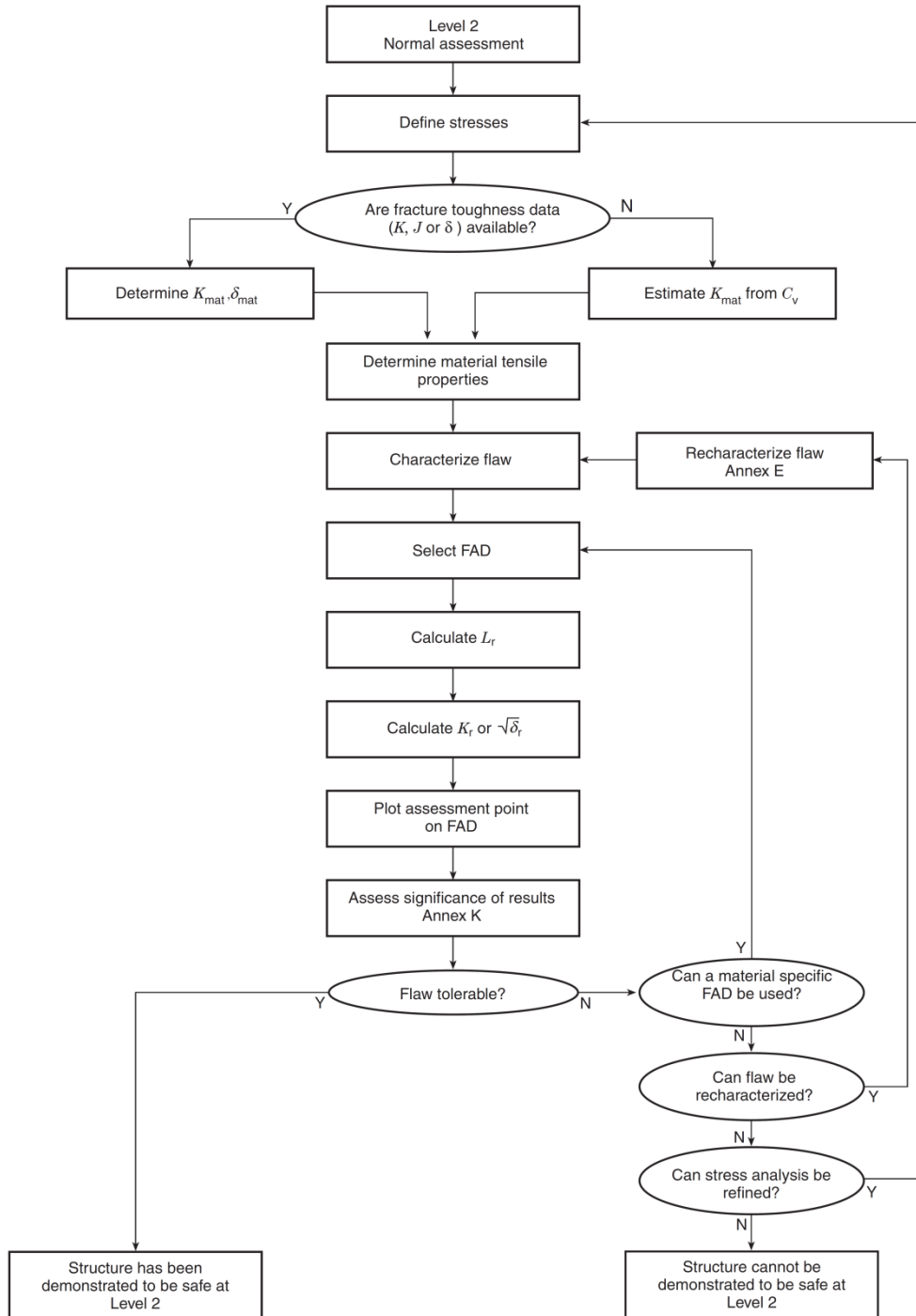
Fig. 6.16. *Schematic algorithm for FAD-2 (level 2) [6.1]*

In case of assessment level 2 – FAD-2, there were done assessments on different flaws type and flaws positon for the in case – billboard tower presented at chapter 4 and 5. The values of the input data are:

- σ_Y (yield strength)= 355 MPa; σ_T (ultimate strength)= 510 MPa; specific for S355J2 steel type;
- K_{mat} = 81,8 MPa·m$^{1/2}$ was determined on the specimens (see chapter 5) and was used in the assessment.
- P_m = 251 MPa - Primary stress. Was determined following the structural analysis (see chapter 4).
- k_{tm} = 1; k_{tb} = 1 (stress concentrators factors)
- Q_{tm} = 0 (thermal membrane stress) and Q_{tb} = 0 (thermal bending stress)
- Q_m = 0 (residual membrane stress) and Q_b = 0 (residual bending stress)

Following cases were assessed (table 6.4):

Table 6.4 - *FAD 2 – Flaws geometry and type - Idealizing of flaws*

	Geometry	Flaw type	Flaw description
1	FP – Flat plate	TTF – Through Thickness Flaw	
2		SF – Surface Flaw	
3		LSF – Long Surface Flaw	
4		BF – Embedded / Buried Flaw	

5		**EF** – Edge Flaw	
6		**TTF** – Through Thickness Flaw	
7		**ISF** – Internal Surface Flaw	
8	**CSAF** – Curved Shell Axial Flaw	**LISF** – Long Internal Surface Flaw	
9		**ESF** – External Surface Flaw	
10		**LESF** – Long External Surface Flaw	
11		**BF** – Embedded / Buried Flaw	

12	**CAF** – Cylinder Axial Flaw	**TTF** – Through Thickness Flaw	
13		**BF** – Embedded / Buried Flaw	
14	**CSCF** – Curved Shell Circumferential Flaw	**TTF** – Through Thickness Flaw	
15		**ISF** – Internal Surface Flaw	
16		**FCISF** – Fully Circumferential Internal Surface Flaw	
17		**ESF** – External Surface Flaw	
18		**FCESF** – Fully Circumferential External Surface Flaw	

19		**BF** – Embedded / Buried Flaw	
20	**CCF** – Cylinder Circumferential flaw	**TTF** – Through Thickness Flaw	
21		**BF** – Embedded / Buried Flaw	
22	**CWJ** – Cruciform Welded Joints	**TTF** – Through Thickness Flaw	
23		**WT** – Weld Toe, Load carrying attachment	

Considering the position of the flaw regarding the stress direction and position in the assembly of the steel shell element, following 6.13, resulted 43 types of assessed flaws as presented in table 6.5. (e.g. FP-LSF-3 represents the position – flat plate(FP), flaw type – long surface flaw (LSF), with the position in the welding joint (3) (figure 6.14). The flaws were considered as present in the steel shell elements. In a conservative manner, the W dimension at some part of the flaws types was considered 200mm, taken into account that the area of tension from the segment joint of the steel pillar, is about 200mm. Increasing the W dimension will decrease the safety of the structure in the area of the joint.

With the presented procedure, further assessment can be made on the joint and steel shell element taken into account different dimensions. In the current assessment there are presented all types of flaws that can be meet in the structure (figure 6.17).
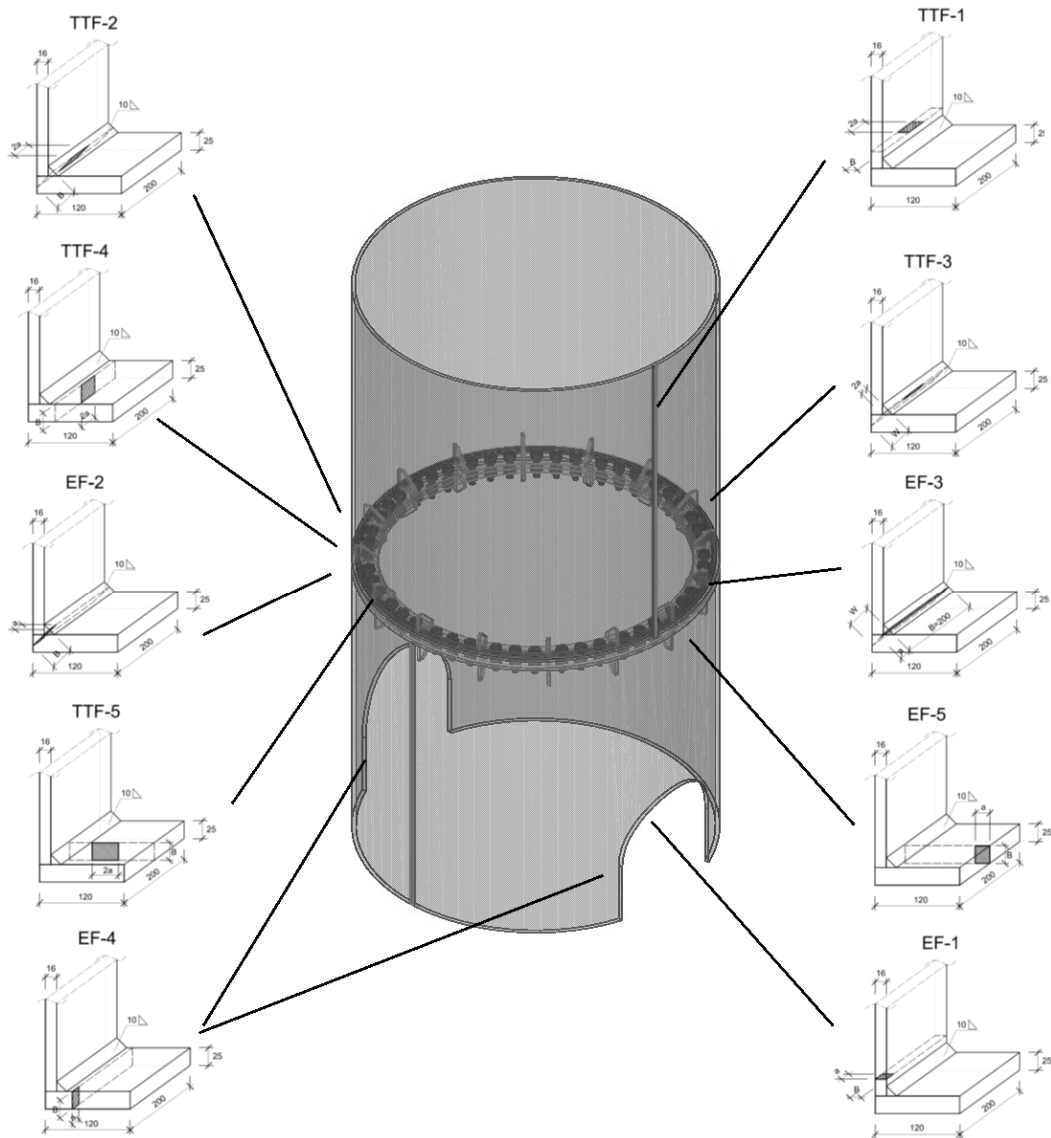
Fig.6.17. – *Typical flaws in a steel shell element and steel shell element joint*

Table 6.5 - *FAD 2 – in case - flaws assed: geometry and results (with corresponding figures and flaw name – figure 6.17 and table 6.4)*

Fig.	Case	B	W	2a	a	2c	p	r_0	h	t_w	L_r	K_r
no.		mm	mm	mm	mm	mm	mm	mm	mm	mm		
6.18	FP-TTF-1	16	200	30							0.8318	0.6755
	FP-TTF-2	32.63	200	30							0.8318	0.6755
	FP-TTF-3	200	32.63	10							1.0195	0.4085
	FP-TTF-4	25	200	30							0.8318	0.6755
	FP-TTF-5	25	120	30							0.9427	0.6930
6.19	FP-SF-1	16	200		5	30					0.8330	0.4183
	FP-SF-2	32.63	200		5	30					0.7429	0.3899
	FP-SF-3	200	32.63		5	10					0.7125	0.2808
	FP-SF-4	25	200		5	30					0.7644	0.3965
	FP-SF-5	25	120		5	30					0.7644	0.3984
6.20	FP-LSF-1	16	200		2						1.0284	0.6580
	FP-LSF-2	32.63	200		5						0.8350	0.4893
	FP-LSF-3	200	32.63		5						0.9427	0.5787
	FP-LSF-4	25	200		5						0.8838	0.5280
	FP-LSF-5	25	120		5						0.8838	0.5280
6.21	FP-BF-1	16	200	5		30	3				1.1888	0.4075
	FP-BF-2	32.63	200	5		30	3				0.8504	0.4075
	FP-BF-3	200	32.63	5		10	3				0.7290	0.2679
	FP-BF-4	25	200	5		30	3				0.9379	0.4075
	FP-BF-5	25	120	5		30	3				0.9379	0.4140
6.22	FP-EF-1	16	200		15						0.7644	0.7688
	FP-EF-2	32.63	200		15						0.7644	0.7688
	FP-EF-3	200	32.63		15						1.3086	1.6678
	FP-EF-4	25	200		15						0.7644	0.7688
	FP-EF-5	25	120		15						0.8080	0.8139
6.23	CSAF-TTF-1	16	200	30				840			0.8600	0.6846
	CSAF-ISF-1	16	200		10	30		840			0.8674	0.5225
	CSAF-LISF-1	16	200		3			840			0.9749	0.6580
	CSAF-ESF-1	16	200		10	30		840			0.8670	0.5225
	CSAF-LESF-1	16	200		3			840			1.2341	0.6580
	CSAF-BF-1	16	200	5		30	3				1.1888	0.4075
6.24	CAF-TTF-1	16	200	30				840			0.8600	0.7334
	CAF-BF-1	16	200	5		30	3				1.1888	0.4075
6.25	CSCF-TTF-1	16	200	30				840			0.7153	0.6755
	CSCF-ISF-1	16	200		10	30		840			0.7233	0.5112
	CSCF-FCISF-1	16	200		3			840			1.0284	0.6580
	CSCF-ESF-1	16	200		10	30		840			0.7230	0.5112
	CSCF-FCESF-1	16	200		3			840			1.0284	0.6580
	CSCF-BF-1	16	200	5		30	3				1.1888	0.4075
6.26	CCF-TTF-1	16	200	30				840			0.7153	0.6959
	CCF-BF-1	16	200	5		30	3				1.1888	0.4075
6.27	CWJ-TTF-1	16	44.28	5	5	30			14.14		0.9133	0.2425
	CWJ-WT-1	16	44.28	10	3	30			14.14	10	0.8969	0.9914

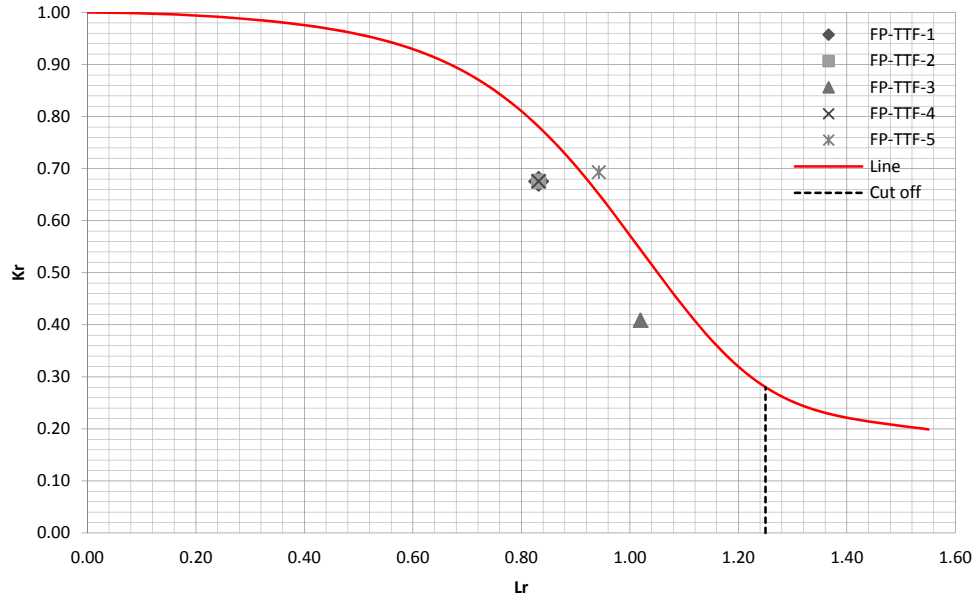Fig. 6.18. *FP-TTF – Group of flaws - assessment*

Fig. 6.19. *FP-SF – Group of flaws - assessment*

Fig. 6.20. *FP-LSF – Group of flaws - assessment*

Fig. 6.21. *FP-BF – Group of flaws - assessment*

Fig. 6.22. *FP-EF – Group of flaws - assessment*

Fig. 6.23. *CSAF – Group of flaws - assessment*
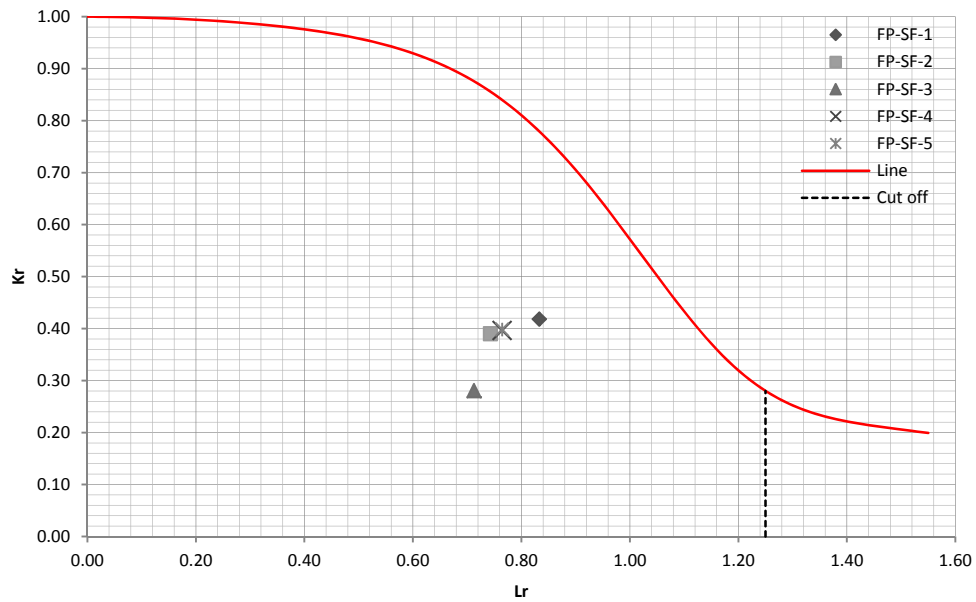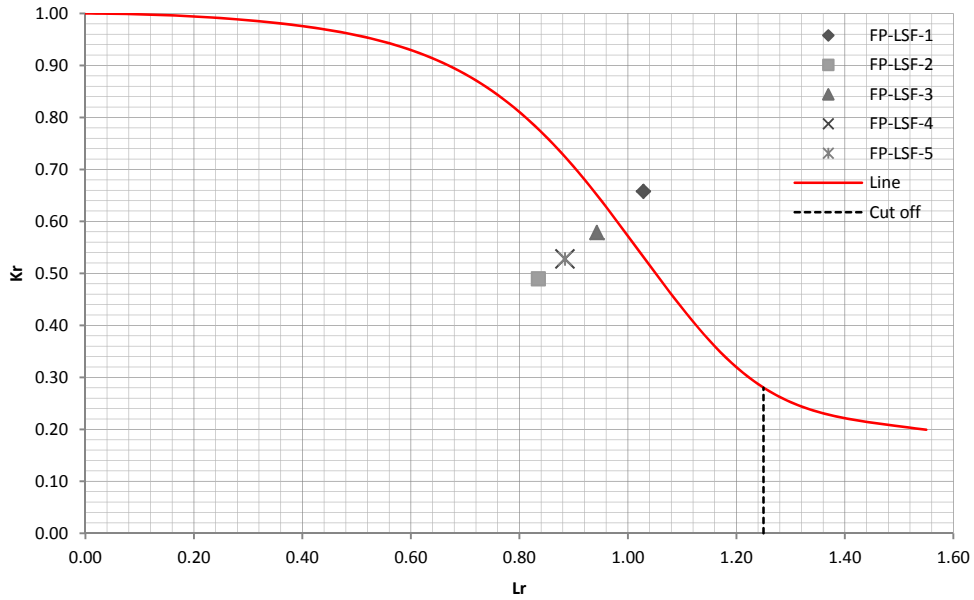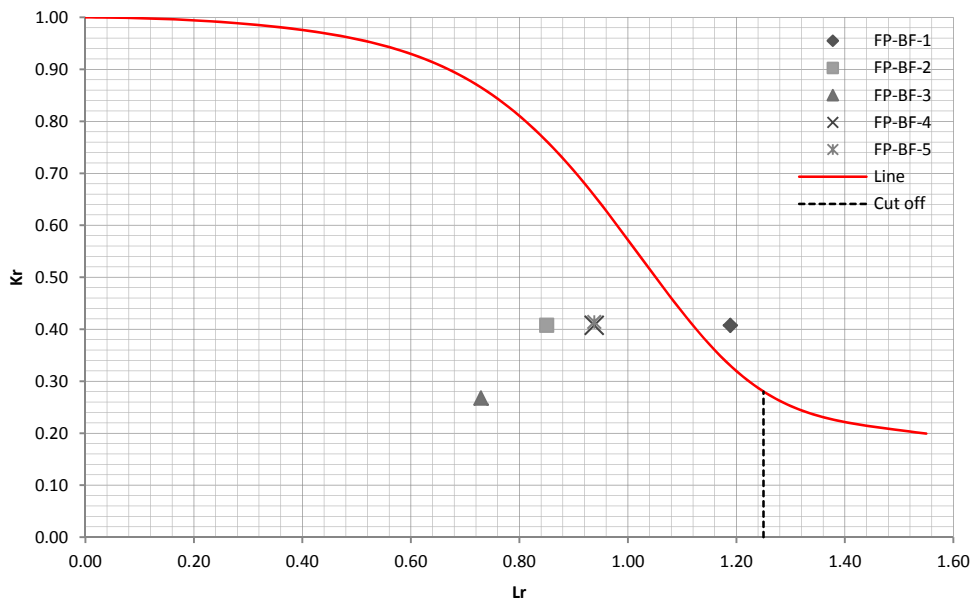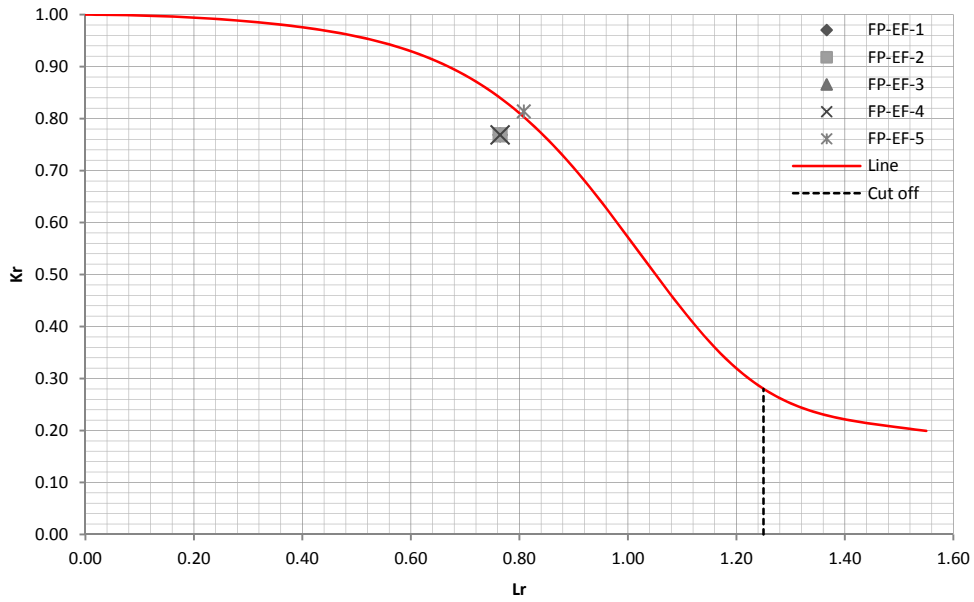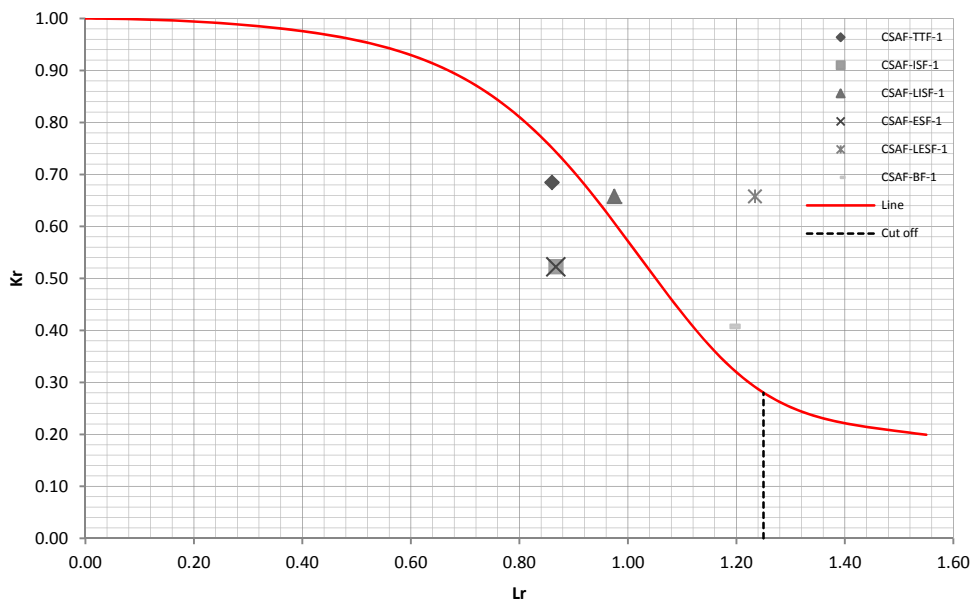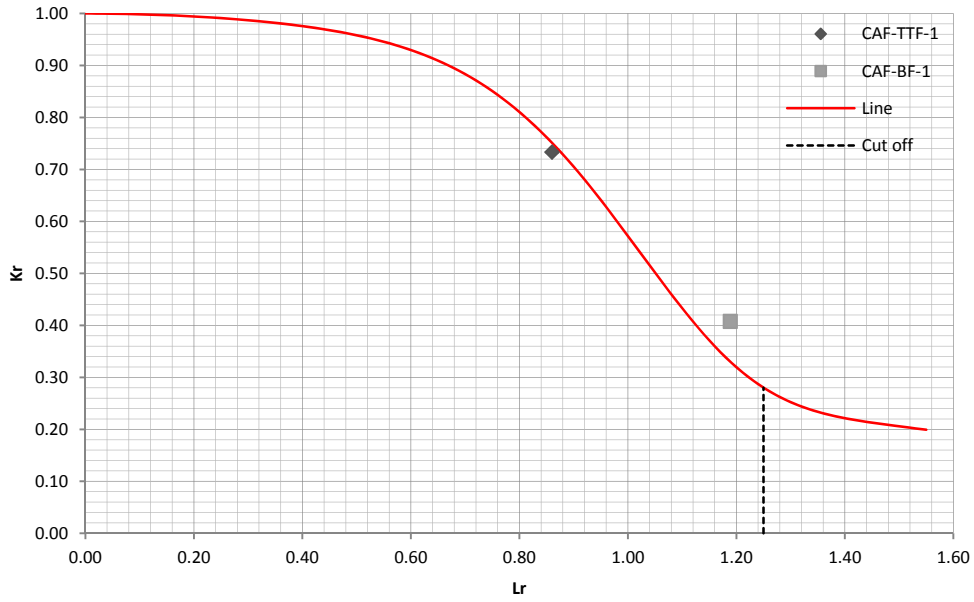
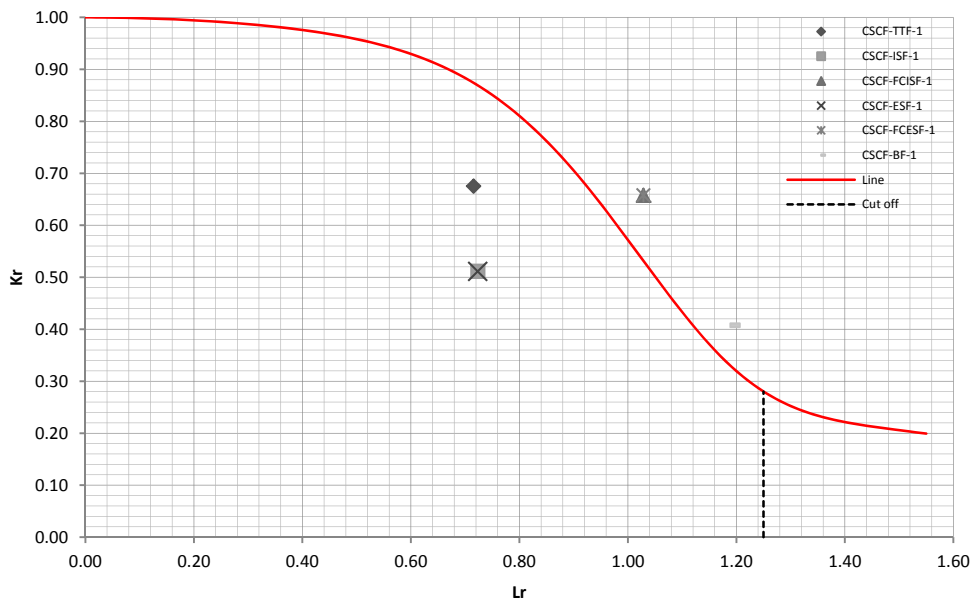Fig. 6.24. *CAF – Group of flaws - assessment*

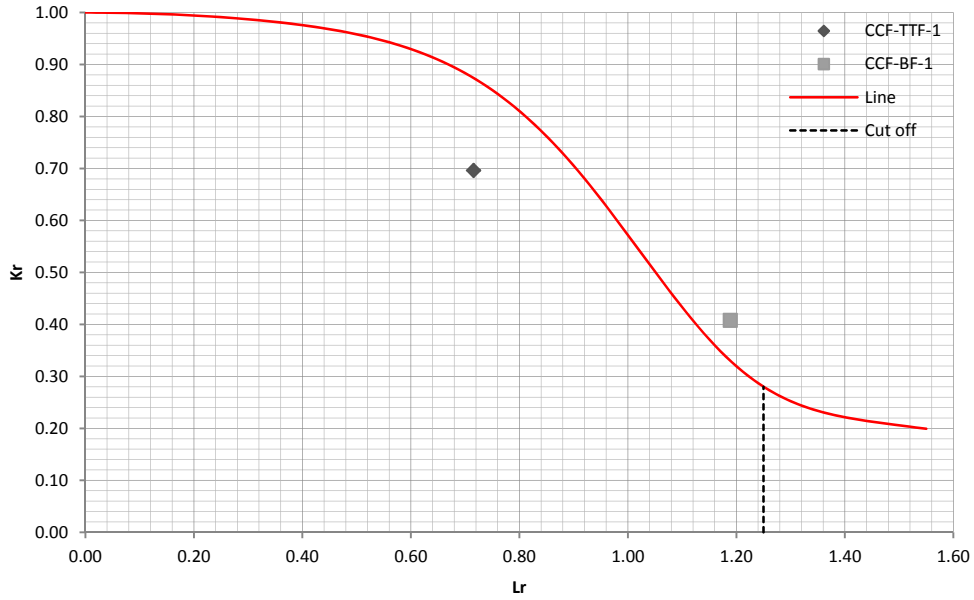Fig. 6.25. *CSCF – Group of flaws - assessment*
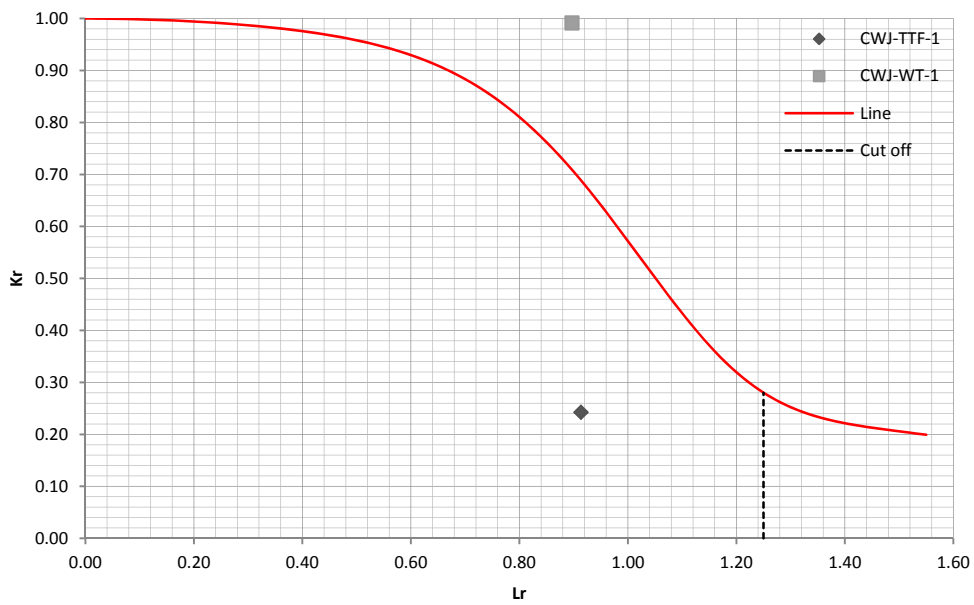
Fig. 6.26. *CCF – Group of flaws - assessment*

Fig. 6.27. *CWJ – Group of flaws - assessment*

6.3.6. Critical value of flaw dimension analyses for fracture assessment

Determining the critical value of the flaws is important because it serves to a limit value for fatigue further analysis based on fracture mechanics principles, needed for determining the number of cycles for a crack to extend from an initial dimension to a critical dimension which means the failure of the element.

Considering the importance of the matter, a detail analysis was done for the presented flaws (chapter 6.3.5). The procedure uses FAD-2 assessment data, and it gives the critical dimension of the crack.

The input data ae the same as for FAD-2 assessment:

- σ_Y (yield strength)= 355 MPa; σ_T (ultimate strength)= 510 MPa; specific for S355J2 steel type;
- K_{mat} = 81,8 MPa·m$^{1/2}$ was determined on the specimens (see chapter 5) and was used in the assessment.
- P_m = 251 MPa - Primary stress. Was determined following the structural analysis (see chapter 4).
- k_{tm} = 1; k_{tb} = 1 (stress concentrators factors)
- Q_{tm} = 0 (thermal membrane stress) and Q_{tb} = 0 (thermal bending stress)
- Q_m = 0 (residual membrane stress) and Q_b = 0 (residual bending stress)

The results are presented in table 6.6.

Table 6.6 - *FAD 2 – critical dimension of the flaw (with corresponding figures and flaw name – figure 6.17 and table 6.4)*

Case no.	Case name	B	W	$2a_0$	a_0	$2c_0$	p_0	r_0	h_0	t_w	Flaw Height Critic	Flaw Length Critic
		mm	mm	mm	mm	mm	mm	mm	mm	mm	mm	mm
1	FP-TTF-1	16	200	30							N/A	36.249
2	FP-TTF-2	32.63	200	30							N/A	36.249
3	FP-TTF-3	200	32.63	10							N/A	11.330
4	FP-TTF-4	25	200	30							N/A	36.243
5	FP-TTF-5	25	120	30							N/A	28.408
6	FP-SF-1	16	200		5	30					5.690	34.440
7	FP-SF-2	32.63	200		5	30					18.261	49.395
8	FP-SF-3	200	32.63		5	10					10.734	23.800
9	FP-SF-4	25	200		5	30					14.755	42.870
10	FP-SF-5	25	120		5	30					14.505	42.420
11	FP-LSF-1	16	200		2						4.536	N/A
12	FP-LSF-2	32.63	200		5						7.470	N/A
13	FP-LSF-3	200	32.63		5						5.360	N/A
14	FP-LSF-4	25	200		5						6.269	N/A
15	FP-LSF-5	25	120		5						6.280	N/A
16	FP-BF-1	16	200	5		30	3				7.590	30.160
17	FP-BF-2	32.63	200	5		30	3				10.984	30.360
18	FP-BF-3	200	32.63	5		10	3				OK	OK
19	FP-BF-4	25	200	5		30	3				10.190	30.365
20	FP-BF-5	25	120	5		30	3				10.106	30.360

21	**FP-EF-1**	16	200		15						N/A	17.230
22	**FP-EF-2**	32.63	200		15						N/A	17.230
23	**FP-EF-3**	200	32.63		5						N/A	7.507
24	**FP-EF-4**	25	200		15						N/A	17.230
25	**FP-EF-5**	25	120		15						N/A	14.750
26	**CSAF-TTF-1**	16	200	30				840			35.012	N/A
27	**CSAF-ISF-1**	16	200		10	30		840			12.682	36.389
28	**CSAF-LISF-1**	16	200		3			840			4.748	N/A
29	**CSAF-ESF-1**	16	200		10	30		840			12.720	36.450
30	**CSAF-LESF-1**	16	200		3			840			3.478	N/A
31	**CSAF-BF-1**	16	200	5		30	3				7.607	30.163
32	**CAF-TTF-1**	16	200	30				840			N/A	31.187
33	**CAF-BF-1**	16	200	5		30	3				7.569	30.160
34	**CSCF-TTF-1**	16	200	30				840			N/A	47.706
35	**CSCF-ISF-1**	16	200		10	30		840			14.801	42.560
36	**CSCF-FCISF-1**	16	200		3			840			4.540	N/A
37	**CSCF-ESF-1**	16	200		10	30		840			14.808	42.560
38	**CSCF-FCESF-1**	16	200		3			840			4.540	N/A
39	**CSCF-BF-1**	16	200	5		30	3				7.569	30.570
40	**CCF-TTF-1**	16	200	30				840			N/A	44.050
41	**CCF-BF-1**	16	200	5		30	3				7.611	30.160
42	**CWJ-TTF-1**	16	44.28	10	5	30			14.14		N/A	OK
43	**CWJ-WT-1**	16	44.28	10	3	30			14.14	10	3.882	33.133

The FAD-2 diagrams and (L_r, K_r) flaw length (and height) from a_0 (c_0) to a_{crit} (c_{crit}) curves are presented in Annex 3.

Conclusions and discussions on the results

There were assessed several types of flaws that can be meet in a steel shell structure – from through thickness flaw or surface flaw to embedded/buried flaw. Different types of locations were taken into account thus resulting groups of flaws which were assessed and compared – from in the plate flaw (e.g. flange plate joint near the welded joint), to the curved shell circumferential flaw (e.g. in the shell element).

The input data took into account the results from the FEM analysis of structure (Chapter 4) and the experimental results for material properties (Chapter 5), all needed in the assessment procedures.

The comparison of the flaws assessment with fracture mechanics procedures, revealed several problems:
- Sensibility of the joints to the through thickness flaw in the endplate of the segment joint (FP-TTF-5). In case of a only 30mm flaw, the element fails;
- In case of long surface flaw (FP-LSF-1) – e.g. a corrosion affected area in the welded joint zone, the shell element is entering in the area of elastic plastic fracture mechanic and fails
- The embedded/buried flaw is also a flaw type that is putting under risk the structural element – for the flat plate embedded flaw (FP-BF-1), the fracture ratio L_r is off the safe area and the flaw is considered inadmissible.
- The edge flaw type – FP-EF-3 (flaw in the fillet welding of the shell element and the endplate – segment joint), is the most dangerous – a 15mm crack depth into welded joint is a critical flaw for which the joint fails.

6.4. Determining the safety in service of the shell steel structures based on fracture mechanics principles

6.4.1. Fatigue assessment of the cracked shell elements (Base metal and weld joint)

The advance methodology presented in the previous chapter, needed for determining the acceptability of the assessed flaws (cracks) in the shell structures, is followed by a fatigue assessment of the shell elements containing cracks. This phase is imposed due to the fact that the in discussion shell structures (tall structures), are subject to cyclic loads. These types of loads, the discovered and assessed defects (cracks) which initially were considered acceptable, increase in size up to the failure of the entire element. In these conditions, is important to know the time period in which the structure can operate in safety conditions without failure / collapse.

The fatigue assessment method of the structural elements with cracks was developed on the modelling possibility with known laws for crack increasing dimension process in fatigue loading. This method is based on the BS 7910/2013 [6.1] being adapted for the case of shell element structures.

6.4.2. Modelling of the crack extension process

Considering that for a crack, the propagation curve is double logarithmic (Paris law figure 6.28), can be easily notice that the domain II is developed on a high percentage of a total extension of a crack, thus the entire crack extension process can be described with Paris law

$$\frac{da}{dN} = C\Delta K^m \tag{6.31}$$

with

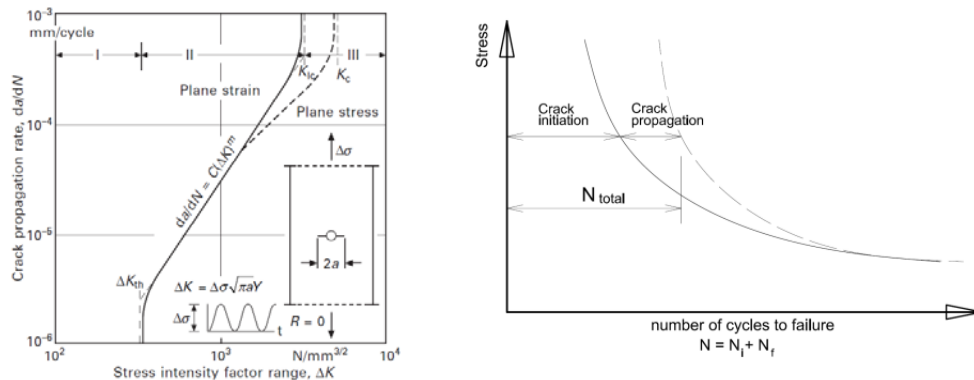$$\Delta K = K_{mat} - K_{min} = Y(\sigma_{max} - \sigma_{min})\sqrt{\pi a} \tag{6.32}$$

Fig. 6.28. *Paris Law and number of crack growth process*

If the values of σ_{max} and σ_{min} are known and the correction factor Y can be calculated, experimentally determine the C and m material factors, it can be

simulated the fatigue crack growth on a procedure which contains the following steps:

- It is calculated the crack growth da_1 corresponding to $dN = 1$ load cycle according with the following relation:

$$da_1 = C \cdot \Delta K^m \tag{6.33}$$

In this phase the following input data are needed: stresses σ_{max} and σ_{min}, material constants C and m and the initial crack dimension a_0 and the dimensions of the analyzed element;

- Based on da_1 growth, it is calculated the crack dimension resulted in the first loading cycle

$$a_1 = a_0 + da_1 \tag{6.34}$$

- It is done the following checking:

$$a_1 < a_f \tag{6.35}$$

where a_f is the final crack length resulted in base of an assessment with Failure Assessment Diagrams (Chapter 6.3.). If the relation is fulfilled, it can be proceed to the next step;

- It is calculated the growth of da_2 corresponding to the second cycle of stress, based on a_1 dimension and on the other input data: $da_2 = C \cdot \Delta K^m$
- Based on da_1 growth, it is calculated the crack dimension resulted in the first loading cycle:

$$a_2 = a_1 + da_2 \tag{6.36}$$

- It is done the following checking:

$$a_2 < a_f \tag{6.37}$$

- This procedure is done until:

$$a_i = a_f \tag{6.38}$$

The number of stress cycles N, for which it is obtained relation (6.38), represents the remaining life of the structural element.

6.4.3. General procedure

Procedures are given for assessing the acceptability of flaws found in service in relation to their effects on fatigue strength, both in welded or nonwelded parts, or for the estimation of tolerable flaw sizes based on fitness for. Planar and non-planar flaws are considered in a fatigue assessment. Fracture mechanics principles are used to describe the behaviour of planar flaws whilst the assessment of non-planar flaws is based on experimental S-N data. The assessment is summarized in following steps [6.1]:

- Determine cyclic stress range from P_m, k_{tm}, P_b, k_{tb}, Q
- Resolve flaw normal to maximum principal stress
- Define flaw dimensions
- Assess un-inspectable regions
- Define limit to crack growth:
  - for unstable fracture Level 1, Level 2, Level 3
  - other failure modes
- *Planar flaws (general procedure)*
- Select values of A, m and ΔK_0
- Determine ΔK for cyclic stress range and flaw height and shape
- Calculate crack growth increments Δa and Δc for one stress cycle

- Repeat steps 7 and 8 for crack height $a + \Delta a$ and continue until the limit to crack growth (step 5) or the specified design life is reached. The flaw is acceptable if the limit to crack growth is not exceeded in the design life
  Planar flaws (using quality categories)
- Select quality category required
- From flaw dimensions, determine initial flaw parameter $\bar{a}_i$
- Determine limit to crack growth (step 5)
- Determine S_i and S_m from $\bar{a}_i$ and $\bar{a}_m$
- Determine quality category for flaw under consideration from $S = \left(S_i^3 - S_m^3 \right)^{1/3}$. If this is equal to or better than quality required, flaw is acceptable
  Non-planar and shape imperfections
- Confirm that flaw does not need to be treated as planar
- Calculate k_m for misalignment
- Determine required quality category
- Determine allowable flaw sizes or shape imperfections
- Compare detected with allowable flaws or imperfections

The general fatigue assessment of the structural elements with cracks is based on Paris law for crack growth modelling. This assessment procedure, as previously shown, is chosen considering that the relation between *da/dN* and *ΔK* is a sigmoidal curve in a graph of log *da/dN* function of *ΔK*. For the middle region of the graph, it can be reasonable approximate a linear relation (e.g. Paris Law), or, for higher precision, through two or more straight lines (figure 6.29)
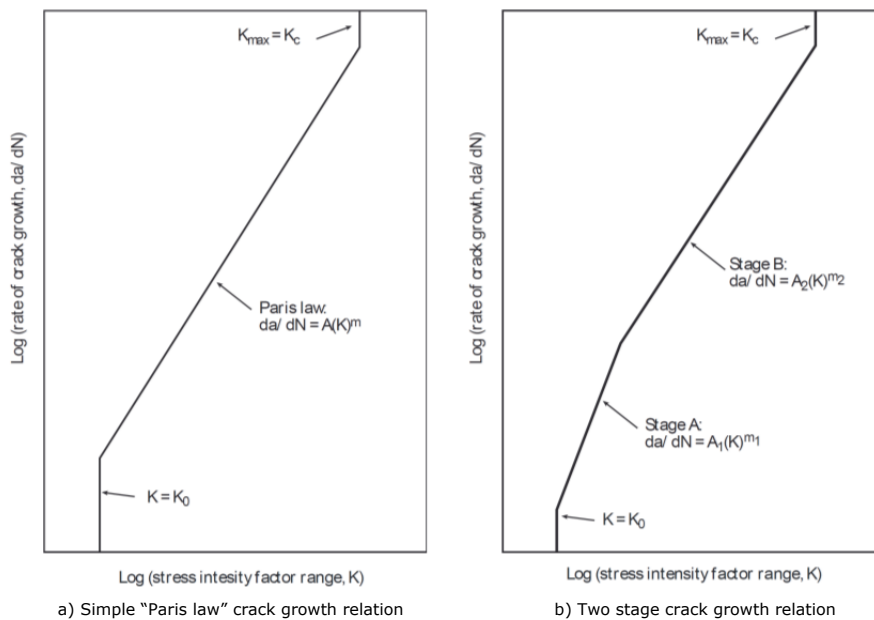

a) Simple "Paris law" crack growth relation   b) Two stage crack growth relation

Fig.6.29. *Schematic crack growth relations [6.1]*

The needed assessment data are:

1. *Stress ranges*

    The fatigue assessment use the applied nominal stress ranges. These are acting on the cross section with flaw and results from the variable loading. The residual stresses are not included in the design stress for ΔK (some thermal influences can be taken into account). Thus is needed to identify the primary and secondary stresses types: P_m, P_b respectively Q_m and Q_b (Ch.6.2.2) and the distribution of these stresses on thickness (if needed and possible). The stresses will be identified during on a fatigue life cycle.

    At welded type structures (in case), there is needed to be calculated also the contribution of the peak stress variation. When is calculated the applied stress, there are included only stress concentrations due to the coarse structural discontinuity and misalignment. The structural discontinuity effect onto stress concentration, given by for example the welded joint geometry, is taken into account only by a fracture mechanic assessment as part of the stress intensity factor calculation. The peak stress due to the misalignment depends only on the membrane component of the applied stress. If a misaligned joint is in the interior of the stress field, due to the coarse structural discontinuity, this stress must include also the effect of the coarse structural discontinuity.

    Calculating procedure for the stress ranges when the stress is divided into P and Q is the following:

    - o Identifying the extreme (max and min) values for the primary and secondary (($P+Q$)$_{max}$ and ($P+Q$)$_{min}$), and if possible in thickness stresses distribution on the entire fatigue loading cycle;
    - o Is calculated the peak stress taken into account the coarse structural discontinuities;
        At the both extremes of the fatigue loading cycle it is determined $k_m(P_m+Q_m)_{max}$ and $k_{tb}(P_b+Q_b)_{min}$. It is separating the membrane stress and bending stress σ_m and $\sigma_b{'}$ which can be conservative linearized through thickness (figure 6.4). In particular, linearization should not underestimate the surface stresses or, as far as possible, the stress acting in the region of the flaw being assessed;
    - o It is calculated the maximum changes of σ_m and $\sigma_b{'}$ to give stress ranges σ_m and $\sigma_b{'}$;
    - o It is calculated the range supplementary stresses due to misalignment under membrane stress range $\Delta\sigma_m[(k_m\text{-}1)\cdot\Delta\sigma_m]$. This is added to the $\Delta\sigma_b$, thus resulting the total bending stress range $\Delta\sigma_b$. *Thus $\Delta\sigma_b = \Delta\sigma_b{'}+(k_m\text{-}1)\,\Delta\sigma_m$.* If misalignment alone is being assessed, it is neglected at this stage ($k_m = 1$), so that $\Delta\sigma_b = \Delta\sigma_b{'}$;
    - o Membrane or bending stress ranges may be used separately or together, depending on the type of assessment being performed (function of the design solution of the ΔK variation);
    - o The variable loading cycle. If the stress range varies in life time of the analyzed structure (in case steel shell tall structures), it is necessary to know these variations. Thus the loading spectrum can be converted into a step type loading history using a numbering method for the loading cycles (e.g. rainflow counting algorithm or reservoir method), being represented through a distribution of

stresses ranges function of the number of occurrences in given time period.

2. *Types and dimensions of the flaw*

The types and idealization of defects were described at chapter 6.3.3 and chapter 6.3.5. The presented remarks are valid also for this chapter.
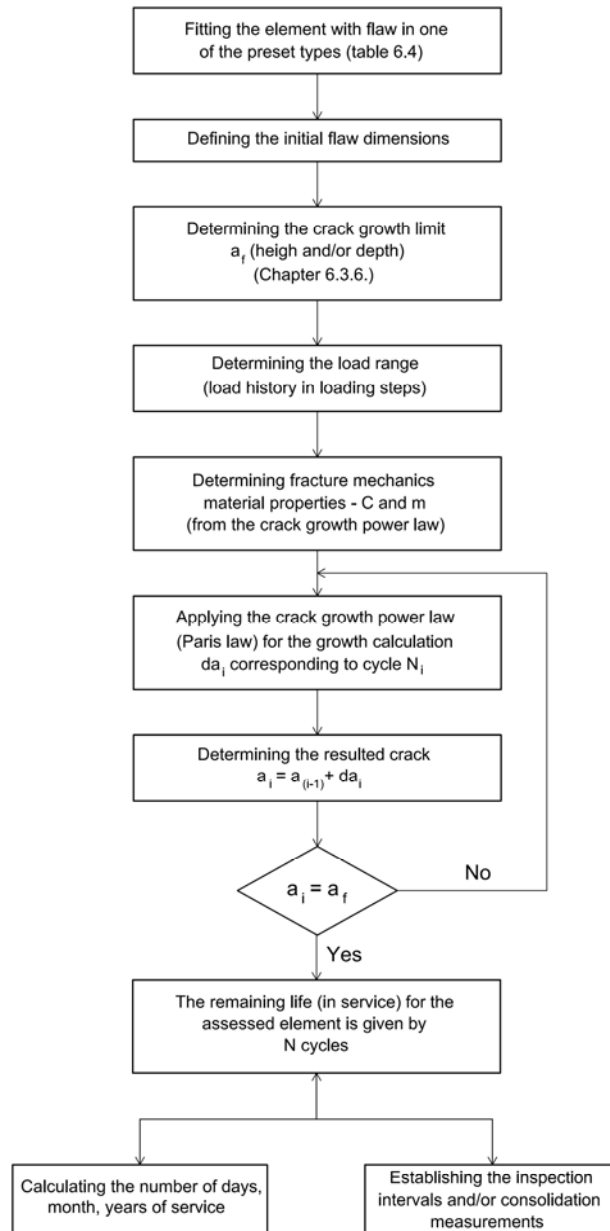

Fig.6.30. *Algorithm for fatigue assessment for with flaw elements*

3. *Fatigue crack grow law*

  The fatigue crack growth laws indicated by [6.1] for structural steels are:
- o   Paris law with one slope (figure 6.29.a)
- o   Two stage crack growth (figure 6.29.b)

When needed in the assessment, the two stage procedure, has a better precision.

  The constants C and m can be determined through material tests or can be calculated according to the method described in BS7910 [6.1]

4. *Limits of the crack growth*

  In fatigue crack growth assessment of the planar flaws, should be fixed a limit in crack growth extension which can be admissible without failure occurrence in service lifetime. The total maximum stress (P_m+P_b+Q+F) is to be used in order to determine the maximum allowable crack / flaw dimension. The procedure described at chapters 6.3.4 and 6.3.6 can be applied. For the in case structure, according to chapter 6.3.6 was assessed the critical flaw length and the critical flow height (depth). Detailed FAD-2 diagrams are presented in Annex3.

  In case of fatigue assessment, the factor ($Y·\sigma$) is given by the following relation [6.1]:

$$(Y·\Delta\sigma)_P = M·f_w·\{k_{tm}·M_{km}·M_m·\ \Delta\sigma_m+k_{tb}·M_{kb}·M_b·\ [\Delta\sigma_b+(k_m\text{-}1)P_m]\} \quad (6.39)$$

where M, f_w, M_m and M_b has values according to the flaw type (same as the fracture assessment). M_{km} and M_{kb} are applied when the flaw/crack is in the area of a local stress concentration. The k_t, k_{tm}, k_{tb} and k_m are described at chapter 6.2.2.

  The procedure for remaining in service lifetime for the steel shell structures, based on BS7910 procedures is presented in the following schematic algorithm (figure 6.30)

6.4.4. ECA using CrackWise software – calculating the structural element service lifetime

  CrackWise is windows based software that automates fracture analysis procedures, taken according with BS9710 / 2005. The ECA for steel shell elements welded joints are carried out using level 2A /3 B analysis procedure according to BS9710. The failure assessment diagrams are based on the specific stress-strain curve of the assessed material [6.12]

  The base principle of the fatigue crack growth calculation methodology is based on the crack type flaw dimension increasing in a cycle loading and determining the number of cycles N from the initial crack a_0 to the critical crack dimension a_f. The analysis is using all the fracture assessment data (geometry of the flaw/crack, fracture mechanics parameters, flow critical dimension, etc.).

  The list of required input data used for ECA of steel shell element with flaws assessments using CRACKWISE is as follows:

Geometry

  The input data for geometry includes type of geometry, type of flaw, weld profile, maximum misalignment, wall thickness B, width or length W, radius, flaw height a, and flaw length $2c$. Stress Intensity Factor (SIF) and reference stress solution depend on the type of flaw and geometry.

Material tensile properties

The tensile properties can be introduced using or not using the Lüders Plateau (with or without yielding discontinuity). For the FAD can be set the Lr cut off position (if needed)

Fracture Toughness

The data regarding fracture toughness in level 2A/3B analysis include fracture resistance curve in the form of J-integral or CTOD as a function of Δa. The value of toughness can be introduced in K or in J parameter.

Primary Stress

This stress value is the input as parameter P_m (primary membrane stress). Bending stress component P_b (primary bending stress), that is induced by misalignment is calculated using SCF (Stress Concentration Factor) in association with Neuber's rule.

Secondary Stress

The input secondary stress is welding residual stress which is given as a parameter Q_m, (secondary membrane stress) and can be introduced: as welded condition, post welded heat treated condition, or known residual stresses.

Sensitivity setting – critical parameter

CrackWise software enables to choose what parameter to assess – to determine the critical dimension. Thus, following the geometry, it can be set the crack height or the crack length. Also the software enables to choose the stress as a parameter – finding the maximum stress (critical).
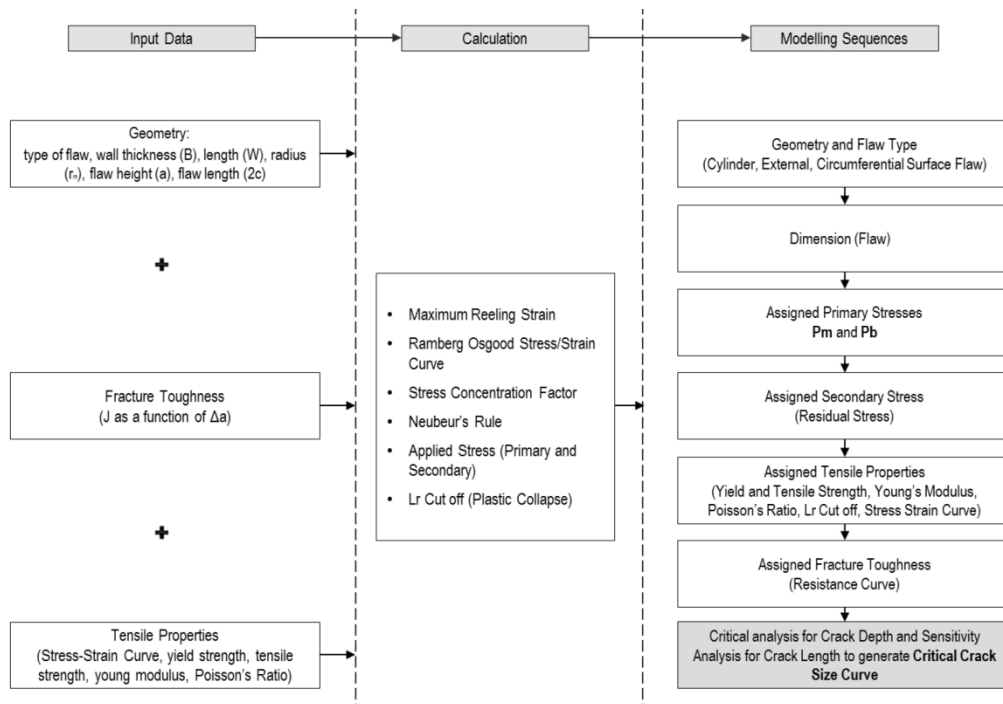
Fig.6.31. *CrackWise software – analysis flowchart (input data, calculation, modelling sequences for fracture mechanics assessment) [6.12]*

Fatigue calculation – crack growth

Furthermore the software can assess the structural element from the fatigue point of view. Based on fracture mechanics assessment results, CrackWise can calculate the crack growth for a given blocks of cyclic loading. The software applies the specified stress ranges sequentially line by line, but each step incorporating the ratio number of blocks (B) to the number of increments (N). Thus for a first line (stress range S_a and the number of cycles C_a), CrackWise solves for stress range S_a applied $C_a \cdot B / N$ times. For the second line, (stress range S_b and the number of cycles C_b), CrackWise solves for stress range S_a applied $C_b \cdot B / N$ times. The procedure is repeated until all the stress ranges in the spectrum have been considered. All the steps are repeated N times or until the analysis is halted (if the flaw growth exceeds the section dimensions, an unacceptable flaw size is predicted in terms of fracture, or a calculation error occurs).

For fatigue crack growth calculation can be used both one slope or two stage crack growth relation (figure 6.29).

6.4.5. Applying fatigue based ECA on a real case assessment

The fatigue assessment on the steel shell element described at chapter 5, focused on fatigue behavior of several types of flaws. Thus, as an input data, was used the same material properties as presented and experimental proofed in chapter 5 (data presented also at Ch. 6.3.5 and 6.3.6):

- σ_Y (yield strength)= 355 MPa; σ_T (ultimate strength)= 510 MPa; specific for S355J2 steel type;
- K_{mat} = 81,8 MPa·m$^{1/2}$ was determined on the specimens (see Chapter 5 – Experimental research);
- P_m = 251 MPa - Primary stress. Was determined following the structural analysis (see Chapter 4).
- k_{tm} = 1; k_{tb} = 1 (stress concentrators factors)
- Q_{tm} = 0 (thermal membrane stress) and Q_{tb} = 0 (thermal bending stress)
- Q_m = 0 (residual membrane stress) and Q_b = 0 (residual bending stress)

Establishing the cyclic loading – wind load

The instant values of the wind speed (figure 6.32), as well as the instant values of the dynamic wind pressure, are containing an average component and a varying component towards the average.
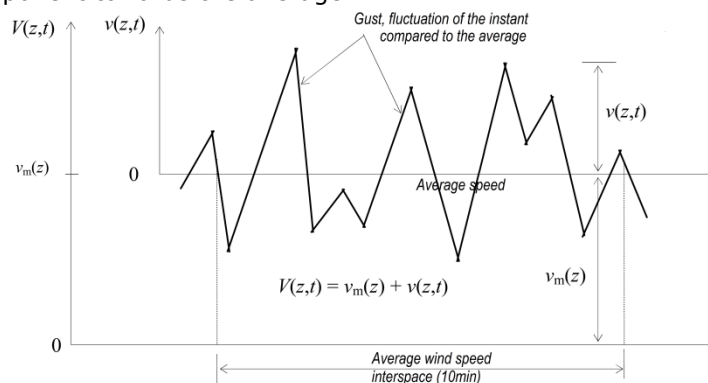

Fig.6.32. *Stochastic process of the wind speed at z height above ground [6.10]*

The wind loading parameter is the wind speed. This parameter is consider in the standards and normatives. The reference wind velocity is defined as the 10 minutes mean wind velocity at 10m above ground of terrain category II (open field with obstacles at a distance of 20 times height of the obstacle), the reference wind speed is to be calculated as following:

$$v_b = c_{dir} \cdot c_{season} \cdot v_{b.0} \tag{6.40}$$

where v_b is the reference wind velocity following the wind direction and season at a height of 10m above ground for a terrain of type II, vb0 is the fundamental value of the wind speed, c_{dir} is the direction coefficient, c_{season} is the season factor.

Mediation wind speed for a period of 10 minutes leads to a stable wind speed for an area greater than that of the construction and for a period of time sufficient for the development of the dynamic response of the structure.

For open ground it is recommended the following conversion relations between averaged wind speeds over different time intervals:

$$1,05 \cdot v_b^{1h} = v_b^{10\,min} = 0,84 \cdot v_b^{1\,min} = 0,67 \cdot v_b^{3s} \tag{6.41}$$

The reference value of the wind speed, having an exceeding probability of 2%, can be determined from statistical analysis of the maximum values of the average wind speed. In the statistical analysis the number of years for which there are meteorological records it is recommended to be compared with the average recurrence interval related to reference wind speed (50 years). For zoning the wind action it is recommended to use the same type of probability repartition of the extreme values. In this way the [SR EN 1991-1-4] recommends using Gumbel repartition for the extreme values. The maximal annual average wind speed, having the probability of not exceeding, p=0.98 is

$$v_{0,98} = m_1 \cdot \left(1 + 2,593 \cdot V_1\right) \tag{6.42}$$

Where m_1 and V_1 are the average and the variation coefficient of the annual maximal wind speed. The variation coefficient of the wind speed annual maximal values, in Romania is in generally lower than 0,35.

The maximal value of the average wind speed, having the probability of not exceed in one year, p can be established as following, relation valid in Gumbel repartition of the maximal annual wind speed values

$$v_{prob} = \frac{1 - \left[0,45 + \dfrac{ln(-\,ln\,p)}{1,282}\right] \cdot V_1}{1 + 2,593 \cdot V_1} \cdot v_{0,98} \tag{6.43}$$

For the structure in case analysed, were used the wind load (as wind speed values) recordings from Romanian National Institute of Meteorology and Hydrology (INMH). Thus was used the figure 6.33 wind speed recording spectrum for a given time of one year.

The distribution of the wind speed was rearranged following a probability density function (PDF) using Weibull Distribution. The description of the methodology is done at chapter 3 . The used parameter in the Weibull distribution were: $k = 2$ and $\sigma_U / \overline{U} = 0.523$.
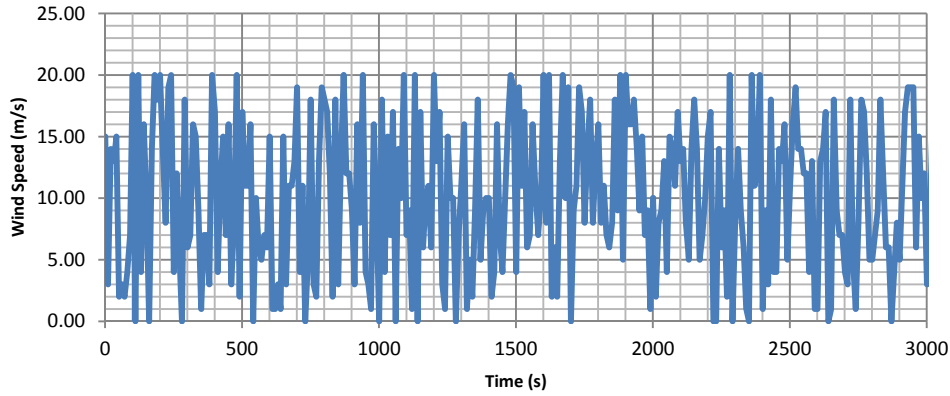
Fig.6.33. *Wind load recording – INMH provided data [6.11]*

Following received data (wind speed values), it were performed five structural analysis for the following wind load – wind speeds: 5m/s, 10m/s, 15m/s, 20m/s, 25m/s, 27m/s. The later value is the wind load – reference wind speed (according to the EN1991-1-4) (table 6.7 and figure 6.34).

Table 6.7. – *Wind load forces at different heights [N/m^2]*

Height	qp(z)	qp(z)	qp(z)	qp(z)	qp(z)	qp(z)
m	5 m/s	10 m/s	15 m/s	20 m/s	25 m/s	27 m/s
2.0	26.8	107.3	241.4	429.1	670.5	782.1
3.0	23.1	92.4	208.0	369.7	577.6	673.8
4.0	21.2	84.7	190.6	338.8	529.4	617.5
5.0	19.9	79.8	179.5	319.2	498.7	581.7
6.0	21.6	86.5	194.7	346.0	540.7	630.7
7.0	23.1	92.4	207.8	369.5	577.3	673.3
8.0	24.4	97.5	219.5	390.2	609.7	711.1
9.0	25.6	102.2	230.0	408.8	638.8	745.1
10.0	26.6	106.4	239.5	425.8	665.2	775.9
11.0	27.6	110.3	248.2	441.3	689.5	804.3
12.0	28.5	113.9	256.3	455.7	712.0	830.4
13.0	29.3	117.3	263.8	469.0	732.9	854.8
14.0	30.1	120.4	270.9	481.5	752.4	877.6
15.0	30.8	123.3	277.5	493.3	770.8	899.1
16.0	31.5	126.1	283.7	504.4	788.2	919.3
17.0	32.2	128.7	289.7	514.9	804.6	938.5
18.0	32.8	131.2	295.3	524.9	820.2	956.7
19.0	33.4	133.6	300.6	534.5	835.1	974.0
20.0	34.0	135.9	305.7	543.6	849.3	990.6
21.0	34.5	138.1	310.6	552.3	862.9	1006.5
22.0	35.0	140.2	315.3	560.6	876.0	1021.7
23.0	35.5	142.2	319.9	568.7	888.5	1036.4
24.0	36.0	144.1	324.2	576.4	900.6	1050.5
25.0	36.5	146.0	328.4	583.8	912.2	1064.0
26.0	36.9	147.8	332.5	591.0	923.5	1077.2
27.0	37.4	149.5	336.4	598.0	934.4	1089.9
28.0	37.8	151.2	340.2	604.7	944.9	1102.1
29.0	38.2	152.8	343.8	611.3	955.1	1114.0
30.0	38.6	154.4	347.4	617.6	965.0	1125.6
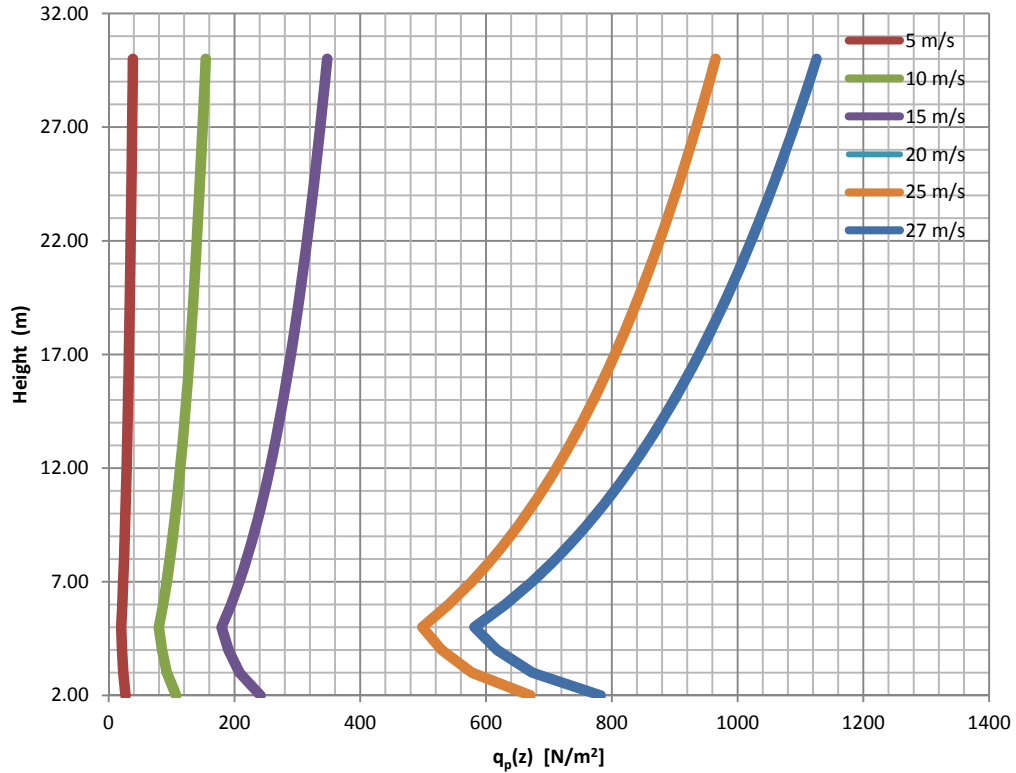
Fig.6.34. *Wind load $q_p(z)$ at different heights for all five wind load speeds*

Following the structural analysis of the five load cases, was assessed the stress in the structure segment joint. Using Rainflow algorithm, the results were processed and was determined the block of stresses with stress ranges ($\Delta\sigma_i$) and the appearance frequency of them (n_i) – table 6.8 and figure 6.35.

Table 6.8. – *Blocks number, stress range and frequency*

Number of blocks	Stress range Ds	Annually frequency	Monthly frequency
	MPa		
1	20	9984.00	832
2	40	5052.00	421
3	60	1332.00	111
4	80	504.00	42
5	100	372.00	31
6	120	60.00	5
7	140	12.00	1
8	160	5.28	0.44
9	180	2.52	0.21
10	200	2.16	0.18
11	220	0.60	0.05
12	240	0.03	0.0025
13	260	0.00	0.00025
	Total of cycles	17327	1444
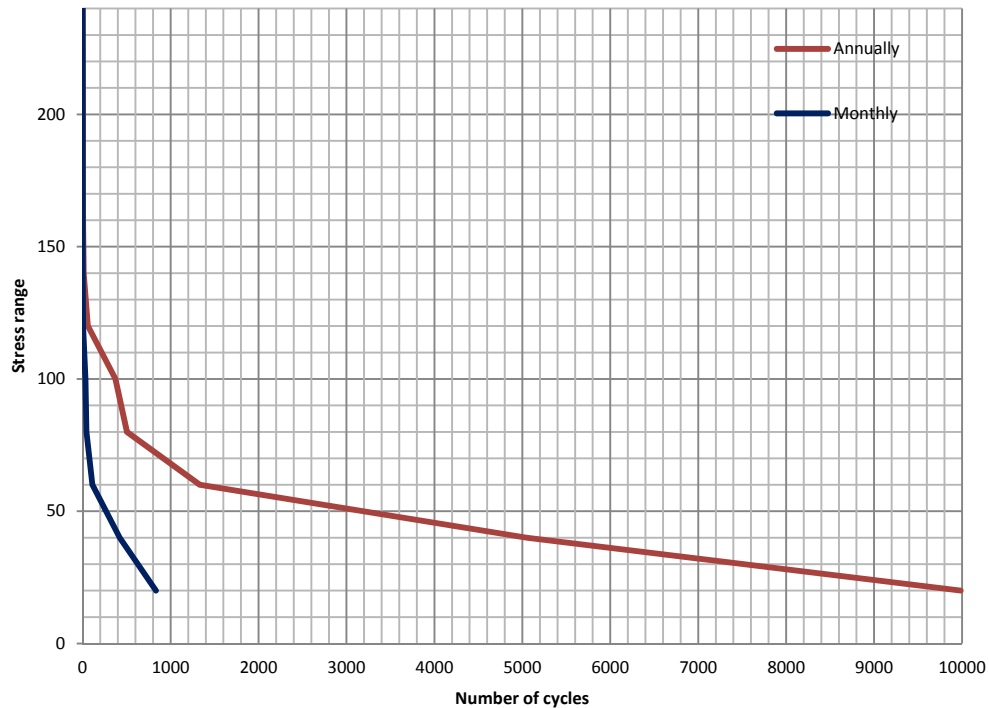
Fig.6.35. *Fatigue stress range and frequency*

Fatigue assessment of the different flaw cases

For the assessment was used the previously described cyclic loading as a block independent iterative solver – applying the specified stress ranges sequentially line by line, repeating the entire cyclic loading (entire group of cycles) for a number of blocks (a block is different in meaning as previous load calculation) – 1 block representing all the applied cycles of stress ranges. In term of time one block represents one year.

Regarding the fatigue crack growth, was used the BS 7910 simple procedure – one slope Paris Law (figure 6.29). Was considered the air environment with the material properties as for an S355J2 steel type.

Description of the each flaw taken into assessment was done in chapter 6.3.5, table 6.4 and figure 6.17). The notations are done accordingly. The initial flaw length is presented in table 6.9 and the description of the group of flaws is done in following paragraph.

Group of flaws – FP-TTF type (flat plate – through thickness flaw)
- FP-TTF-1 – the flaw / crack is a through thickness type into the shell element (*B*=16mm) with the length of *2a*=30mm;
- FP-TTF-2 – the flaw / crack is a through thickness type into welded joint – flange plate of the segment joint to the segment shell element. The flaw is having a *2a*=30mm height into a welded joint of 32.63mm through height (*B*);

- FP-TTF-3 – the flaw / crack is a through thickness type into welded joint – flange plate of the segment joint to the segment shell element. The flaw is having a *2a*=30mm height into a welded joint of 32.63mm cut through height (*W*);
- FP-TTF-4 – the flaw / crack is a through thickness type into flange of the segment joint (*B*=25mm) in the circumferential direction;
- FP-TTF-5 – the flaw / crack is a through thickness type into flange of the segment joint (*B*=25mm) in the perpendicular to circumferential direction;

Group of flaws – FP-SF type (flat plate – surface flaw)
- FP-SF-1 – the flaw / crack is a surface type into the shell element (*B*=16) with the length of *2c*=30mm and a height of *a*=5mm;
- FP-SF-2 – the flaw / crack is a surface type into welded joint – flange plate of the segment joint to the segment shell element. The flaw is having a the length of *2c*=30mm and a height of *a*=5mm into a welded joint of 32.63mm through height (*B*);
- FP-SF-3 – the flaw / crack is a surface type into welded joint – flange plate of the segment joint to the segment shell element. The flaw is having a *2c*=10mm length and *a*=5mm height of the welded joint of 32.63mm through height (*W*);
- FP-SF-4 – the flaw / crack is a surface type into flange of the segment joint (*B*=25mm) in the circumferential direction with length of *2c*=3mm and height of *a*=5mm;
- FP-SF-5 – the flaw / crack is a surface type into flange of the segment joint (*B*=25mm) in the perpendicular to circumferential direction with length of *2c*=3mm and height of *a*=5mm;

Group of flaws – FP-LSF type (flat plate – long surface flaw)
- FP-LSF-1 – the flaw / crack is in surface long into the shell element flaw (*B*=16) with height of *a*=2mm;
- FP-LSF-2 – the flaw / crack is in surface long into welded joint flaw – flange plate of the segment joint to the segment shell element. The flaw is having a height of *a*=5mm into a welded joint of 32.63mm through height (*B*);
- FP-LSF-3 – the flaw / crack is in surface long welded joint flaw – flange plate of the segment joint to the segment shell element. The flaw is having *a*=5mm height into the welded joint of 32.63mm through height (*W*);
- FP-LSF-4 – the flaw / crack is in surface long flaw flange of the segment joint flaw (*B*=25mm) in the circumferential direction with height of *a*=5mm;
- FP-LSF-5 – the flaw / crack is in surface long into flange of the segment joint flaw (*B*=25mm) in the perpendicular to circumferential direction with height of *a*=5mm;

Group of flaws – FP-BF type (flat plate – embedded/buried flaw)
- FP-BF-1 – the flaw / crack is an embedded type into the shell element (*B*=16) with the length of *2c*=30mm and a height of *2a*=5mm;
- FP-BF-2 – the flaw / crack is an embedded type into welded joint – flange plate of the segment joint to the segment shell element. The flaw is having a the length of *2c*=30mm and a height of *2a*=5mm into a welded joint of 32.63mm through height (*B*);

- FP-BF-3 – the flaw / crack is a embedded type into welded joint – flange plate of the segment joint to the segment shell element. The flaw is having a *2c=10mm* length and *2a=5mm* height of the welded joint of 32.63mm through height (*W*);
- FP-BF-4 – the flaw / crack is an embedded type into flange of the segment joint (*B=25mm*) in the circumferential direction with length of *2c=3mm* and height of *2a=5mm*;
- FP-BF-5 – the flaw / crack is an embedded type into flange of the segment joint (*B=25mm*) in the perpendicular to circumferential direction with length of *2c=3mm* and height of *2a=5mm*;

Group of flaws – CSAF type (Curved shell axial flaw)
- CSAF-TTF-1 – the flaw / crack is a curved shell axial through thickness flaw into the shell element with the height of *2a=30mm*. The outer radius is r_o=840mm;
- CSAF-ISF-1 – the flaw / crack is a curved shell axial internal surface flaw into the shell element. The flaw is having a the length of *2c=30mm* and a height of *a=10mm*. The outer radius is r_o=840mm;
- CSAF-LISF-1 – the flaw / crack is a curved shell axial long internal surface flaw into the shell element. The flaw is having a height of *a=3mm*. The outer radius is r_o=840mm;
- CSAF-ESF-1 – the flaw / crack is a curved shell axial external surface flaw into the shell element with the length of *2c=30mm*. The flaw is having a height of *a=10mm*. The outer radius is r_o=840mm;
- CSAF-LESF-1 – the flaw / crack is a curved shell axial long external surface flaw into the shell element. The flaw is having a height of *a=3mm*. The outer radius is r_o=840mm;
- CSAF-BF-1 – the flaw / crack is a curved shell axial embedded flaw into the shell element. The flaw is having a height of *a=5mm* and length of *2c=30mm*. The outer radius is r_o=840mm;

Group of flaws – CAF type (Cylinder axial flaw)
- CAF-TTF-1 – the flaw / crack is a cylinder axial through thickness flaw into the shell element with the height of *2a=30mm*. The outer radius is r_o=840mm;
- CAF-BF-1 – the flaw / is a cylinder axial through thickness flaw into the shell element. The flaw is having a height of *a=5mm* and length of *2c=30mm*. The outer radius is r_o=840mm;

Group of flaws – CSCF type (Curved shell circumferential flaw)
- CSCF-TTF-1 – the flaw / crack is a curved shell circumferential through thickness flaw into the shell element with the height of *2a=30mm*. The outer radius is r_o=840mm;
- CSCF-ISF-1 – the flaw / crack is a curved shell circumferential internal surface flaw into the shell element. The flaw is having a the length of *2c=30mm* and a height of *a=10mm*. The outer radius is r_o=840mm;
- CSCF-FCISF-1 – the flaw / crack is a curved shell fully circumferential internal surface flaw into the shell element. The flaw is having a height of *a=3mm*. The outer radius is r_o=840mm;
- CSCF-ESF-1 – the flaw / crack is a curved shell circumferential external surface flaw into the shell element with the length of *2c=30mm*. The flaw is having a height of *a=10mm*. The outer radius is r_o=840mm;

- CSCF-FCESF-1 – the flaw / crack is a curved shell fully circumferential external long external surface flaw into the shell element. The flaw is having a height of $a=3$mm. The outer radius is $r_o=840$mm;
- CSCF-BF-1 – the flaw / crack is a curved shell circumferential embedded flaw into the shell element. The flaw is having a height of $a=5$mm and length of $2c=30$mm. The outer radius is $r_o=840$mm;

Group of flaws – CCF type (Cylinder circumferential flaw)
- CCF-TTF-1 – the flaw / crack is a cylinder circumferential through thickness flaw into the shell element with the height of $2a=30$mm. The outer radius is $r_o=840$mm;
- CSCF-BF-1 – the flaw / crack is a cylinder circumferential embedded flaw into the shell element. The flaw is having a height of $a=5$mm and length of $2c=30$mm. The outer radius is $r_o=840$mm;

Group of flaws – CWJ type (Cruciform welded joints)
- CWJ-TTF-1 – the flaw / crack is a cruciform welded joint through thickness flaw with the height of $2a=30$mm.
- CWJ-WT-1 – the flaw / crack is a cruciform welded joint – weld toe flaw. The flaw is having a height of $2a=10$mm and length of $2c=30$mm.

Table 6.9 – *Fatigue flaw case name and dimensions – initial flaw length*

No.	Case	Initial flaw length								
		B	W	$2a_0$	a_0	$2c_0$	p_0	r_0	h_0	t_w
		mm	mm	mm	mm	mm	mm	mm	mm	mm
1	**FP-TTF-1**	16	200	30						
2	**FP-TTF-2**	32.63	200	30						
3	**FP-TTF-3**	200	32.63	10						
4	**FP-TTF-4**	25	200	30						
5	**FP-TTF-5**	25	120	30						
6	**FP-SF-1**	16	200		5	30				
7	**FP-SF-2**	32.63	200		5	30				
8	**FP-SF-3**	200	32.63		5	10				
9	**FP-SF-4**	25	200		5	30				
10	**FP-SF-5**	25	120		5	30				
11	**FP-LSF-1**	16	200		2					
12	**FP-LSF-2**	32.63	200		5					
13	**FP-LSF-3**	200	32.63		5					
14	**FP-LSF-4**	25	200		5					
15	**FP-LSF-5**	25	120		5					
16	**FP-BF-1**	16	200	5		30	3			
17	**FP-BF-2**	32.63	200	5		30	3			
18	**FP-BF-3**	200	32.63	5		10	3			
19	**FP-BF-4**	25	200	5		30	3			
20	**FP-BF-5**	25	120	5		30	3			
21	**FP-EF-1**	16	200		15					
22	**FP-EF-2**	32.63	200		15					
23	**FP-EF-3**	200	32.63		5					
24	**FP-EF-4**	25	200		15					
25	**FP-EF-5**	25	120		15					
26	**CSAF-TTF-1**	16	200	30				840		
27	**CSAF-ISF-1**	16	200		10	30		840		

No.	Case									
28	CSAF-LISF-1	16	200		3			840		
29	CSAF-ESF-1	16	200		10	30		840		
30	CSAF-LESF-1	16	200		3			840		
31	CSAF-BF-1	16	200	5		30	3			
32	CAF-TTF-1	16	200	30				840		
33	CAF-BF-1	16	200	5		30	3			
34	CSCF-TTF-1	16	200	30				840		
35	CSCF-ISF-1	16	200		10	30		840		
36	CSCF-FCISF-1	16	200		3			840		
37	CSCF-ESF-1	16	200		10	30		840		
38	CSCF-FCESF-1	16	200		3			840		
39	CSCF-BF-1	16	200	5		30	3			
40	CCF-TTF-1	16	200	30				840		
41	CCF-BF-1	16	200	5		30	3			
42	CWJ-TTF-1	16	44.28	10	5	30			14.14	
43	CWJ-WT-1	16	44.28	10	3	30			14.14	10

Following the fatigue assessment with the procedures described at this chapter, it results the number of cycles until reaching the critical flaw dimension (length or height) for all 43 cases. The results are presented under tabular form (as final results) and in detail, graphically in annex 4 – for each flaw case is presented the fatigue assessment diagram – number of cycles (transformed into blocks / years). Each block (year) is having a number of 17.327 cycles applied in sequence with stress range and number of cycles per each range according to table 6.8.

In table 6.10 are presented the fatigue assessment for all 43 flaw cases.

Table 6.10 – *Fatigue flaw assessment - results*

		Fatigue assessment			
No.	Case	Number of cycles	Number of blocks	Flaw Height Critic	Flaw Length Critic
			years	mm	mm
1	FP-TTF-1	694119.62	40.06	N/A	36.249
2	FP-TTF-2	174136.35	10.05	N/A	36.249
3	FP-TTF-3	173963.08	10.04	N/A	11.330
4	FP-TTF-4	174136.35	10.05	N/A	36.243
5	FP-TTF-5	741768.87	42.81	N/A	28.408
6	FP-SF-1	173616.54	10.02	5.690	34.440
7	FP-SF-2	2139364.69	123.47	18.261	49.395
8	FP-SF-3	3457083.04	199.52	10.734	23.800
9	FP-SF-4	1657327.55	95.65	14.755	42.870
10	FP-SF-5	1570692.55	90.65	14.505	42.420
11	FP-LSF-1	780061.54	45.02	4.536	N/A
12	FP-LSF-2	264929.83	15.29	7.470	N/A
13	FP-LSF-3	33267.84	1.92	5.360	N/A
14	FP-LSF-4	128219.8	7.40	6.269	N/A
15	FP-LSF-5	129086.15	7.45	6.280	N/A
16	FP-BF-1	679738.21	39.23	7.590	30.160
17	FP-BF-2	953678.08	55.04	10.984	30.409
18	FP-BF-3	-	-	-	-

19	FP-BF-4	918504.27	53.01	10.190	30.365
20	FP-BF-5	871374.83	50.29	10.106	30.360
21	FP-EF-1	87154.81	5.03	N/A	17.230
22	FP-EF-2	87154.81	5.03	N/A	17.230
23	FP-EF-3	267009.07	15.41	N/A	7.507
24	FP-EF-4	87154.81	5.03	N/A	17.230
25	FP-EF-5	263543.67	15.21	N/A	14.750
26	CSAF-TTF-1	137229.84	7.92	35.012	N/A
27	CSAF-ISF-1	301489.8	17.40	12.682	36.389
28	CSAF-LISF-1	299410.56	17.28	4.748	N/A
29	CSAF-ESF-1	304608.66	17.58	12.720	36.450
30	CSAF-LESF-1	124061.32	7.16	3.478	N/A
31	CSAF-BF-1	680951.1	39.30	7.607	30.163
32	CAF-TTF-1	34827.27	2.01	N/A	31.187
33	CAF-BF-1	675233.19	38.97	7.569	30.160
34	CSCF-TTF-1	392803.09	22.67	N/A	47.706
35	CSCF-ISF-1	523621.94	30.22	14.801	42.560
36	CSCF-FCISF-1	280524.13	16.19	4.540	N/A
37	CSCF-ESF-1	524141.75	30.25	14.808	42.570
38	CSCF-FCESF-1	280524.13	16.19	4.540	N/A
39	CSCF-BF-1	675233.19	38.97	7.569	30.160
40	CCF-TTF-1	346540	20.00	N/A	44.050
41	CCF-BF-1	681470.91	39.33	7.611	30.160
42	CWJ-TTF-1	-		N/A	-
43	CWJ-WT-1	109333.37	6.31	3.882	33.133

Following the presented results, a comparison was made between groups of flaws, in order to detect and underline the most critical flaws in term of fast crack growth and number of cycles until reaching the critical dimensions – remaining in service life time. Thus were grouped the following flaws types: Flat Plate Through Thickness Flaw – FP-TTF (see figure 6.14), Flat Plate Surface Flaw – FP-SF, Flat Plate Long Surface Flaw – FP-LSF, Flat Plate Edge Flaw – FP-EF (see figure 6.14), Curved Shell Axial Flaw – CSAF, Cylinder Axial Flaw – CAF, Curved Shell Circumferential Flaw – CSCF, Cylinder Circumferential Flaw – CCF and Cruciform Welded Joints – CWJ. Due to ease of representation, the X axis (number of cycles/blocks) is represented in logarithmic scale – base 2. The comparatives graphs are presented in following figures – figure 6.36 to figure 6.45.
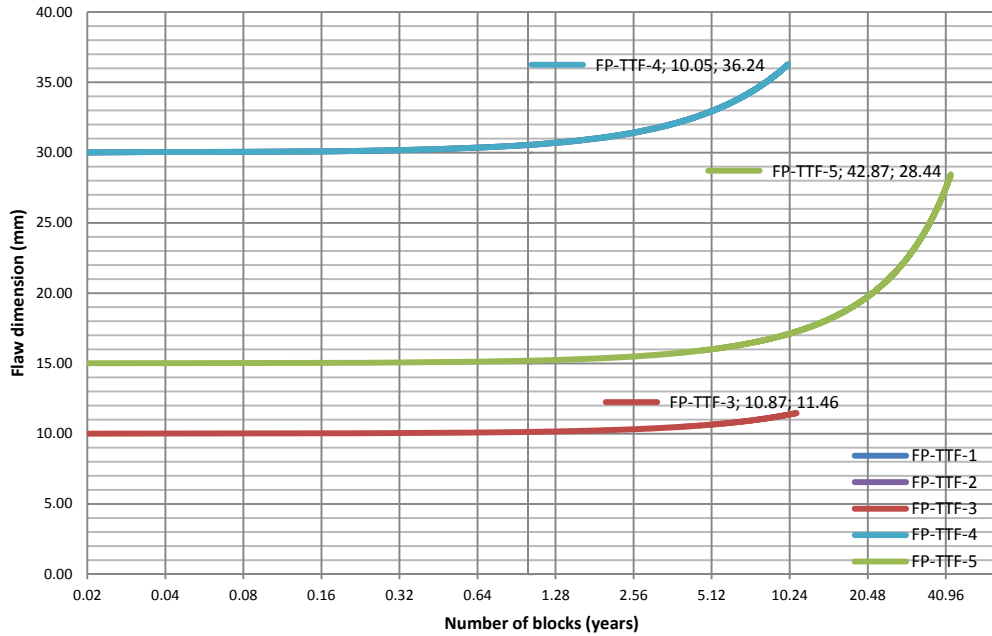
Fig.6.36. *Flat Plate Through Thickness Flaw – FP-TTF – Flaw types comparison*
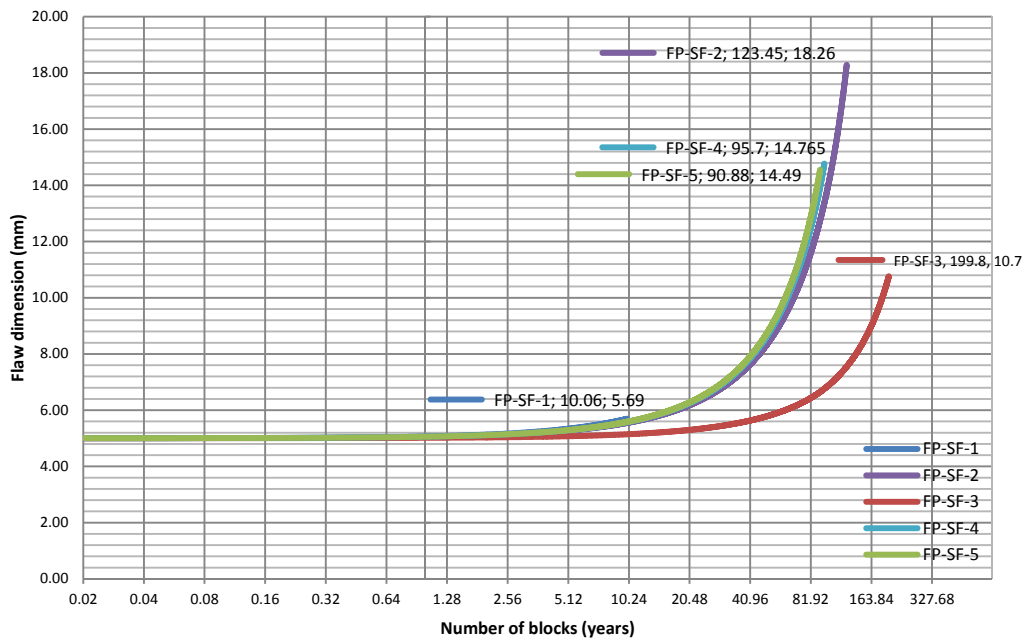
Fig.6.37. *Flat Plate Surface Flaw – FP-SF – Flaw types comparison*
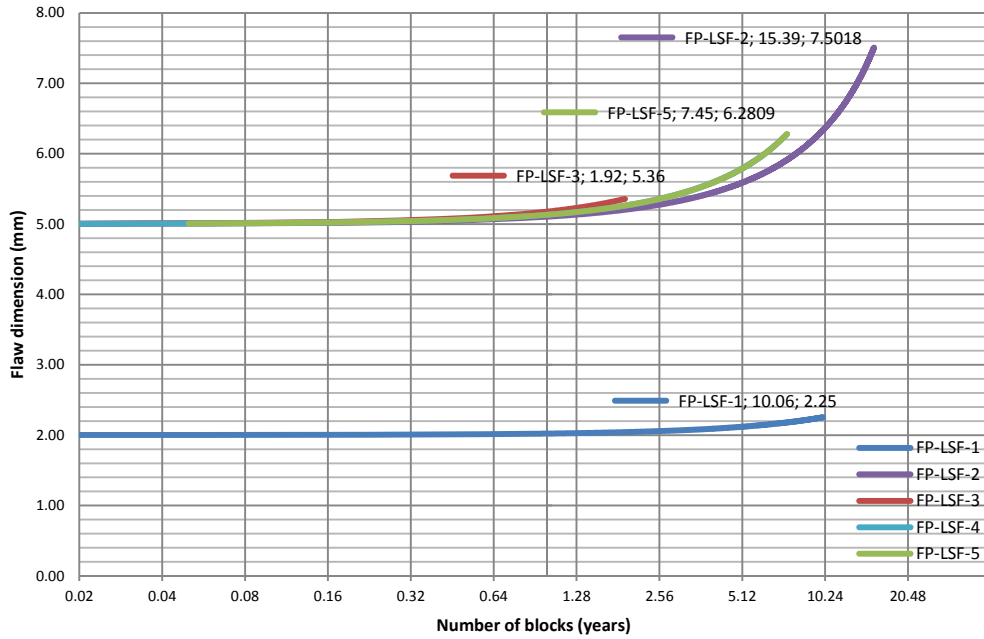
Fig.6.38. *Flat Plate Long Surface Flaw – FP-LSF – Flaw types comparison*
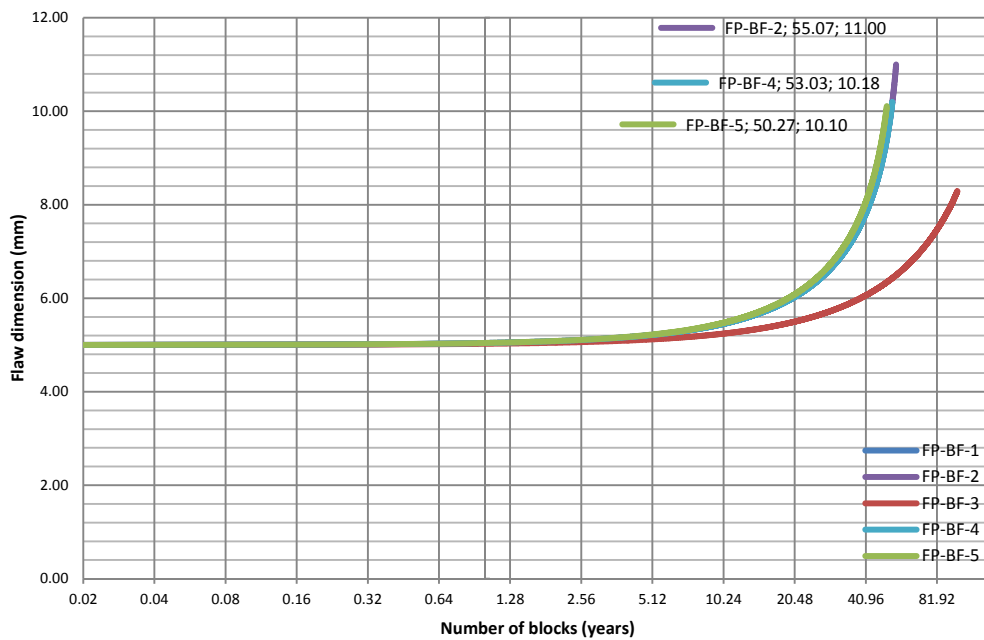
Fig.6.39. *Flat Plate Embedded/Buried Flaw – FP-BF – Flaw types comparison*
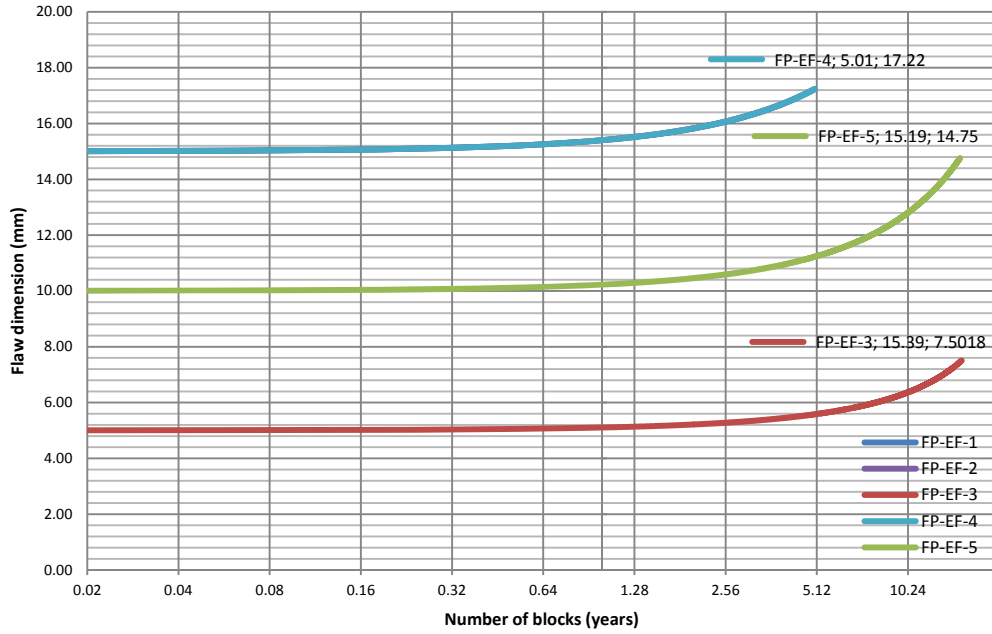
Fig.6.40. *Flat Plate Edge Flaw – FP-EF – Flaw types comparison*
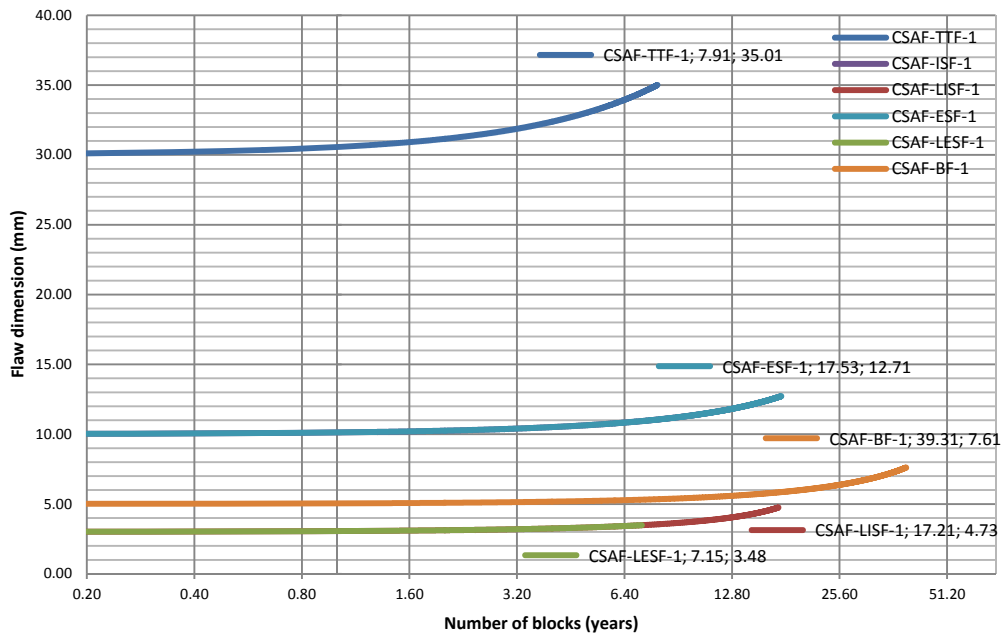
Fig.6.41. *Curved Shell Axial Flaw – CSAF – Flaw types comparison*
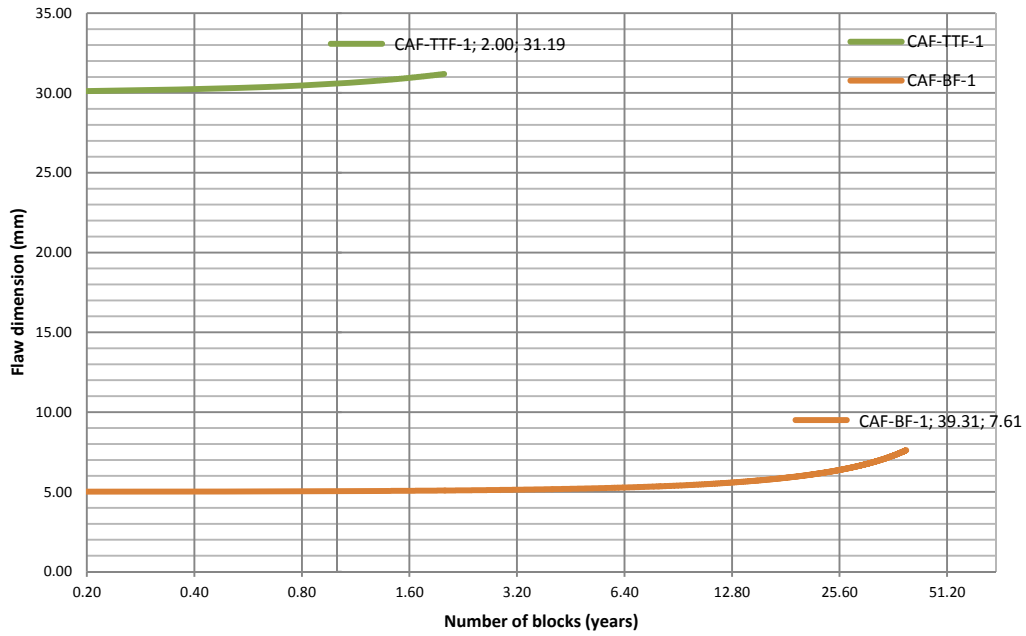
Fig.6.42. *Cylinder Axial Flaw – CAF – Flaw types comparison*
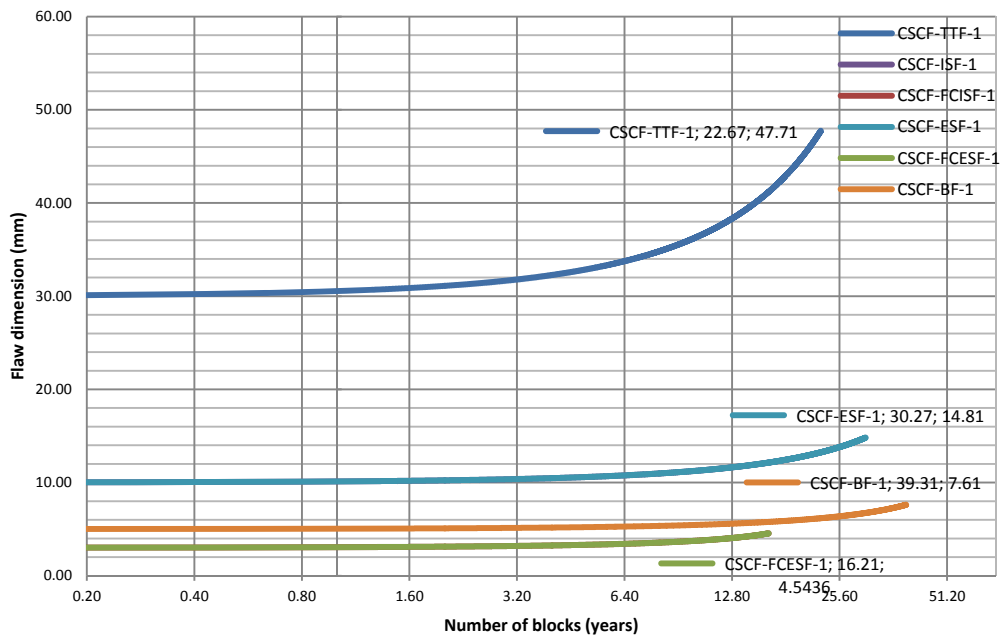
Fig.6.43. *Curved Shell Circumferential Flaw – CSCF – Flaw types comparison*
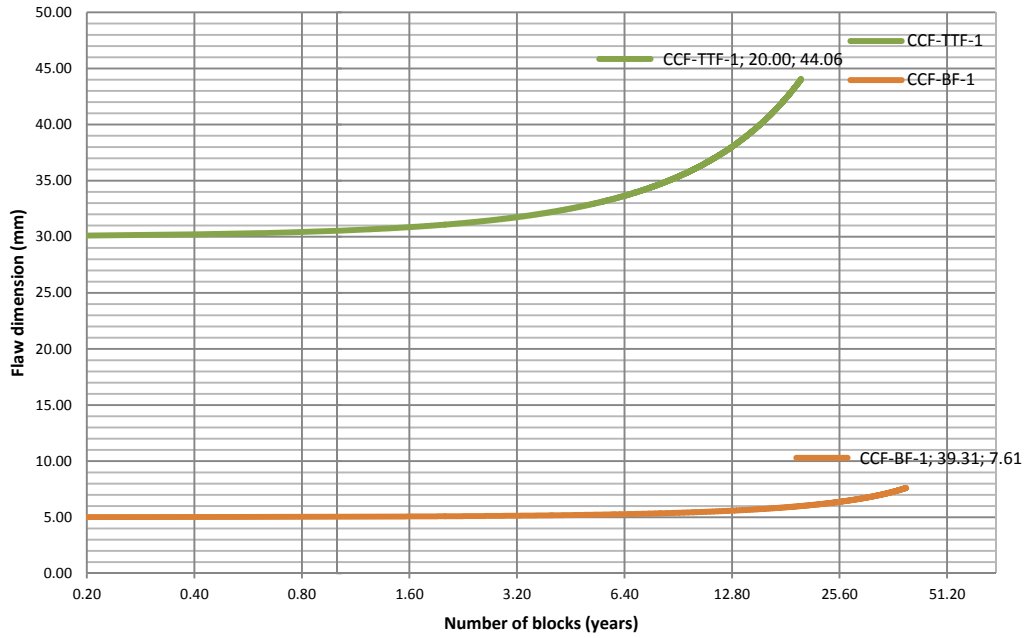
Fig.6.44. *Cylinder Circumferential Flaw – CCF – Flaw types comparison*
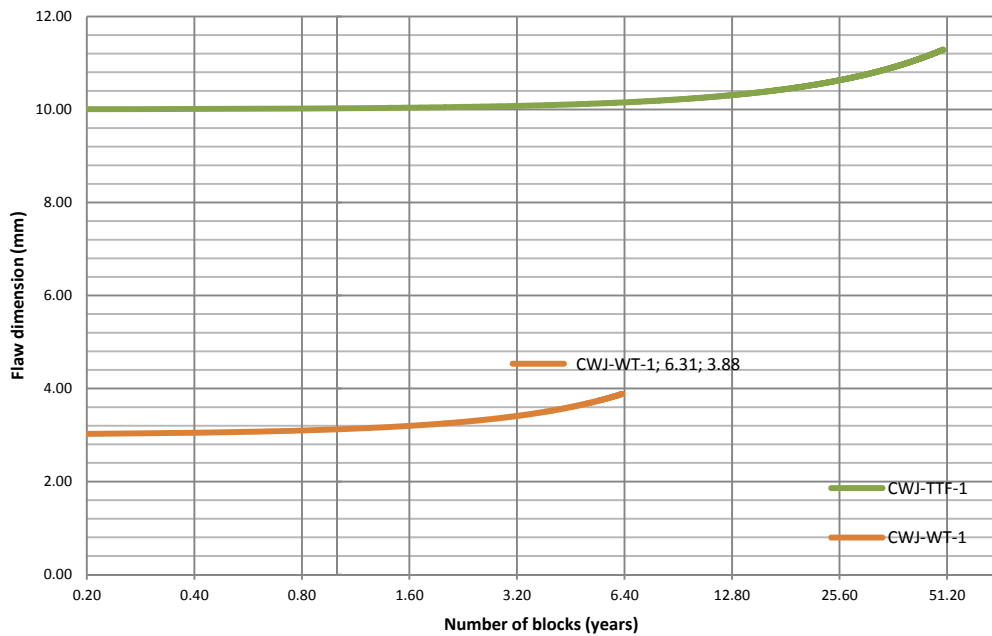
Fig.6.45. *Cruciform Welded Joint Flaw – CWJ – Flaw types comparison*

Concluding remarks

Following the fatigue assessment, the following conclusions can be made:

- For the flat plate through thickness flaw (FP-TTF), the most critical flaw type is the flaw FP-TTF-3 – crack of 10mm in flange to shell joint which is reaching a depth of 11.33mm in 10.04 years, time when the element is consider to fail under given loads;
- For the flat plate surface flaw type (FP-SF), the most critical flaw is FP-SF-1 type - on surface flaw of 5mm with length of 30mm in the shell in the area of high stress. The fatigue assessment reveals 10.02 years for the flaw to reach the critical dimensions – a_{cr} = 5,69 mm and $2c$ = 34.44 mm;
- For the flat plate long surface flaw – for FP-LSF-3 type flaw in 1.92 years (!!) a 5mm flaw is reaching a critical dimension of a_{cr} = 5.36mm;
- For the flat plate embedded/buried flaw, the most critical flaw type is the FP-BF-1 – embedded flaw in the area of shell wall nearby the segment joint. Thus, for this flaw, a length of 30, and a depth of 5mm in the wall thickness of 16mm, under cycling loads is producing a critical dimension in 39,23 years – a_{cr} = 7,59mm. The same type of flaw, but in the welding, is not producing major changes – no implication at the level of failure from fracture;
- For flat plate edge flaw type, the most critical flaw type are the FP-EF-1 and FP-EF-2 type, which represents edge flaw into the shell wall flaw EF-1 (near the service openings or technological holes), and the into the welding joint flange to shell wall (segment joint) – EF-2. Both flaw types are reaching critical values of a_{cr}=17.23 mm from a_0=15mm in 5.03 years (!!). The same values and speed of crack propagation are meet for the FP-EF-4 type flaw – flat plate edge flaw – edge flow in flange of the segment joint;
- For curved shell axial flaw (CSAF), the most critical type is the CSAF-LESF – curved shell axial long external surface flaw which is reaching a depth of 3.47mm from 3.00 mm in 7.16 years;
- For the cylindrical axial flaw, the most critical flaw is the CAF-TTF – through thickness type, flaw which is reaching a $2c_{cr}$ = 31.187mm from initial length of $2c_0$ = 30mm in 2.01 years (!!);
- For the curved shell circumferential flaw (CSCF), the most critical type is the fully circumferential internal surface flaw (FCISF) type, with a crack critical depth of 4.54 mm (from 3.00mm) reached in 16.19 years. Same results are for the fully circumferential external surface flaw (FCESF);
- The cylinder circumferential flaw is having critical values of TTF – through thickness type flaw, which is reaching from 30mm length to a critical $2c_{cr}$=30.166mm in 20 years;
- Regarding the cruciform welded joints (CWJ), the weld toe type (WT) is the most critical one with a critical depth of 3.88mm reached from 3.00mm in 6,31 years (!!).

Important note

All the assessment was done taken into account common flaws met in the life time of a shell type structure. For the flat plate (FP) type flaw was taken into account a length of the element of 200mm, considering that the major stress in the area of shell wall nearby and in segment joints elements (flange, welds) is

concentrated in the area of approximately 200mm. This distance was taken conservatively considering that can be the case of stress redistribution in the area of the shell wall. Thus further study was done considering a length of 500mm and 1000mm for the same type of flaws. The results are the same in matter of crack growth susceptibility. Below are presented some in comparison results.

FP-EF-1 – Flat plate – edge flaw – type 1 flaw

For W=500mm, the blocks (years) number increase from 5.03 (as for W=200mm) to 10.61, and the critical crack depth is increased from 17.23mm to 19.747mm. It can be noticed that considering the stress redistribution for an area of 500mm the lifetime of the structure is almost doubled.

For W=1000mm, the number of blocks (years) increase to 11.97 with a critical crack of 20.75mm.

It can be noticed that for this type of flaw the stress redistribution is not having major influence for areas larger than 500mm.

FP-LSF-4 – Flat plate – long surface flaw – type 4 flaw

For W=500mm, the blocks (years) number increase from 7.40 (as for W=200mm) to 7.42, and the critical crack depth is increased from 6.29mm to 6.27mm. It can be noticed that considering the stress redistribution for an area of 500mm the lifetime of the structure is almost unchanged.

For W=1000mm, the number of blocks (years) increase to 7.42 with a critical crack of 6.274mm.

It can be noticed that for this type of flaw the stress redistribution is not having major influence for areas larger than 200mm.

It can be concluded that taken into account stress redistribution in the area of the cylinder shell wall, the crack susceptibility remains.

Further study can be done reconsidering flaws for lower W dimensions and to re-evaluate the influence of stress distribution to a larger dimension scale.

References

[6.1] ***, BS 7910 / 2013, *"Guide to methods for assessing the acceptability of flaws in metallic structures"*, BSI British Standards

[6.2] M.F. Kanninen and C.H. Popelar, *"Advanced Fracture Mechanics"*, Oxford University Press, 1985

[6.3] R.H.Leggatt, *"Residual stresses in welded structures"*, International Journal of Pressure Vessels and Piping 85(3):144-151 · March 2008

[6.4] E. Petzek, *"Elaborarea de instructiuni pentru aplicarea principiilor mecanicii ruperii la stabilirea sigurantei in explatare si a duratei de viata ramase a podurilor metalice existente"*, Orizonturi Universitare Publishing house, Timisoara 2006

[6.5] D.Radu, A. Sedmak, *"Welding joints failure assessment – Fracture mechanics approach"*, Bulletin of the Transilvania University of Brasov, Vol.x.-2016, Series I: Engineering Sciences

[6.6] A. Sedmak, S. Sedmak, Lj. Milović, *"Pressure Equipment Integrity Assessment by Elastic-Plastic Fracture Mechanics Methods"*, DIVK, 2011

[6.7] Manjgo, M., et al, Sedmak, A., *"Analysis of welded tensile plates with a surface notch in the weld metal and heat affected zone"* ENGINEERING FRACTURE MECHANICS   Vol. 77 No.15, pp. 2958-2970 2010

[6.8] Medjo, B.; et al; Sedmak, A. *"Influence of crack length on ductile fracture initiation in welded joints with one and two weld metals"*, MATERIALS STRUCTURE & MICROMECHANICS OF FRACTURE 2011, 465:578-581

[6.9] Anderson, T.L., *"Fracture Mechanics – Fundamentals and Application"*, CRC Press Inc., Florida 1991

[6.10] Lungu D., van Gelder P., Trandafir R.,1996. *Comparative study of Eurocode 1, ISO and ASCE procedures for calculating wind loads*. IABSE Colloquium, Basis of Design and Actions on Structures, Background and Application of EUROCODE 1. Delft University of Technology, March 27-29, p.345-354

[6.11] INMH – wind load data in 2011, 2012 and 2013

[6.12] TWI CrackWise Software ver.5.0 – Documentation

[6.13] D.Radu, A. Sedmak, *"Design of cylindrical shell steel structures with billboard tower as the case study"*, TEAM2015 Conference, Belgrade 2015.

[6.14] A. Sedmak, D.Radu, *"Truss beams welded joints – manufacturing imperfections and strengthening solutions"*, DIVK Society for Integrity and life of Structures Journal Vol.14, No1, 2014, pp.29–34

[6.15] ***, EN 1090-2, *"Technical requirements for the execution of steel structures"*, European Committee for Standardisation (CEN), Brussels

[6.16] Radu D., Sedmak A., Simon Sedmak, Momčilo Dunjić *" Stress analysis of a steel structure comprising cylindrical shell with billboard tower"* – Technical Gazette Vol.25/no.2 (ISI Journal - Impact factor 2015: 0.464) – Accept for publication / Accept pentru publicare – see proof.

[6.17] Radu D., Feier A., Petzek E., Băncilă R., *"Refurbishment of existing steel structures – an actual problem"*, Periodica Polytehnica Civil Engineering (ISI Journal - Impact factor 2015: 0.271) Volumn 2016 paper 9140 DOI 10.3311/Ppci.9140 – Accept for publication / Accept pentru publicare – see proof.

7. CONCLUSIONS AND CONTRIBUTIONS

Life safety of the structures, which includes several important aspects of vulnerabilities, represents great importance matter in a society. When structures are collapsing, the after event consequences can be severe, with economic losses or even casualties.

In case of steel structures, existing of flaws in critical parts of structural elements may lead to failures of the element and in case of lack of redundancy, even to the collapse of the entire structure.

The present thesis research is focused on fracture mechanics approach in assessing the existing flaws in steel shell structures and also presenting algorithms and procedures for designing structural elements taken into account future potential flaws affect.

Engineering critical assessment (ECA) is a fracture mechanic approach applied in expertise of the existing pipeline, pressure vessels and offshore type structures. A design and expertise ECA type is imposed also at common bridge or civil type structures. The Eurocode provisions and standards are presenting only a conservative approach with two implications:

- Designing process with requirements in the calculation of the elements [7.1] and or the joints (e.g. welded joints) [7.2]
- Manufacturing and erection with requirements for the quality of the steel structure [7.3] (which includes also the welding as a manufacturing process)

In present standards, there are not so clear indications about the need of additional investigations or assessment of possible flaw occurrence, but at European Commission level there are several proposals to change perspective regarding the need for assessment of the structures. Future provisions will include the inspection intervals and expertise of the structures as a mandatory procedure for existing buildings.

The thesis is presenting a detailed methodology for assessment and determination of the acceptability of flaws resulted from service life and detected in shell steel structures. Based on fracture mechanics approach, there are presented procedures and rules needed in maintenance, expertise and checking of these types of structures. This method of assessment of flaws/cracks represents the first step within a complex methodology based on fracture mechanics principle and followed by fatigue analysis of the assessed elements through which can be determined the remaining in service lifetime of the structure/elements of the structure.

The content of the thesis is described below:

Chapter 1

In Chapter 1 – Introduction is presented the importance of the topic. There are detailed several main flaws possible present in the steel shell type structures, factors for brittle fracture and different types of flaws causes.

Also is presented a study case – Aleksander Kielland drilling rig capsize, with direct cause – failure of a bracing due to fatigue. A fracture mechanics and fatigue approach is imposed for studying the fitness for service of the existing and designed structures.

Chapter 2

In Chapter 2 there is presented a synthesizing information regarding the fracture mechanics and application at steel shell structures. Linear elastic fracture

mechanics to elastic plastic fracture mechanics and fatigue calculation are prerequisite for the subsequent chapters research. Standards methods for fracture parameters testing are presented.

Following fracture mechanics approach, based on damage cumulation principle, in service structure safety assessment can be made. A detailed procedure of this process is presented.

Chapter 3

The chapter is presenting the EN design approach [7.4] for steel shell elements. The buckling strength is the most important parameter in the design of these types of structures. Generally buckling may be defined as the sudden failure, or instability, of a structural member subject to compression load. This instability occurs at a maximum point on the load-deflection curve at which point instability may fall into one of two categories: *Bifurcation of Equilibrium* or *Limit Load Buckling.* The important of imperfections of the shell elements is underlined and several design principles with direct application are revealed.

The thesis is presenting a study case – a steel shell structure billboard tower thirty meters high. There is presented EN load design procedure together with the load assumption process. In order to provide the needed input data for the Chapter 6 fatigue design, a detailed wind load calculation was done. Wind load evaluation is done for the given case – a detailed load evaluation is presented in Annex 1.

For determining the stresses in the shell elements, an in depth FEM type analysis was done in the area of a segment joint. Following the results, there were revealed stresses in the area of the welded joints.

Chapter 4

The Finite Element Method is applied for the shell structure billboard tower type. The tower presents a circular cross section with a diameter of 1680mm and is mate of four segments - from the base to the top: Tube 1680 x 20 mm – 7 m, Tube 1680 x16 mm – 8 m, Tube 1680 x 12 – 7 m and Tube 1680 x 10 – 8 m. In a first step, the entire structure is considered and analysed – linear structural analysis (LA), in order to determine the stresses in the critical sections. Following the results, the main internal forces on each section and the maximum Von Mises stress of the tower are presented.

After the linear analysis (LA), the buckling design forces are analytical calculated. Determining the critical stresses, the meridian and circumferential stress, is done using annex D ([7.4] – buckling design of the unstiffened shell element. The design of the stresses which appear in the walls of the tube pillar is done using annex A2 [7.4] using shell theory. A detailed design for the shell elements (each segment) is presented in Annex 2.

A second step of the design is using FEM to the segment joint design – the joint with the higher stress is taken into account. Different sections stress results were compared with the previous FEM analysis – the results were similar (with slight differences).

For the segment joint model is done also an advanced analysis - linear buckling analysis (LBA). The elastic critical buckling resistance ratio r_{Rcr} is determined from this eigenvalue analysis (LBA) applied to the linear elastic calculated stress state in the geometrically perfect shell (LA) under the design values of the load combination. The first ten buckling eigenvalues were calculated, thus resulting the critical buckling resistance value $r_{Rcr} = 1.154$, value used as a multiplication factor for the elastic loads ($F_{Rk} = r_{Rcr} \cdot F_{Ed}$).

All buckling eigenmodes present deformed shapes (buckling) at the lower part of the 16 mm thickness segment – nearby the joint area (immediately to the joint stiffeners).

A comparison is done between values analytical calculated based on LA results [7.4] – Annex 2, and the LBA results. The conclusion is that the EN analytical calculated results are conservative.

Chapter 4 presents also the application of FEM in analysis of behaviour of steel elements and welded joints with cracks as a prerequisite for chapter 6.

Chapter 5

At chapter 5 is presented a detailed experimental part for material and fracture mechanic testing which include the chemical analysis of the steel composition, traction tests, Charpy V-notch test, in order to determine the amount of energy absorbed by a material during fracture, the J integral curve, the fatigue crack growth.

The laboratory testing and measurements were done at Faculty of Mechanical Engineering – University of Belgrade and also at the Technical University of Timișoara.

Following the test results complex fracture and fatigue calculations were done (chapter 6).

Chapter 6

The structural integrity and life assessment can be considered as a mandatory request in the designing and manufacturing process.

Chapter 6 is presenting the procedure for determination of crack acceptability based on fracture toughness with Failure Assessment methods (FAD-1 and FAD-2) which can be applied to any type of steel shell structure with welded joints. Different types of locations were taken into account – from in the plate flaw (e.g. flange plate joint near the welded joint), to the curved shell circumferential flaw (e.g. in the shell element).

The assessment is using BS7910 /2013. Thus were assessed common ten types of flaws met at steel shell cylindrical structure elements using failure assessment diagrams – level 1 – FAD -1. The results are presented the acceptability level for each type of flaw with comparative graphs, determining also the critical dimension of the flaw.

The level 2 assessment approach (FAD-2) is done for 43 types of steel shell elements flaws.

For each flaw was calculated the failure assessment diagram (FAD-2) (presented in Annex 3). Different comparisons between group of flaws were done, revealing the critical crack like flaw. Also the critical value of flaw dimensions were calculated for each flaw type.

A major contribution is done in Chapter 6, presenting the procedure for determining the safety in service of the shell steel structures using engineering critical assessment approach.

The methodology establishes clear rules for assessment of structural elements with cracks, determining the initial flaws, assessed flaws and critical values of the cracks. A detailed fatigue design and assessment procedures are presented.

Using CrackWise software, there was applied fatigue based engineering critical assessment on a real case – the billboard tower like steel shell cylindrical structure. For the fatigue evaluation, a detailed wind load calculation was done taken into account the cycles given for a wind recording (data supplied by the

Romanian INMH institute). Following the structural analysis of the five load cases, was assessed the stress in the structure segment joint. Using Rainflow algorithm, the results were processed and was determined the block of stresses with stress ranges and the appearance frequency of them.

For all 43 flaw type cases, the fatigue ECA approach was applied, revealing the number of cycles – cumber of blocks (years) until failure. For the flat plate type flaws (FP type), several assessments were done – the B dimension (indicated the length of the stress affected area), was taken as 200mm, 500mm and 1000mm, thus underlining the stress redistribution in the shell element.

For each type of flaw the ECA was applied and resulted a plotted graph indicating the number of years until failure and the critical flaw dimension (results presented in Annex 4). All the results were compared and were revealed the most critical flaws – with the lower number of years until failure.

Based on the detailed procedures described in Chapter 6, on conclusions to the assessment done on each type of flaw, the assessment methods can be applied very easy in current design practice with different material characteristics.

The presented study is based on experimental results done at Faculty of Mechanical Engineering University of Belgrade and also at the Technical University Timișoara, and revealed the needed parameters ($K, J, δ$) on which are based the fracture mechanics principles.

The main personal contributions, through the research, are the followings:

- Fracture mechanic approach for steel shell structures

- Shell type structures FEM design for a given case

- Experimental research for determining the fracture mechanics parameters

- Engineering critical assessment, a prerequisite in design and expertise of steel shell structures

The main features of ECA approach in this thesis are:
- o   Better safety of the shell structures
- o   Defining the service inspections intervals
- o   Risk under control
- o   In service lifetime assessment
- o   Determining the inspection intervals

ECA is an engineering design approach trend that will continue to evolve from the structural design from to the manufacturing process.

Future study directions

The present thesis is revealing the importance of the engineering critical assessment for the steel shell structures – cylindrical type. Future study and research direction may be the improvement of the assessment using ECA fracture mechanics and fatigue for different types of structures and structural elements.

Standards and provisions must be more interdisciplinary. In order to reduce the failure risk, based on optimisation procedures and to determine the in service life time of the structures, the ECA approach must be a prerequisite for expertise and even design of the steel shell elements.

Reference

[7.1] ***, Eurocode 1993 - *Design of steel structures, part 1–1: General rules*, European Committee for Standardisation (CEN), Brussels, 2006

[7.2] ***, Eurocode 1993 - *Design of steel structures, part 1–8: Joints design*, European Committee for Standardisation (CEN)., Brussels; 2006

[7.3] ***, EN 1090-2, "*Technical requirements for the execution of steel structures*", European Committee for Standardisation (CEN)

[7.4] ***, Eurocode 1993 - *Design of steel structures, part 1-6: Strength and Stability of Shell Structures*, European Committee for Standardisation (CEN), Brussels, 2006

Annex 1 – Tower loads evaluation

A1.1. Self weight load

The self weight load is taken by the analysis software.

A1.2. Dead load

- Dead load of the billboard   =   1,35 kN/m

A1.3. Live load

- Service load due to maintenance   =   1,50 kN/m^2

A1.4. Wind load

A1.4.1. Calculation of $q_p(z_e)$

According with SR EN 1991-1-4/2006 NB/2007, Brasov city is in the wind load with – $v_{b,0}$ = 27 m/s.

$$q_p(z) = [1+7 \cdot I_v(z)] \cdot 0,50 \cdot \rho \cdot v^2_m(z)$$

$z_e = h$ = 28,00 m
ρ = 1.25 kg/m^3
cdir   = 1,00
cseason   = 1,00

v_b = $c_{dir} \cdot c_{season} \cdot v_{b,0}$ = 1,00 $\cdot$ 1,00 $\cdot$ 27,00 m/s   = 27,00 m/s
$v_m(z)$ = $c_r(z) \cdot c_0(z) \cdot v_{b,0}$= 0.975 $\cdot$ 1,00 $\cdot$ 27,00 m/s = 26,33 m/s

where: $c_0(z)$ = 1,00
            $c_r(z)$ = $k_r \cdot \ln(z/z_0)$ = 0.975
            z_0 = 0,30m (Terrain category III)
            k_r = 0,19 $\cdot$ $(z_0/z_{0II})^{0,07}$ = 0,215

$I_v(z)$ = $k_1 / (c_0(z) \cdot \ln(z/z_0))$ = 0,220

$q_p(z)$ = 1102 N/m^2 = 1,102 kN/m^2

Conclusion: **w_e =   1,102$\cdot$ c_{pe} [kN/m^2]**

Table A1.1. *Values of the wind forces at different heights*

Height	cr(z)	$v_m(z)$	$I_v(z)$	$q_p(z)$	
(m)				(N/m²)	
2	0.605	16.332	0.527		782
3	0.605	16.332	0.434		674
4	0.605	16.332	0.386		617
5	0.605	16.332	0.355		581
6	0.644	17.390	0.334		631
7	0.677	18.285	0.317		673
8	0.706	19.060	0.305		711
9	0.731	19.744	0.294		745
10	0.754	20.356	0.285		776
11	0.774	20.909	0.278		804
12	0.793	21.414	0.271		830
13	0.810	21.879	0.265		855
14	0.826	22.309	0.260		878
15	0.841	22.709	0.256		899
16	0.855	23.084	0.251		919
17	0.868	23.436	0.248		938
18	0.880	23.768	0.244		957
19	0.892	24.082	0.241		974
20	0.903	24.379	0.238		991
21	0.913	24.663	0.235		1007
22	0.923	24.933	0.233		1022
23	0.933	25.191	0.230		1036
24	0.942	25.438	0.228		1050
25	0.951	25.675	0.226		1064
26	0.959	25.902	0.224		1077
27	0.967	26.121	0.222		1090
28	0.975	26.333	0.220		1102

A1.4.2. Calculation of $c_s \cdot c_d$ coefficient

$$c_s c_d = \frac{1 + 2 \cdot k_p \cdot I_v(z_s) \cdot \sqrt{B^2 + R^2}}{1 + 7 \cdot I_v(z_s)}$$

$$z_s = z_e \qquad = 28,00 \text{ m}$$

$$k_p = \sqrt{2 \cdot ln(v \cdot T)} + \frac{0,6}{\sqrt{2 \cdot ln(v \cdot T)}}$$

$$v = n_{1,x} \sqrt{\frac{R^2}{B^2 + R^2}}$$

Dynamic analysis results

Table A1.2. *Frequency results in each mode*

Mode	f	T
	[Hz]	[s]
1	0.79	1.26
2	0.79	1.26
3	1.31	0.76
4	3.16	0.32
5	3.16	0.32
6	5.26	0.19
7	8.05	0.12
8	8.07	0.12
9	8.07	0.12
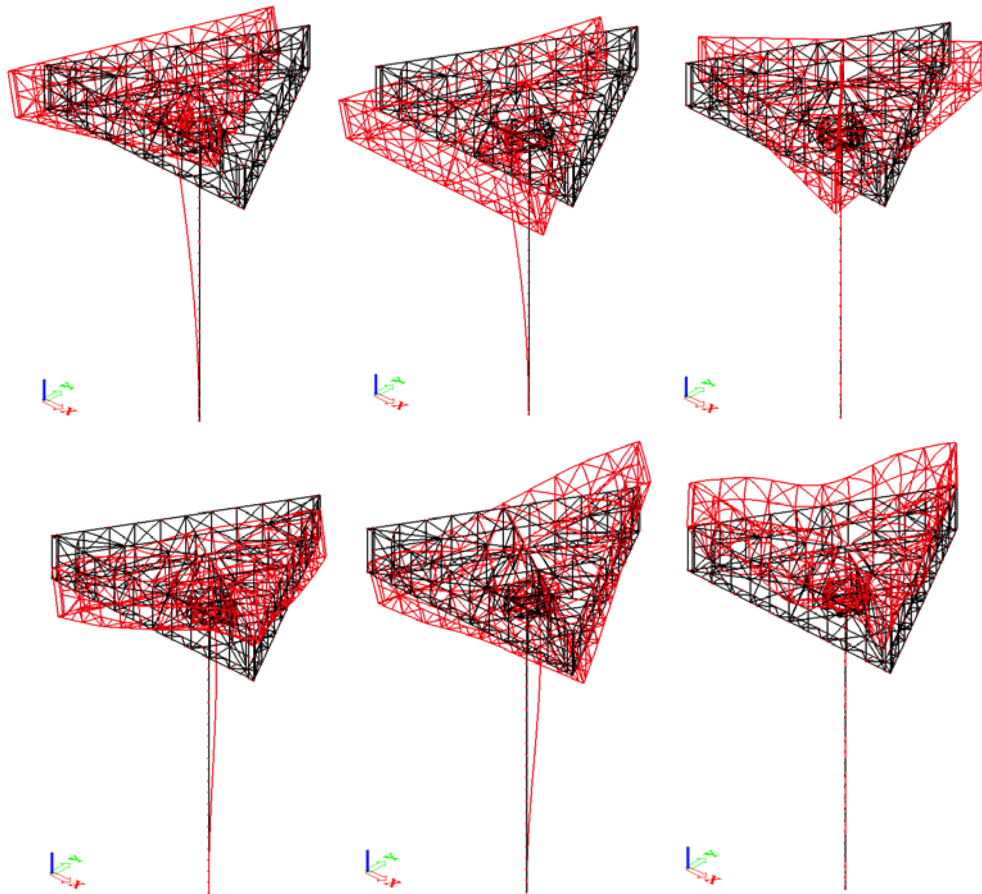
Fig.A1.1. *Dynamic analysis results – deformed structure in mode 1, 2, 3, 4, 5, 6*

$\eta_{1,x}$ = 0,79 Hz   (following dynamic analysis of the structure)

$$B^2 = \frac{1}{1 + 0,9 \cdot \left(\frac{b+h}{L(z_s)}\right)^{0,63}}$$

$$L(z_s) = L_t \cdot \left(\frac{z_s}{z_t}\right)^a \qquad \text{for } z_{min} \leq z_s \leq z_{max}$$

$$L(z_s) = L(z_{min}) \text{ for } z < z_{min}$$

z_t = 200 m, $\qquad\qquad$ L_t = 300m

α = 0,67 + 0,05 ln(z_0) = 0,59

$L(z_s)$ $\qquad\qquad$ = 94,133 m

$$B^2 = \frac{1}{1 + 0,9 \cdot \left(\frac{21+4}{94,133}\right)^{0,63}}$$

B^2 $\quad$ = 0,719

$$R^2 = \frac{\pi^2}{2 \cdot \delta} \cdot S_L(z_s, n_{1,x}) \cdot R_h(\eta_h) \cdot R_b(\eta_b)$$

$$S_L(z_s, n_{1,x}) = \frac{6,8 \cdot f_L(z_s, n_{1,x})}{(1 + 10,2 \cdot f_L(z, n_{1,x}))^{5/3}}$$

$$f_L(z_s, n_{1,x}) = \frac{n_{1,x} \cdot L(z_s)}{v_m(z_s)}$$

$v_m(z_s) = c_r(z_s) v_b = 0,975 \cdot 27,00$ $\qquad$ = 26,32 m/s

$$f_L(z_s, n_{1,x}) = \frac{0,79 \cdot 94,133}{25,348}$$

f_L = (0,79 · 94,133) / 26,32 $\qquad\qquad$ = 2,825

S_L = (6,8 · 2,825) / (1+10,2 · 2,825)$^{5/3}$ $\qquad$ = 0,067

$\delta = \delta_s + \delta_a + \delta_d$

$$\delta_a = \frac{c_f \cdot \rho \cdot b \cdot v_m(z_s)}{2 \cdot n_1 \cdot m_e}$$

c_f $\qquad$ = 1,80

ρ $\qquad$ = 1.25 kg/m^3

b $\qquad$ = 21,00 m

n_1 $\qquad$ = 0,69 Hz

$v_m(z_s)$ = 26,32 m/s

$$m_e = \frac{\int_0^l m(s) \cdot \varphi_1^2(s)ds}{\int_0^l \varphi_1^2(s)ds}$$

m_e = 3433,643 kg/m

δ_a = (1,80 · 1,25 · 21 · 26,32) / (2 · 0,69 · 3433,643) = 0,262 m
δ_s = 0,05 m
δ_d = 0,00 m

$\delta = \delta_s + \delta_a + \delta_d$ = 0,05 + 0,221 + 0,00 **= 0,312 m**

$$R_h = \frac{1}{\eta_h} - \frac{1}{2 \cdot \eta_h^2}\left(1 - e^{-2 \cdot \eta_h}\right)$$

$$R_b = \frac{1}{\eta_b} - \frac{1}{2 \cdot \eta_b^2}\left(1 - e^{-2 \cdot \eta_b}\right)$$

$$\eta_h = \frac{4,6 \cdot h}{L(z_s)} \cdot f_L(z_s, n_{1,x})$$

$$\eta_b = \frac{4,6 \cdot b}{L(z_s)} \cdot f_L(z_s, n_{1,x})$$

η_h = (4,6 · 4 · 2,825) / 94,133   = 0,552
η_b = (4,6 · 21 · 2,825) / 94,133   = 2,899

R_h = 1 / 0,552 − 1 / (2 · 0,552^2) · (1-e$^{-2 · 0,573}$)   = 0,692
R_b = 1 / 2,899 − 1 / (2 · 2,899^2) · (1-e$^{-2 · 3,011}$)   = 0,285

$$R^2 = \frac{\pi^2}{2 \cdot \delta} \cdot S_L(z_s, n_{1,x}) \cdot R_h(\eta_h) \cdot R_b(\eta_b)$$

R^2   = (π^2/2*0,312) * 0,067 * 0,692 * 0,285   **= 0,208**

$$v = n_{1,x} \cdot \sqrt{\frac{R^2}{B^2 + R^2}}$$

$$v = 0,69\sqrt{\frac{0,208}{0,719 + 0,208}} = 0,326 Hz > 0,08 Hz$$

$$k_p = \sqrt{2 \cdot In(v \cdot T)} + \frac{0,6}{\sqrt{2 \cdot In(v \cdot T)}} = \sqrt{2 \cdot In(0,326 \cdot 600)} + \frac{0,6}{\sqrt{2 \cdot In(0,326 \cdot 600)}}$$

k_p = 3,486

$$I_v(z) = k_1 / (c_0(z) \cdot \ln(z/z_0)) \qquad = 0{,}202$$

$$c_s c_d = \frac{1 + 2 \cdot k_p \cdot I_v(z_s) \cdot \sqrt{B^2 + R^2}}{1 + 7 \cdot I_v(z_s)} = \frac{1 + 2 \cdot 3{,}486 \cdot 0{,}220 \cdot \sqrt{0{,}719 + 0{,}208}}{1 + 7 \cdot 0{,}220}$$

$c_s c_d$ = 0,984

A1.4.3. Wind load onto the billboard

The load is considered according with SR EN 1991-1-4 – Ch.7.4.3.
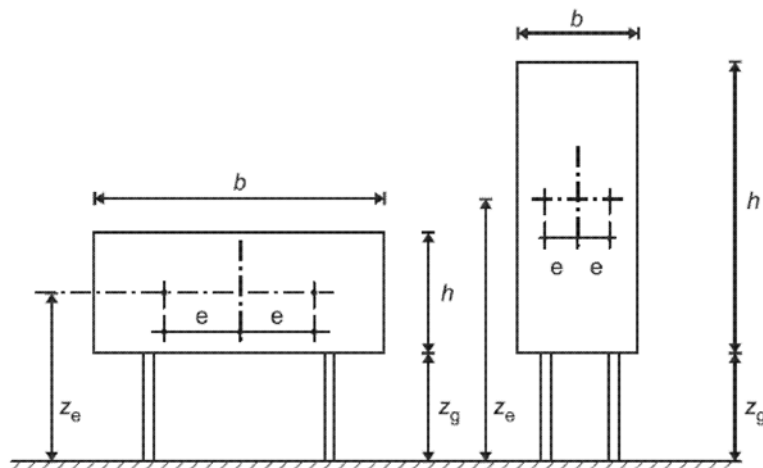
Fig. A1.2. *EN1991-1-4 Definition of denominations*

b   = 21,00 m
h   = 4,00 m
z_g = 26,00 m
z_e = 28,00 m
e   = +/- 0,25b   = +/- 5,25 m
c_f = 1,80
$c_s \cdot c_d$ = 0,984

$$F_w = c_s \cdot c_d \cdot c_f \cdot q_p(ze) \cdot A_{ref} = 0{,}984 \cdot 1{,}80 \cdot 1{,}102 \cdot 21{,}00 \cdot 4{,}00 \qquad = 163{,}95 \text{ kN}$$

A1.4.4. Wind load onto the cylindrical tower

A1.4.4.1. Calculation of the external pressure w_e

According with SR EN 1991-1-4 – Ch.5.2.
$$we = q_p(z_e) \cdot c_{pe}$$
Calculation of the external pressure is done according with SR EN 1991-1-4 – Ch.7.9.1.

BUPT

Pressure coefficients of circular sections depend upon the Reynolds number Re, defined as:

$$Re = \frac{b \cdot v(z_e)}{v}$$

Where   b   = 1,68 m   – diameter of the cylinder
        v = 15 · 10⁻⁶ m²/s   – kinematic viscosity of the air

$$v(z_e) = \sqrt{\frac{2 \cdot q_p(z_e)}{\rho}}$$ – main wind velocity at height of z_e

In our case:
        z_e = 28,00 m
        $v(z_e)$ = 41,99 m/s
        Re = 4,702 · 10⁶

Following the interpolation results:

        α_{min} = 78,52°

        $C_{p0,min}$ = 1,782

        α_A = 115,6°

        $c_{p0,h}$ = 0,730

$$\begin{cases} \psi_{\lambda a} = 1 \\ \psi_{\lambda a} = \psi_\lambda + (1 - \psi_\lambda) \cdot \cos\left(\frac{\pi}{2} \cdot \left(\frac{a - a_{min}}{a_A - a_{min}}\right)\right) \\ \psi_{\lambda a} = \psi_\lambda \end{cases} \text{ when } \begin{cases} 0° \le a \le a_{min} \\ a_{min} < a < a_A \\ a_A \le a \le 180° \end{cases}$$

        b   = 1,68 m
        h   = 26,00 m

When α = 90°

        $h_1 \ge 50,00m$ $\Rightarrow$ $\lambda_1 = min\left(0,7 \cdot \frac{h}{b}, 70\right)$ = 10,833

        $h_2 \le 15,00m$ $\Rightarrow$ $\lambda_2 = min\left(\frac{h}{b}, 70\right)$ = 15,476

                           $\Rightarrow$ λ = 14,01
                                           φ = 1,00
                                           ψ_λ = 0,72
                                           $\psi_{\lambda\alpha}$ = 0,968

Table A1.3 *Values of the distributed wind forces on the tower surface*

α	c_{p0}	$\psi_{\lambda a}$	c_{pe}	w_e (kN/m^2)
0°	1	1,00	1	1,102
30°	0,1	1,00	0,1	0,110
60°	-1,25	1,00	-1,25	-1,377
90°	-1,65	0,968	-1,597	-1,759
120°	-0,75	0,720	-0,540	-0,595
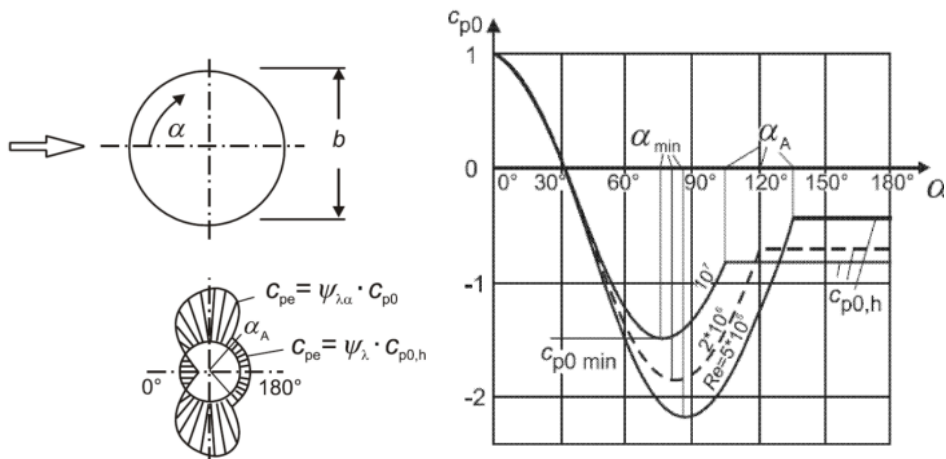
Fig.A1.3. *Pressure distribution for cilinders for differrent Reynolds number values*

A1.4.4.1. Calculation of the force coefficient (for the wind force)

$$\mathbf{C_f = C_{f,0} \cdot \psi_\lambda}$$

k	= 0,20 mm	Tab. 7.13 (SR EN 1991-1-4)
b	= 1680 mm	

$\dfrac{k}{b} = \dfrac{0,20}{1680}$ = 1,19 $\cdot 10^{-4}$

Re   = 4,702 $\cdot 10^6$

$$c_{f,0} = 1,2 + \frac{0,18 \cdot log\left(10 \cdot \dfrac{k}{b}\right)}{1 + 0,4 \cdot log\left(\dfrac{Re}{10^6}\right)} = 0,782$$

$c_f = c_{f,0} \cdot \psi_\lambda$ = 0,562

A1.4.4.3. Wind force calculation F_w

b	= 1,68 m
c_f	= 0,562

$$c_s \cdot c_d \quad = 0.984$$
$$A_{ref} \quad = b \cdot l$$

$$F_w = c_s \cdot c_d \cdot c_f \cdot q_p(z_e) \cdot A_{ref}$$

Table A1.4 *Values of the concentrated wind forces on the tower surface*

z_e	l	A_{ref}	$q_p(z_e)$	F_w	F_w/l
2.00	2.00	3.36	0.782	1.453	0.727
5.00	3.00	5.04	0.581	1.619	0.540
9.00	4.00	6.72	0.745	2.769	0.692
13.00	4.00	6.72	0.855	3.177	0.794
17.00	4.00	6.72	0.938	3.486	0.871
21.00	4.00	6.72	1.007	3.742	0.936
24.00	3.00	5.04	1.050	2.927	0.976
26.00	2.00	3.36	1.077	2.001	1.001

Annex 2 – Tower shell elements design

A2.1. Segment Section t = 10 mm

D_1 = 1680 mm

t = 10 mm

$D_c = D_1 - 2 \cdot t$ = 1660 mm

l = 30,00 m

$A_t = \pi \cdot \left[\left(\dfrac{D_1}{2} \right)^2 - \left(\dfrac{D_2}{2} \right)^2 \right]$ = 52464,6 mm^2

ρ_{OL} = 7850 kg/m^3

$g_t = \rho_{OL} - A_t$ = 411,847 kg/m

$r = \dfrac{D_1}{2} - \dfrac{t}{2}$ = 835 mm - over the median surface

- **Forces**

N_{Ed} = 372,91 kN

$V_{y,Ed}$ = 130,56 kN

$V_{z,Ed}$ = 224,70 kN

$M_{t,Ed}$ = 1120,24 kNm

$M_{y,Ed}$ = 1430,97 kNm

$M_{z,Ed}$ = 673,47 kNm

For z_e = 26,00 m

$q_{w,max}$ = 0,95 kN/m^2

c_θ = 0,60   - (EN1993-1-6 - D.3 annex D)

q_s = 0 MPa

$\omega = \dfrac{l}{r} \cdot \sqrt{\dfrac{r}{t}}$ = 328,305   - (EN1993-1-6 - annex D)

$k_w = max\left[0{,}46 \cdot \left(1 + 0{,}1 \cdot \sqrt{\dfrac{c_\theta}{\omega} \cdot \dfrac{r}{t}} \right); 0{,}65 \right]$ = 0,65

$q_{eq} = k_w \cdot q_{w,max}$ = 0,000617 MPa

- **Calculation of the stresses**

Materials

f_{yk} = 355 MPa

E = 2,1 · 10^5 MPa

f_u = 510 MPa

γ_{M0} = 1,0

γ_{M1} = 1,1

γ_{M2} = 1,25

Stresses calculations

$$\sigma_{x,Ed,1} = -\frac{N_{Ed}}{2 \cdot \pi \cdot r \cdot t} + \frac{M_{y,Ed}}{\pi \cdot r^2 \cdot t} + \frac{M_{z,Ed}}{\pi \cdot r^2 \cdot t} \qquad = 88,968 \text{ MPa}$$

$$\sigma_{x,Ed,2} = -\frac{N_{Ed}}{2 \cdot \pi \cdot r \cdot t} - \frac{M_{y,Ed}}{\pi \cdot r^2 \cdot t} - \frac{M_{z,Ed}}{\pi \cdot r^2 \cdot t} \qquad = -103,184 \text{ MPa}$$

$$\sigma_{x,Ed} = max\left(\left|\sigma_{x,Ed,1}\right|, \left|\sigma_{x,Ed,2}\right|\right) \qquad = 103,184 \text{ MPa}$$

$$\sigma_{\theta,Ed} = \left(q_{eq} + q_s\right) \cdot \left(\frac{r}{t}\right) \qquad = 0,052 \text{ MPa}$$

$$\tau_{x,\theta,Ed,1} = \frac{M_{t,Ed}}{2 \cdot \pi \cdot r^2 \cdot t} + \frac{V_{z,Ed}}{\pi \cdot r \cdot t} \qquad = 33,909 \text{ MPa}$$

$$\tau_{x,\theta,Ed,2} = \frac{M_{t,Ed}}{2 \cdot \pi \cdot r^2 \cdot t} - \frac{V_{z,Ed}}{\pi \cdot r \cdot t} \qquad = 16,778 \text{ MPa}$$

$$\tau_{x,\theta,Ed} = max\left(\left|\tau_{x,\theta,Ed,1}\right|, \left|\sigma_{\tau_{x,\theta,Ed,2}}\right|\right) \qquad = 33,909 \text{ MPa}$$

$$\tau_{x,n,Ed} \qquad = 0 \text{ MPa}$$

$$\tau_{\theta,n,Ed} \qquad = 0 \text{ MPa}$$

According with EN 1993-1-6 Cap 6.2.1(6), equivalent stress is calculated with:

$$\sigma_{eq,Ed} = \sqrt{\sigma_{x,Ed}^2 + \sigma_{\theta,Ed}^2 - \sigma_{x,Ed} \cdot \sigma_{\theta,Ed} + 3 \cdot \left(\tau_{x,\theta,Ed}^2 + \tau_{x,n,Ed}^2 + \tau_{\theta,n,Ed}^2\right)}$$

$$= 118,706 \text{ MPa}$$

$$f_{eq,Rd} = \frac{f_{yk}}{\gamma_{M0}} = 355 \text{ MPa}$$

The stress check:

$$\sigma_{eq,Rd} \leq f_{eq,Rd}$$

$$Ratio_1 = \frac{\sigma_{eq,Rd}}{f_{eq,Rd}} = 0,334$$

- **Buckling design**

   According with EN 1993-1-6 Ch. 8.5 & Annex D:

$$\omega = \frac{l}{r} \cdot \sqrt{\frac{r}{t}} \qquad\qquad = 328,305$$

$$c_\theta \qquad\qquad = 3$$

$$c_x = \begin{cases} 1, \text{if } 1{,}7 \leq \omega \leq 0{,}5 \cdot \dfrac{r}{t} \\[2mm] \left(1{,}36 - \dfrac{1{,}83}{\omega} + \dfrac{2{,}07}{\omega^2}\right), \text{if } \omega \leq 1{,}7 \\[2mm] max\left[0{,}6, 1 + \dfrac{0{,}2}{c_{xb}} \cdot \left(1 - 2 \cdot \omega \cdot \dfrac{t}{r}\right)\right], \text{if } \omega > 0{,}5 \end{cases} \qquad c_x = 0{,}6$$

$$\sigma_{x,Rcr} = 0{,}605 \cdot E \cdot c_x \cdot \frac{t}{r} \qquad\qquad = 912{,}934 \text{ MPa}$$

$$Q \qquad\qquad\qquad = 16 \qquad\qquad \text{- Tab D.2 - Annex D}$$

$$\Delta w_k = \frac{1}{Q} \cdot \sqrt{\frac{r}{t}} \cdot t \qquad = 5{,}711 \text{ mm}$$

$$a_x = \frac{0{,}62}{1 + 1{,}91 \cdot \left(\dfrac{\Delta w_k}{t}\right)^{1{,}44}} \qquad\qquad = 0{,}335$$

$$\lambda_{x0} \quad = 0{,}20$$

$$\beta_x \quad = 0{,}60$$

$$\eta_x \quad = 1{,}00$$

$$\frac{r}{t} \leq 0{,}03 \cdot \frac{E}{f_{yk}} = 0$$

c_θ $= 0{,}60$

$c_{\theta s} = 0{,}60 + \dfrac{1}{\omega^2} - \dfrac{0{,}30}{\omega^3}$ $= 0{,}60$ (Tab D.4 - Annex D)

$$\sigma_{\theta,Rcr} = \begin{vmatrix} \left(0{,}92 \cdot E \cdot \dfrac{c_\theta}{\omega} \cdot \dfrac{t}{r}\right), if \, 20 \leq \dfrac{\omega}{c_\theta} \leq 1{,}63 \cdot \dfrac{r}{t} \\[2em] \left(0{,}92 \cdot E \cdot \dfrac{c_{\theta s}}{\omega} \cdot \dfrac{t}{r}\right), if \, 20 < \dfrac{\omega}{c_\theta} \\[2em] \left[E \cdot \left(\dfrac{t}{r}\right)^2 \cdot \left[0{,}275 + 2{,}03 \cdot \left(\dfrac{c_\theta}{\omega} \cdot \dfrac{r}{t}\right)^4\right]\right], if \, \dfrac{\omega}{c_\theta} > 1{,}63 \end{vmatrix}$$

$\sigma_{\theta,Rcr} = 8{,}316$ MPa

α_θ $= 0{,}50$ - (Tab D.4- Annex D)

$\lambda_{\theta 0}$ $= 0{,}40$

β_θ $= 0{,}60$

η_θ $= 1{,}00$

$\dfrac{r}{t} \leq 0{,}21 \cdot \sqrt{\dfrac{E}{f_{yk}}}$ $= 0$

ω $= 328{,}305$

$$c_T = \begin{vmatrix} 1, if \, 10 \leq \omega \leq 8{,}7 \cdot \dfrac{r}{t} \\[1.5em] \sqrt{1 + \dfrac{42}{\omega^3}}, if \, \omega \leq 10 \\[1.5em] \left(\dfrac{1}{3} \cdot \sqrt{\omega \cdot \dfrac{t}{r}}\right), if \, \omega > 8{,}7 \cdot \dfrac{r}{t} \end{vmatrix}$$
$c_T = 1{,}00$

$\tau_{x\theta,Rcr} = 0{,}75 \cdot E \cdot c_T \cdot \sqrt{\dfrac{1}{\omega}} \cdot \left(\dfrac{t}{r}\right) = 104{,}101$ MPa

α_T $= 0{,}50$ - (Tab D.6- Annex D)

λ_{T0} $= 0{,}40$

β_T $= 0{,}60$

η_T $= 1{,}00$

$$\frac{r}{t} \leq 0{,}16 \cdot \left(\frac{E}{f_{yk}}\right)^{0{,}67} = 0$$

Design of the buckling resistance

a_x = 0,335

λ_{x0} = 0,20

β_x = 0,60

η_x = 1,00

$\sigma_{x,Rcr}$ = 912,934 MPa

$$\lambda_x = \sqrt{\frac{f_{yk}}{\sigma_{x,Rcr}}} \qquad = 0{,}624$$

$$\lambda_{p,x} = \sqrt{\frac{a_x}{1-\beta_x}} \qquad = 0{,}915$$

$$X_x = \begin{vmatrix} 1, if\lambda_x \leq \lambda_{x0} \\[2mm] \left[1 - \beta_x \cdot \left(\dfrac{\lambda_x - \lambda_{x0}}{\lambda_{p,x} - \lambda_{x0}}\right)^{\eta_x}\right], if\lambda_{x0} < \lambda_x < \lambda_{p,x} \\[2mm] \dfrac{a_x}{\lambda_x^2}, if\lambda_{p,x} \leq \lambda_x \end{vmatrix} \qquad \chi_x = 0{,}644$$

$\sigma_{x,Rcr} = X_x \cdot f_{yk}$ = 228,762 MPa

a_θ = 0,50

$\lambda_{\theta 0}$ = 0,40

β_θ = 0,60

η_θ = 1,00

$\sigma_{\theta,Rcr}$ = 8,316 MPa

$$\lambda_\theta = \sqrt{\frac{f_{yk}}{\sigma_{\theta,Rcr}}} \qquad = 6{,}534$$

$$\lambda_{p,\theta} = \sqrt{\frac{a_\theta}{1-\beta_\theta}} \qquad = 1{,}118$$

$$X_\theta = \begin{vmatrix} 1, if\lambda_\theta \le \lambda_{\theta 0} \\ \left[1 - \beta_\theta \cdot \left(\dfrac{\lambda_\theta - \lambda_{\theta 0}}{\lambda_{p,\theta} - \lambda_{\theta 0}} \right)^{\eta_\theta} \right], if\lambda_{\theta 0} < \lambda_\theta < \lambda_{p,\theta} \\ \dfrac{a_\theta}{\lambda_\theta{}^2}, if\lambda_{p,\theta} \le \lambda_\theta \end{vmatrix} \qquad \chi_\theta = 0,012$$

$$\sigma_{\theta,Rk} = X_\theta \cdot f_{yk} \qquad = 4,158 \text{ MPa}$$

$a_T \qquad = 0,50$
$\lambda_{T0} \qquad = 0,40$
$\beta_T \qquad = 0,60$
$\eta_T \qquad = 1,00$

$\tau_{x\theta,Rcr} \qquad\qquad = 104,101 \text{ MPa}$

$$\lambda_T = \sqrt{\dfrac{\left(\dfrac{f_{yk}}{\sqrt{3}} \right)}{\tau_{x\theta,Rcr}}} \qquad = 1,403$$

$$\lambda_{p,T} = \sqrt{\dfrac{a_T}{1 - \beta_T}} \qquad = 1,118$$

$$X_T = \begin{vmatrix} 1, if\lambda_T \le \lambda_{T0} \\ \left[1 - \beta_T \cdot \left(\dfrac{\lambda_T - \lambda_{T0}}{\lambda_{p,T} - \lambda_{T0}} \right)^{\eta_T} \right], if\lambda_{T0} < \lambda_T < \lambda_{p,T} \\ \dfrac{a_T}{\lambda_T{}^2}, if\lambda_{p,T} \le \lambda_T \end{vmatrix} \qquad \chi_\tau = 0,254$$

$$\tau_{x\theta,Rk} = \dfrac{\left(X_\theta \cdot f_{yk} \right)}{\sqrt{3}} \qquad = 52,051 \text{ MPa}$$

$\chi_x \qquad = 0,644$
$\chi_\theta \qquad = 0,012$
$\chi_\tau \qquad = 0,254$

$$k_x = 1,25 + 0,75 \cdot \chi_x \qquad\qquad = 1,733$$

$$k_\theta = 1{,}25 + 0{,}75 \cdot \chi_\theta \qquad\qquad = 1{,}259$$

$$k_\tau = 1{,}75 + 0{,}25 \cdot \chi_\tau \qquad\qquad = 1{,}813$$

$$k_i = (\chi_x \cdot \chi_\theta)^2 \qquad\qquad = 0{,}000057$$

$$\sigma_{x,Rd} = \frac{\sigma_{x,Rk}}{\gamma_{M1}} \qquad\qquad = 207{,}965 \text{ MPa}$$

$$\sigma_{\theta,Rd} = \frac{\sigma_{\theta,Rk}}{\gamma_{M1}} \qquad\qquad = 3{,}78 \text{ MPa}$$

$$\tau_{x\theta,Rd} = \frac{\tau_{x\theta,Rk}}{\gamma_{M1}} \qquad\qquad = 47{,}319 \text{ MPa}$$

$$\sigma_{x,Ed} \le \sigma_{x,Rd} = 1 \qquad\qquad Ratio_{\sigma_x} = \frac{\sigma_{x,Ed}}{\sigma_{x,Rd}} = 0{,}496$$

$$\sigma_{\theta,Ed} \le \sigma_{\theta,Rd} = 1 \qquad\qquad Ratio_{\sigma_\theta} = \frac{\sigma_{\theta,Ed}}{\sigma_{\theta,Rd}} = 0{,}014$$

$$\tau_{x\theta,Ed} \le \tau_{x\theta,Rd} = 1 \qquad\qquad Ratio_{\tau_\theta} = \frac{\tau_{x\theta,Ed}}{\tau_{x\theta,Rd}} = 0{,}717$$

$$\left(\frac{\sigma_{x,Ed}}{\sigma_{x,Rd}}\right)^{k_x} - k_i \cdot \left(\frac{\sigma_{x,Ed}}{\sigma_{x,Rd}}\right) \cdot \left(\frac{\sigma_{\theta,Ed}}{\sigma_{\theta,Rd}}\right) + \left(\frac{\sigma_{\theta,Ed}}{\sigma_{\theta,Rd}}\right)^{k_\theta} + \left(\frac{\tau_{x\theta,Ed}}{\tau_{x\theta,Rd}}\right)^{k_\tau} = 0{,}848$$

$$Ratio_2 = \left(\frac{\sigma_{x,Ed}}{\sigma_{x,Rd}}\right)^{k_x} - k_i \cdot \left(\frac{\sigma_{x,Ed}}{\sigma_{x,Rd}}\right) \cdot \left(\frac{\sigma_{\theta,Ed}}{\sigma_{\theta,Rd}}\right) + \left(\frac{\sigma_{\theta,Ed}}{\sigma_{\theta,Rd}}\right)^{k_\theta} + \left(\frac{\tau_{x\theta,Ed}}{\tau_{x\theta,Rd}}\right)^{k_\tau} = 0{,}848$$

$$Ratio = max\left(Ratio_1, Ratio_{\sigma_x}, Ratio_{\sigma_\theta}, Ratio_{\tau_\theta}, Ratio_2\right) = 0{,}848$$

A2.2. Segment Section t = 12 mm

D_1 = 1680 mm

t = 12 mm

$D_c = D_1 - 2 \cdot t$ = 1656 mm

l = 30,00 m

$A_t = \pi \cdot \left[\left(\dfrac{D_1}{2} \right)^2 - \left(\dfrac{D_2}{2} \right)^2 \right]$ = 62882,12 mm^2

ρ_{OL} = 7850 kg/m^3

$g_t = \rho_{OL} - A_t$ = 493,625 kg/m

$r = \dfrac{D_1}{2} - \dfrac{t}{2}$ = 834 mm- Over the median surface

- **Internal forces**

N_{Ed} = 418,63 kN

$V_{y,Ed}$ = 136,28 kN

$V_{z,Ed}$ = 235,64 kN

$M_{t,Ed}$ = 1110,97 kNm

$M_{y,Ed}$ = 3052,07 kNm

$M_{z,Ed}$ = 1611,56 kNm

For z_e = 26,00 m

$q_{w,max}$ = 0,95 kN/m^2

c_θ = 0,60 - (EN1993-1-6 - D.3 Annex D)

q_s = 0 MPa

$\omega = \dfrac{l}{r} \cdot \sqrt{\dfrac{r}{t}}$ = 299,88 - (EN1993-1-6 - Annex D)

$k_w = max \left[0,46 \cdot \left(1 + 0,1 \cdot \sqrt{\dfrac{c_\theta}{\omega} \cdot \dfrac{r}{t}} \right) ; 0,65 \right]$ = 0,65

$q_{eq} = k_w \cdot q_{w,max}$ = 0,000617 MPa

- **Calculation of the stresses (resistance)**

Materials

f_{yk} = 355 MPa

E = 2,1 $\cdot 10^5$ MPa

f_u = 510 MPa

$$\gamma_{M0} \quad = 1,0$$
$$\gamma_{M1} \quad = 1,1$$
$$\gamma_{M2} \quad = 1,25$$

Calculation of the stresses

$$\sigma_{x,Ed,1} = -\frac{N_{Ed}}{2 \cdot \pi \cdot r \cdot t} + \frac{M_{y,Ed}}{\pi \cdot r^2 \cdot t} + \frac{M_{z,Ed}}{\pi \cdot r^2 \cdot t} \qquad = 171,195 \text{ MPa}$$

$$\sigma_{x,Ed,2} = -\frac{N_{Ed}}{2 \cdot \pi \cdot r \cdot t} - \frac{M_{y,Ed}}{\pi \cdot r^2 \cdot t} - \frac{M_{z,Ed}}{\pi \cdot r^2 \cdot t} \qquad = -184,51 \text{ MPa}$$

$$\sigma_{x,Ed} = max\left(\left|\sigma_{x,Ed,1}\right|, \left|\sigma_{x,Ed,2}\right|\right) \qquad = 184,51 \text{ MPa}$$

$$\sigma_{\theta,Ed} = \left(q_{eq} + q_s\right) \cdot \left(\frac{r}{t}\right) \qquad = 0,043 \text{ MPa}$$

$$\tau_{x,\theta,Ed,1} = \frac{M_{t,Ed}}{2 \cdot \pi \cdot r^2 \cdot t} + \frac{V_{z,Ed}}{\pi \cdot r \cdot t} \qquad = 28,679 \text{ MPa}$$

$$\tau_{x,\theta,Ed,2} = \frac{M_{t,Ed}}{2 \cdot \pi \cdot r^2 \cdot t} - \frac{V_{z,Ed}}{\pi \cdot r \cdot t} \qquad = 13,689 \text{ MPa}$$

$$\tau_{x,\theta,Ed} = max\left(\left|\tau_{x,\theta,Ed,1}\right|, \left|\sigma_{\tau_{x,\theta,Ed,2}}\right|\right) \qquad = 28,679 \text{ MPa}$$

$$\tau_{x,n,Ed} \qquad = 0 \text{ MPa}$$
$$\tau_{\theta,n,Ed} \qquad = 0 \text{ MPa}$$

According with EN 1993-1-6 Ch.6.2.1. (6), the equivalent stress is:

$$\sigma_{eq,Ed} = \sqrt{\sigma_{x,Ed}{}^2 + \sigma_{\theta,Ed}{}^2 - \sigma_{x,Ed} \cdot \sigma_{\theta,Ed} + 3 \cdot \left(\tau_{x,\theta,Ed}{}^2 + \tau_{x,n,Ed}{}^2 + \tau_{\theta,n,Ed}{}^2\right)}$$
$$= 191,059 \text{ MPa}$$

The stress limit

$$f_{eq,Rd} = \frac{f_{yk}}{\gamma_{M0}} \quad = 355 \text{ MPa}$$

$$\sigma_{eq,Rd} \leq f_{eq,Rd}$$

$$Ratio_1 = \frac{\sigma_{eq,Rd}}{f_{eq,Rd}} = 0,538$$

- **Buckling design**

According with EN 1993-1-6 Ch.8.5 & Annex D:

$$\omega = \frac{l}{r} \cdot \sqrt{\frac{r}{t}} \qquad\qquad = 299,88$$

$$c_\theta \qquad\qquad = 3$$

$$c_x = \begin{vmatrix} 1, if\ 1,7 \leq \omega \leq 0,5 \cdot \dfrac{r}{t} \\[2mm] \left(1,36 - \dfrac{1,83}{\omega} + \dfrac{2,07}{\omega^2}\right), if\ \omega \leq 1,7 \\[2mm] max\left[0,6,1 + \dfrac{0,2}{c_{xb}} \cdot \left(1 - 2 \cdot \omega \cdot \dfrac{t}{r}\right)\right], if\ \omega > 0,5 \end{vmatrix} \qquad c_x = 0,60$$

$$\sigma_{x,Rcr} = 0,605 \cdot E \cdot c_x \cdot \frac{t}{r} \qquad = 1,097 \cdot 10^3\ MPa$$

$$Q \qquad\qquad\qquad = 16 \qquad\qquad \text{- Tab D.2 - Annex D}$$

$$\Delta w_k = \frac{1}{Q} \cdot \sqrt{\frac{r}{t}} \cdot t \qquad = 6,252\ mm$$

$$a_x = \frac{0,62}{1 + 1,91 \cdot \left(\dfrac{\Delta w_k}{t}\right)^{1,44}} \qquad = 0,355$$

$$\lambda_{x0} \quad\ = 0,20$$

$$\beta_x \quad\ = 0,60$$

$$\eta_x \quad\ = 1,00$$

$$\frac{r}{t} \leq 0,03 \cdot \frac{E}{f_{yk}} = 0$$

$$c_\theta \qquad\qquad\qquad = 0,60$$

$$c_{\theta s} = 0,60 + \frac{1}{\omega^2} - \frac{0,30}{\omega^3} \qquad = 0,60 \quad \text{- (Tab D.4- Annex D)}$$

$$\sigma_{\theta,Rcr} = \begin{vmatrix} \left(0,92 \cdot E \cdot \dfrac{c_\theta}{\omega} \cdot \dfrac{t}{r}\right), & if\ 20 \leq \dfrac{\omega}{c_\theta} \leq 1,63 \cdot \dfrac{r}{t} \\[3mm] \left(0,92 \cdot E \cdot \dfrac{c_{\theta s}}{\omega} \cdot \dfrac{t}{r}\right), & if\ 20 < \dfrac{\omega}{c_\theta} \\[3mm] \left[E \cdot \left(\dfrac{t}{r}\right)^2 \cdot \left[0,275 + 2,03 \cdot \left(\dfrac{c_\theta}{\omega} \cdot \dfrac{r}{t}\right)^4\right]\right], & if\ \dfrac{\omega}{c_\theta} > 1,63 \end{vmatrix}$$

$\sigma_{\theta,Rcr}$ = 11,989 MPa

a_θ = 0,50

$\lambda_{\theta 0}$ = 0,40

β_θ = 0,60

η_θ = 1,00

$$\frac{r}{t} \leq 0,21 \cdot \sqrt{\frac{E}{f_{yk}}} \ = 0$$

ω = 299,88

$$c_T = \begin{vmatrix} 1, & if\ 10 \leq \omega \leq 8,7 \cdot \dfrac{r}{t} \\[3mm] \sqrt{1 + \dfrac{42}{\omega^3}}, & if\ \omega \leq 10 \\[3mm] \left(\dfrac{1}{3} \cdot \sqrt{\omega \cdot \dfrac{t}{r}}\right), & if\ \omega > 8,7 \cdot \dfrac{r}{t} \end{vmatrix}$$ c_T = 1,00

$$\tau_{x\theta,Rcr} = 0,75 \cdot E \cdot c_T \cdot \sqrt{\frac{1}{\omega}} \cdot \left(\frac{t}{r}\right) \ = 130,865\ MPa$$

a_T = 0,50

λ_{T0} = 0,40

β_T = 0,60

η_T = 1,00

$$\frac{r}{t} \leq 0,16 \cdot \left(\frac{E}{f_{yk}}\right)^{0,67} \ = 0$$

Resistance for the buckling

a_x = 0,355

λ_{x0} = 0,20

β_x = 0,60

η_x = 1,00

$\sigma_{x,Rcr}$ = $1,097 \cdot 10^3$ MPa

$$\lambda_x = \sqrt{\frac{f_{yk}}{\sigma_{x,Rcr}}} \qquad = 0,569$$

$$\lambda_{p,x} = \sqrt{\frac{a_x}{1 - \beta_x}} \qquad = 0,942$$

$$X_x = \begin{vmatrix} 1, if \lambda_x \leq \lambda_{x0} \\ \left[1 - \beta_x \cdot \left(\dfrac{\lambda_x - \lambda_{x0}}{\lambda_{p,x} - \lambda_{x0}} \right)^{\eta_x} \right], if \lambda_{x0} < \lambda_x < \lambda_{p,x} \\ \dfrac{a_x}{\lambda_x^2}, if \lambda_{p,x} \leq \lambda_x \end{vmatrix} \qquad X_x = 0,702$$

$\sigma_{x,Rcr} = X_x \cdot f_{yk}$ = 249,09 MPa

a_θ = 0,50

$\lambda_{\theta 0}$ = 0,40

β_θ = 0,60

η_θ = 1,00

$\sigma_{\theta,Rcr}$ = 11,989 MPa

$$\lambda_\theta = \sqrt{\frac{f_{yk}}{\sigma_{\theta,Rcr}}} \qquad = 5,442$$

$$\lambda_{p,\theta} = \sqrt{\frac{a_\theta}{1 - \beta_\theta}} \qquad = 1,118$$

$$\chi_\theta = \begin{vmatrix} 1, if\lambda_\theta \le \lambda_{\theta0} \\ \left[1 - \beta_\theta \cdot \left(\dfrac{\lambda_\theta - \lambda_{\theta0}}{\lambda_{p,\theta} - \lambda_{\theta0}}\right)^{\eta_\theta}\right], if\lambda_{\theta0} < \lambda_\theta < \lambda_{p,\theta} \\ \dfrac{a_\theta}{\lambda_\theta^2}, if\lambda_{p,\theta} \le \lambda_\theta \end{vmatrix} \qquad \chi_\theta = 0{,}017$$

$$\sigma_{\theta,Rk} = \chi_\theta \cdot f_{yk} \qquad = 5{,}994 \text{ MPa}$$

$a_T \qquad = 0{,}50$

$\lambda_{T0} \qquad = 0{,}40$

$\beta_T \qquad = 0{,}60$

$\eta_T \qquad = 1{,}00$

$\tau_{x\theta,Rcr} \qquad = 130{,}865 \text{ MPa}$

$$\lambda_T = \sqrt{\dfrac{\left(\dfrac{f_{yk}}{\sqrt{3}}\right)}{\tau_{x\theta,Rcr}}} \quad = 1{,}251$$

$$\lambda_{p,T} = \sqrt{\dfrac{a_T}{1 - \beta_T}} \quad = 1{,}118$$

$$\chi_T = \begin{vmatrix} 1, if\lambda_T \le \lambda_{T0} \\ \left[1 - \beta_T \cdot \left(\dfrac{\lambda_T - \lambda_{T0}}{\lambda_{p,T} - \lambda_{T0}}\right)^{\eta_T}\right], if\lambda_{T0} < \lambda_T < \lambda_{p,T} \\ \dfrac{a_T}{\lambda_T^2}, if\lambda_{p,T} \le \lambda_T \end{vmatrix} \qquad \chi_\tau = 0{,}319$$

$$\tau_{x\theta,Rk} = \dfrac{\left(\chi_\theta \cdot f_{yk}\right)}{\sqrt{3}} \qquad = 65{,}432 \text{ MPa}$$

$\chi_x \qquad = 0{,}702$

$\chi_\theta \qquad = 0{,}017$

$\chi_\tau \qquad = 0{,}319$

$$k_x = 1{,}25 + 0{,}75 \cdot \chi_x \quad = 1{,}776$$

$$k_\theta = 1{,}25 + 0{,}75 \cdot \chi_\theta \quad = 1{,}263$$

$$k_T = 1{,}75 + 0{,}25 \cdot \chi_T \quad = 1{,}830$$

$$k_i = \left(\chi_x \cdot \chi_\theta\right)^2 \qquad = 0{,}00014$$

$$\sigma_{x,Rd} = \frac{\sigma_{x,Rk}}{\gamma_{M1}} \qquad = 226{,}445 \text{ MPa}$$

$$\sigma_{\theta,Rd} = \frac{\sigma_{\theta,Rk}}{\gamma_{M1}} \qquad = 5{,}45 \text{ MPa}$$

$$\tau_{x\theta,Rd} = \frac{\tau_{x\theta,Rk}}{\gamma_{M1}} \qquad = 59{,}484 \text{ MPa}$$

$$\sigma_{x,Ed} \leq \sigma_{x,Rd} = 1 \qquad Ratio_{\sigma_x} = \frac{\sigma_{x,Ed}}{\sigma_{x,Rd}} = 0{,}815$$

$$\sigma_{\theta,Ed} \leq \sigma_{\theta,Rd} = 1 \qquad Ratio_{\sigma_\theta} = \frac{\sigma_{\theta,Ed}}{\sigma_{\theta,Rd}} = 0{,}008$$

$$\tau_{x\theta,Ed} \leq \tau_{x\theta,Rd} = 1 \qquad Ratio_{T_\theta} = \frac{\tau_{x\theta,Ed}}{\tau_{x\theta,Rd}} = 0{,}482$$

$$\left(\frac{\sigma_{x,Ed}}{\sigma_{x,Rd}}\right)^{k_x} - k_i \cdot \left(\frac{\sigma_{x,Ed}}{\sigma_{x,Rd}}\right) \cdot \left(\frac{\sigma_{\theta,Ed}}{\sigma_{\theta,Rd}}\right) + \left(\frac{\sigma_{\theta,Ed}}{\sigma_{\theta,Rd}}\right)^{k_\theta} + \left(\frac{\tau_{x\theta,Ed}}{\tau_{x\theta,Rd}}\right)^{k_T} = 0{,}960$$

$$Ratio_2 = \left(\frac{\sigma_{x,Ed}}{\sigma_{x,Rd}}\right)^{k_x} - k_i \cdot \left(\frac{\sigma_{x,Ed}}{\sigma_{x,Rd}}\right) \cdot \left(\frac{\sigma_{\theta,Ed}}{\sigma_{\theta,Rd}}\right) + \left(\frac{\sigma_{\theta,Ed}}{\sigma_{\theta,Rd}}\right)^{k_\theta} + \left(\frac{\tau_{x\theta,Ed}}{\tau_{x\theta,Rd}}\right)^{k_T} = 0{,}960$$

$$Ratio = max\left(Ratio_1, Ratio_{\sigma_x}, Ratio_{\sigma_\theta}, Ratio_{T_\theta}, Ratio_2\right) \quad = 0{,}960$$

A2.3. Segment Section t = 16 mm

D_1 = 1680 mm

t = 16 mm

$D_c = D_1 - 2 \cdot t$ = 1648 mm

l = 30,00 m

$A_t = \pi \cdot \left[\left(\dfrac{D_1}{2} \right)^2 - \left(\dfrac{D_2}{2} \right)^2 \right]$ = 83641,76 mm²

ρ_{OL} = 7850 kg/m³

$g_t = \rho_{OL} - A_t$ = 656,588 kg/m

$r = \dfrac{D_1}{2} - \dfrac{t}{2}$ = 832 mm Over the median surface

- **Internal forces**

N_{Ed} = 488,87 kN

$V_{y,Ed}$ = 142,53 kN

$V_{z,Ed}$ = 247,44 kN

$M_{t,Ed}$ = 1111,46 kNm

$M_{y,Ed}$ = 4997,56 kNm

$M_{z,Ed}$ = 2731,71 kNm

For z_e = 26,00 m

$q_{w,max}$ = 0,95 kN/m²

c_θ = 0,60   - (EN1993-1-6 - D.3 Annex D)

q_s = 0 MPa

$\omega = \dfrac{l}{r} \cdot \sqrt{\dfrac{r}{t}}$ = 260,016   - (EN1993-1-6 - Annex D)

$k_w = max \left[0,46 \cdot \left(1 + 0,1 \cdot \sqrt{\dfrac{c_\theta \cdot r}{\omega \cdot t}} \right); 0,65 \right]$ = 0,65

$q_{eq} = k_w \cdot q_{w,max}$ = 0,000617 MPa

- **Calculation of the stresses (resistance)**

Materials

f_{yk} = 355 MPa

E = 2,1 ·10⁵ MPa

f_u = 510 MPa

γ_{M0} = 1,0
γ_{M1} = 1,1
γ_{M2} = 1,25

Calculation of the stresses

$$\sigma_{x,Ed,1} = -\frac{N_{Ed}}{2 \cdot \pi \cdot r \cdot t} + \frac{M_{y,Ed}}{\pi \cdot r^2 \cdot t} + \frac{M_{z,Ed}}{\pi \cdot r^2 \cdot t}$$ = 216,293 MPa

$$\sigma_{x,Ed,2} = -\frac{N_{Ed}}{2 \cdot \pi \cdot r \cdot t} - \frac{M_{y,Ed}}{\pi \cdot r^2 \cdot t} - \frac{M_{z,Ed}}{\pi \cdot r^2 \cdot t}$$ = -227,982 MPa

$$\sigma_{x,Ed} = max\left(\left|\sigma_{x,Ed,1}\right|, \left|\sigma_{x,Ed,2}\right|\right)$$ = 227,982 MPa

$$\sigma_{\theta,Ed} = \left(q_{eq} + q_s\right) \cdot \left(\frac{r}{t}\right)$$ = 0,032 MPa

$$\tau_{x,\theta,Ed,1} = \frac{M_{t,Ed}}{2 \cdot \pi \cdot r^2 \cdot t} + \frac{V_{z,Ed}}{\pi \cdot r \cdot t}$$ = 21,888 MPa

$$\tau_{x,\theta,Ed,2} = \frac{M_{t,Ed}}{2 \cdot \pi \cdot r^2 \cdot t} - \frac{V_{z,Ed}}{\pi \cdot r \cdot t}$$ = 10,055 MPa

$$\tau_{x,\theta,Ed} = max\left(\left|\tau_{x,\theta,Ed,1}\right|, \left|\sigma_{\tau_{x,\theta,Ed,2}}\right|\right)$$ = 21,888 MPa

$\tau_{x,n,Ed}$ = 0 MPa
$\tau_{\theta,n,Ed}$ = 0 MPa

According with EN 1993-1-6 Ch.6.2.1. (6), the equivalent stress is:

$$\sigma_{eq,Ed} = \sqrt{\sigma_{x,Ed}^2 + \sigma_{\theta,Ed}^2 - \sigma_{x,Ed} \cdot \sigma_{\theta,Ed} + 3 \cdot \left(\tau_{x,\theta,Ed}^2 + \tau_{x,n,Ed}^2 + \tau_{\theta,n,Ed}^2\right)}$$
= 231,097 MPa

$$f_{eq,Rd} = \frac{f_{yk}}{\gamma_{M0}}$$ = 355 MPa

The stress limit

$$\sigma_{eq,Rd} \le f_{eq,Rd}$$

$$Ratio_1 = \frac{\sigma_{eq,Rd}}{f_{eq,Rd}} = 0,651$$

- **Buckling design**

    According with EN 1993-1-6 Ch.8.5 & Annex D:

$$\omega = \frac{l}{r} \cdot \sqrt{\frac{r}{t}} \qquad\qquad = 260,016$$

$$c_\theta \qquad\qquad\qquad = 3$$

$$c_x = \begin{vmatrix} 1, if\, 1,7 \le \omega \le 0,5 \cdot \frac{r}{t} \\[2mm] \left(1,36 - \frac{1,83}{\omega} + \frac{2,07}{\omega^2} \right), if\, \omega \le 1,7 \\[2mm] max\left[0,6, 1 + \frac{0,2}{c_{xb}} \cdot \left(1 - 2 \cdot \omega \cdot \frac{t}{r} \right) \right], if\, \omega > 0,5 \end{vmatrix} \qquad c_x = 0,6$$

$$\sigma_{x,Rcr} = 0,605 \cdot E \cdot c_x \cdot \frac{t}{r} \qquad\qquad = 1,466 \cdot 10^3 \text{ MPa}$$

- Meridian buckling parameters

    $$Q \qquad\qquad\qquad = 16 \qquad\qquad\qquad \text{- Tab D.2 - Annex D}$$

    $$\Delta w_k = \frac{1}{Q} \cdot \sqrt{\frac{r}{t}} \cdot t \qquad = 7,211 \text{ mm}$$

    $$a_x = \frac{0,62}{1 + 1,91 \cdot \left(\frac{\Delta w_k}{t} \right)^{1,44}} \qquad = 0,386$$

    $$\lambda_{x0} \quad = 0,20$$
    $$\beta_x \quad = 0,60$$
    $$\eta_x \quad = 1,00$$

    $$\frac{r}{t} \le 0,03 \cdot \frac{E}{f_{yk}} \quad = 0$$

- Circumferentially Critical buckling stress

    $$c_\theta \qquad\qquad = 0,60$$

    $$c_{\theta s} = 0,60 + \frac{1}{\omega^2} - \frac{0,30}{\omega^3} = 0,60 \qquad\qquad \text{- (Tab D.4- Annex D)}$$

$$\sigma_{\theta,Rcr} = \left| \begin{array}{l} \left(0,92 \cdot E \cdot \dfrac{c_\theta}{\omega} \cdot \dfrac{t}{r} \right), if\ 20 \le \dfrac{\omega}{c_\theta} \le 1,63 \cdot \dfrac{r}{t} \\[3mm] \left(0,92 \cdot E \cdot \dfrac{c_{\theta s}}{\omega} \cdot \dfrac{t}{r} \right), if\ 20 < \dfrac{\omega}{c_\theta} \\[3mm] \left[E \cdot \left(\dfrac{t}{r} \right)^2 \cdot \left[0,275 + 2,03 \cdot \left(\dfrac{c_\theta}{\omega} \cdot \dfrac{r}{t} \right)^4 \right] \right], if\ \dfrac{\omega}{c_\theta} > 1,63 \end{array} \right.$$

$\sigma_{\theta,Rcr}$ = 21,39 MPa

a_θ = 0,50   - (Tab D.4- Annex D)
$\lambda_{\theta 0}$ = 0,40
β_θ = 0,60
η_θ = 1,00

$$\dfrac{r}{t} \le 0,21 \cdot \sqrt{\dfrac{E}{f_{yk}}} \ = 0$$

ω = 260,016

$$c_T = \left| \begin{array}{l} 1, if\ 10 \le \omega \le 8,7 \cdot \dfrac{r}{t} \\[3mm] \sqrt{1 + \dfrac{42}{\omega^3}}, if\ \omega \le 10 \\[3mm] \left(\dfrac{1}{3} \cdot \sqrt{\omega \cdot \dfrac{t}{r}} \right), if\ \omega > 8,7 \cdot \dfrac{r}{t} \end{array} \right.$$
                                                c_T = 1,00

$$\tau_{x\theta,Rcr} = 0,75 \cdot E \cdot c_T \cdot \sqrt{\dfrac{1}{\omega}} \cdot \left(\dfrac{t}{r} \right) \qquad = 130,865\ MPa$$

a_T = 0,50   - (Tab D.6- Annex D)
λ_{T0} = 0,40
β_T = 0,60
η_T = 1,00

$$\dfrac{r}{t} \le 0,16 \cdot \left(\dfrac{E}{f_{yk}} \right)^{0,67} \ = 0$$

- Resistance for the buckling

$$a_x \quad = 0,386$$
$$\lambda_{x0} \quad = 0,20$$
$$\beta_x \quad = 0,60$$
$$\eta_x \quad = 1,00$$

$$\sigma_{x,Rcr} \qquad = 1,466 \cdot 10^3 \text{ MPa}$$

$$\lambda_x = \sqrt{\frac{f_{yk}}{\sigma_{x,Rcr}}} \qquad = 0,492$$

$$\lambda_{p,x} = \sqrt{\frac{a_x}{1 - \beta_x}} \qquad = 0,982$$

$$X_x = \begin{cases} 1, & if \lambda_x \le \lambda_{x0} \\ \left[1 - \beta_x \cdot \left(\dfrac{\lambda_x - \lambda_{x0}}{\lambda_{p,x} - \lambda_{x0}} \right)^{\eta_x} \right], & if \lambda_{x0} < \lambda_x < \lambda_{p,x} \\ \dfrac{a_x}{\lambda_x{}^2}, & if \lambda_{p,x} \le \lambda_x \end{cases} \qquad X_x = 0,776$$

$$\sigma_{x,Rcr} = X_x \cdot f_{yk} \qquad = 275,474 \text{ MPa}$$

$$a_\theta \quad = 0,50$$
$$\lambda_{\theta 0} \quad = 0,40$$
$$\beta_\theta \quad = 0,60$$
$$\eta_\theta \quad = 1,00$$

$$\sigma_{\theta,Rcr} \qquad = 21,39 \text{ MPa}$$

$$\lambda_\theta = \sqrt{\frac{f_{yk}}{\sigma_{\theta,Rcr}}} \qquad = 4,074$$

$$\lambda_{p,\theta} = \sqrt{\frac{a_\theta}{1 - \beta_\theta}} \qquad = 1,118$$

$$\chi_\theta = \left| \begin{array}{l} 1, if \lambda_\theta \le \lambda_{\theta 0} \\ \left[1 - \beta_\theta \cdot \left(\dfrac{\lambda_\theta - \lambda_{\theta 0}}{\lambda_{p,\theta} - \lambda_{\theta 0}} \right)^{\eta_\theta} \right], if \lambda_{\theta 0} < \lambda_\theta < \lambda_{p,\theta} \\ \dfrac{a_\theta}{\lambda_\theta^2}, if \lambda_{p,\theta} \le \lambda_\theta \end{array} \right. \qquad \chi_\theta = 0{,}03$$

$\sigma_{\theta,Rk} = \chi_\theta \cdot f_{yk}$ = 10,695 MPa

a_T = 0,50
λ_{T0} = 0,40
β_T = 0,60
η_T = 1,00

$\tau_{x\theta,Rcr}$ = 187,835 MPa

$$\lambda_T = \sqrt{\dfrac{\left(\dfrac{f_{yk}}{\sqrt{3}} \right)}{\tau_{x\theta,Rcr}}} \; = 1{,}045$$

$$\lambda_{p,T} = \sqrt{\dfrac{a_T}{1 - \beta_T}} \; = 1{,}118$$

$$\chi_T = \left| \begin{array}{l} 1, if \lambda_T \le \lambda_{T0} \\ \left[1 - \beta_T \cdot \left(\dfrac{\lambda_T - \lambda_{T0}}{\lambda_{p,T} - \lambda_{T0}} \right)^{\eta_T} \right], if \lambda_{T0} < \lambda_T < \lambda_{p,T} \\ \dfrac{a_T}{\lambda_T^2}, if \lambda_{p,T} \le \lambda_T \end{array} \right. \qquad \chi_\tau = 0{,}461$$

$$\tau_{x\theta,Rk} = \dfrac{\left(\chi_\theta \cdot f_{yk} \right)}{\sqrt{3}} \qquad = 94{,}563 \text{ MPa}$$

χ_x = 0,776
χ_θ = 0,03
χ_T = 0,461

$k_x = 1{,}25 + 0{,}75 \cdot \chi_x$ = 1,832
$k_\theta = 1{,}25 + 0{,}75 \cdot \chi_\theta$ = 1,273
$k_T = 1{,}75 + 0{,}25 \cdot \chi_T$ = 1,865

$$k_i = (\chi_x \cdot \chi_\theta)^2 \qquad\qquad = 0{,}000547$$

$$\sigma_{x,Rd} = \frac{\sigma_{x,Rk}}{\gamma_{M1}} \qquad\qquad = 250{,}431 \text{ MPa}$$

$$\sigma_{\theta,Rd} = \frac{\sigma_{\theta,Rk}}{\gamma_{M1}} \qquad\qquad = 9{,}723 \text{ MPa}$$

$$\tau_{x\theta,Rd} = \frac{\tau_{x\theta,Rk}}{\gamma_{M1}} \qquad\qquad = 85{,}966 \text{ MPa}$$

$$\sigma_{x,Ed} \le \sigma_{x,Rd} = 1 \qquad\qquad Ratio_{\sigma_x} = \frac{\sigma_{x,Ed}}{\sigma_{x,Rd}} = 0{,}91$$

$$\sigma_{\theta,Ed} \le \sigma_{\theta,Rd} = 1 \qquad\qquad Ratio_{\sigma_\theta} = \frac{\sigma_{\theta,Ed}}{\sigma_{\theta,Rd}} = 0{,}003$$

$$\tau_{x\theta,Ed} \le \tau_{x\theta,Rd} = 1 \qquad\qquad Ratio_{\tau_\theta} = \frac{\tau_{x\theta,Ed}}{\tau_{x\theta,Rd}} = 0{,}255$$

$$\left(\frac{\sigma_{x,Ed}}{\sigma_{x,Rd}}\right)^{k_x} - k_i \cdot \left(\frac{\sigma_{x,Ed}}{\sigma_{x,Rd}}\right) \cdot \left(\frac{\sigma_{\theta,Ed}}{\sigma_{\theta,Rd}}\right) + \left(\frac{\sigma_{\theta,Ed}}{\sigma_{\theta,Rd}}\right)^{k_\theta} + \left(\frac{\tau_{x\theta,Ed}}{\tau_{x\theta,Rd}}\right)^{k_\tau} = 0{,}921$$

$$Ratio_2 = \left(\frac{\sigma_{x,Ed}}{\sigma_{x,Rd}}\right)^{k_x} - k_i \cdot \left(\frac{\sigma_{x,Ed}}{\sigma_{x,Rd}}\right) \cdot \left(\frac{\sigma_{\theta,Ed}}{\sigma_{\theta,Rd}}\right) + \left(\frac{\sigma_{\theta,Ed}}{\sigma_{\theta,Rd}}\right)^{k_\theta} + \left(\frac{\tau_{x\theta,Ed}}{\tau_{x\theta,Rd}}\right)^{k_\tau} = 0{,}921$$

$$Ratio = max\left(Ratio_1, Ratio_{\sigma_x}, Ratio_{\sigma_\theta}, Ratio_{\tau_\theta}, Ratio_2\right) \qquad = 0{,}921$$

A2.4. Segment section t = 20 mm

D_1 = 1680 mm

t = 20 mm

$D_c = D_1 - 2 \cdot t$ = 1640 mm

l = 30,00 m

$$A_t = \pi \cdot \left[\left(\frac{D_1}{2} \right)^2 - \left(\frac{D_2}{2} \right)^2 \right]$$ = 104300,88 mm^2

ρ_{OL} = 7850 kg/m^3

$g_t = \rho_{OL} - A_t$ = 818,762 kg/m

$r = \dfrac{D_1}{2} - \dfrac{t}{2}$ = 830 mm Over the median surface

- **Internal forces**

N_{Ed} = 566,03 kN

$V_{y,Ed}$ = 147,01 kN

$V_{z,Ed}$ = 255,93 kN

$M_{t,Ed}$ = 1111,6 kNm

$M_{y,Ed}$ = 6772,14 kNm

$M_{z,Ed}$ = 3749,79 kNm

For z_e = 26,00 m

$q_{w,max}$ = 0,955 kN/m^2

c_θ = 0,60

q_s = 0 MPa

$\omega = \dfrac{l}{r} \cdot \sqrt{\dfrac{r}{t}}$ = 232,845

$k_w = max \left[0,46 \cdot \left(1 + 0,1 \cdot \sqrt{\dfrac{c_\theta}{\omega} \cdot \dfrac{r}{t}} \right) ; 0,65 \right]$ = 0,65

$q_{eq} = k_w \cdot q_{w,max}$ = 0,000621 MPa

- **Calculation of the stresses (resistance)**

Materials

f_{yk} = 355 MPa

E = 2,1 $\cdot 10^5$ MPa

f_u = 510 MPa

γ_{M0} = 1,0

γ_{M1} = 1,1

γ_{M2} = 1,25

Calculation of the stresses

$$\sigma_{x,Ed,1} = -\frac{N_{Ed}}{2 \cdot \pi \cdot r \cdot t} + \frac{M_{y,Ed}}{\pi \cdot r^2 \cdot t} + \frac{M_{z,Ed}}{\pi \cdot r^2 \cdot t} \qquad = 237{,}659 \text{ MPa}$$

$$\sigma_{x,Ed,2} = -\frac{N_{Ed}}{2 \cdot \pi \cdot r \cdot t} - \frac{M_{y,Ed}}{\pi \cdot r^2 \cdot t} - \frac{M_{z,Ed}}{\pi \cdot r^2 \cdot t} \qquad = -248{,}513 \text{ MPa}$$

$$\sigma_{x,Ed} = max\left(\left|\sigma_{x,Ed,1}\right|, \left|\sigma_{x,Ed,2}\right|\right) \qquad = 248{,}513 \text{ MPa}$$

$$\sigma_{\theta,Ed} = \left(q_{eq} + q_s\right) \cdot \left(\frac{r}{t}\right) \qquad = 0{,}026 \text{ MPa}$$

$$\tau_{x,\theta,Ed,1} = \frac{M_{t,Ed}}{2 \cdot \pi \cdot r^2 \cdot t} + \frac{V_{z,Ed}}{\pi \cdot r \cdot t} \qquad = 17{,}748 \text{ MPa}$$

$$\tau_{x,\theta,Ed,2} = \frac{M_{t,Ed}}{2 \cdot \pi \cdot r^2 \cdot t} - \frac{V_{z,Ed}}{\pi \cdot r \cdot t} \qquad = 7{,}933 \text{ MPa}$$

$$\tau_{x,\theta,Ed} = max\left(\left|\tau_{x,\theta,Ed,1}\right|, \left|\sigma_{\tau_{x,\theta,Ed,2}}\right|\right) \qquad = 17{,}748 \text{ MPa}$$

$\tau_{x,n,Ed}$ = 0 MPa

$\tau_{\theta,n,Ed}$ = 0 MPa

According with EN 1993-1-6 Ch.6.2.1. (6), the equivalent stress is:

$$\sigma_{eq,Ed} = \sqrt{\sigma_{x,Ed}^2 + \sigma_{\theta,Ed}^2 - \sigma_{x,Ed} \cdot \sigma_{\theta,Ed} + 3 \cdot \left(\tau_{x,\theta,Ed}^2 + \tau_{x,n,Ed}^2 + \tau_{\theta,n,Ed}^2\right)}$$
= 250,394 MPa

$$f_{eq,Rd} = \frac{f_{yk}}{\gamma_{M0}} \quad = 355 \text{ MPa}$$

The stress limit
$\sigma_{eq,Rd} \leq f_{eq,Rd}$

$$Ratio_1 = \frac{\sigma_{eq,Rd}}{f_{eq,Rd}} = 0,705$$

- **Buckling design**

    According with EN 1993-1-6 Ch.8.5 & Annex D:

    Meridian compression

$$\omega = \frac{l}{r} \cdot \sqrt{\frac{r}{t}} \qquad\qquad = 232,845$$

c_θ $\qquad\qquad\qquad\qquad$ = 3 $\qquad$ - Tab D.1 - Annex D

$$c_x = \left| \begin{array}{l} 1, if\ 1,7 \le \omega \le 0,5 \cdot \dfrac{r}{t} \\[2mm] \left(1,36 - \dfrac{1,83}{\omega} + \dfrac{2,07}{\omega^2} \right), if\ \omega \le 1,7 \\[2mm] max\left[0,6 , 1 + \dfrac{0,2}{c_{xb}} \cdot \left(1 - 2 \cdot \omega \cdot \dfrac{t}{r} \right) \right], if\ \omega > 0,5 \end{array} \right. \qquad c_x = 0,6$$

$$\sigma_{x,Rcr} = 0,605 \cdot E \cdot c_x \cdot \frac{t}{r} \qquad = 1,837 \cdot 10^3 \text{ MPa}$$

Q $\qquad\qquad\qquad\qquad$ = 16 $\qquad$ - Tab D.2 - Annex D

$$\Delta w_k = \frac{1}{Q} \cdot \sqrt{\frac{r}{t}} \cdot t \qquad\qquad = 8,053 \text{ mm}$$

$$a_x = \frac{0,62}{1 + 1,91 \cdot \left(\dfrac{\Delta w_k}{t} \right)^{1,44}} \qquad = 0,409$$

λ_{x0} $\quad$ = 0,20

β_x $\quad$ = 0,60

η_x $\quad$ = 1,00

$$\frac{r}{t} \le 0,03 \cdot \frac{E}{f_{yk}} = 0$$

c_θ $\qquad\qquad$ = 0,60

$$c_{\theta s} = 0,60 + \frac{1}{\omega^2} - \frac{0,30}{\omega^3} = 0,60 \qquad\qquad \text{(Tab D.4- Annex D)}$$

$$\sigma_{\theta,Rcr} = \left| \begin{array}{l} \left(0,92 \cdot E \cdot \dfrac{c_\theta}{\omega} \cdot \dfrac{t}{r}\right), if\, 20 \le \dfrac{\omega}{c_\theta} \le 1,63 \cdot \dfrac{r}{t} \\[3mm] \left(0,92 \cdot E \cdot \dfrac{c_{\theta s}}{\omega} \cdot \dfrac{t}{r}\right), if\, 20 < \dfrac{\omega}{c_\theta} \\[3mm] \left[E \cdot \left(\dfrac{t}{r}\right)^2 \cdot \left[0,275 + 2,03 \cdot \left(\dfrac{c_\theta}{\omega} \cdot \dfrac{r}{t}\right)^4 \right] \right], if\, \dfrac{\omega}{c_\theta} > 1,63 \end{array} \right.$$

$\sigma_{\theta,Rcr}$ = 33,564 MPa

a_θ	= 0,50	(Tab D.5- Annex D)
$\lambda_{\theta 0}$	= 0,40	
β_θ	= 0,60	
η_θ	= 1,00	

$$\dfrac{r}{t} \le 0,21 \cdot \sqrt{\dfrac{E}{f_{yk}}} \quad = 0$$

ω = 232,845

$$c_T = \left| \begin{array}{l} 1, if\, 10 \le \omega \le 8,7 \cdot \dfrac{r}{t} \\[3mm] \sqrt{1 + \dfrac{42}{\omega^3}}, if\, \omega \le 10 \\[3mm] \left(\dfrac{1}{3} \cdot \sqrt{\omega \cdot \dfrac{t}{r}}\right), if\, \omega > 8,7 \cdot \dfrac{r}{t} \end{array} \right. \qquad c_T = 1,00$$

$$\tau_{x\theta,Rcr} = 0,75 \cdot E \cdot c_T \cdot \sqrt{\dfrac{1}{\omega}} \cdot \left(\dfrac{t}{r}\right) = 248,713\ MPa$$

a_T	= 0,50	(Tab D.6- Annex D)
λ_{T0}	= 0,40	
β_T	= 0,60	
η_T	= 1,00	

$$\dfrac{r}{t} \le 0,16 \cdot \left(\dfrac{E}{f_{yk}}\right)^{0,67} \quad = 0$$

Resistance for the buckling

a_x = 0,409
λ_{x0} = 0,20
β_x = 0,60
η_x = 1,00

$\sigma_{x,Rcr}$ = $1,837 \cdot 10^3$ MPa

$$\lambda_x = \sqrt{\frac{f_{yk}}{\sigma_{x,Rcr}}} \qquad = 0,44$$

$$\lambda_{p,x} = \sqrt{\frac{a_x}{1 - \beta_x}} \qquad = 1,011$$

$$X_x = \begin{vmatrix} 1, if \lambda_x \leq \lambda_{x0} \\ \left[1 - \beta_x \cdot \left(\dfrac{\lambda_x - \lambda_{x0}}{\lambda_{p,x} - \lambda_{x0}} \right)^{\eta_x} \right], if \lambda_{x0} < \lambda_x < \lambda_{p,x} \\ \dfrac{a_x}{\lambda_x{}^2}, if \lambda_{p,x} \leq \lambda_x \end{vmatrix} \qquad X_x = 0,823$$

$\sigma_{x,Rcr} = X_x \cdot f_{yk}$ = 292,096 MPa

a_θ = 0,50
$\lambda_{\theta 0}$ = 0,40
β_θ = 0,60
η_θ = 1,00

$\sigma_{\theta,Rcr}$ = 33,564 MPa

$$\lambda_\theta = \sqrt{\frac{f_{yk}}{\sigma_{\theta,Rcr}}} \qquad = 3,252$$

$$\lambda_{p,\theta} = \sqrt{\frac{a_\theta}{1 - \beta_\theta}} \qquad = 1,118$$

$$\chi_\theta = \begin{vmatrix} 1, if\lambda_\theta \le \lambda_{\theta 0} \\[2mm] \left[1 - \beta_\theta \cdot \left(\dfrac{\lambda_\theta - \lambda_{\theta 0}}{\lambda_{p,\theta} - \lambda_{\theta 0}} \right)^{\eta_\theta} \right], if\lambda_{\theta 0} < \lambda_\theta < \lambda_{p,\theta} \\[2mm] \dfrac{a_\theta}{\lambda_\theta{}^2}, if\lambda_{p,\theta} \le \lambda_\theta \end{vmatrix} \qquad \chi_\theta = 0,047$$

$\sigma_{\theta,Rk} = \chi_\theta \cdot f_{yk}$ $= 16,782$ MPa

a_T $= 0,50$
λ_{T0} $= 0,40$
β_T $= 0,60$
η_T $= 1,00$

$\tau_{x\theta,Rcr}$ $= 248,713$ MPa

$$\lambda_T = \sqrt{\dfrac{\left(\dfrac{f_{yk}}{\sqrt{3}} \right)}{\tau_{x\theta,Rcr}}} = 0,908$$

$$\lambda_{p,T} = \sqrt{\dfrac{a_T}{1 - \beta_T}} = 1,118$$

$$\chi_T = \begin{vmatrix} 1, if\lambda_T \le \lambda_{T0} \\[2mm] \left[1 - \beta_T \cdot \left(\dfrac{\lambda_T - \lambda_{T0}}{\lambda_{p,T} - \lambda_{T0}} \right)^{\eta_T} \right], if\lambda_{T0} < \lambda_T < \lambda_{p,T} \\[2mm] \dfrac{a_T}{\lambda_T{}^2}, if\lambda_{p,T} \le \lambda_T \end{vmatrix} \qquad \chi_\tau = 0,576$$

$$\tau_{x\theta,Rk} = \frac{\left(\chi_\theta \cdot f_{yk} \right)}{\sqrt{3}} \qquad = 117,992 \text{ MPa}$$

χ_x $= 0,823$
χ_θ $= 0,047$
χ_T $= 0,576$

$k_x = 1,25 + 0,75 \cdot \chi_x$ $= 1,867$

$k_\theta = 1{,}25 + 0{,}75 \cdot \chi_\theta$ $= 1{,}285$

$k_\tau = 1{,}75 + 0{,}25 \cdot \chi_\tau$ $= 1{,}894$

$k_i = (\chi_x \cdot \chi_\theta)^2$ $= 0{,}001513$

$\sigma_{x,Rd} = \dfrac{\sigma_{x,Rk}}{\gamma_{M1}}$ $= 265{,}542 \text{ MPa}$

$\sigma_{\theta,Rd} = \dfrac{\sigma_{\theta,Rk}}{\gamma_{M1}}$ $= 15{,}256 \text{ MPa}$

$\tau_{x\theta,Rd} = \dfrac{\tau_{x\theta,Rk}}{\gamma_{M1}}$ $= 107{,}265 \text{ MPa}$

$\sigma_{x,Ed} \leq \sigma_{x,Rd} = 1$ $Ratio_{\sigma_x} = \dfrac{\sigma_{x,Ed}}{\sigma_{x,Rd}} = 0{,}936$

$\sigma_{\theta,Ed} \leq \sigma_{\theta,Rd} = 1$ $Ratio_{\sigma_\theta} = \dfrac{\sigma_{\theta,Ed}}{\sigma_{\theta,Rd}} = 0{,}002$

$\tau_{x\theta,Ed} \leq \tau_{x\theta,Rd} = 1$ $Ratio_{\tau_\theta} = \dfrac{\tau_{x\theta,Ed}}{\tau_{x\theta,Rd}} = 0{,}165$

$$\left(\frac{\sigma_{x,Ed}}{\sigma_{x,Rd}}\right)^{k_x} - k_i \cdot \left(\frac{\sigma_{x,Ed}}{\sigma_{x,Rd}}\right) \cdot \left(\frac{\sigma_{\theta,Ed}}{\sigma_{\theta,Rd}}\right) + \left(\frac{\sigma_{\theta,Ed}}{\sigma_{\theta,Rd}}\right)^{k_\theta} + \left(\frac{\tau_{x\theta,Ed}}{\tau_{x\theta,Rd}}\right)^{k_\tau} = 0{,}917$$

$$Ratio_2 = \left(\frac{\sigma_{x,Ed}}{\sigma_{x,Rd}}\right)^{k_x} - k_i \cdot \left(\frac{\sigma_{x,Ed}}{\sigma_{x,Rd}}\right) \cdot \left(\frac{\sigma_{\theta,Ed}}{\sigma_{\theta,Rd}}\right) + \left(\frac{\sigma_{\theta,Ed}}{\sigma_{\theta,Rd}}\right)^{k_\theta} + \left(\frac{\tau_{x\theta,Ed}}{\tau_{x\theta,Rd}}\right)^{k_\tau} = 0{,}917$$

$$Ratio = max\left(Ratio_1, Ratio_{\sigma_x}, Ratio_{\sigma_\theta}, Ratio_{\tau_\theta}, Ratio_2\right) = 0{,}936$$

Annex 3 – FAD-2 Critical flaw dimensions

A3.1. Critical flaw height (depth)
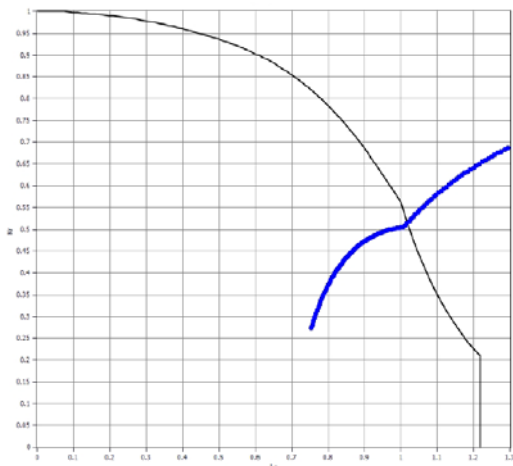
Fig. A3.1. *FP-SF-1*
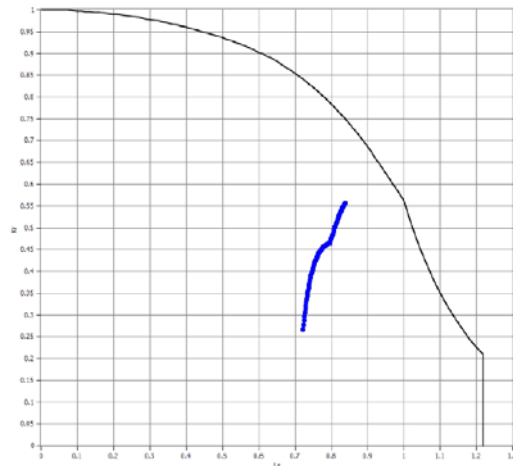
Fig. A3.2. *FP-SF-2*
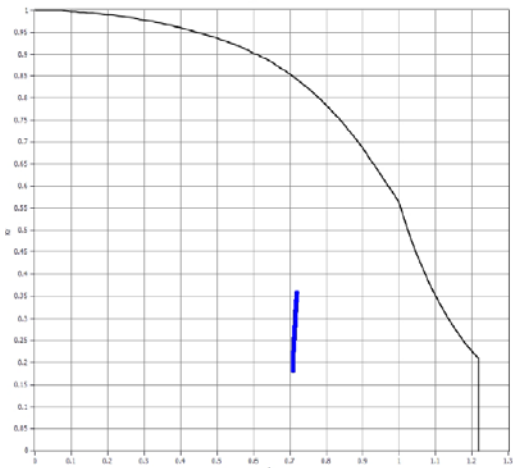
Fig. A3.3. *FP-SF-3*
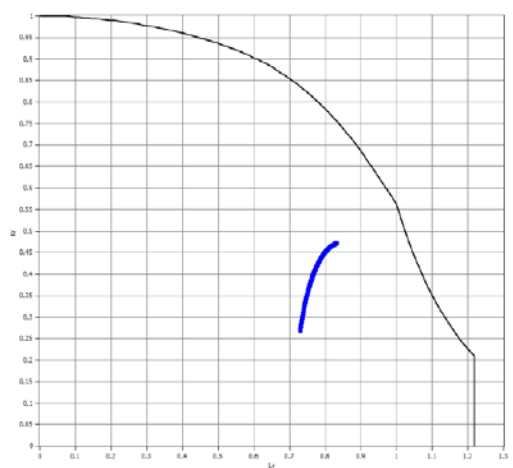
Fig. A3.4. *FP-SF-4*
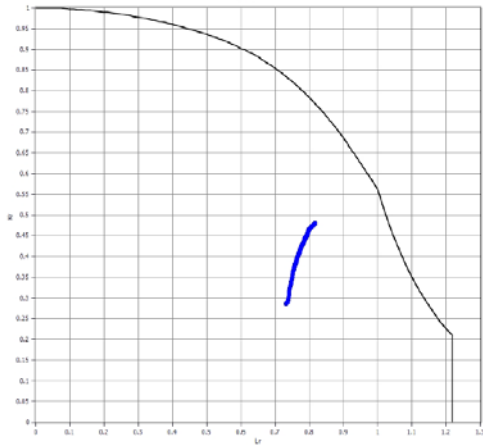
Fig. A3.5. *FP-SF-5*
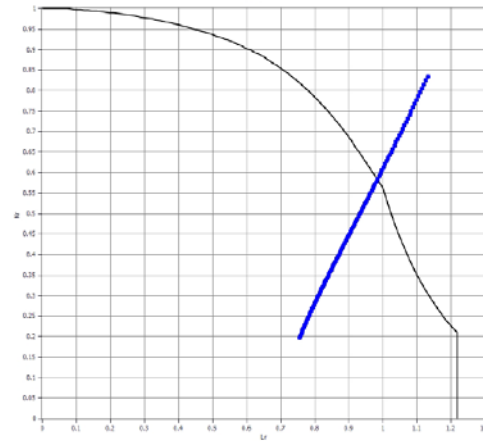
Fig. A3.6. *FP-LSF-1*
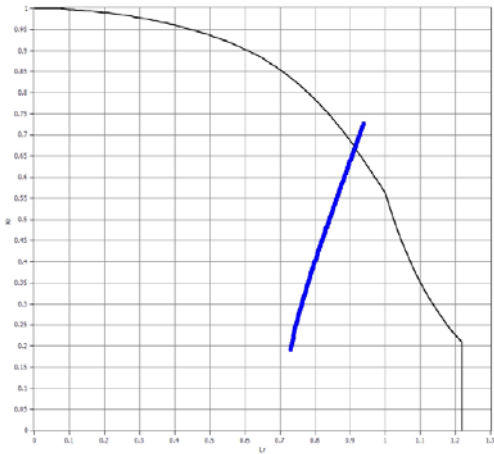
Fig. A3.7. *FP-LSF-2*
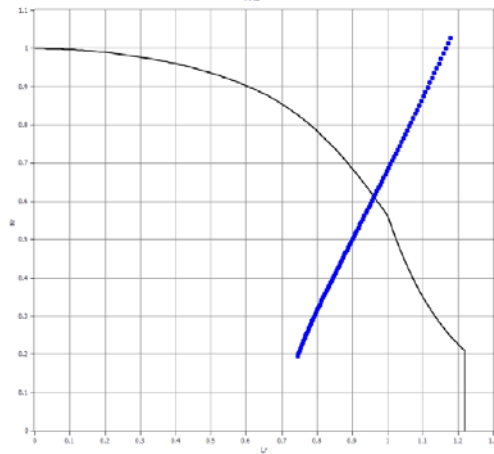
Fig. A3.8. *FP-LSF-3*
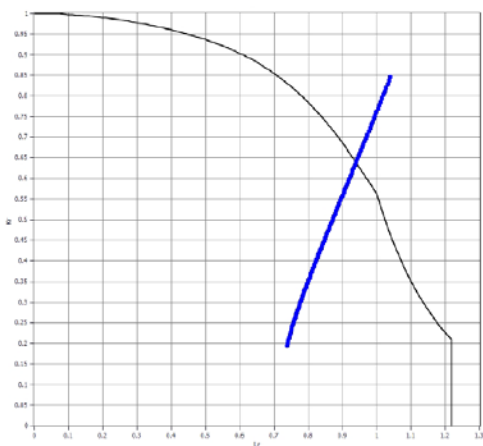
Fig. A3.9. *FP-LSF-4*
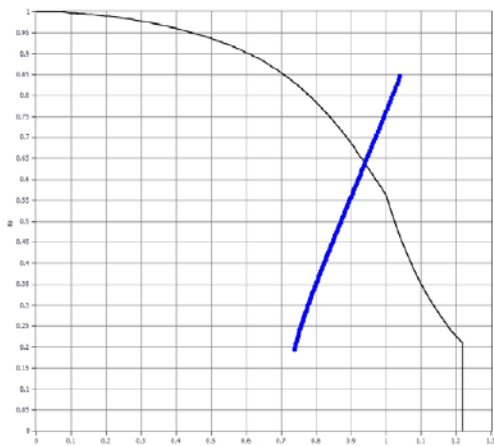
Fig. A3.10. *FP-LSF-5*
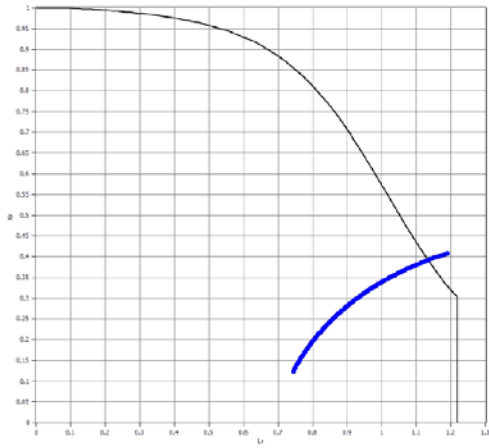
Fig. A3.11. *FP-BF-1*
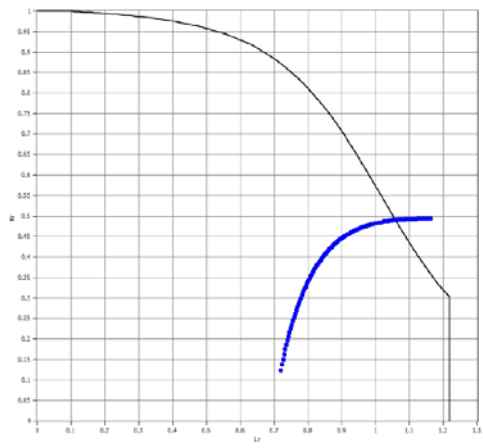
Fig. A3.12. *FP-BF-2*
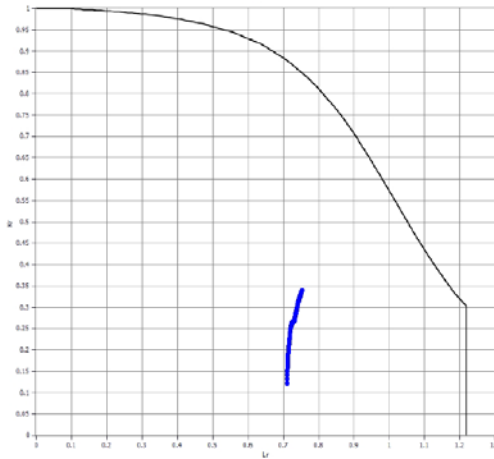
Fig. A3.13. *FP-BF-3*
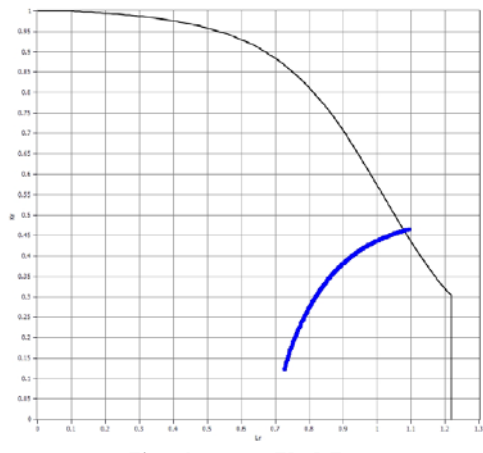
Fig. A3.14. *FP-BF-4*
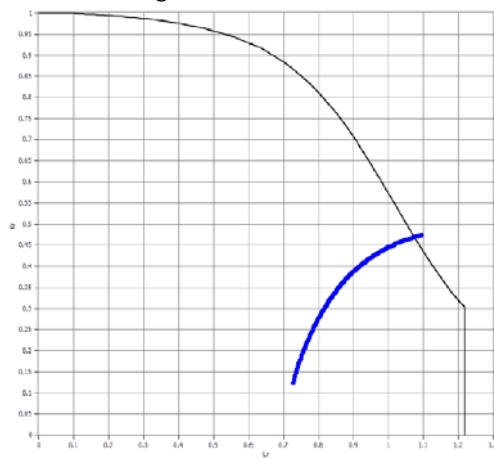
Fig. A3.15. *FP-BF-5*
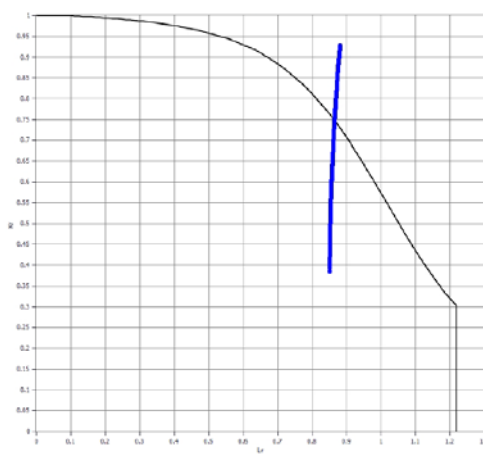
Fig. A3.16. *CSAF-TTF-1*
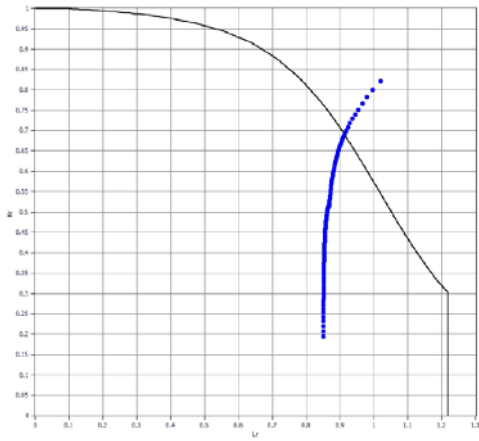
Fig. A3.17. *CSAF-ISF-1*
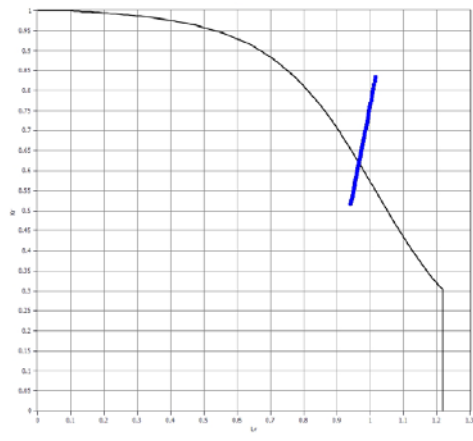
Fig. A3.18. *CSAF-LISF-1*
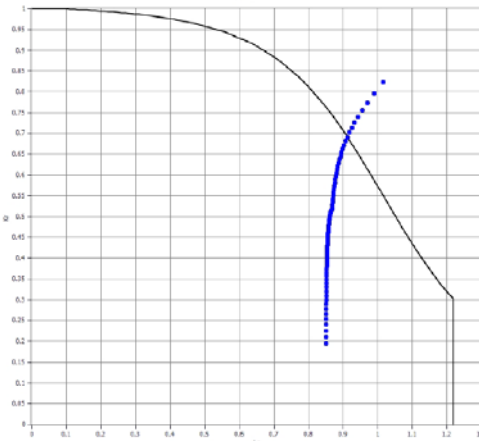
Fig. A3.19. *CSAF-ESF-1*
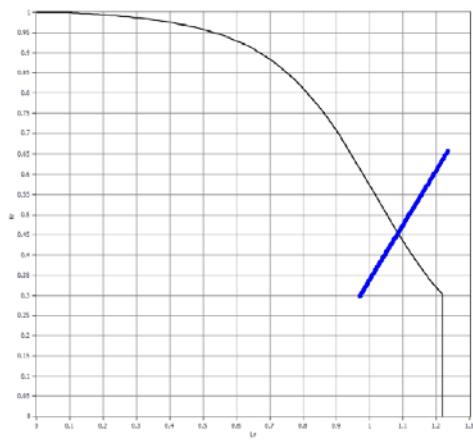
Fig. A3.20. *CSAF-LESF-1*
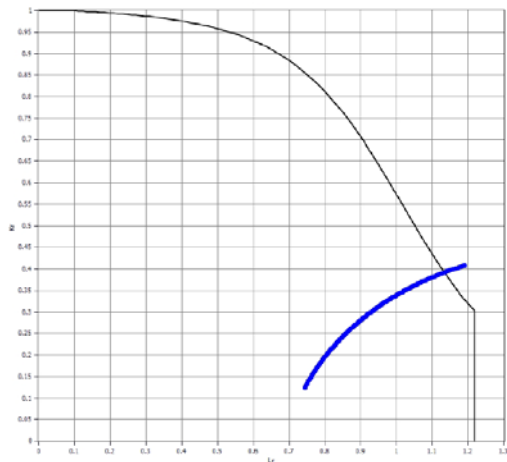
Fig. A3.21. *CSAF-BF-1*
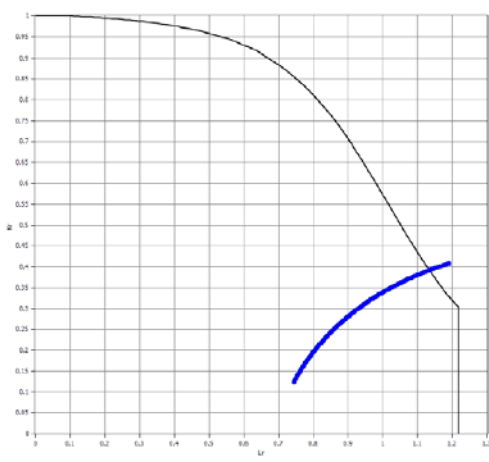
Fig. A3.22. *CAF-BF-1*
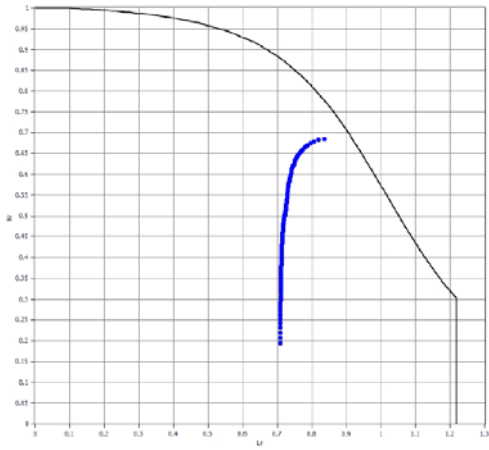
Fig. A3.23. *CSCF-ISF-1*
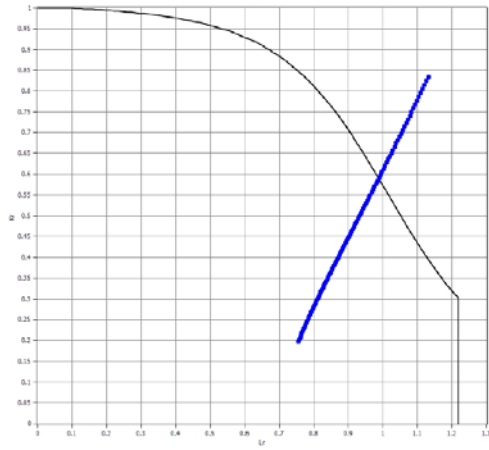
Fig. A3.24. *CSCF-FCESF-1*
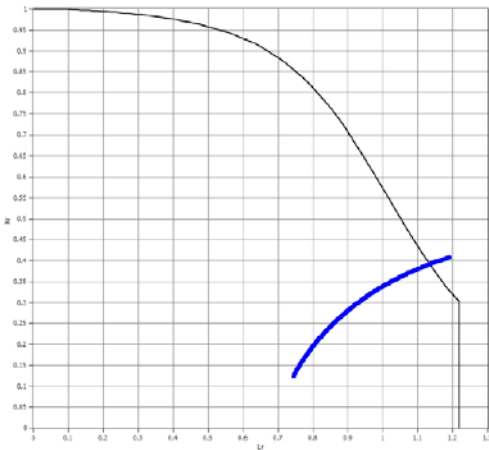
Fig. A3.25. *CSCF-BF-1*
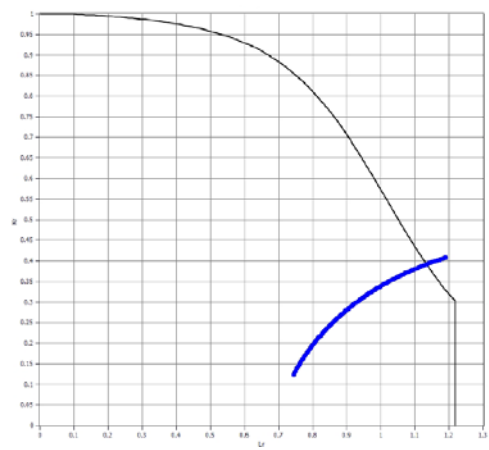
Fig. A3.26. *CCF-BF-1*
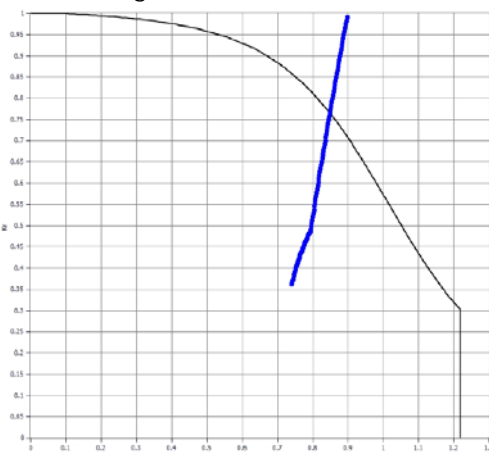
Fig. A3.27. *CWJ-WT-1*

A3.2. Critical flaw length
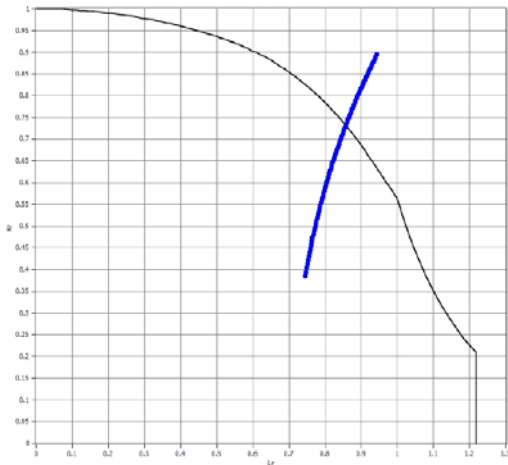
Fig. A3.28. *FP-TTF-1*
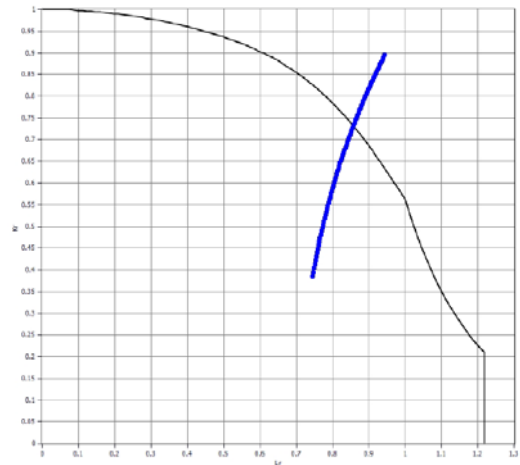
Fig. A3.29. *FP-TTF-2*
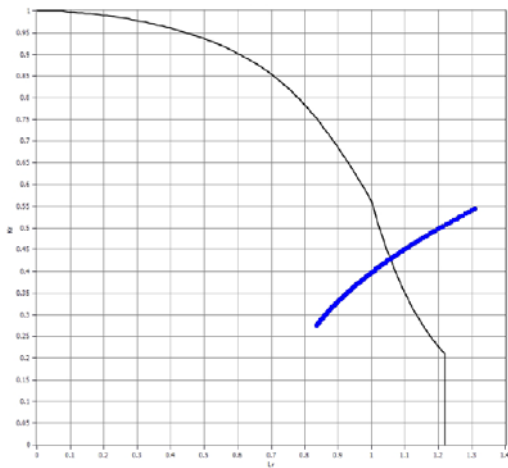
Fig. A3.30. *FP-TTF-3*
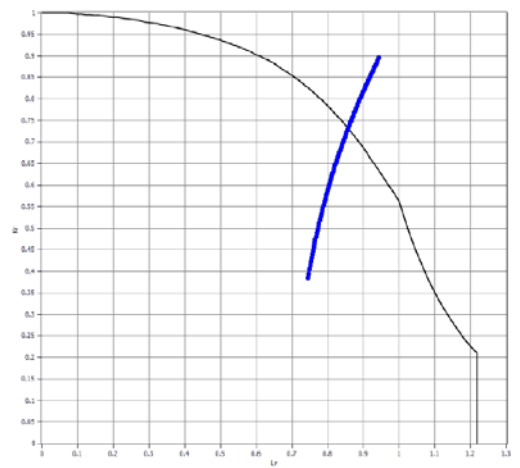
Fig. A3.31. *FP-TTF-4*
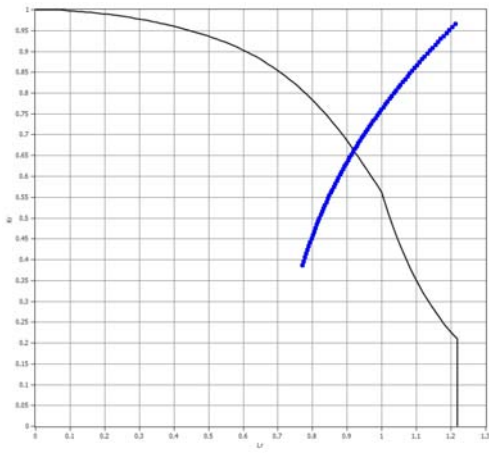
Fig. A3.32. *FP-TTF-5*
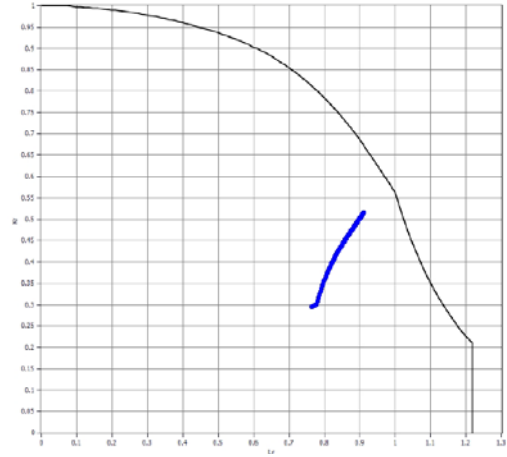
Fig. A3.33. *FP-SF-1*
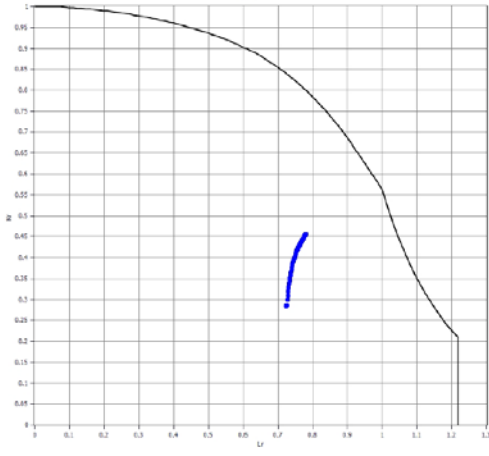
Fig. A3.34. *FP-SF-2*
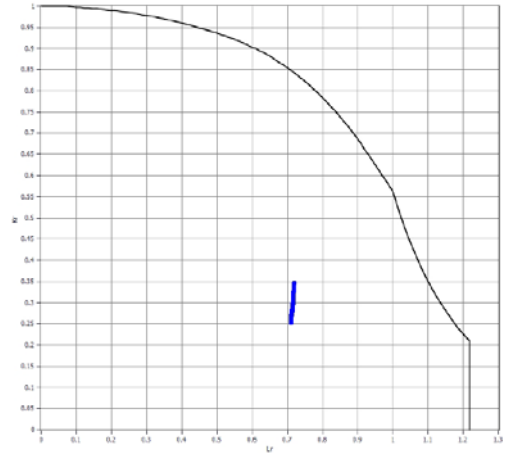
Fig. A3.35. *FP-SF-3*
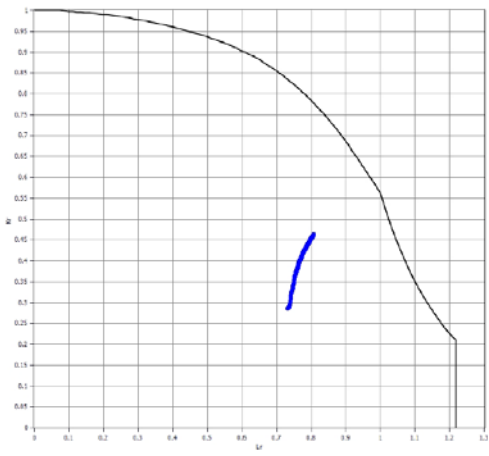
Fig. A3.36. *FP-SF-4*
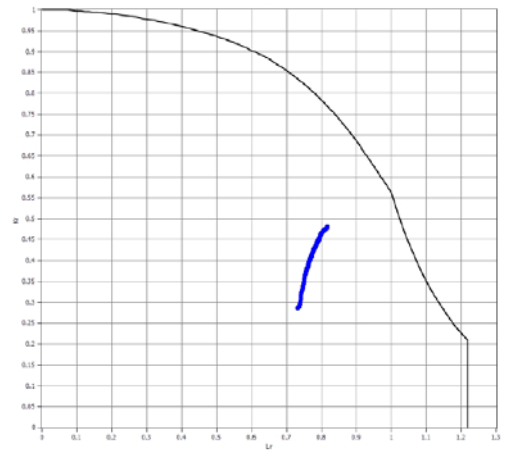
Fig. A3.37. *FP-SF-5*
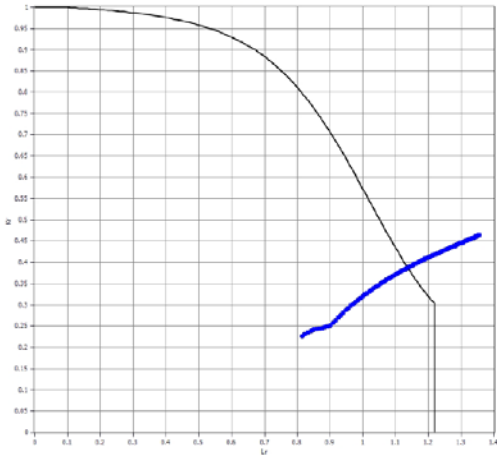
Fig. A3.38. *FP-BF-1*
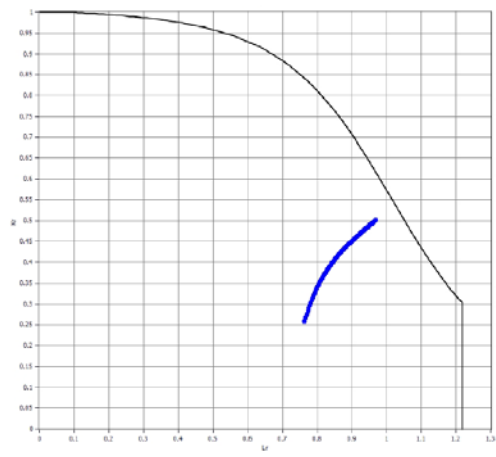
Fig. A3.39. *FP-BF-2*
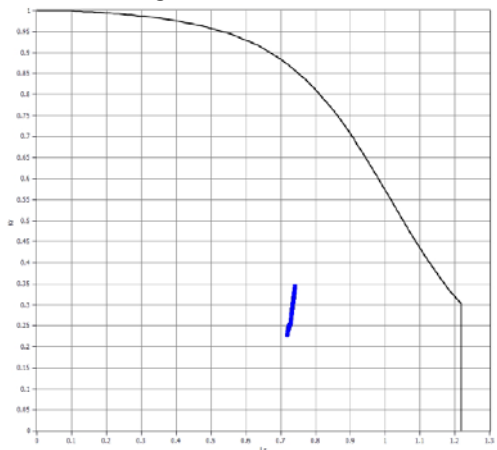
Fig. A3.40. *FP-BF-3*
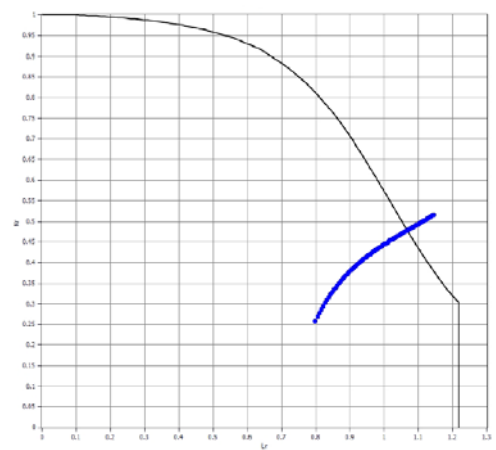
Fig. A3.41. *FP-BF-4*
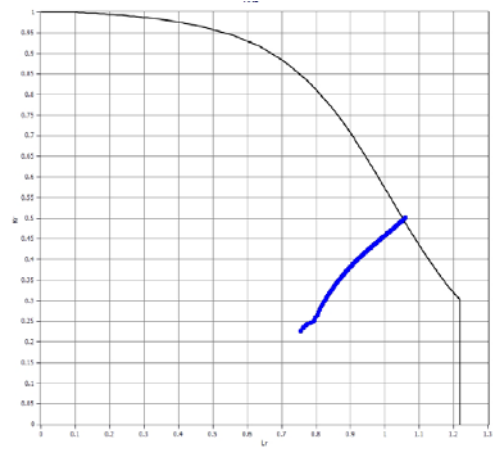
Fig. A3.42. *FP-BF-5*
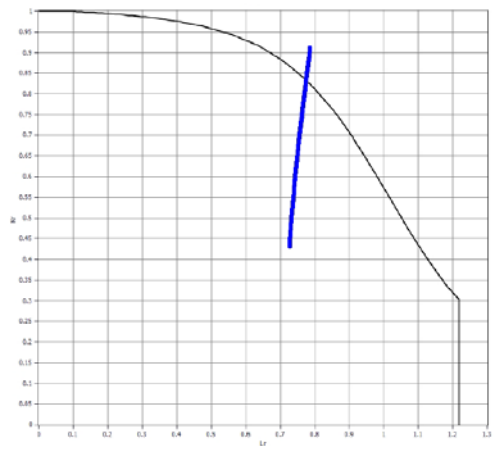
Fig. A3.43. *FP-EF-1*
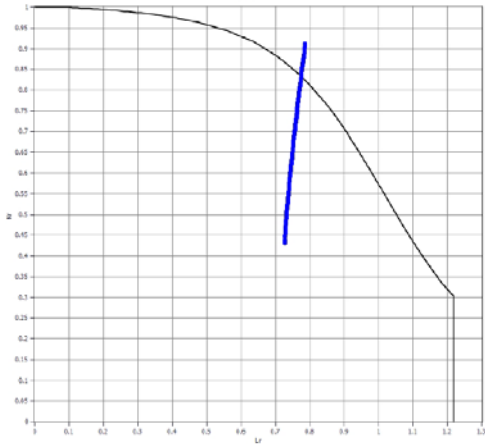
Fig. A3.44. *FP-EF-2*
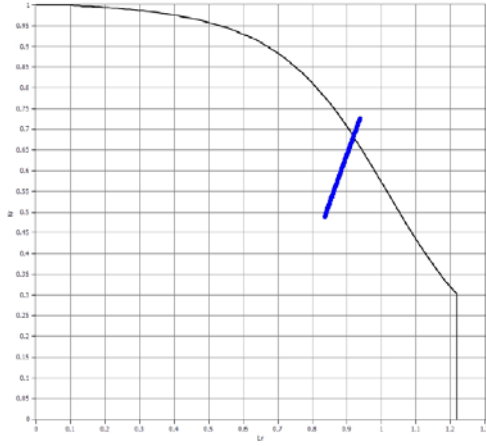
Fig. A3.45. *FP-EF-3*
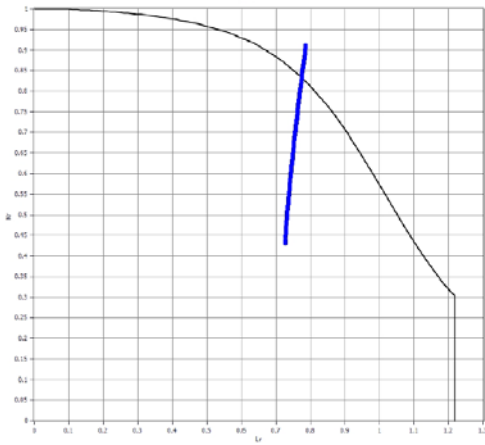
Fig. A3.46. *FP-EF-4*
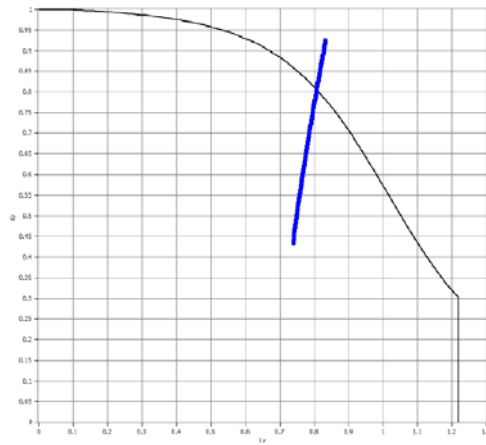
Fig. A3.47. *FP-EF-5*
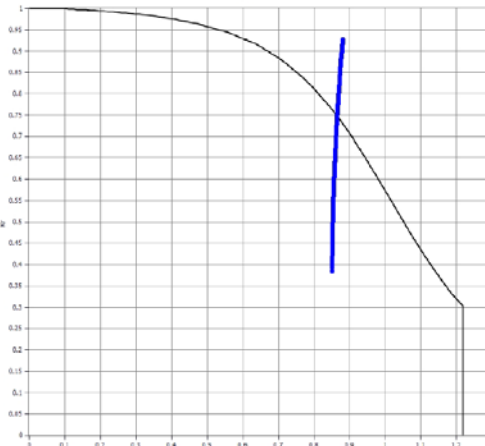
Fig. A3.48. *CSAF-ISF-1*
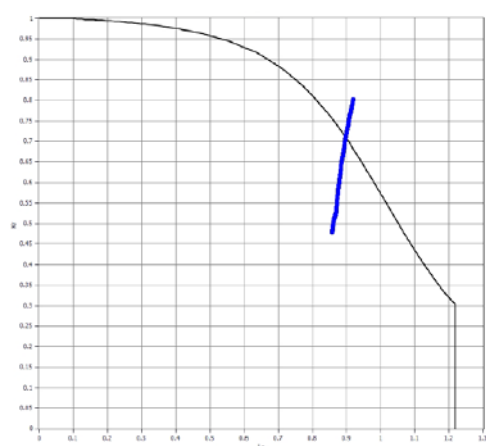
Fig. A3.49. *CSAF-ESF-1*
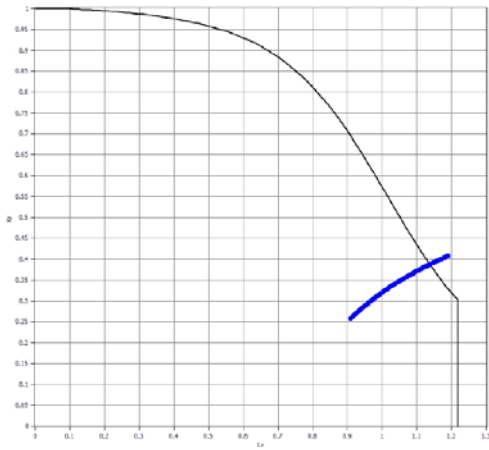
Fig. A3.50. *CSAF-BF-1*
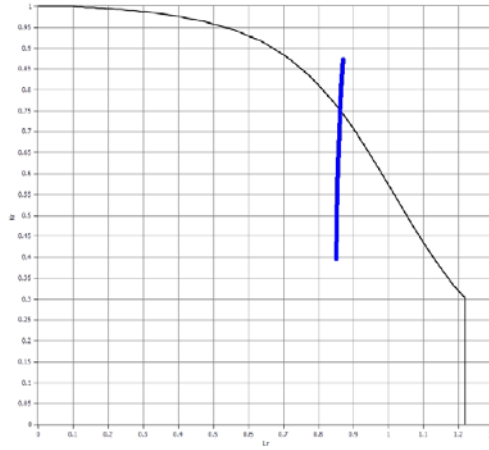
Fig. A3.51. *CAF-TTF-1*
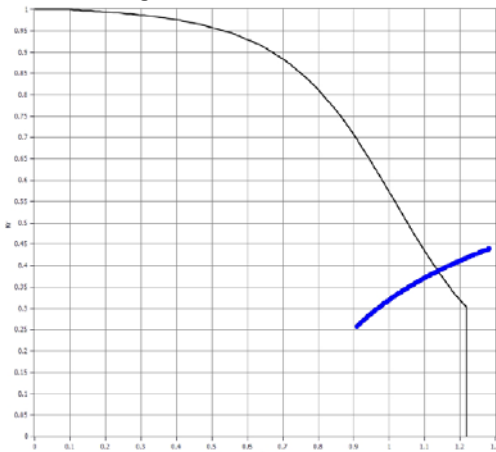
Fig. A3.52. *CAF-BF-1*
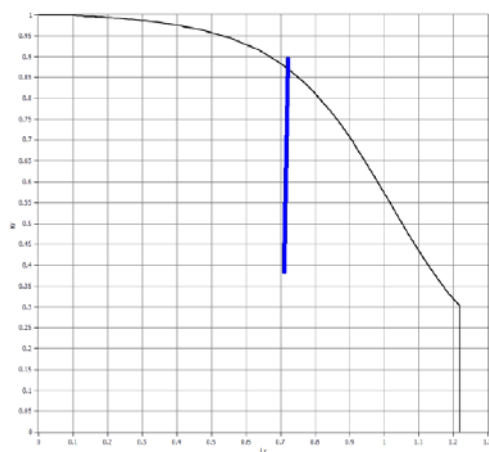
Fig. A3.53. *CSCF-TTF-1*
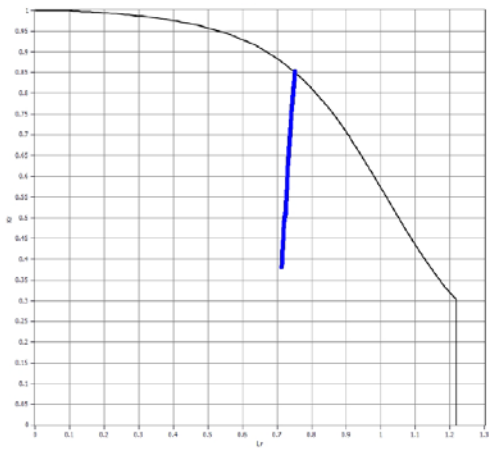
Fig. A3.54. *CSCF-ISF-1*
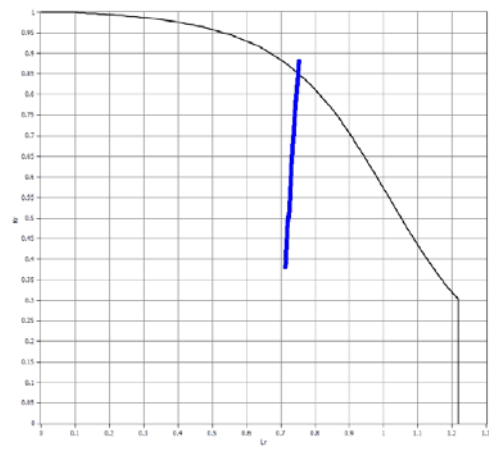
Fig. A3.55. *CSCF-ESF-1*
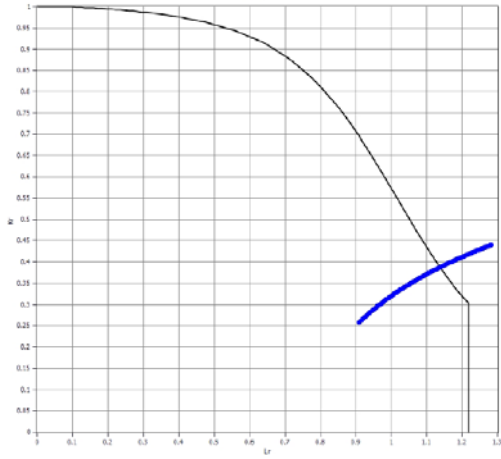
Fig. A3.56. *CCF-BF-1*
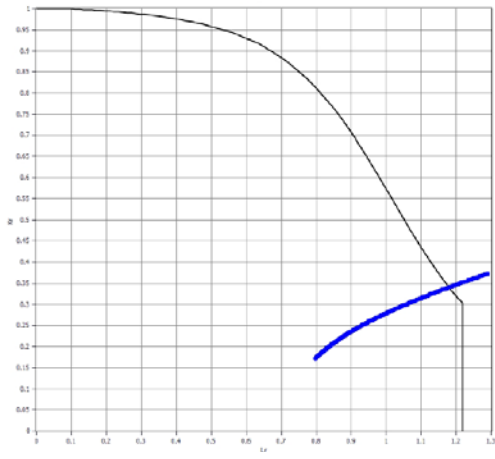
Fig. A3.57. *CWJ-TTF-1*
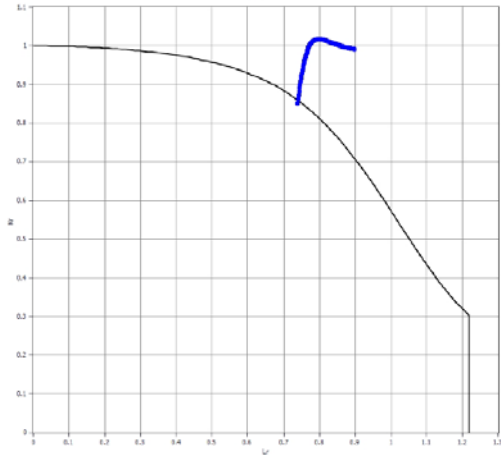
Fig. A3.58. *CWJ-WT-1*

Annex 4 – Fatigue assessments results
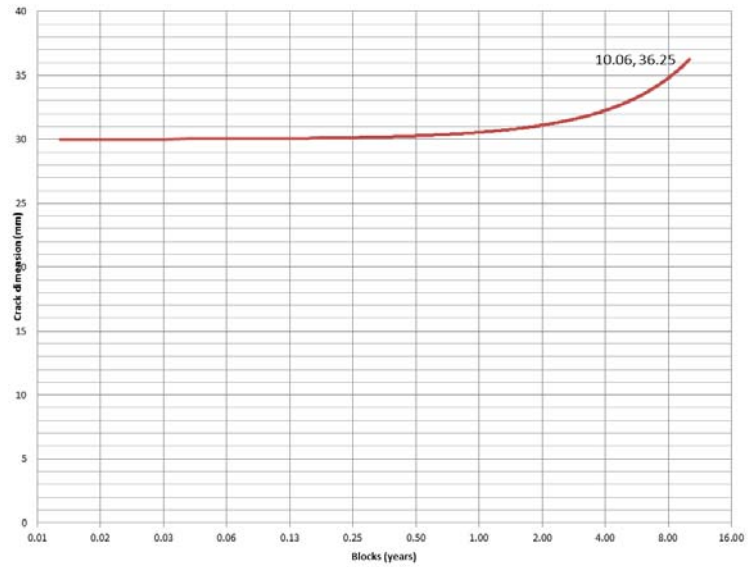
Fig.A4.1. *Fatigue assessment - Flat Plate – Through Thickness Flaw-1 – FP-TTF-1*
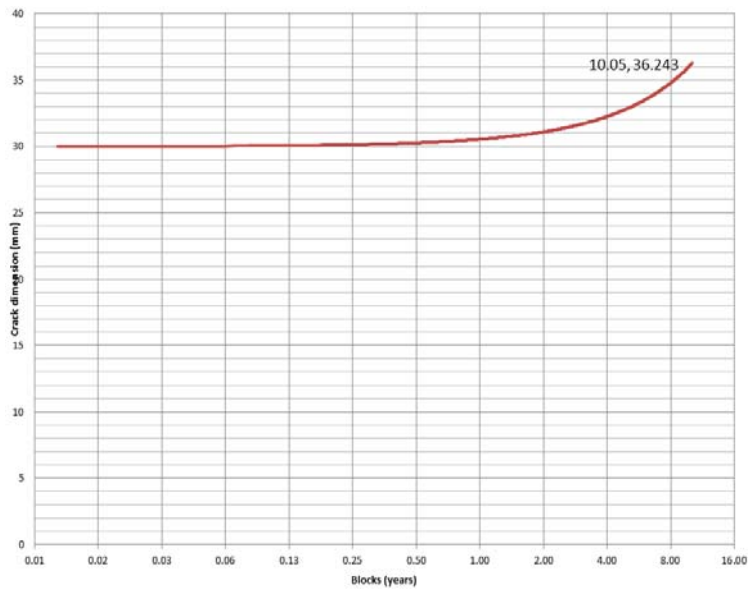
Fig.A4.2. *Fatigue assessment - Flat Plate – Through Thickness Flaw-2 – FP-TTF-2*
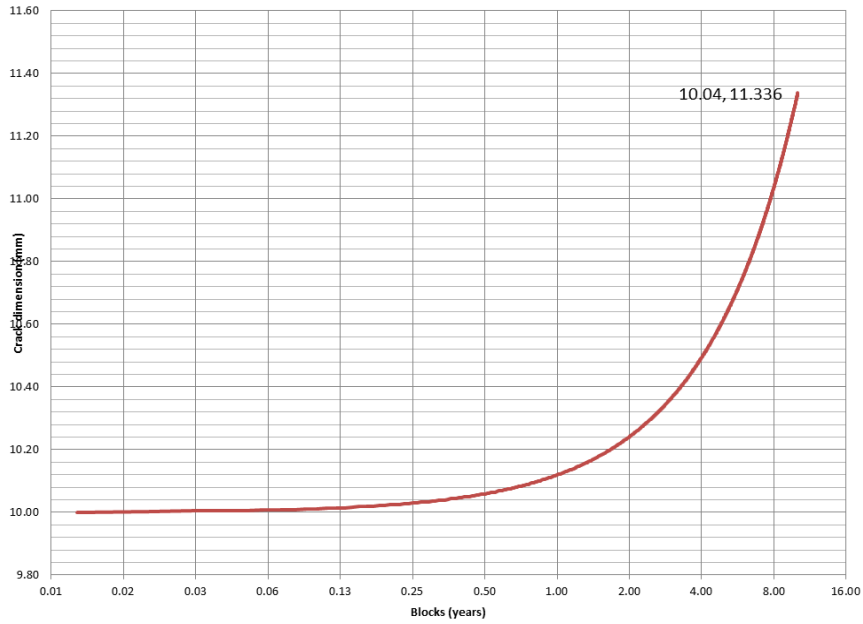
Fig.A4.3. *Fatigue assessment - Flat Plate – Through Thickness Flaw-3 – FP-TTF-3*
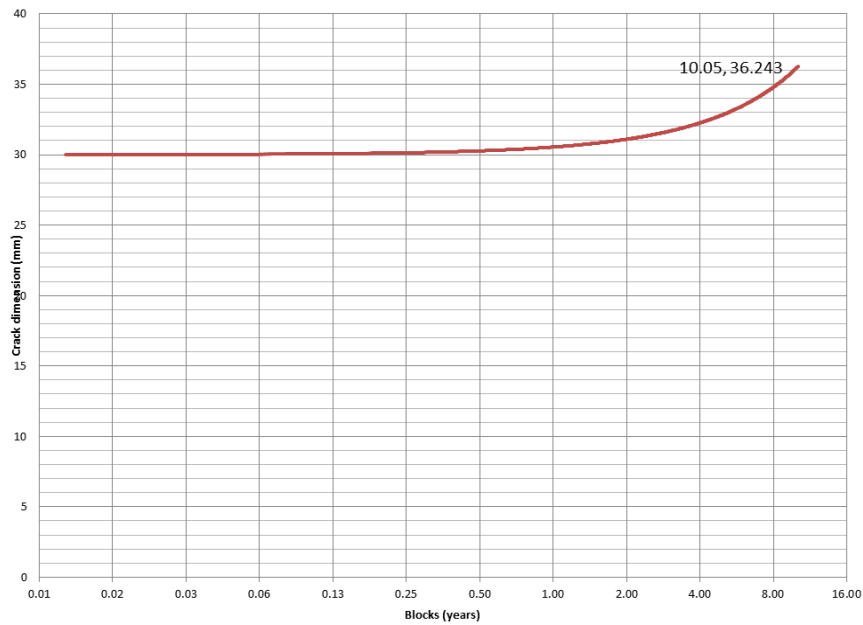
Fig.A4.4. *Fatigue assessment - Flat Plate – Through Thickness Flaw-4 – FP-TTF-4*
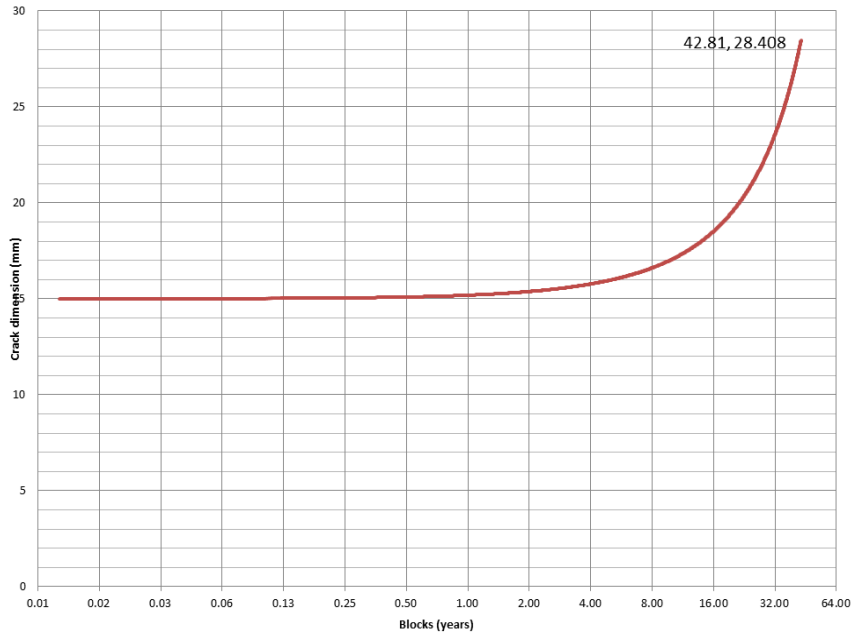
Fig.A4.5. *Fatigue assessment - Flat Plate – Through Thickness Flaw-5 – FP-TTF-5*
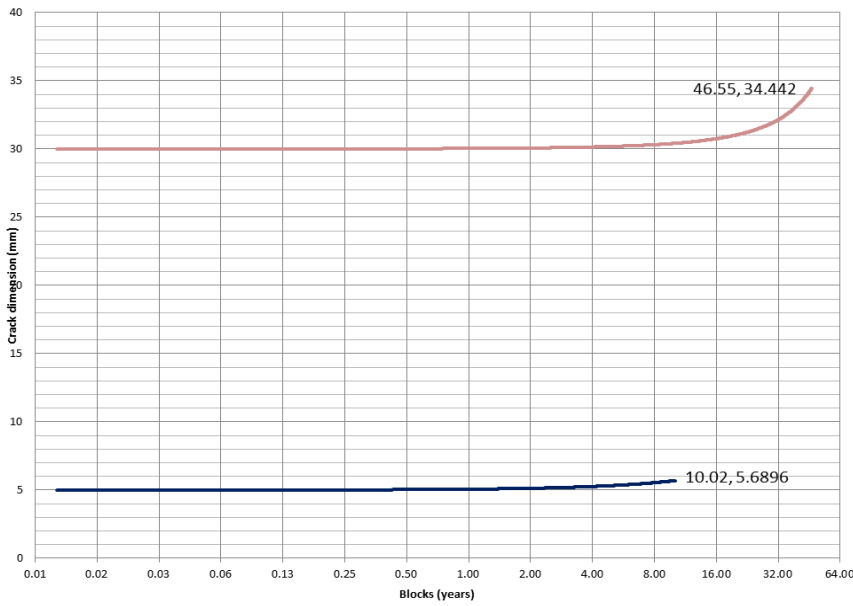
Fig.A4.6. *Fatigue assessment - Flat Plate – Surface Flaw-1 – FP-SF-1*
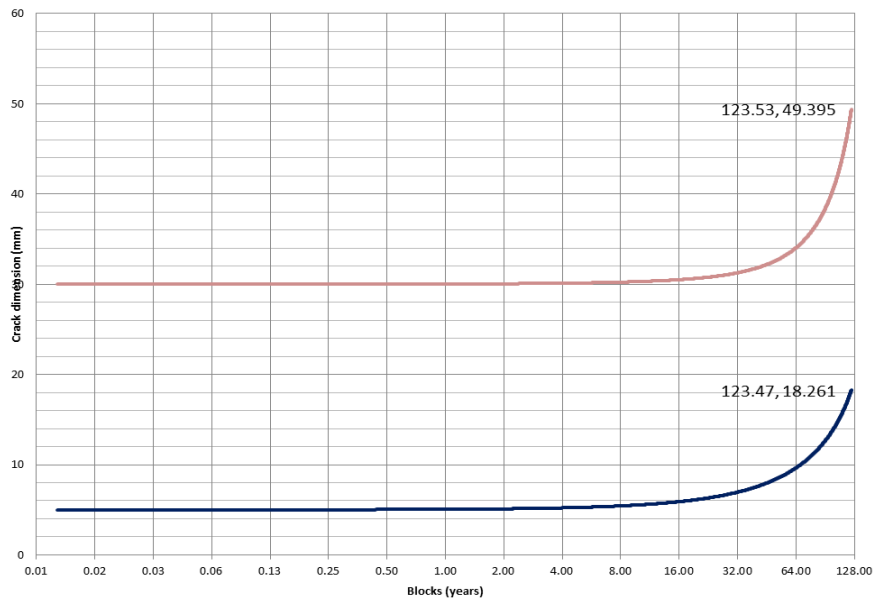
Fig.A4.7. *Fatigue assessment - Flat Plate – Surface Flaw-2 – FP-SF-2*
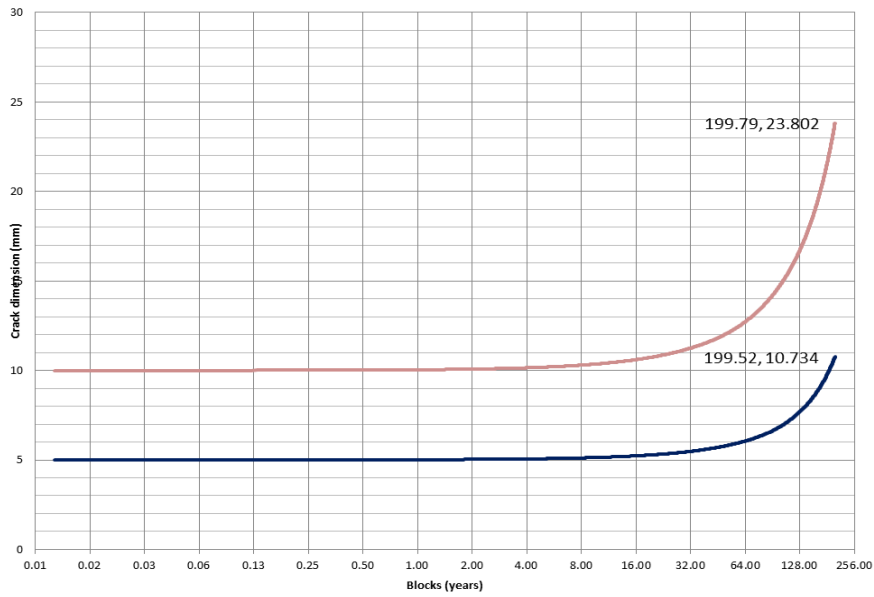
Fig.A4.8. *Fatigue assessment - Flat Plate – Surface Flaw-3 – FP-SF-3*
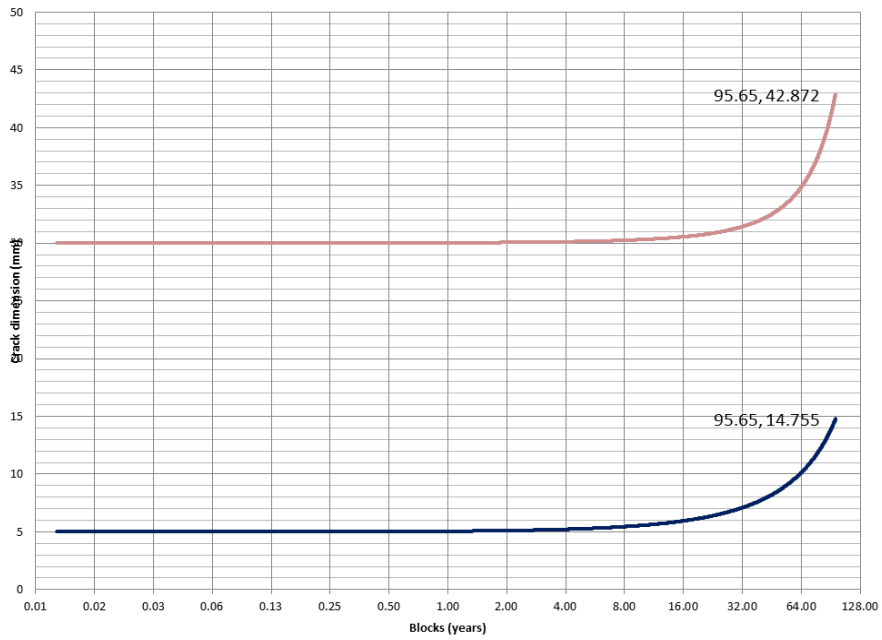
Fig.A4.9. *Fatigue assessment - Flat Plate – Surface Flaw-4 – FP-SF-4*
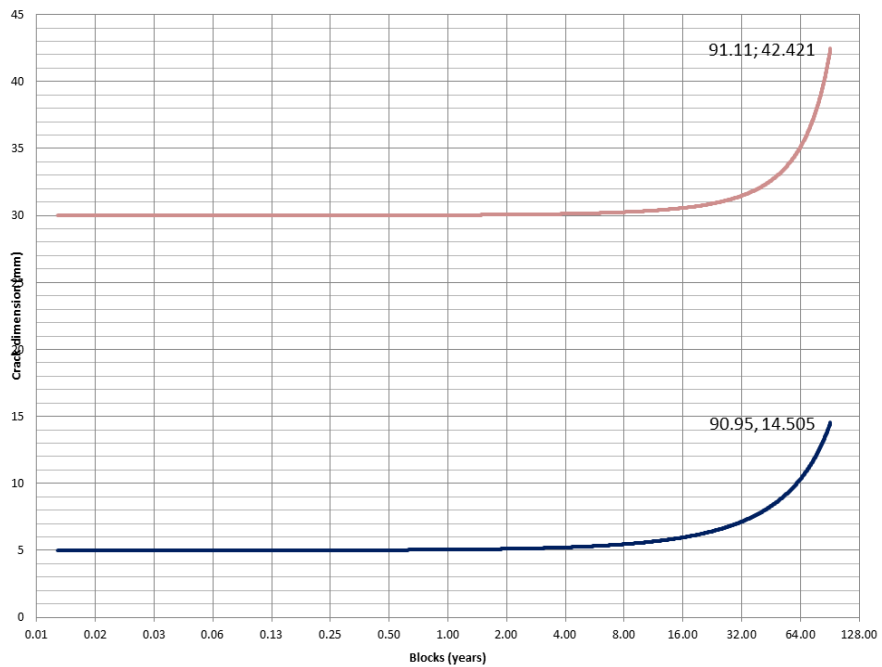
Fig.A4.10. *Fatigue assessment - Flat Plate – Surface Flaw-5 – FP-SF-5*
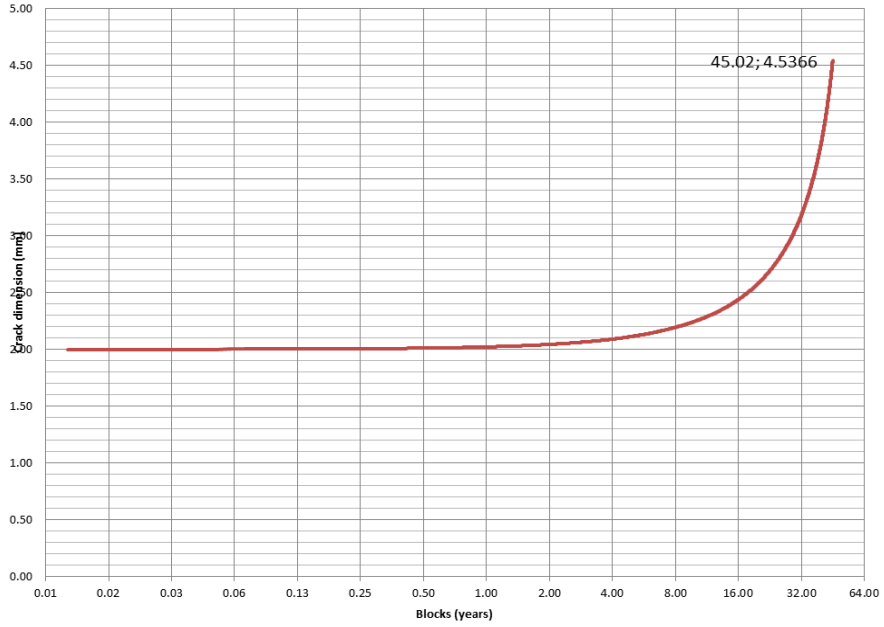
Fig.A4.11. *Fatigue assessment - Flat Plate – Long Surface Flaw-1 – FP-LSF-1*
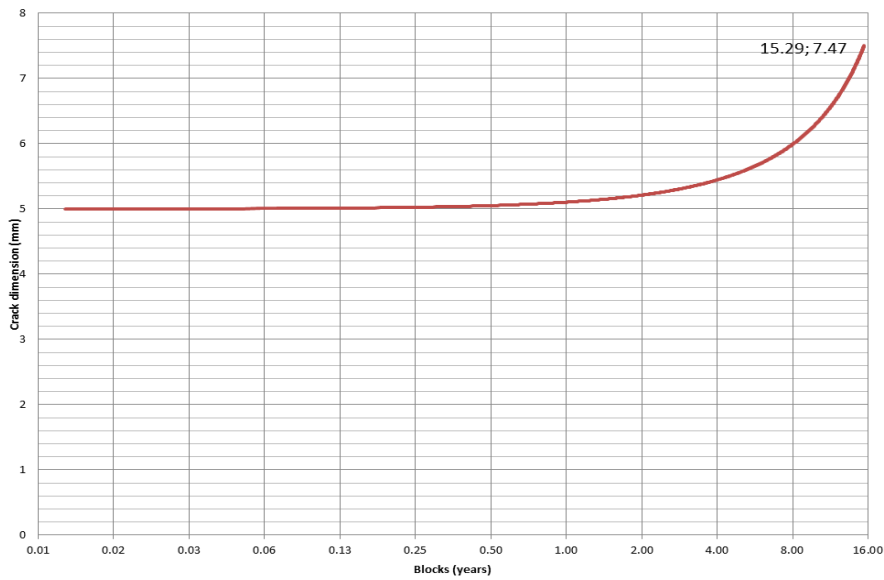
Fig.A4.12. *Fatigue assessment - Flat Plate – Long Surface Flaw-2 – FP-LSF-2*
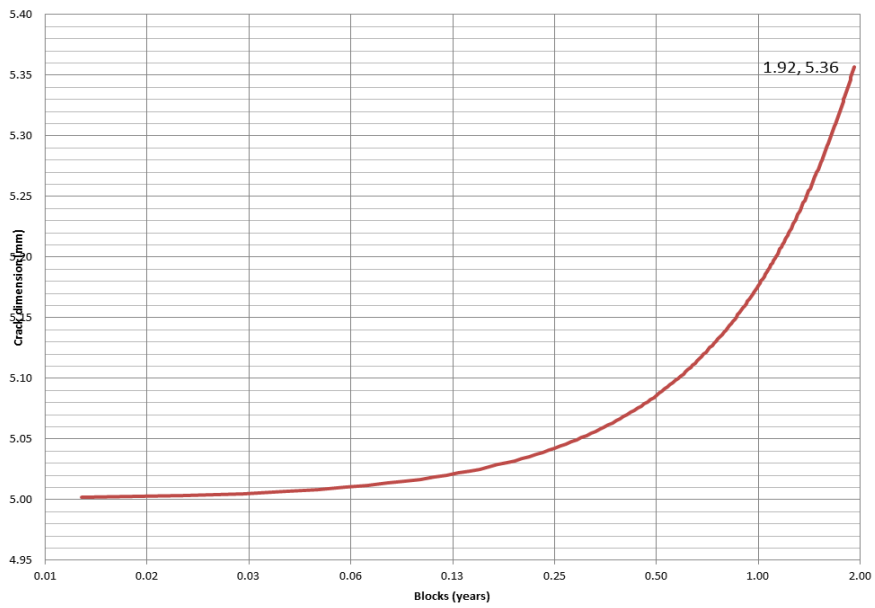
Fig.A4.13. *Fatigue assessment - Flat Plate – Long Surface Flaw-3 – FP-LSF-3*
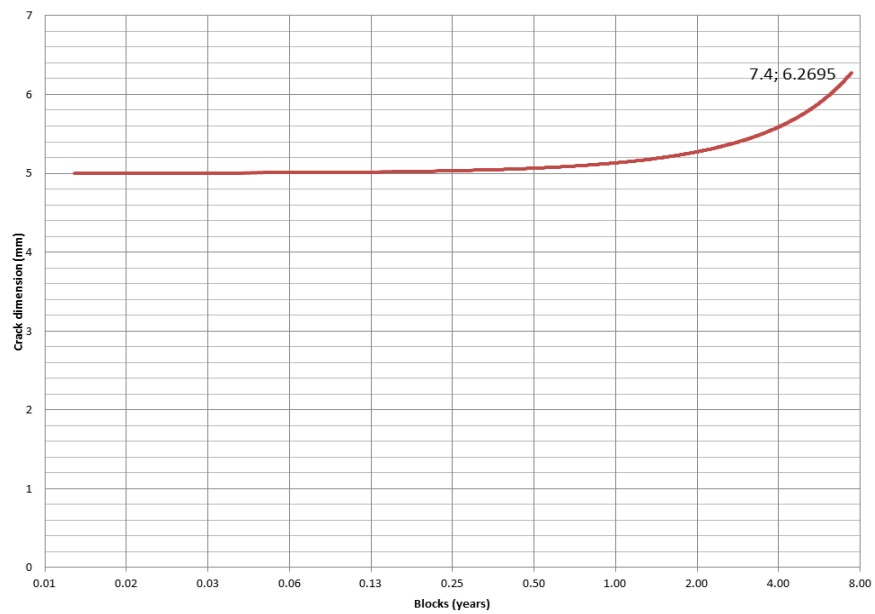
Fig.A4.14. *Fatigue assessment - Flat Plate – Long Surface Flaw-4 – FP-LSF-4*
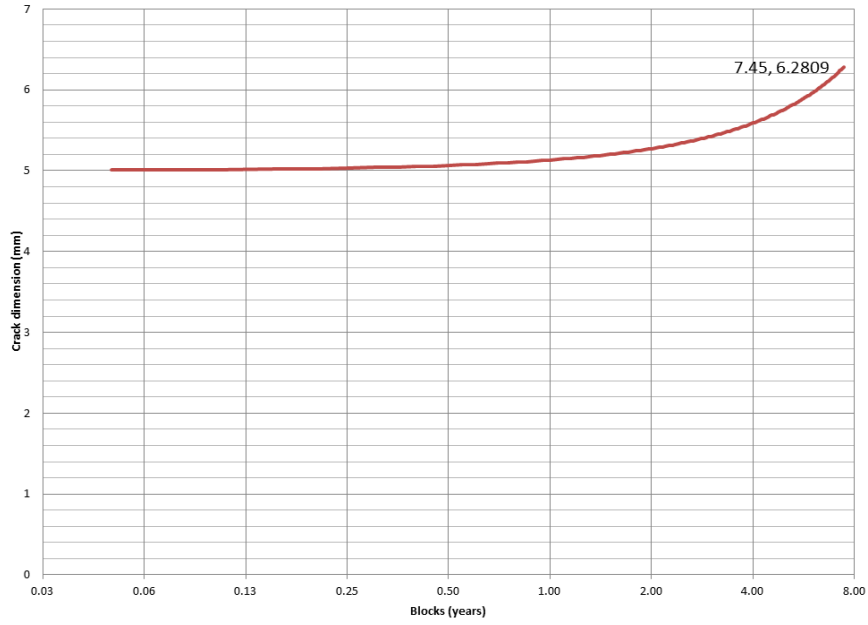
Fig.A4.15. *Fatigue assessment - Flat Plate – Long Surface Flaw-5 – FP-LSF-5*
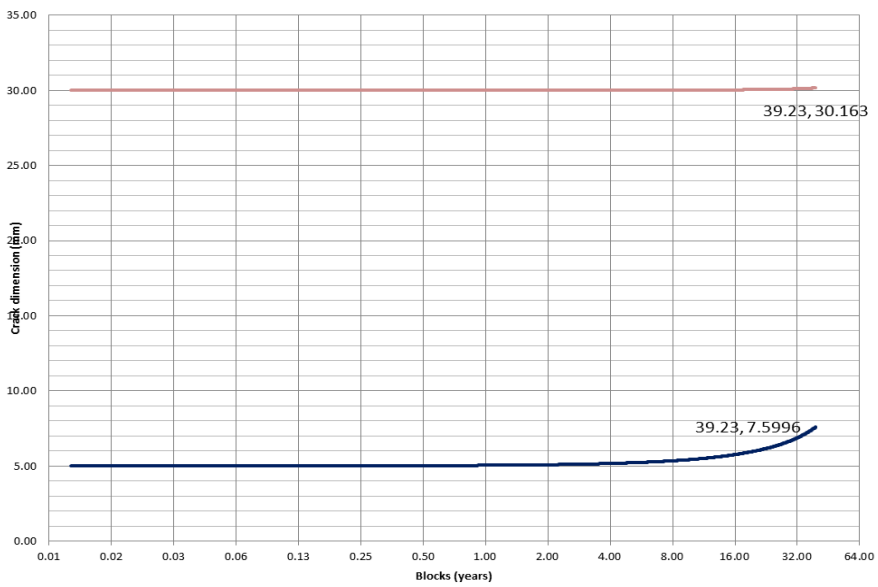
Fig.A4.16. *Fatigue assessment - Flat Plate – Embedded flaw-1 – FP-BF-1*
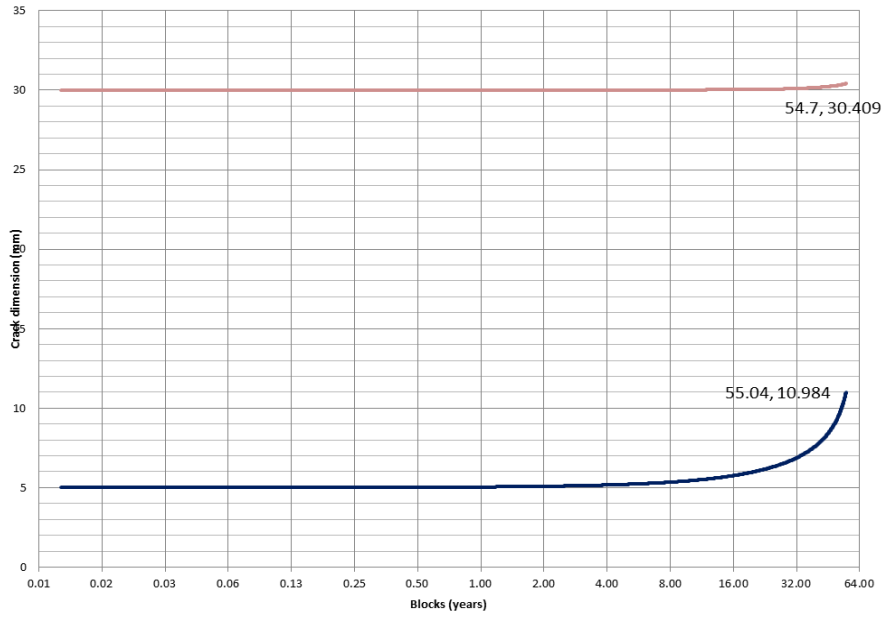
Fig.A4.17. *Fatigue assessment - Flat Plate – Embedded flaw-2 – FP-BF-2*
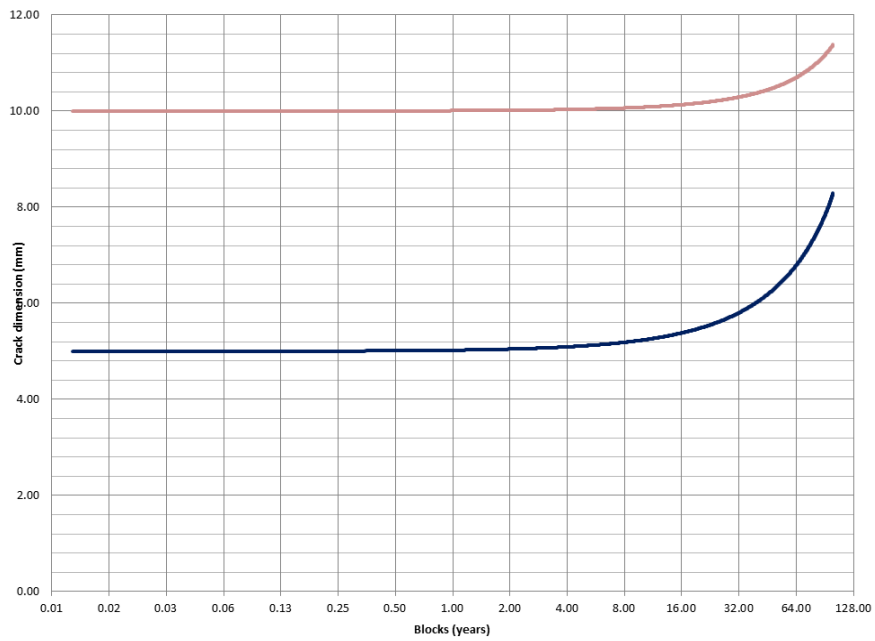
Fig.A4.18. *Fatigue assessment - Flat Plate – Embedded flaw-3 – FP-BF-3*
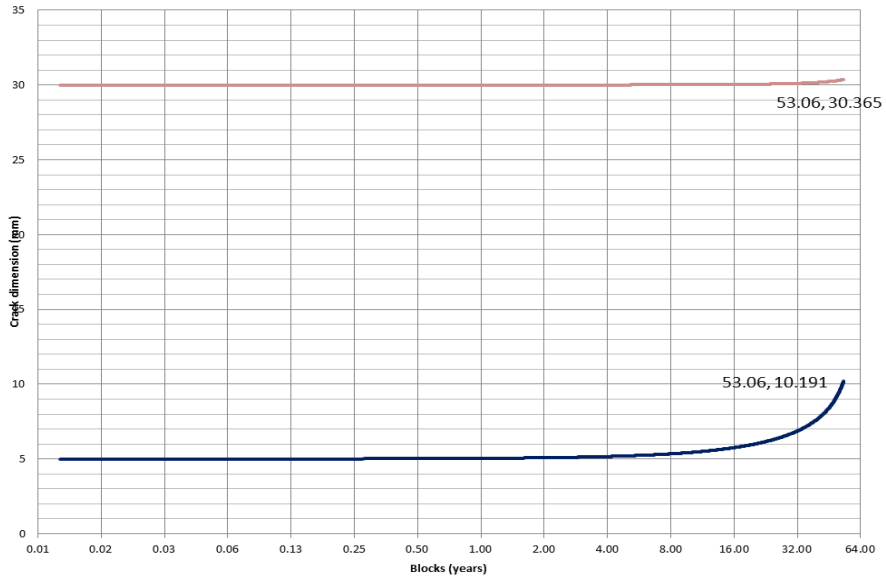
Fig.A4.19. *Fatigue assessment - Flat Plate – Embedded flaw-4 – FP-BF-4*
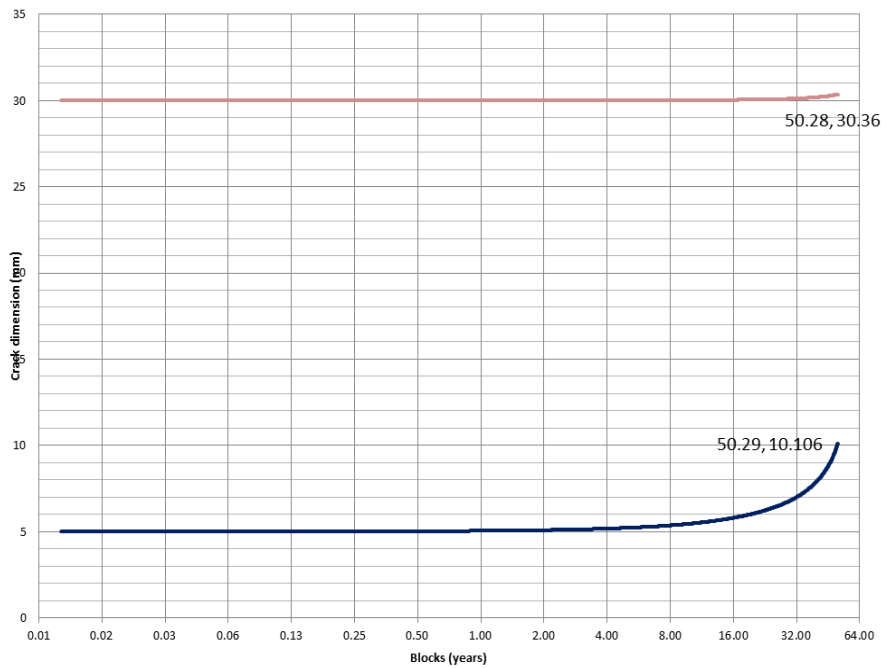
Fig.A4.20. *Fatigue assessment - Flat Plate – Embedded flaw-5 – FP-BF-5*
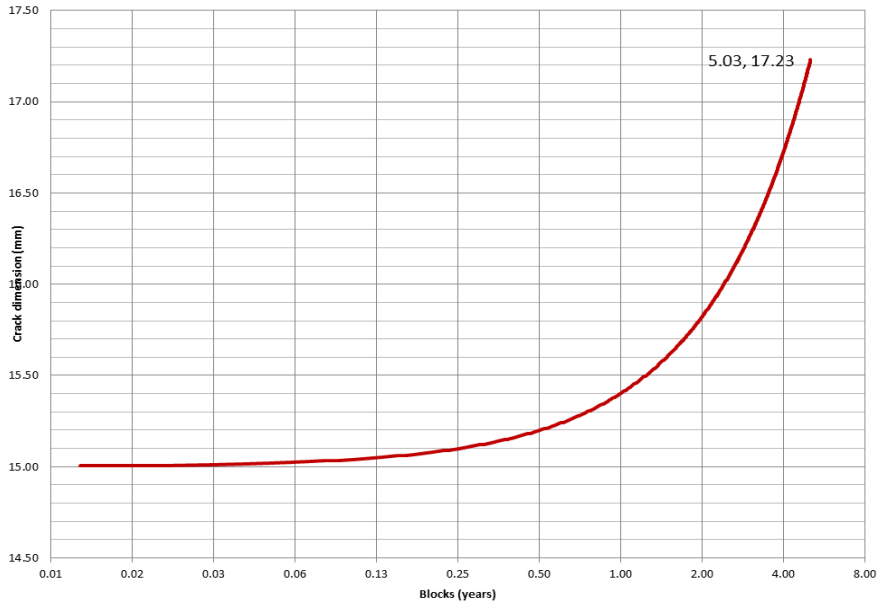
Fig.A4.21. *Fatigue assessment - Flat Plate – Edge flaw-1 – FP-EF-1*
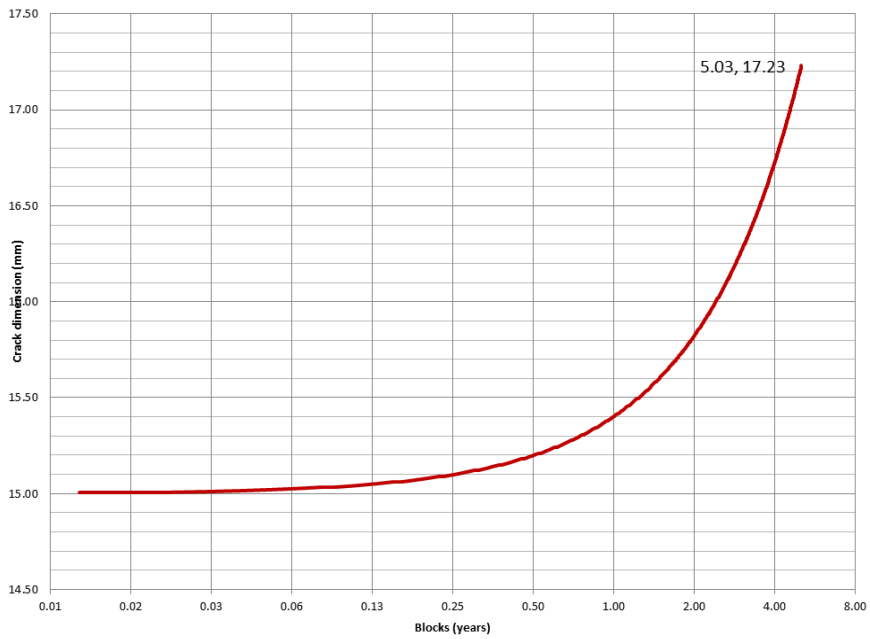
Fig.A4.22. *Fatigue assessment - Flat Plate – Edge flaw-2 – FP-EF-2*
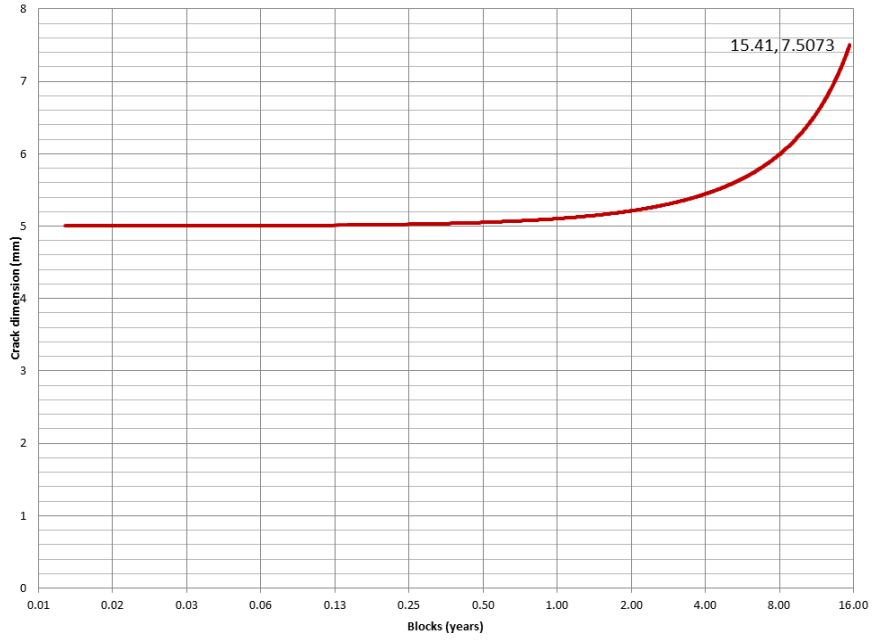
Fig.A4.23. *Fatigue assessment - Flat Plate – Edge flaw-3 – FP-EF-3*
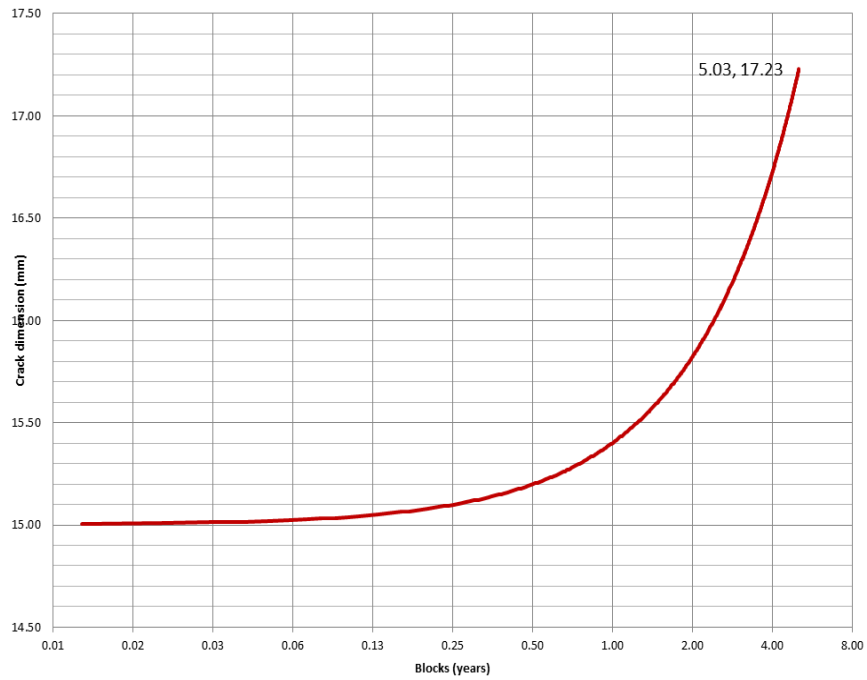
Fig.A4.24. *Fatigue assessment - Flat Plate – Edge flaw-4 – FP-EF-4*
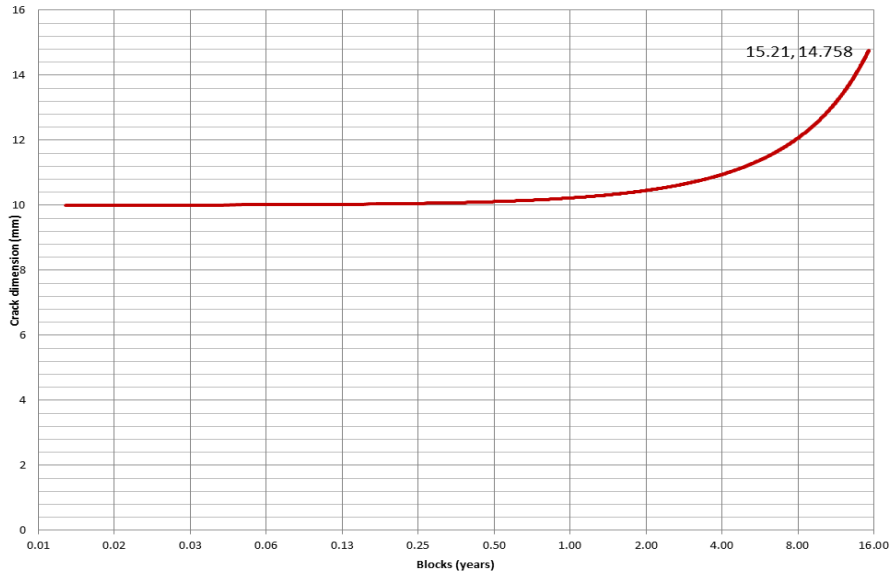
Fig.A4.25. *Fatigue assessment - Flat Plate – Edge flaw-5 – FP-EF-5*
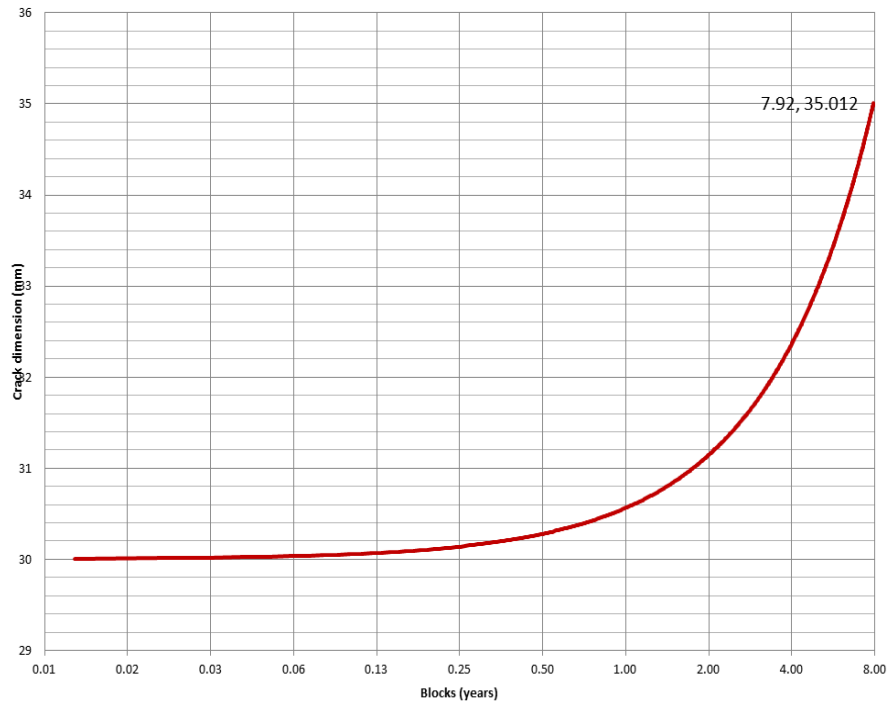
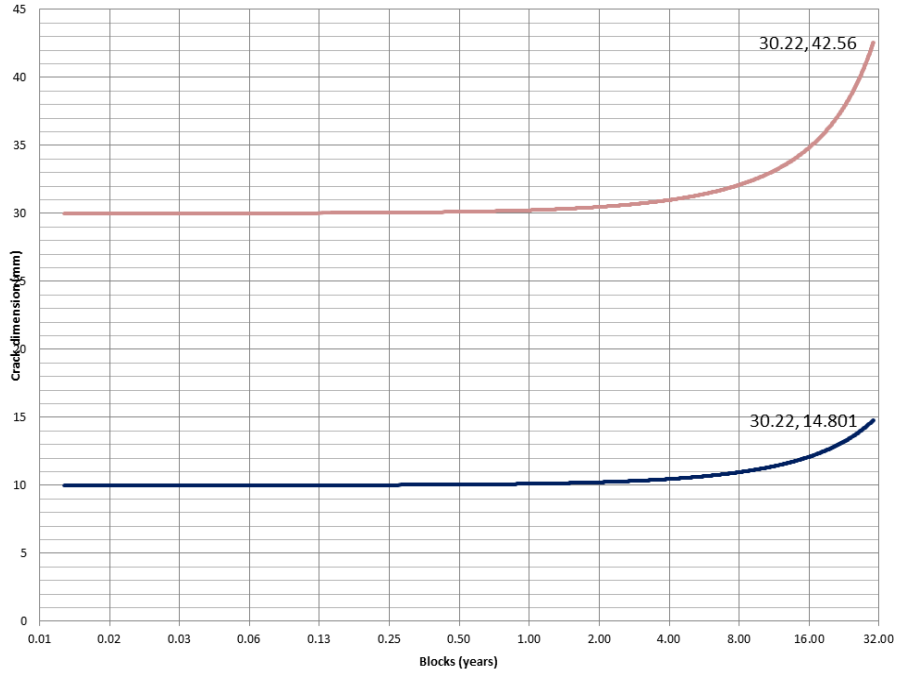Fig.A4.26. *Fatigue assessment – Curved Shell Axial – Through Thickness flaw-1 – CSAF-TFF-1*
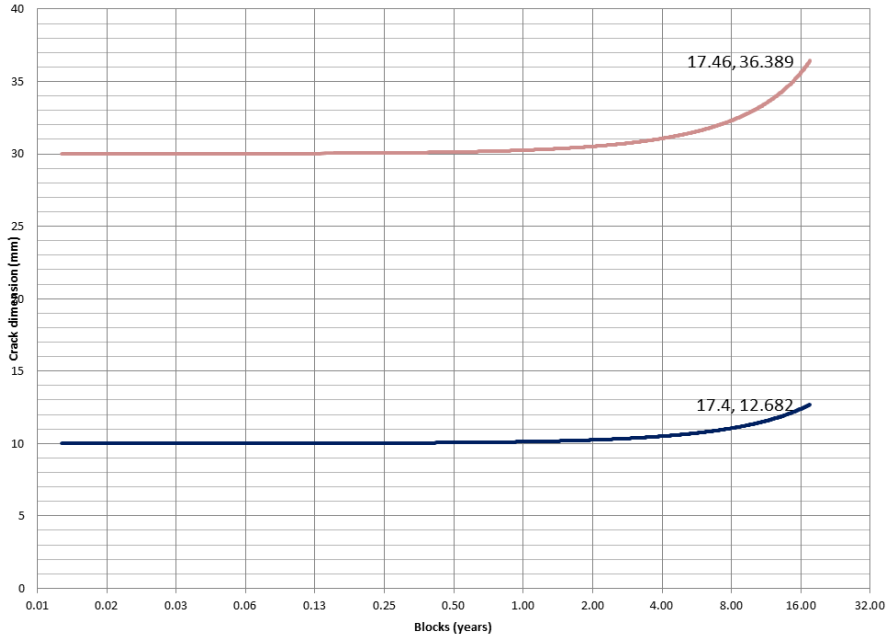
Fig.A4.27. *Fatigue assessment – Curved Shell Axial – Internal Surface flaw-1 – CSAF-ISF-1*
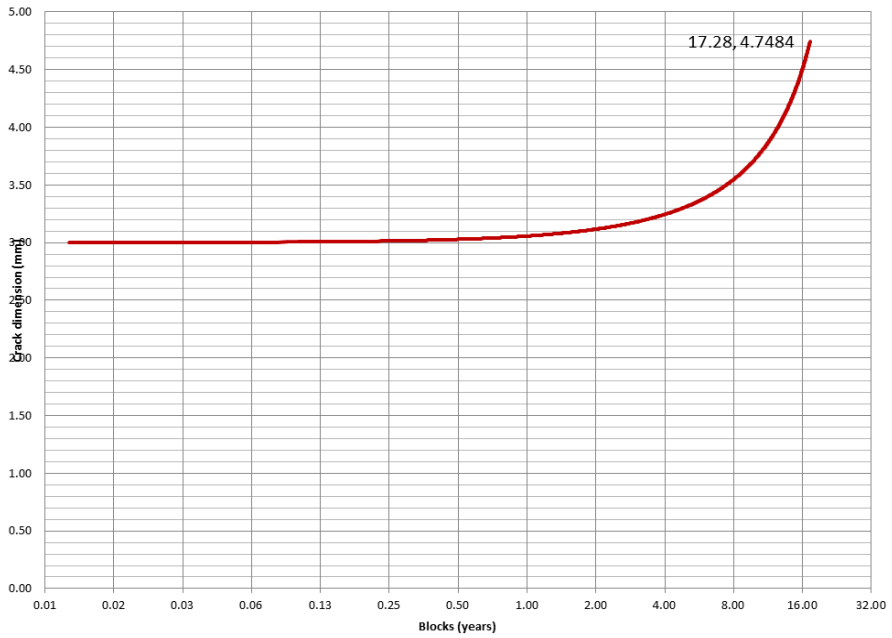
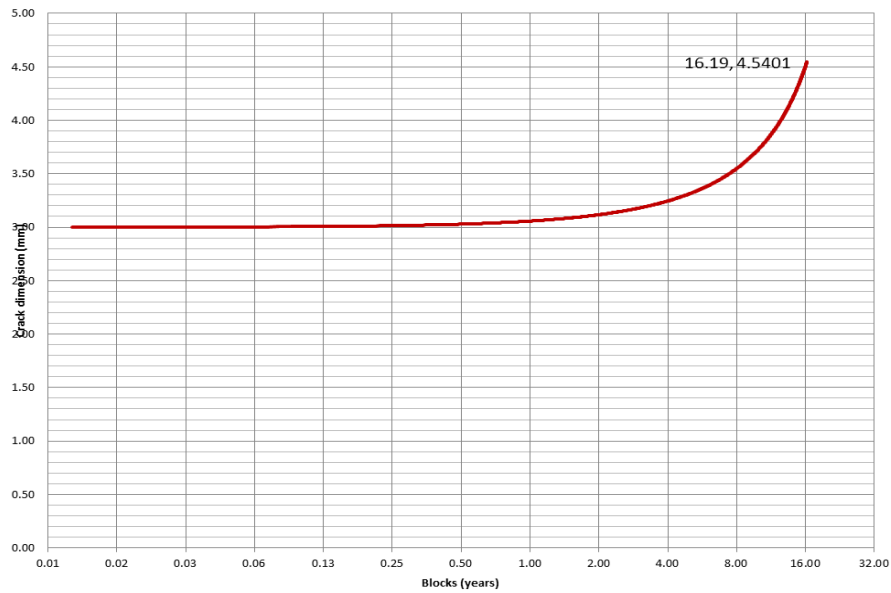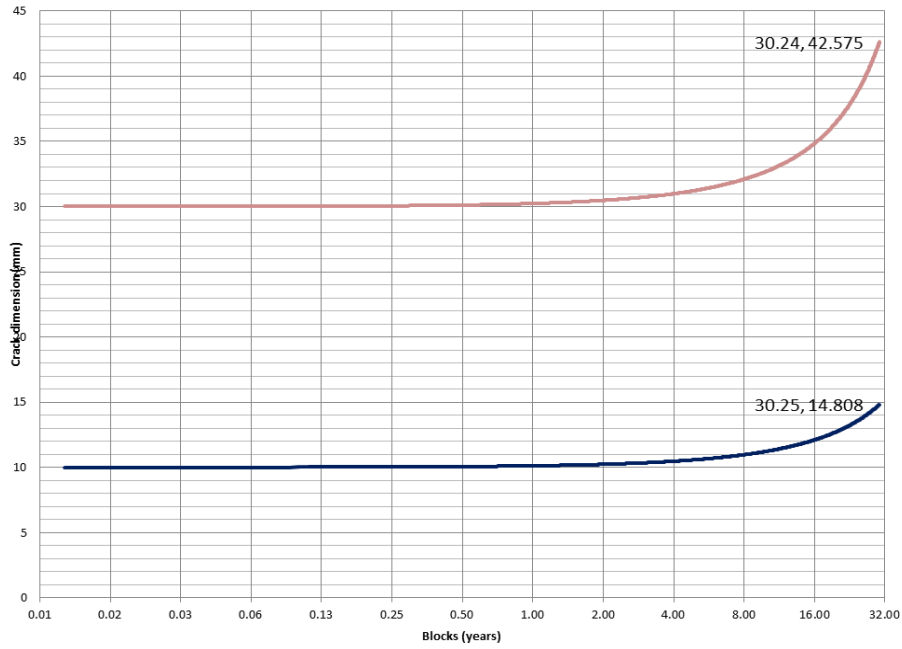Fig.A4.28. *Fatigue assessment – Curved Shell Axial – Long Internal Surface flaw-1 – CSAF-LISF-1*
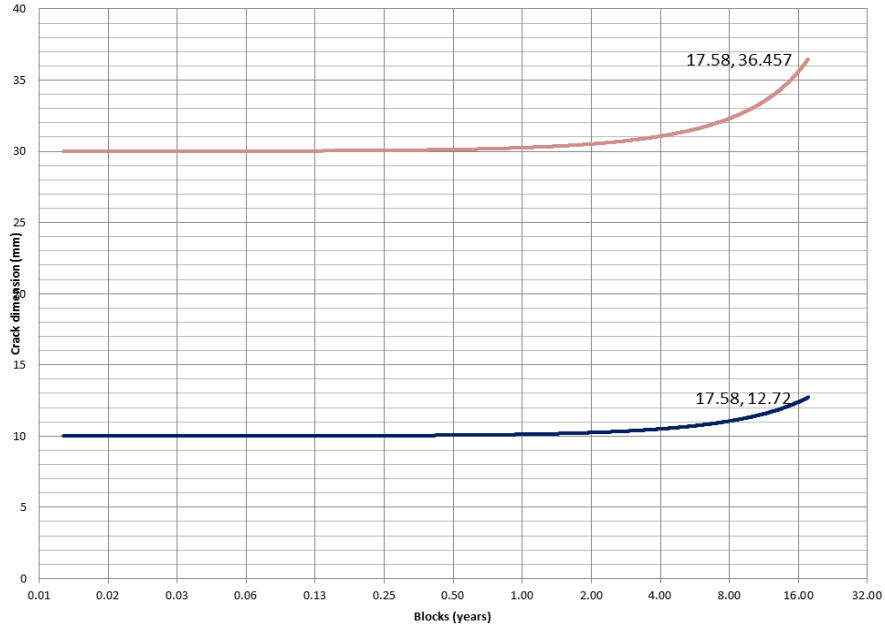
Fig.A4.29. *Fatigue assessment – Curved Shell Axial – External Surface flaw-1 – CSAF-ESF-1*
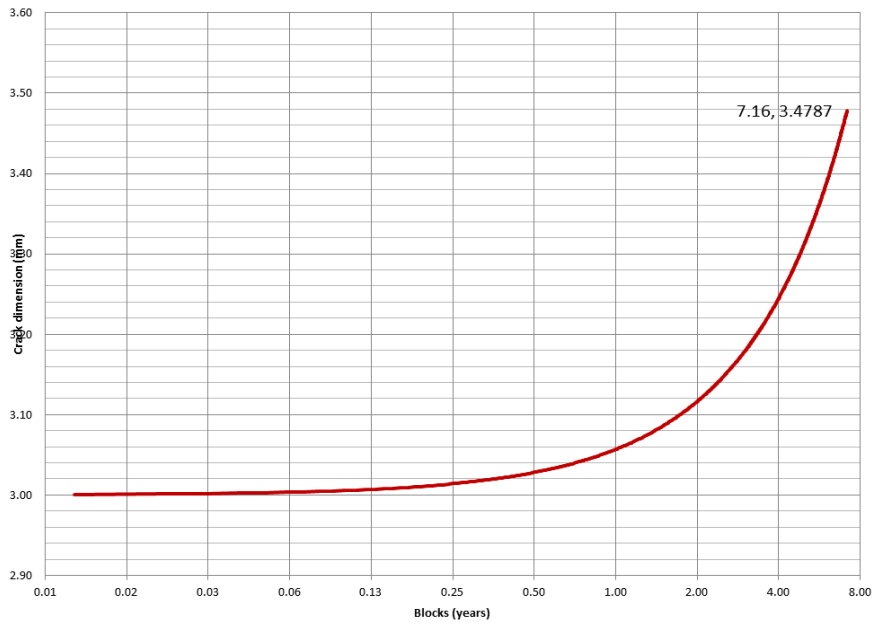
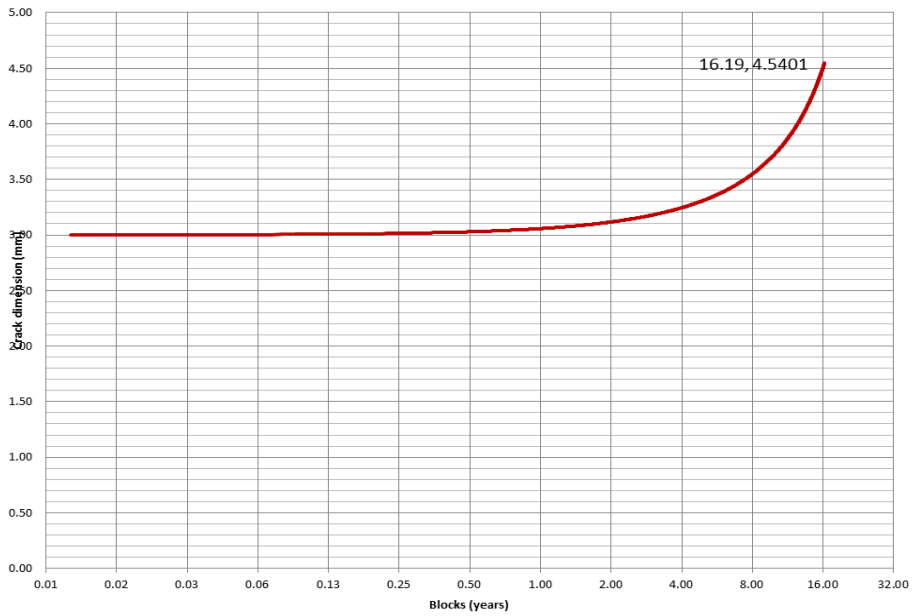Fig.A4.30. *Fatigue assessment – Curved Shell Axial – Long External Surface flaw-1 – CSAF-LESF-1*
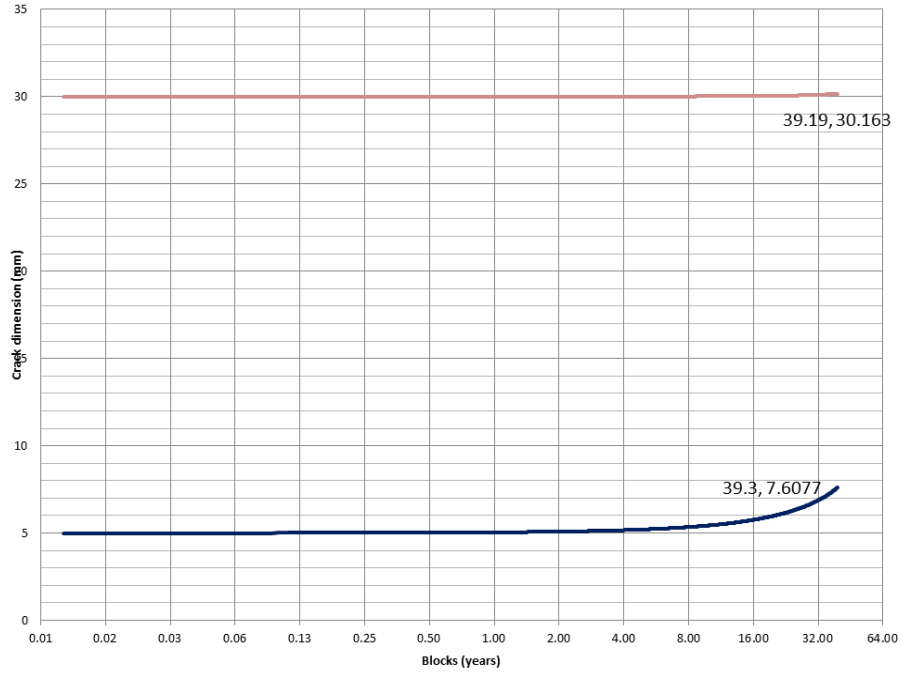
Fig.A4.31. *Fatigue assessment – Curved Shell Axial – Embedded flaw-1 – CSAF-BF-1*
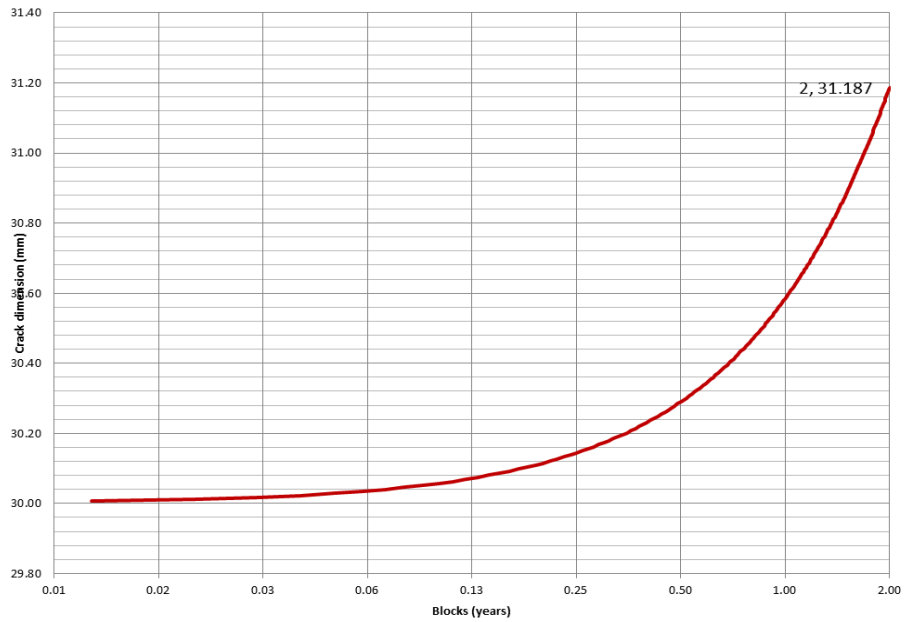
Fig.A4.32. *Fatigue assessment – Cylinder Axial – Through Thickness flaw-1 – CAF-TTF-1*
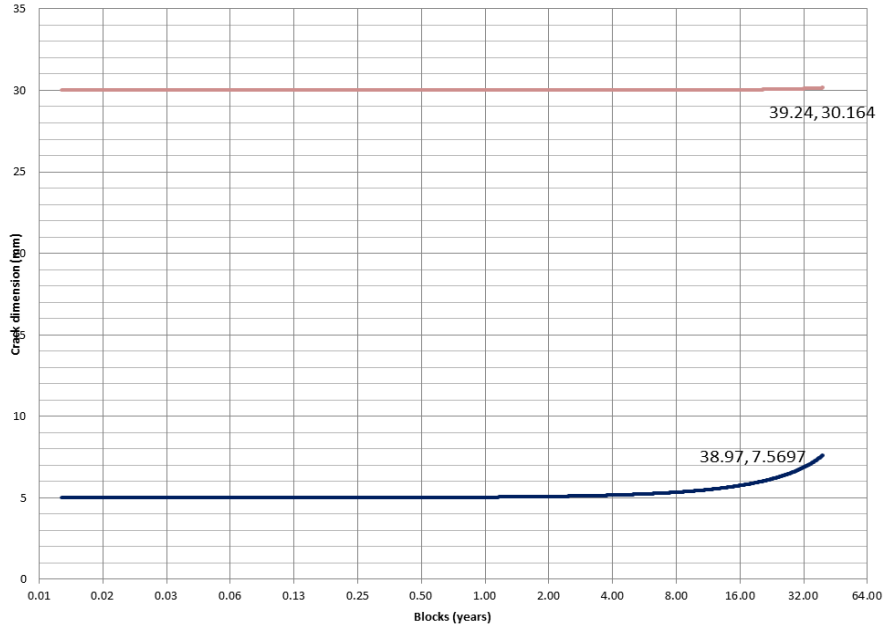
Fig.A4.33. *Fatigue assessment – Cylinder Axial – Embedded flaw-1 – CAF-BF-1*
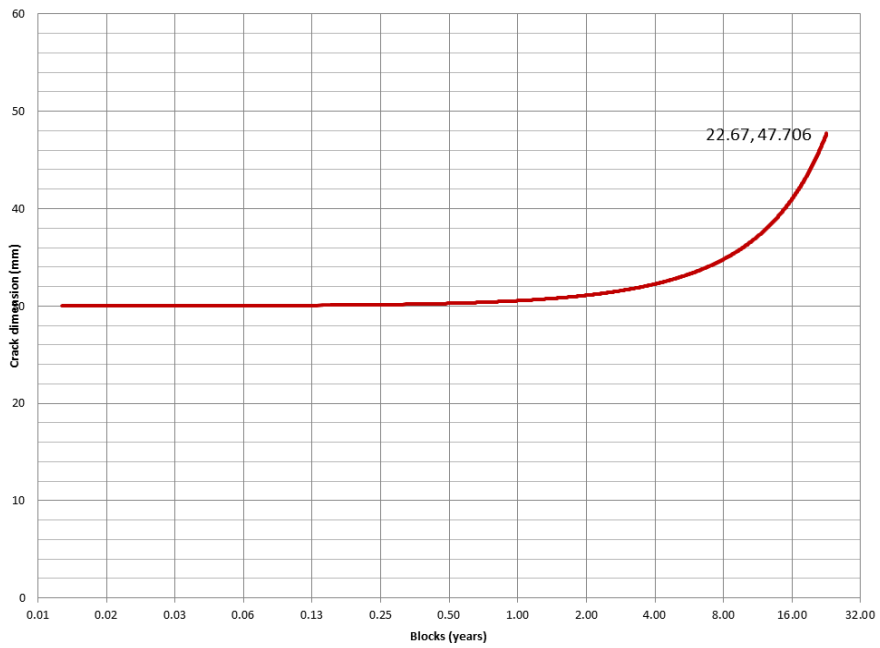
Fig.A4.34. *Fatigue assessment – Curved Shell Circumferential – Through thickness flaw-1 – CSCF-TTF-1*

Fig.A4.35. *Fatigue assessment – Curved Shell Circumferential – Internal Surface flaw-1 – CSCF-ISF-1*

Fig.A4.36. *Fatigue assessment – Curved Shell Circumferential – Fully Circumferential Internal Surface flaw-1 – CSCF-FCISF-1*
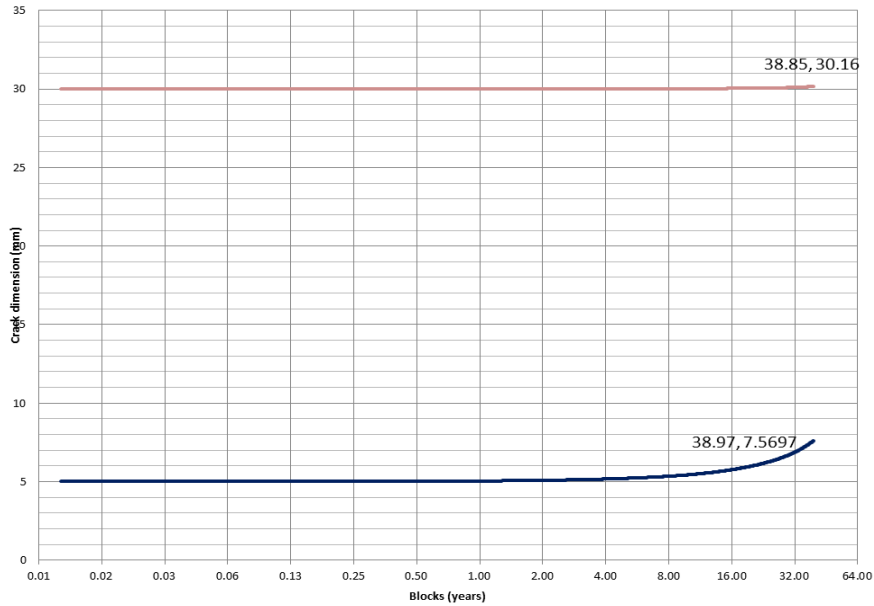
Fig.A4.37. *Fatigue assessment – Curved Shell Circumferential – External Surface flaw-1 – CSCF-ESF-1*

Fig.A4.38. *Fatigue assessment – Curved Shell Circumferential – Fully Circumferential External Surface flaw-1 – CSCF-FCESF-1*

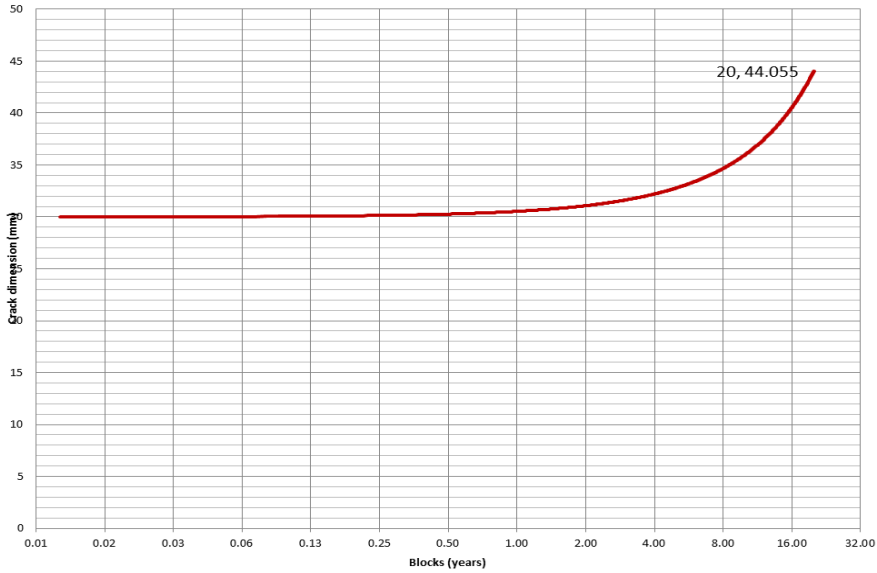Fig.A4.39. *Fatigue assessment – Curved Shell Circumferential – Embedded flaw-1 – CSCF-BF-1*

Fig.A4.40. *Fatigue assessment – Cylinder Circumferential – Through Thickness flaw-1 – CCF-TTF-1*
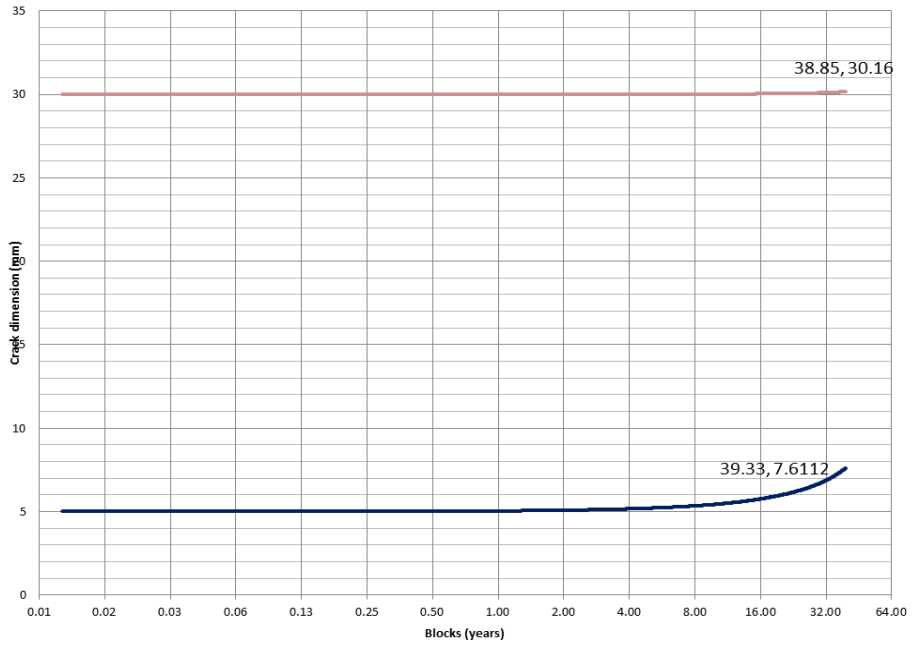
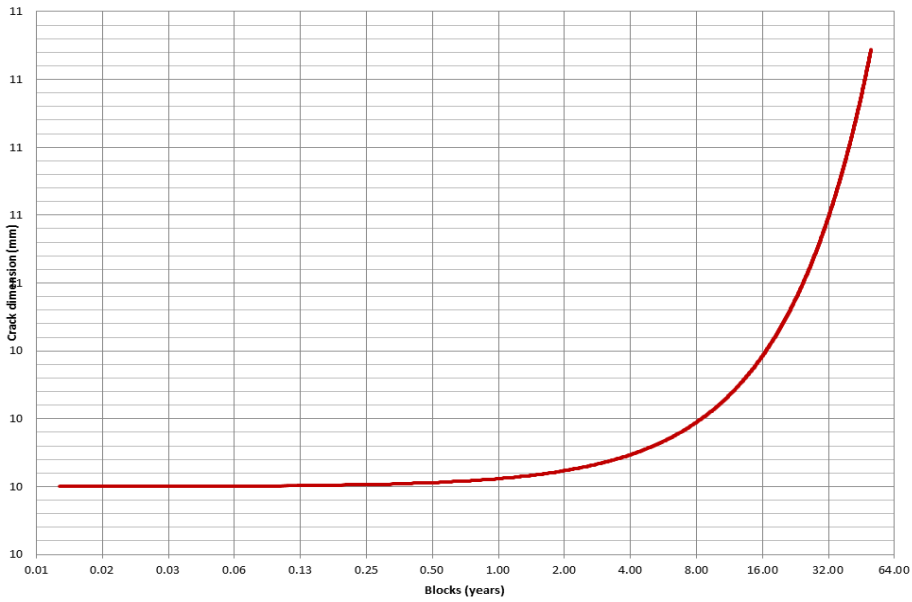Fig.A4.41. *Fatigue assessment – Cylinder Circumferential – Embedded flaw-1 – CCF-BF-1*

Fig.A4.42. *Fatigue assessment – Cruciform Welded Joint – Through Thickness flaw -1 – CWJ-TTF-1*
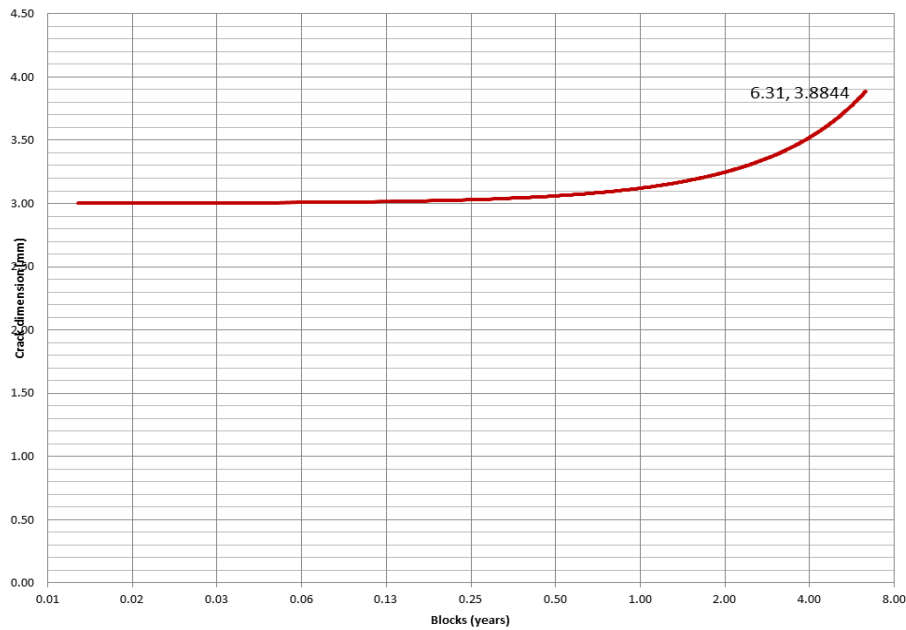
Fig.A4.43. *Fatigue assessment – Cruciform Welded Joint – Weld Toe flaw -1 – CWJ-WT-1*

Legend

——— Line for description of the crack / flaw height

——— Line for description of the crack / flaw length

Note

For ease of representation, for each graphic plot, the values of the X axis are presented in logarithmic scale – base 2.